Theoretical Modeling from Functionalized Gold Nanoparticles to Repair of Lesions in DNA for cancer radiotherapy

Chen Hui Chan

Numéro National de Thèse : 2019LYSEN020

THESE de DOCTORAT DE L'UNIVERSITE DE LYON

opérée par

l'Ecole Normale Supérieure de Lyon

Ecole Doctorale N°206
Ecole Doctorale de Chimie (Chimie, Procédés, Environnement)

Spécialité de doctorat : Chimie

Discipline : Chimie théorique

Soutenue publiquement le 09/07/2019, par :

Chen-Hui CHAN

Theoretical Modeling from Functionalized Gold Nanoparticles to Repair of Lesions in DNA for Cancer Radiotherapy

Modélisation théorique depuis les nanoparticules d'or fonctionnalisées vers la réparation des lésions dans l'ADN pour le traitement du cancer par radiothérapie

---

Devant le jury composé de :

Mme Christine MOTTET	Directrice de Recherche Université Aix-Marseille	Rapporteure
M. Florent BARBAULT	Maître de Conférence Université Paris Diderot	Rapporteur
Mme Corinne LACAZE-DUFAURE	Professeure ENSIACET	Examinatrice
M. Christophe MORELL	Professeur Université de Lyon	Examinateur
Mme Elise DUMONT	Professeure Ecole Normale Supérieure de Lyon	Directrice de thèse
M. David LOFFREDA	Directeur de Recherche Ecole Normale Supérieure de Lyon	Co-encadrant de thèse

Remerciements

Je remercie tout d'abord le Labex Primes pour avoir financé cette thèse, et Mme Chantal Andraud pour m'avoir accueilli durant mes trois année de thèse au sein du Laboratoire de Chimie de l'ENS de Lyon.

J'addresse un grand remerciement à mes deux directeurs de thèse, Pr. Elise Dumont et Dr. David Loffreda pour m'avoir guidé tout au long de ce travail. Vos disponibilités, vos conseils et vos rigeurs scientifiques ont été une aide précieuse pour moi qui me permettait de réaliser ma thèse dans un cadre optimal. Encore merci!

Je souhaite addresser mes remerciements à l'ensemble des membres du jury. Merci au Pr. Christophe Morell d’avoir accepté de présider le jury de cette thèse. Merci à Dr. Christine Mottet et Dr. Florent Barbault d'avoir accepté de rapporter ce manuscit. Je remercie également Pr. Corinne Lacaze-Dufaure pour avoir participé à mon jury de thèse.

Je souhaite ensuite remercier toutes les personnes avec qui j'ai collaboré durant ces trois années: Dr. Jean-Luc Ravanat, Dr. Thierry Douki, Dr. Antonio Monari, Dr. François Dehez, Cecilia Hognon, Pr. Michaël Beuve, Dr. Floriane Poignant, et Dr. Ricardo Ramos. Je remercie notamment Dr. Emmanuelle Bignon pour son aide en calculs de dynamique moléculaire classique.

Je remercie les secrétaires et gestionnaires du laboratoire: Edwige Royboz, Marie-Françoise Guiot et Damien Seon. Merci à Dr. Tao Jiang et Christian Melkonian d'avoir m’aidé à résoudre les problèmes techniques.

I also want to thank my past and present co-workers: Carles, Kamila, Martin, and all the PhD students and post-docs of this lab for all the nice moments we spent together. Special thanks to Qing Yi, Chong Zhi and all my other Chinese friends of ENSL for the good friendship.

Finally, I would like to thank my family and my close friends: Wei Kiat, Wei Shyon, Hie Ming, Azim and Niels for their support and encouragement over the past few years.

Résumé

Le potentiel des nanoparticules pour améliorer l'efficacité de la radiothérapie est démontré par de nombreuses études expérimentales in vivo et in vitro. Ces particules métalliques mettent en jeu des atomes de numéro atomique élevé qui augmentent l'effet de la radiosensibilisation. La réaction en jeu est la radiolyse de l'eau: une fois excitées par un rayon X, elles génèrent des électrons secondaires et des espèces réactives oxygénées (ROS) qui amplifient les dégâts d'ADN et mènent à une plus grande destruction des cellules cancéreuses.

Les nanoparticules d'or (AuNPs) sont le radiosensibilisateur le plus étudié aujourd'hui car elles sont généralement peu toxiques et elles ont une longue durée de circulation sanguine grâce à la fonctionnalisation des ligands hydrophiles. Pour une efficacité thérapeutique plus optimale, plusieurs propriétés des AuNPs doivent être prises en compte lors de la synthèse comme leur taille, leur forme et leur surface qui sont suspectibles d'influencer ses effets catalytiques (sites actif) et son interaction avec le rayonnement dans l'environnement biologique (majoritairement de liquide d'eau). Ces aspects structuraux ne sont pas encore examinés dans l'état de l'art, ni expérimentalement ni théoriquement.

Ce travail de thèse a pour but de rationaliser le comportement et la stabilité de AuNPs dans un environnement chimique ou biologique avant l'irradiation par des outils de modélisation théorique. Dans un premier temps, nous nous sommes intéressés à la stabilité des polyèdres d'or dans la gamme de 1- 3.4 nm, une gamme ou l'effet radiosensibilisant est intéressant en fonction de leur taille et leur morphologie. Nous comparons nos résultats obtenus à l'aide de la théorie de la fonctionnelle de la densité (DFT) qui tient compte de la correction de dispersion semi-empirique (DFT-D3) avec d'autres résultats issus de la littérature obtenus principalement par les méthodes d'optimisation globale. Nous étudions ensuite le comportement de ces nanoparticules dans un environnement biologique (hydratation) et chimique modèle (PEGylation), et la combinaison des deux environnements. Quand les nanoclusters de 0.9-1.8 nm sont en interaction avec une couche de molécules d'eau à saturation, nous avons montré qu'il y a une transformation de NPs métastables (dans le vide) telles que l'ino-décaèdre en NPs métastables plus favorables telles que l'icosaèdre. Alors qu'en présence d'une couche de ligands PEG, la liaison forte Au-S et

les liaisons hydrogène entre les ligands entraînent une déformation significative de la morphologie de la nanoparticule, à savoir une stellation du décaèdre Au_{54}. La déformation induite par la PEGylation est encore plus forte en présence de molécules d'eau co-adsorbées. Par ailleurs, nous avons montré que les ligands PEG promeuvent le confinement de quelques molécules d'eau à proximité des AuNPs. Nos conclusions ouvrent des perspertives intéressantes pour la modélisation théorique de la radiolyse de l'eau. Les résultats DFT obtenus à partir de nos modèles permettront aussi d'affiner les simulations Monte-Carlo mises au point par les collègues de l'Institut de Physique Nucléaire de Lyon (Pr. M. Beuve).

Parallèlement à ces études, nous nous sommes intéressés à la caractérisation de différents types de lésions d'ADN induites par les ROS et aussi par le rayonnement ultraviolet, plus spécifiquement sur la formation et la réparation difficile de certaines lésions observées expérimentalement, qui seraient à l'origine de la mutation de l'ADN. Deux projets ont été menés dans ce contexte, pour lesquels la méthode de dynamique moléculaire classique a été utilisée. Premièrement, nous démontrons l'interaction d'un peptide trilysine (KKK) avec un oligonucléotide qui pourrait conduire à la formation de pontage d'ADN-polyamine. Ensuite, le deuxième projet porte sur la rationalisation de differents taux de réparation de dimères de cyclobutane pyrimidine (CPD): T<>T, T<>C, C<>T, et C<>C en présence de l'enzyme de reconnaissance DDB2 à l'échelle atomique.

Table of Contents

Chapter 1: General Introduction

The importance of deoxyribonucleic acid (DNA) to store biological information within human body is unquestionable. The sequence of the four nucleobases of the double helix, adenine (A), cytosine (C), guanine (G), thymine (T) encodes the genetic information which is essential for growth, development, functioning, and reproduction of any living organism. Nevertheless, DNA stability is continuously being threatened by many damaging agents originating from exogenous (such as ultraviolet from sun light) and endogenous ones (such as reactive oxygen species (ROS) generated by oxidative stress). At least 10,000 and up to 1 million of structural modifications, or so-called DNA lesions are produced per cell everyday[1], many of them being rare, yet extremely mutagenic and carcinogenic. If not recognized and removed efficiently and rapidly by DNA repair enzymes, these lesions can be replicated in an uncontrolled way, ultimately leading to the development of cancer but also of neurodegenerative and ageing diseases. A detailed understanding of mechanistic pathways at the atomic level leading to the formation of DNA lesions is therefore very important for both the treatment and prevention of cancer.

A prerequisite is to understand the mechanisms of DNA lesions induction, and also the interaction of damaged oligonucleotides with repair enzymes. Many structures of DNA repair complexes are available in the PDB databank, yet the DNA repair machinery turns out to be very sophisticated and many insights are currently lacking. X-ray structural studies completed by molecular dynamics simulations[2] probably offer the most insightful investigations. In fact, obtaining X-ray structures of DNA repair enzymes caught in act remains tedious. Computational biochemistry can start from one X-ray structure to evaluate free energy profiles related to repair, or to investigate the effects of protein mutation or sequence effects.

To date, cancer remains a difficult disease to cure, and it is expected that the number of new cases of cancer in human beings will be risen by 70% in the next two decades, according to World Health Organization (WHO). Radiotherapy is the most commonly used approach in cancer treatment, with 50 to 60% of cancerous patients being treated by radiotherapy, alone or combined with others treatments. However, within such technique, the killing of cancerous cells is not selective, since ionizing radiation can damage as well the healthy tissues surrounding the tumors. An effective way to improve radiotherapeutic outcomes is the use of metallic nanoparticles based on heavy atoms, which can act as both radiosensitizers and radical dose-enhancing agents. Indeed, water radiolysis (an indirect reaction of ionizing radiation which generates highly reactive free radicals) can be enhanced when the nanoparticles are irradiated in aqueous media (biological natural environment), leading to an increased production of ROS responsible for cancerous cell death.

Due to many exciting chemical and physical properties, high Z gold nanoparticles (AuNPs) have been studied extensively for their radiosensitizing ability. With the incredible progress of nanotechnology, gold nanomaterials with diverse size and shape, such as sphere, rod, and star can be synthesized. Nevertheless, the synthesis of AuNPs with well-defined geometry, optimal and cost-efficient for radiotherapy applications, requires in part the knowledge of their relative stability in vacuum or in the presence of synthesis environment. This can be investigated experimentally by using high-angle annular dark-field imaging (HAADF-STEM) measurements, or explored theoretically by Heuristic approaches using accurate predictions from density-functional theory (DFT) or by global optimization methods based on well-parametrized and effective semi-empirical potentials.[3] Although many efforts have been devoted to advance on this question at the atomic scale, the relative stability of AuNPs is still a debate due to controversies regarding the results available in the literature.

The surface of metallic nanoparticles can be further functionalized by thiolated ligands in order to improve their stability and biocompatibility. Poly-ethylene glycol (PEG) is the most widely used ligand in experiments, despite the fact that the strong Au-S bond and high grafting density may have a strong effect on the NP structures. The size and morphology of those PEGylated AuNPs can tune significantly their catalytic properties and dose-enchancement, especially when the AuNPs are in the fluxional regime (below 4 nm).[4] Furthermore, the uptake of AuNPs by cancerous cell membrane, is an important process which determines the rate of radiosensitization, and it is also dependent on NP size and morphology.[5] Therefore, for radiotherapy applications, the design of functionalized AuNPs with an optimal therapeutic property is highly desired.

Up to date, little is known about the mechanisms of water radiolysis occurring at the proximity of the AuNPs, from both experimental and theoretical standpoints. The role of the synthesis ligands decorating the nanoparticles, as well as their synergy and interaction with the biological environment (mainly water) are open questions. The mechanisms of internalization of the AuNPs inside the targeted cancerous cells are also the subject of difficult scientific questions, apart from the understanding of the DNA lesions and damages caused by free radical and reactive oxygen species.

The exploration of NPs properties as radiosensitizers is one of the main areas of research within the framework of LABEX PRIMES (Physics, Radiobiology, Imaging and Simulation). This work was supported by the LABEX PRIMES (ANR-11-LABX-0063) of Université de Lyon, within the program "Investissements d'Avenir" (ANR-11-IDEX-0007) operated by the French National Research Agency (ANR). Some of the multidisciplinary research activities include on the one hand, the synthesis, characterization of metallic-based (iron, gadolinium and gold) nanoparticles, and the evaluation of their radiosensitization efficiency in vitro and in vivo. On the other hand, as a predictive tool complementary to experiments, Monte Carlo (MC) simulations are performed in the framework of LABEX PRIMES to examine the enhancement of ROS

dose and the physico-chemical processes which are radio-induced in the presence of nanoparticles. However, to include the effect of water environment in contact with heavy element, the lack of accurate parameters provided at the atomic scale is a limitation in MC simulations since information concerning the electronic structures at the AuNPs/water interface are scarce.

The purpose of the present thesis is to provide at the theoretical level, dynamical and mechanical features of damaged DNA which contribute in many biological processes linked to cancer. Simultaneously we aim to evaluate AuNPs stability in the presence of biological and chemical environment in the context of radiotherapy by using theoretical approaches at the atomic scale. By developing theoretical models, one key objective of this thesis is also to open the scientific discussion and exchanges between three communities of theoreticians working on the topic of radiotherapy at various scales (from the atom to the cell scale). One outcome is the generation of a set of ab initio results to improve the parametrization and predictive power of MC simulations and related code developed by colleagues at IPNL. This re-parametrization is expected to improve their relevance with respect to experiments. This thesis has been developed in the Theory group of Laboratory of Chemistry of Ecole Normale Supérieure de Lyon. Most of the calculations were performed using the data center and cluster of the Pôle Scientifique de Modélisation Numérique (PSMN) at Lyon. The research works have been effected in close collaboration with Dr. Jean-Luc Ravanat and Dr Thierry Douki (experimentalists at CEA de Grenoble), Dr. Antonio Monari and Dr François Dehez (theoreticians at University of Nancy), and Pr Michaël Beuve and Floriane Poignant (theoreticians at Institut de Physique Nucléaire in Lyon).

The outline of the manuscript is organized as follows. In Chapter 2, the state-of-the-art and the corresponding limitations are exposed. Chapter 3 introduces the computational methods employed throughout this thesis. The following three Chapters 4-6 of results are devoted to the investigation of the relative stability of AuNPs at three levels of

description by using DFT: i) AuNPs in vacuum; ii) AuNPs in the presence of water monolayers (biological natural environment) and iii) AuNPs in the presence of an organic coating composed of monolayers of hydrated PEG ligands (chemical synthesis environment). The last chapter deals with the use of molecular dynamics simulations to study the association of small trilysine with DNA, and the interaction of different cyclobutane pyrimidine dimers (CPD) photo-lesions with DDB2 enzyme. The general conclusion and perspectives are finally addressed at the end of this manuscript.

References

1. Lindahl T., Barnes D. Repair of endogenous DNA damage. *Cold Spring Harb Symp Quant Biol*, **2000**, 65, 127–133.

2. Qi, Y., Spong, M. C., Nam, K., Banerjee, A., Jiralerspong, S., Karplus, M., & Verdine, G. L. Encounter and extrusion of an intrahelical lesion by a DNA repair enzyme. *Nature*, **2009**, 462(7274), 762.

3. Baletto, F. Structural properties of sub nanometer metallic clusters. *Journal of Physics: Condensed Matter*, **2018**, 31,113001.

4. Misawa, M., & Takahashi, J. Generation of reactive oxygen species induced by gold nanoparticles under x-ray and UV Irradiations. *Nanomedicine: Nanotechnology, Biology and Medicine*, **2011**, 7(5), 604-614.

5. Zhang, S., Gao, H., & Bao, G. Physical principles of nanoparticle cellular endocytosis. *ACS nano*, **2015**, 9(9), 8655-8671.

Chapter 2: Context of DNA Lesions and Role of Nanoparticles in Radiotherapy

2.1 DNA lesion, Mutation and Cancer

2.1.1 Introduction

Cancer is currently the second cause of death in the world after cardiovascular diseases. Data from the Global cancer statistics (GLOBOCAN) estimated that 18.1 million new cases and 9.6 million death was diagnosed due to cancer in 2018.[1] About 1 over 6 deaths is caused by cancer-related diseases. Among patients, lung cancer is the most frequent for men, followed by prostate and colorectal cancer, whereas for women, breast cancer is the most commonly diagnosed one, followed by colorectal and lung cancer.[1] According to World Health Organization (WHO), tobacco use, alcohol consumption, unhealthy diet, high body mass index and lack of physical activity are the main factors contributing to this deleterious disease.

DNA lesions, defined as alternations of the chemical structures of the DNA double helix, are an important cause of cancer.[2] Indeed, even though DNA is tremendously important as it acts as genetic information storage, their structures are labile and have a limited chemical stability upon exposure to different carcinogenic agents (whereas photostability is remarkable)

DNA is a polymer containing a phosphate backbone, 2-deoxyribose sugar, and a nitrogenous base. The molecule exhibits a double helix structure with two polynucleotide strands running in antiparallel directions held together by hydrogen bonds between the bases of the nucleotides.[3] There are four different bases within DNA: adenine (A), guanine (G), cytosine (C) and thymine (T). A always pairs with T and G always pairs with C, which is referred as the Watson-Crick pairing. The double helix interacts with small coiling protein called histones to form nucleosome[5], as shown in Figure 2.1 (b).

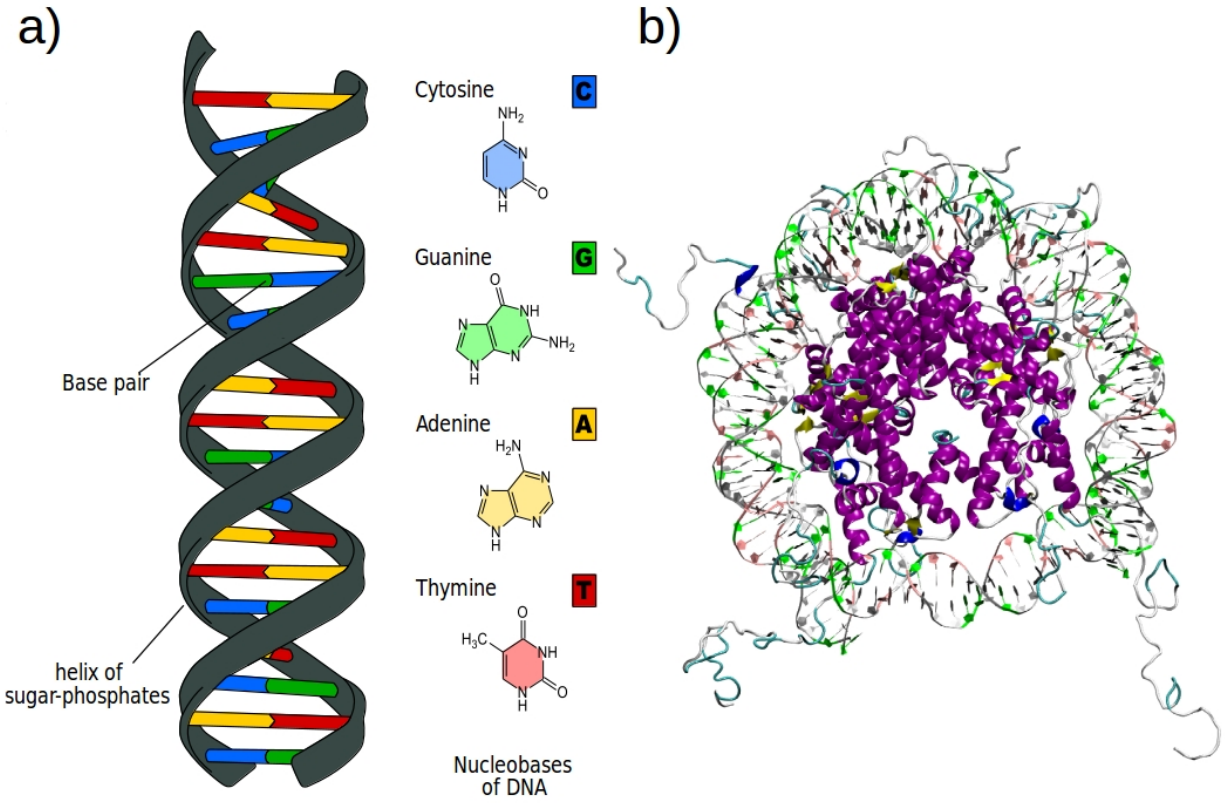

Figure 2.1. *a) Illustration of the DNA double-stranded and the nucleobases of DNA. This schema was adapted from [4]. b) a structure of nucleosome at 1.9 resolution taken from Protein Data Bank: 1kx5 [5]*

Just like any molecule, DNA can be involved in various chemical reactions that undergo structural changes of its structure and form lesions. It has been estimated that lesions can occur 10^3 to 10^6 times per cell per day.[6] To maintain genome integrity, human body possesses multiple most efficient repair systems that operate at the rate of 10^{16}-10^{18} per day to cope with such huge amount of lesions. However, if these repair machinery fails to identify and fix the different type of lesions, the accumulation of DNA lesions lead to genomic mutations and promote cell death, neurodegeneration, aging and tumor development.

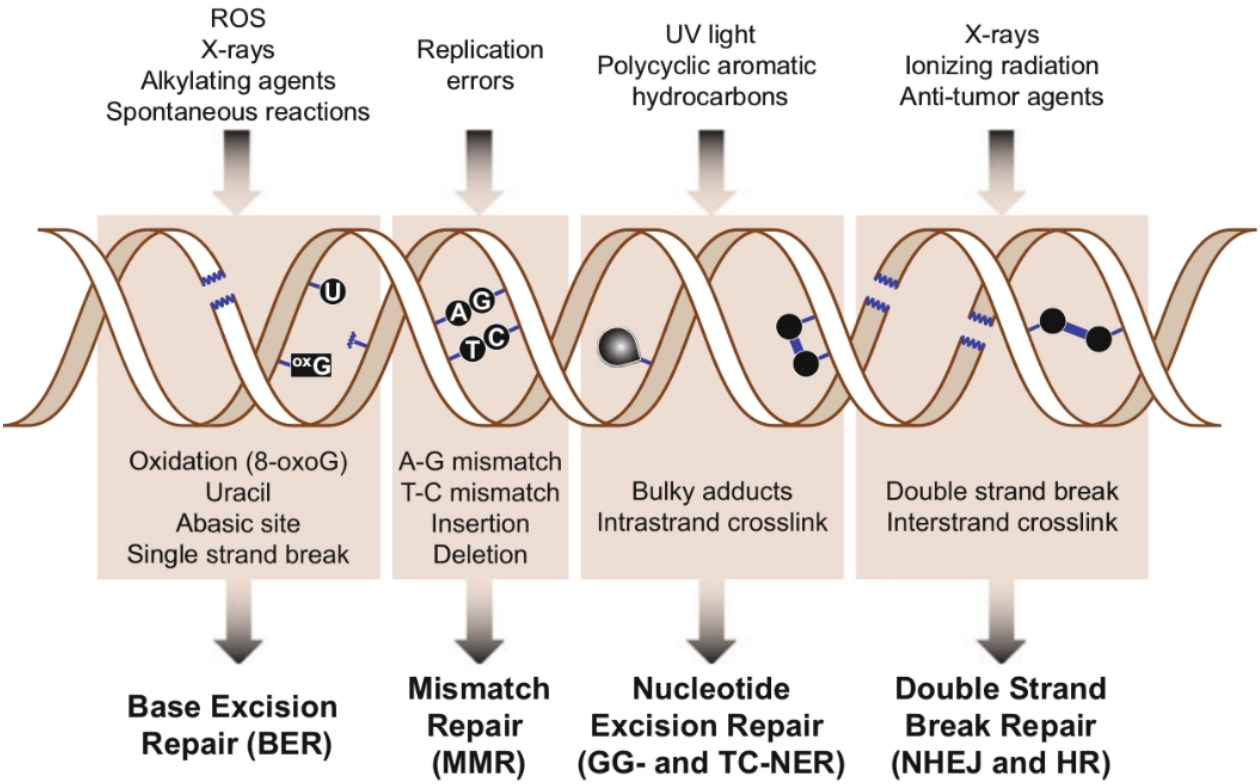

Figure 2.2. *Common DNA damaging agents, type of DNA lesions and the corresponding repair mechanisms. The figure is taken from ref [7].*

A large variety of endogenous and exogenous damaging agents results in DNA lesions. Endogenous damage is generated from natural molecules present in cells that spontaneously react with the DNA, and exogenous damage are resulting from the activity of external chemical and physical agents onto the DNA macromolecule. Figure 2.2 provides a summary of the most common sources that leads to DNA damage, the lesions formed, and the corresponding repair pathway.

2.1.2 Endogenous DNA Lesions

The majority of the DNA damage are endogenous in origin.[8] Indeed, the endogenous damages occur naturally during the cellular and hydrolytic processes. Normal cellular metabolism produced reactive oxygen species (ROS) such as superoxide anion (O_2^{-}), singlet oxygen ($^1O_2$), hydroxyl radical ($HO^{\bullet}$), hydroperoxyl radical ($HOO^{\bullet}$) and hydrogen peroxide (H_2O_2), whereas hydrolysis cleaves chemical bonds between bases and deoxyribose in DNA.

ROS react readily with heterocyclic bases of DNA and generate over 100 oxidative products.[9] 8-oxoguanine (8oxoG) is the most common oxidative adducts. It is produced by or oxidation of guanine at C8-position. 8oxoG is highly mutagenic because it can cause G●C to T●A transversion mutation during replication.[10] Apurinic/apirimidic (AP) sites are another ubiquitous endogenous lesions produced upon spontaneous hydrolysis of N-glycosylic bond linking the nucleobases to the sugar-phosphate backbone or during the removal of damaged bases by N-glycosylases.[11] The absence of nucleobase, meaning that the loss of the genetic coding information lead to mutation during replication.[12] AP sites can also lead to single strand break via beta-elimination of the phosphate residue on the 3'-side of the abasic site, or react with the exocyclic N2-amino group of guanine or aldenine on the opposite strand to form interstrand cross-link cytotoxic lesions.[13] Spontaneous deamination of DNA nucleotide bases carrying exocyclic amino groups results in the formation of highly mutagenic uracil, hypoxanthine and xanthine.[15]

DNA-protein cross-links (DPCs) cover another oxidatively generated DNA lesions, more recently characterized, that can cause deleterious biological effects such as cellular aging, mutagenesis, and carcinogenesis.[14] Polyamines have proved to react with guanine cation radical and induce such bulky lesions. Indeed, free polyamines are compounds that can be extensively found in different cell compartments, showing particular accumulation in the nuclei.[16,17,18,19] Low-mass polyamines are widespread in different living organisms,

spanning as varied organisms as bacteria, plant and superior animals. Even though they biological role has not been fully characterized yet, there are evidences suggesting their involvement in regulatory signaling, plant development, or even cancerogenesis.[20] In addition to the presence of ubiquitous free polyamines, DNA interacts non-covalently with many proteins which implies that the presence of some amino acids with amine functional groups in their side chain, such as lysine or asparagine. Furthermore, DNA coiling proteins such as histones in eukaryotes or histone-like DNA binding proteins (HU) in bacteria present a large density of ammonium groups in the DNA contact region, necessary to induce coiling by promoting favorable electrostatic interactions with the negatively-charged DNA backbone, an observation also coherent with the action of free polyamines in promoting DNA condensation.[21]

The formation of covalent DNA-proteins cross-link adducts[22] has been recently evidenced in nucleosomes[23] at the cellular level, which have been traced back to the involvement of amine groups from lysines of the histone tails (but also from arginine). The chemical and biochemical stability of guanine-amine cross-link adducts has been explored[24]. Their repair is difficult[25] as these lesions prevent a good recruitment and the optimal operating conditions of the enzymatic repair machinery. Hence, since they lead to bulky adducts that significantly distort the DNA helical structure and induce the replication block, they result in a high cytotoxicity. The high-yield formation for DNA-polyamine cross-links adducts has been quantified for the three most prevalent free natural polyamines[26] (spermine, putrescine and spermidine), and for a trilysine peptide[27], interacting with the TGT trioligonucleotide or a 15-bp double-stranded DNA sequence with the central TGT motif (see Figure 2.3). The formation of a covalent carbon-nitrogen adduct (Figure 2.3-c, pathway B) leading to a guanine-lysine cross-link at the C8 position, 8-N-Gua, has been detected and quantified owing to tandem mass spectrometry[28]. Whereas the structure of KKK interacting with oligonucleotides is still unknown, the characterization of the resulting guanine-lysine adducts suggests a spatial proximity for the stabilization of the prereactive complex.

To rationalize those observation a mechanistic pathway involving the nucleophilic addition of the ε-amino group of a neutral polyamine onto the radical cation G•+, i.e. one of the most common DNA oxidative lesion intermediate[29], has been proposed[30], based on density functional theory (DFT) calculations on methylamine small model systems[30,31,32]. Other pathways have also been delineated, involving the participation of the ethylenic C4 and C5 positions[30], and a mechanism that can possibly proceed through $^1O_2$ photosensitization or radical coupling[32]. However, these DFT investigations have been mostly performed considering the neutral -NH2 form of amine groups, while, given its pKa, at physiological conditions, the former ought to be predominantly protonated (NH3+). Furthermore, one has also to consider that at physiological pH G•+ rapidly deprotonates to give the guanine radical G•. An equilibrium between the N1 and the N2 deprotonated form of G• has also been evidenced[33]. Hence, some questions remain open mostly related to the high efficiency of the process, that is even more competitive than water addition despite the larger abundance of the former[27]. This requires to consider from the one side the structural and dynamical properties of DNA-polyamines or DNA-polypeptides non-covalent adducts (i.e. the prereactive complexes) and on the other side taking into account the equilibrium of protonated and deprotonated species involving the guanine radical cation and the amines.

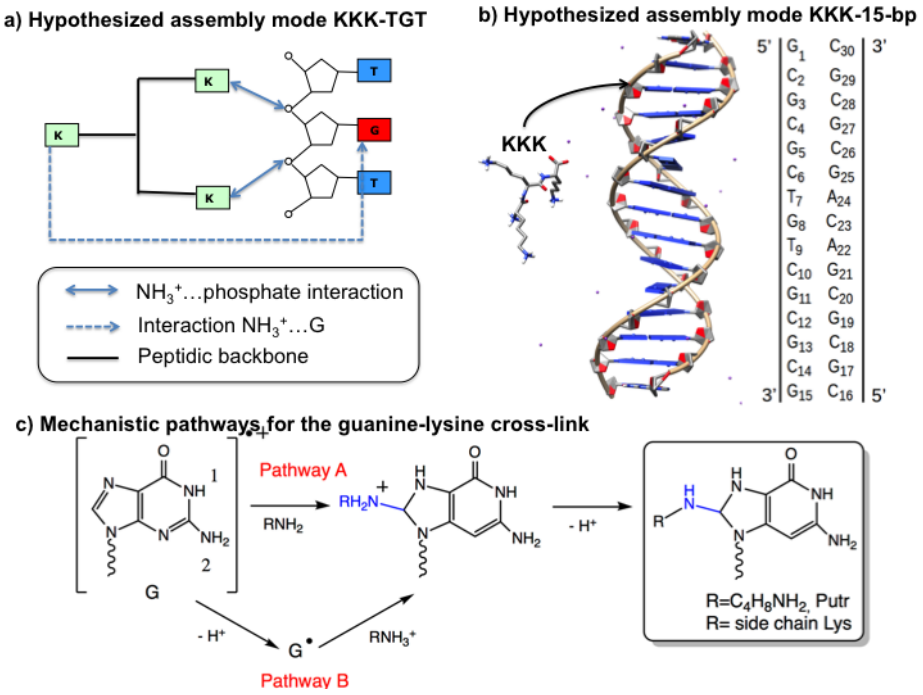

Figure 2.3. *a) Scheme for the postulated KKK-TGT interaction b) scheme of KKK interacting with a guanine-rich 15-bp oligonucleotide (water is omitted) c) Two mechanistic pathways for the formation of a covalently-tethered adduct between guanine at C8 position and a generic amine RNH2 (polyamine or lysine derivative). After one-electron ionization, the guanine radical cation can direct react with the neutral amine (pathway A), or deprotonates at N1 or N2 positions to generate the guanine radical G•[-H].*

2.1.3 Exogenous DNA Lesions

Besides the various endogenous sources of DNA damage exposed in the previous section, DNA is also continuously subject to exogenous or environmental DNA-damaging agents. Example of external source are ionizing radiation (IR) and ultraviolet (UV) radiation from sunlight.

2.1.3.1 Ionizing Radiation

Ionizing radiation (IR) is an external source of DNA damage and can be in the form of electromagnetic radiation (eg. X-rays or gamma rays) or in the form of subatomic particle (eg. alpha and beta particles). IR consists of using these electromagnetic waves to produce high energy for ionizing a molecule by removing an electron and generate ions and free electrons. IR can directly affect DNA structures during its passage and induce various types of DNA lesions including cluster of damaged bases, single-strand breaks (SSBs) and double-strand breaks (DSBs).[34] The latter is difficult to repair and considered as the most relevant lesion for mutation and carcinogenesis.[35] In addition, IR interact with the molecules surrounding the DNA (particularly of water) which undergoes radiolysis reaction, resulting in the production of reactive oxygen species (ROS) that are able to diffuse over distance and interact with DNA and then cause damages. This is called the indirect action of IR. Despite of the harmful effect, IR can be use in radiotherapy to kill cancer cells, as explained in section 2.2.

2.1.3.2 UV Light

Overexposure to the sunlight is recognized as a cause of the insurgence of malignant skin lesions that may evolve to skin cancer.[36,37,38,39,40,41,42,43] Indeed, it is well established that, despite the global photostability of DNA[44], UV light can induce the formation of DNA photolesions mostly present in the form of cyclobutane pyrimidine dimers (CPD) upon direct absorption of UVB light (in the spectrum of 290-300nm) by the DNA nucleobase.[45] CPDs are formed upon dimerization at the four possible sequences harboring two adjacent pyrimidine bases located on the same strand, namely CC, CT, TC and TT.[39,46,47,48,49] UVB radiation also triggers the formation of pyrimidine (6-4) pyrimidone photoproducts (6-4PP) present in a 3-fold lower yield than CPDs[47,50,51,52]. These two lesions are most harmful for the cell[53] for two opposite reasons. Indeed, while CPDs are

characterized by a low repair rate hence leading to accumulation of these defects in cells, 64-PPs although extremely mutagenic are much faster repaired than CPDs.[36] The differential effects have been correlated to the relate change produced in the DNA mechanical properties and in particular flexibility[54,55,56,57,58] CPDs tend to rigidify the whole oligonucleotide with minor structural differences as compared to the native B-DNA, whereas 64-PP on the contrary exhibits an extended polymorphism characterized by the simultaneous presence of very different conformations, and their rapid interconversion over the microsecond time-scale[59]. Hence, while CPDs may efficiently escape the recognition by the repair machinery, nucleotide excision repair (NER), 64-PPs is easily recognized, but its flexibility induces a much lesser replication resistance or fork blockages.[60,61,62,63]

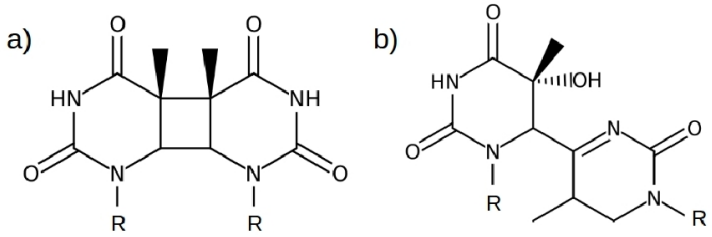

Figure 2.4. *The two most common UV induced photo-lesions, a) CPD and b) 64-PP.*

Even though, CPDs are known to be less rapidly repaired than 64-PPs, important differences in the processing rate of the four CPDs have been observed on the basis of highly specific mass spectrometry measurement[45], depending on the nature of the pyrimidine composing the lesion. The quantification of the repair rate of human skin cell, either fibroblasts or keratinocytes, indicates that the processing efficiency can vary up to a very important factor, along the four possible adducts as shown in Figure 2.5.

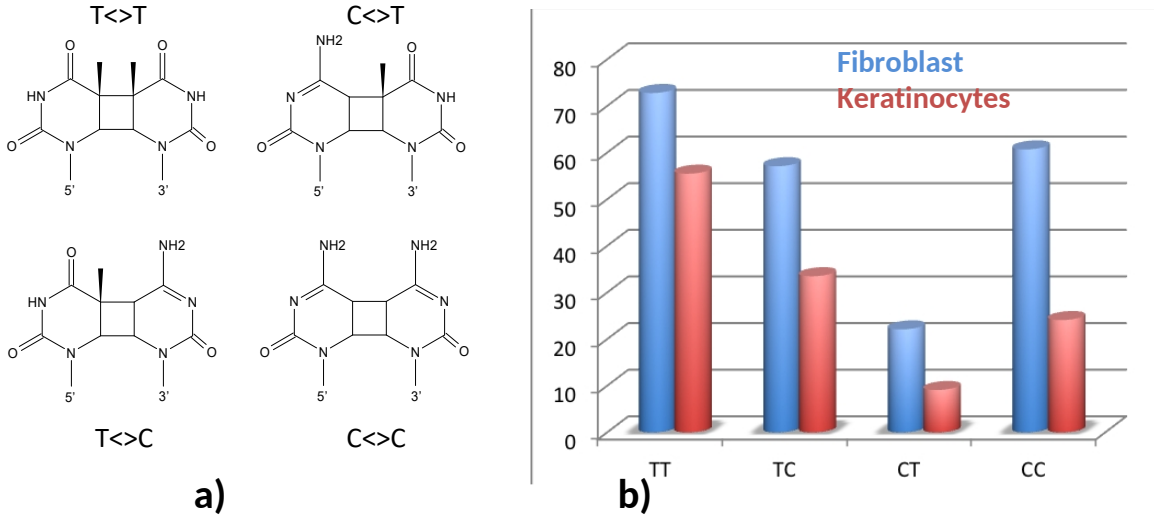

Figure 2.5. *a) The chemical structures of the specific CPD investigated here, i.e. T<>T, C<>T , T<>C , C<>C; b) Repair with respect to CPD lesions and expressed as percentage of lesion still present after 24h from light exposure. Data are adapted from Reference 64.*

Indeed, keratinocytes show a globally better repair rate than fibroblasts. In addition, T<>T undergo a slow repair and may persist up to a level of 70%, in drastic contrast in both cell types with C<>T that may reach level of less than 10%. T<>C and C<>C exhibit intermediate repair rates. Therefore, by the analysis of the data reported in Figure 2.5, it is possible to sketch a repair efficiency performance order that can be summarized as follows:

$$T<>T < T<>C << C<>C < C<>T$$

Indeed, T<>T is the slowest repaired lesion, followed by T<>C that is only slightly less refractory. On the contrary, C<>C shows a definitive improvement in the repair rate and finally C<>T is by far the best repaired lesion. Hence it is apparent that the presence of a cytosine at the 5' position results in a net increase of the repair efficiency. Interestingly,

this order of repair rate is reminiscent of mutation frequency in skin tumors and UV-irradiated cells[65,66]. Indeed, the most frequent mutations are observed at the 3'-end of T<>C sequences and to a lesser extent at C<>C sites. Conversely, C<>T sequences are very rarely mutagenic. These mutation frequencies follow the increasing rate of CPD removal.[64] Mutation at T<>T are also quite rare but this is explained by the fact that the two thymines in a T<>T CPD preserve their coding properties without inducing mutations upon replication.[67,68]

2.2 Cancer Therapy

2.2.1 Types of Cancer Treatment

Different approaches are available nowadays and continuously under development to treat cancer and to prolong patient survival. The choice is depending on the type and stage of cancer. The three conventional therapeutic methods that have been employed clinically include surgery, chemotherapy, radiation therapy and their combinations. Surgery was considered as the most effective methods to kill local tumor completely (cancerous cell that are not been widespread yet) because surgery operates by zero-order kinetics and excise 100% of the malignant cells.[69] This approach become conservative since the arrival of radiotherapy in the 1920s and chemotherapy after 1940s. Chemotherapy use chemical agents such as antimetabolites, plant alkaloids, alkylating agents, antitumor antibiotics to stop cell growth and cell division, with the objective of killing tumor cells.[70] However, the effectiveness of these compounds are limited due to non-selectivity and inability to control metastasis or secondary growth.[69]

Radiotherapy is the third conventional method of cancer treatment which relies on the use of ionizing radiation (described in section 2.1.3.1) aimed at shrinking the tumor cells. There are two classes of RT depending on the radiation sources : brachytherapy and

external beam radiation therapy (EBRT).[71] Brachytherapy relies on the irradiation of radioisotope materials (eg. ^{131}I, ^{125}I, ^{188}Re and ^{177}Lu) placed nearby the tumor to destruct solid tumor. While EBRT can be divided into proton therapy, heavy ion therapy, and X-ray therapy, the latter being the most widely used in clinical applications. Indeed, half of patients diagnosed with cancer receiving the X-ray radiotherapy treatment.

Other treatments such as phototherapies including photothermal therapy (PTT) and photodynamic therapy (PDT), are still-emerging cancer-treatment techniques.[72] PTT use photothermal agent to absorb light in the near-infrared (NIR) region and convert the corresponding optical energy into heat for thermal ablation of cancerous cells. PDT, on the other hand, relies on the use of photosensitizer, light and oxygen to produce singlet oxygen and ROS, both extremely cyctotoxic and leading to cancerous cell death via apoptosis or necrosis.[72,73]

2.2.2 Nanoparticles as Radiosensitizers

In the previous section, we have shown that most of the cancer therapies available nowadays failed to kill tumor cells selectively and as a consequence, most of the patients suffer from serious side effects or even secondary cancer which may be develop. More attention has been given particularly to improve conventional radiotherapy performance as it is the leading choice of cancer treatment. The use of direct ionizing radiation in this method lead to severe damage of surrounding healthy tissues. On the other side, limiting the dose results in poor treatment. Some cancer needs even a greater amount of radiation to kill tumors that are resistant to long-term radiotherapy.[74]

The development of a more precise and effective radiotherapy thus becomes an urgent priority. To this aim, a variety of radiosensitizers (radiosensitizing agent), molecule/materials that are able to target cancer cells and reduce radiation dosage have been proposed.[75] Some common radiosensitizer including halogenated nucleosides and

cispatin derivatives, but in the last decade, metallic nanoparticles, with a diameter of 100 nm or less have been extensively studied in the researches domain as promising radiosensitizing agents.[75,76] The first experiment evidence come from Hainfield et al,[77] in which small gold nanoparticles (1.9nm) combined with x rays were used to irradiate mice' tumors. A significant increase of one year survival rate was reported, 86% compared to 20% with radiotherapy alone. Starting from this pioneering work, a vast amount of experimental works have been proposed to improving radiotherapy performance by testing on silver (Z= 47),[79] gadolinium (Z= 64)[80,81] platinum (Z=78)[82,83], gold,[71,78,84] and bismuth nanoparticles.[85] Indeed, these high Z nanoparticles are able to emit, absorb and scatter ionizing radiations energy thus, increase the radical production due to the photoelectric effect.[86,87,88,89]. They contribute to radiosensitization effects making tumor cells more responsive to ionizing radiation,[90,91] since they preferentially accumulate in tumor tissues over healthy tissues thanks to the enchanced permeability and retention (EPR) effect exhibited by solid tumors.[92]

2.3 Gold Nanoparticles in Radiotherapy

Among the various high Z materials being proposed as radiosensitizer, functionalized gold nanoparticles (AuNPs) have received a significant attention to be employed in cancer diagnosis and treatment due to their facile synthesis, excellent biocompatibility and long circulation time.[71,87,93,94,95,96] Another unique physical property exhibited by AuNPs is the surface plasmon resonance (SPR) which is defined as the collective oscillation of free electrons (conduction band electrons) when exposed to light.[88] The excitation of the plasmonic AuNPs induces high temperature and can be used in photothermal therapy for the destruction of cancerous cells.[72,88]

The size of AuNPs can affect significantly its radiosensitization effect. Indeed, when the size of a particle decreases, its surface area to volume ratio increase severely and this

leads to the prevalence of surface atoms. The latter have a lower coordination number, and these low-coordinated surface atoms (eg, edge, kink, or corner sites) are known to influence strongly nanoparticle properties, so small size of NP exhibits unique size-dependent chemical reactivity. For example, the radiosensitizing effect in water under irradiations of X-ray and UV light was performed on AuNPs in the range 5-250 nm.[97] Smaller AuNPs (size below 5nm) with larger surface area showed a greater production of hydroxyl radical and superoxide anion, leading to a stronger radiosensitizing effect. Other ultrasmall size of AuNPs have been proposed in this context: $Au_{10-12}(SG)_{10-12}$,[98]and GSH-Au_{25}NC[100], both containing both several atoms embedded inside a glutahione peptide. They can be efficiently cleared by the kidney after the treatment and thus minimizing the potential side effects due to the accumulation in the body.

2.3.1 Isolated AuNPs in Model Condition

The physicochemical and catalytic properties of AuNPs are highly dependent on their size and morphology. Therefore, structure determination of nanometer-size of AuNPs with both crystalline and non-crystalline geometry is critical in order to have a NP design having an optimal performance in radiotherapy. Various experimental and numerical tools have been developed to sample their configuration space as a function of size and temperature.[99] A few of theoretical investigations have been proposed in the literature by using different computational tools on the basis of AuNPs modeled in vacuum by explicit 3D structures[101,102 103,104,105,106,107,108] Density functional theory (DFT) is a powerful atomic scale simulation method to find energy minima, but rather limited to small size of the particle due to computational cost. The size restriction may be overcome by using other approaches based on empirical potentials, simulated annealing and genetic algorithms. Most of the studies focus on the comparison of face-centered-cubic (fcc) gold nanoclusters based on three high point-group symmetry: I_h, D_5h, and O_h. For instance, a DFT study (with PBE and TPSS functional) have been performed recently to compare the relative stability of gold nanoclusters with icosahedral, Ino-decahedral and cuboctahedral

morphologies in the range of 1.1-3.5nm.[106] As shown in Figure 2.6, they have plotted the cohesive energy per atom against $N^{-1/3}$ which exhibits a linear relationship with the size of the particle. In this fluxional regime, the authors have shown that the cohesive energy is very close to each other, with a preference for icosahedral morphology (decahedral and octahedral ones being metastable). However, other morphologies such as truncated-octahedra and Marks- decahedra, which are competitive energetically are not considered in this study.

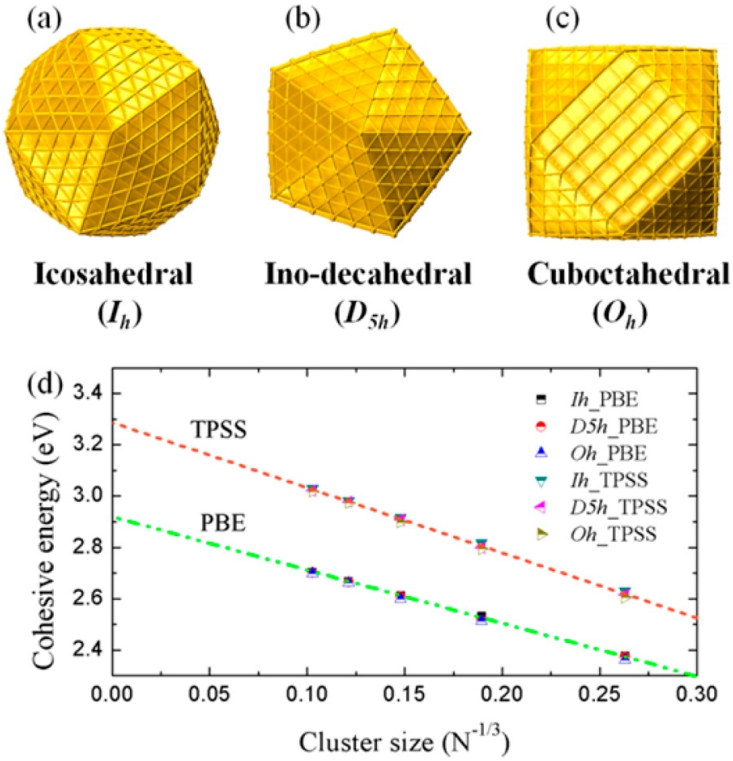

Figure 2.6. *Structures of (a) icosahedral (I_h), (b) Ino-decahedral (D_5h), and (c) cuboctahedral (O_h) Au_{923} clusters. (d) Cohesive energies of AuNPs versus $N^{-1/3}$. This figure was taken from the reference [106].*

Another recent study have been proposed to explore more configurations of metallic particles with six distinct morphologies (including octahedron (not truncated), truncated octahedron, cuboctahedron, icosahedron, regular decahedron, and Marks-decahedron) in

the range of 1-7nm (see Figure 2.7) by using global optimization methods based on semiempirical potentials.[109] Based on their calculations, for AuNPs, I_h motif is only stable for small size less than 200 atoms, D_h and TO motif being competitive, in contrast with the previous DFT study of large NP size.[106] At a larger scale (above 1000 atoms), TO motif become more stable than Dh and Ih, in agreement with others results based on global optimizations methods.[105,101,102] From these latter methods, the versatility of gold shapes has been demonstated in the fluxional regime (below 100 atoms).[103,104]

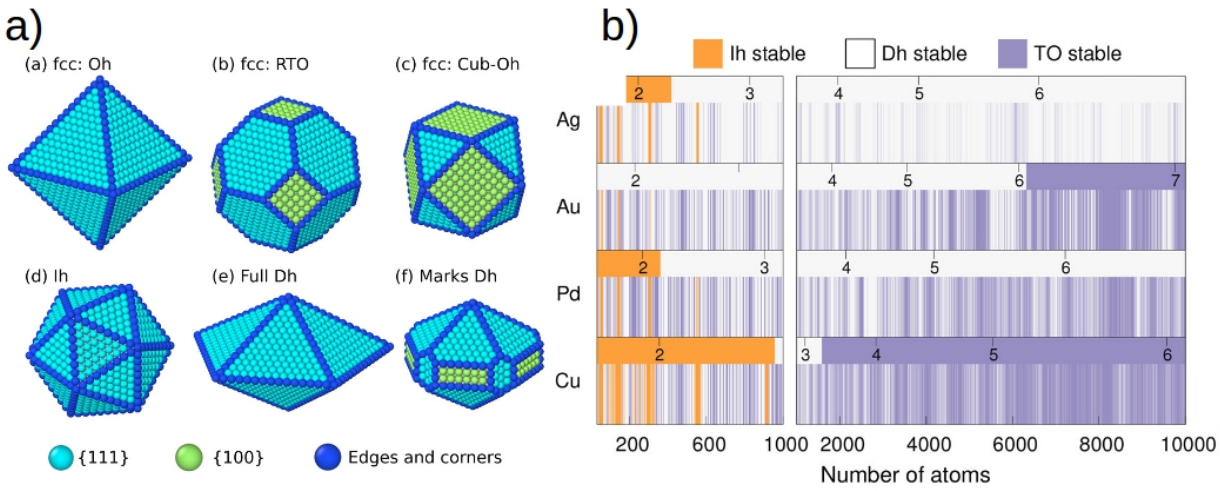

Figure 2.7. *a) the structure of octahedron (not truncated), regular truncated octahedron, cuboctahedron, icosahedron, regular decahedron, and Marks decahedron. b) the relative stability of the three different motifs for Ag, Au Pd and Cu particles. This figure is adapted from the reference [109].*

The structures of AuNPs can also be examined in model conditions by experimental diffraction and microscopic measurements.[110,111,112,113,114,115,116,117] X-ray powder diffraction coupled with atomistic modeling shows that in the range of 1-2nm, the most stable structures belong to truncated decahedral motif.[110] Annealing effects on the AuNPs investigated by using high-resolution electron microscopic (HREM) revealed a structural transformation from metastable icosahedral to decahedral morphology in the range 3-14nm just below the melting points.[113] High-angle annular dark-field imaging (HAADF-

STEM) measurements have been reported for the determination of the structure of gold nanoclusters, especially for particular sizes 309,[114] 561,[115] and 923[116] atoms. The reported images in these publications and the estimated proportions of structural isomers show the preference of defective decahedral and face-centered cubic forms with respect to icosahedral shape (see Figure 2.8 for HAADF STEM images of Au_{561}[115]).

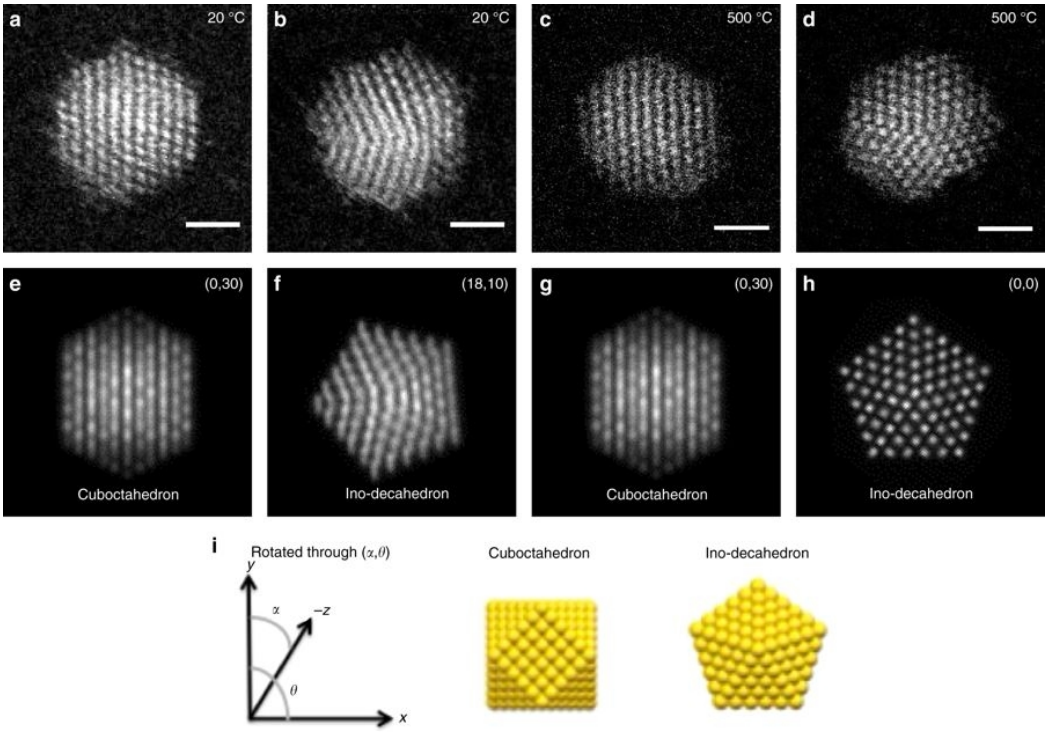

Figure 2.8. *HAADF STEM images of Au_{561} clusters recorded at 20 °C and 500 °C. (a)–(d) HAADF STEM images of Au_{561} clusters and (e)–(h) matching multi-slice electron scattering simulations of the cuboctahedron and Ino-decahedron at different orientations. This figure was taken from the reference [115]*

2.3.2 Interaction of AuNPs with Water

In radiotherapy, the ionizing radiation can damage DNA directly or other part of the cells such as mitochondria, but the main pathway of DNA damage is through the indirect reaction of water radiolysis (see illustration in Figure 2.9) due to the fact that water is the main constituent of human body (65% approximately).[118] The yield of the secondary products (such as hydroxyl radicals HO•, hydrogen radical H•, superoxide O2•-, and hydrogen peroxide H_2O_2) of water molecules can be further amplified in the presence of AuNPs.[77,78]

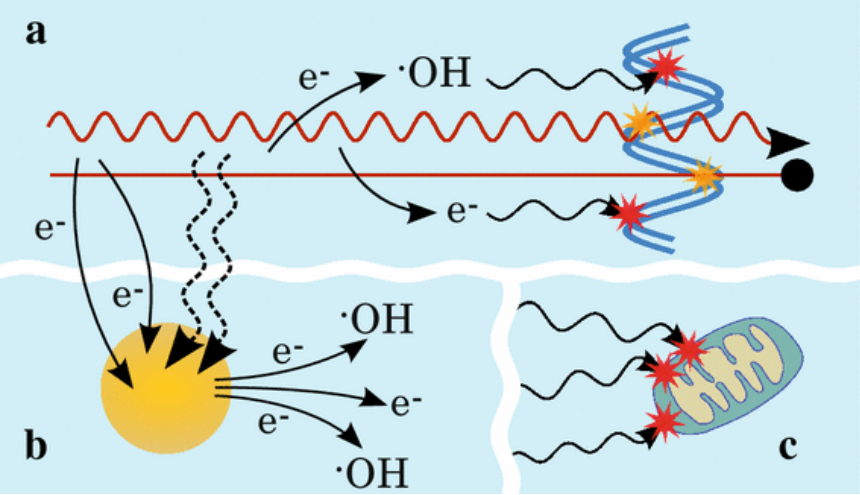

Figure 2.9. *Schematic of the mechanism of ionising radiation in the presence of AuNPs. Yellow and red stars correspond to the direct and indirect damage, respectively. (a) the incident radiation interact with NPs. b) secondary electrons produced by the radiation or by AuNPs in the water medium to amplify the production of secondary electron. c) the damage of other parts of the cell (like mitochondria). This figure is taken from Reference [118] to simply illustate the damage pathways.*

The interaction of AuNPs with water can be investigated by theoretical modeling. For instance, interfacial chemical and physical processes happening at the vicinity of functionalized AuNPs can be explored by atomistic calculations while water radiolysis can be studied by continuous models and Monte Carlo simulations like LiQuiD code.[119,120]

These two complementary approaches may provide a better understanding of interfacial properties while Monte Carlo simulations may benefit from useful atomistic information.

Concerning the modeling of the interface between AuNPs and water solvation at the atomic scale, DFT is a powerful method to predict optimal geometries and energetics. In DFT studies, static approaches are often considered to describe water adsorption on Au surfaces,[121,122, 123,124,125,126]and nanoclusters up to 20 atoms,[127] although the explicit interface between metallic nanoparticles and liquid water can be described by ab initio molecular dynamics simulations.[128] To date, a few studies based on parametrized force fields and classical molecular dynamics simulations have been reported in the literature for gold/water interfaces.[125,129,130]

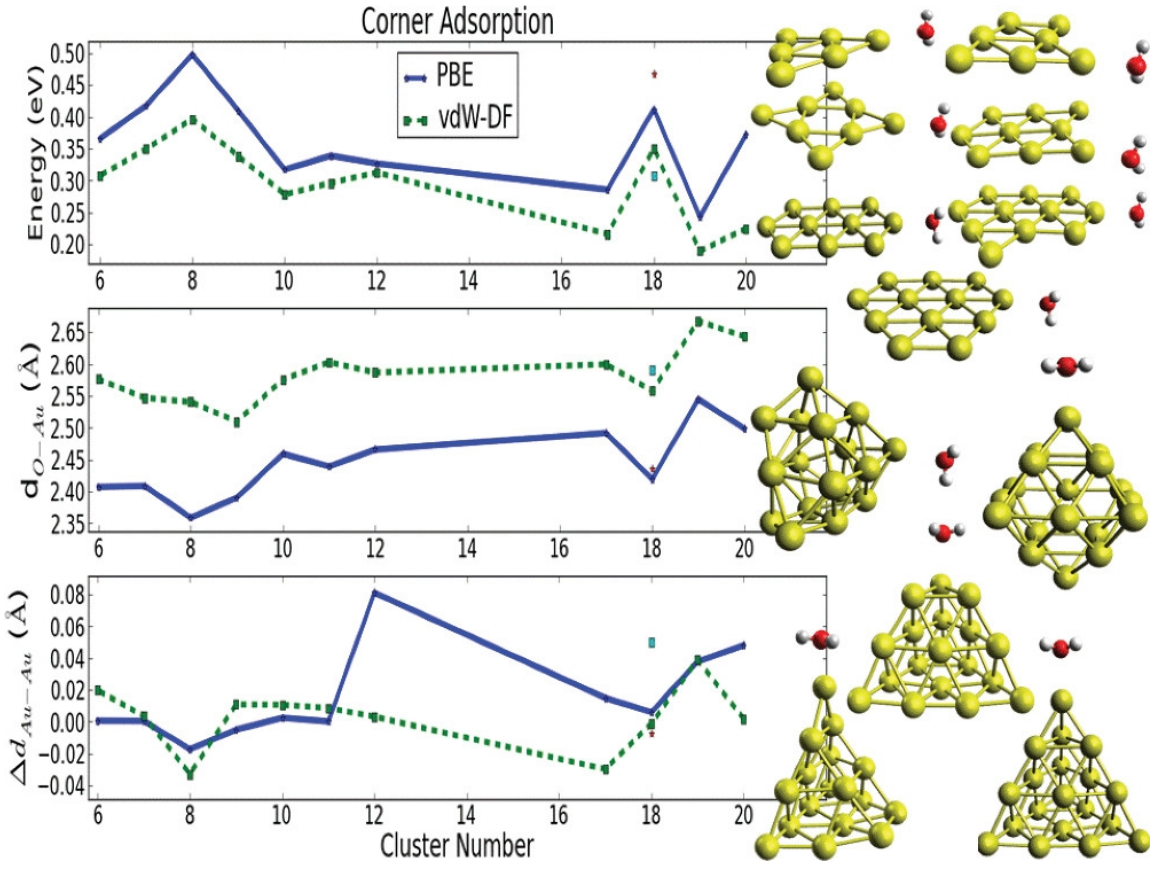

Figure 2.10. *Adsorption energies (at PBE and with vdW-DF level) and geometries of one water molecules on Au clusters (N < 20 atoms) for corner adsorption. The upperfigure on the left shows the adsorption energy in eV. The middle figure on the left show the distance between water O atom and the closest Au corner atom in Å. The lower figure on the left shows the adsorption induced change in the average Au–Au nearest-neighbor bond length in Å. This figure was taken from reference [127] .*

The interaction between water molecule with planar (n= 6-12) and three-dimensional (3D) Au clusters (n= 17-20) are studied at DFT level.[127] As shown in Figure 2.10, a water monomer on small gold nanoclusters (less than 20 atoms) mainly interacts with gold at corner adsorption sites. For 3D clusters, water exhibits a near-flat surface adsorption geometry with the O atom of water sitting nearly atop a surface Au atom. The adsorption strength is rather weak and depends slightly on the choice of the DFT functional (0.2-0.4 eV with vdW-DF and 0.25-0.5 eV with PBE).[127] This stability is larger than the adsorption energy calculated on Au(111) (-0.105/-0.14 eV with PW91[121,122] -0.11 eV with PBE,[123,124] -0.24 eV with PBE-D2,[123] -0.30 eV with optB86b-vdW,[123] and -0.192 eV with revPBE-vdW[124]).

Studies have also performed on AuNPs in a water vapor environment described by extended metallic surfaces calculated by DFT and Wulff construction for predicting thermal properties.[131] The water vapor effect on Au nanoparticle shape is rather small by comparison with other metals, and consists of a progressive transformation of {100} facets in favor of {111} ones becoming larger in truncated octahedra.

The size effect on the adsorption mechanism of water molecules was investigated on icosahedral AuNPs using molecular dynamics simulation.[129] The authors showed that the average interaction energy increases when the size increases concomitantly (-0.174, -0.259 and -0.295 eV for Au_{13}, Au_{55}, and Au_{147} respectively). The authors showed that for larger AuNPs (Au_{55}, and Au_{147}) , the hydrogen bonding between adsorbed water molecules

lead to an arrangement on the surface in a two-dimensional structure. In the case of Au_{13}, the hydrogen bonding of the water molecules generates a three-dimensional structure (see Figure 2.11).

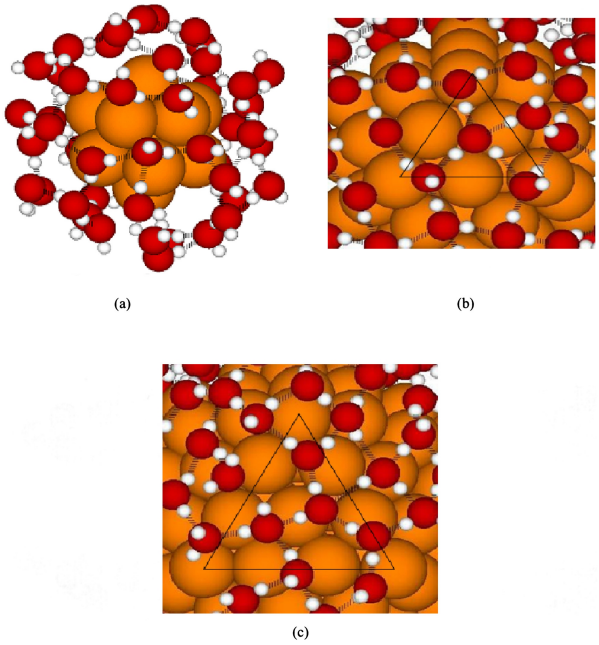

Figure 2.11. *Morphologies of water molecules surrounding icosahedra a) Au_{13}, b) Au_{55}, and c) Au_{147}. Dashed line between oxygen and hydrogen indicates the hydrogen bonding. This figure was taken from the reference [129].*

2.3.3 AuNPs functionalized by PEG ligands

Uncoated AuNPs are toxic and unstable in the biological fluid, therefore their surface must be functionalized by organic ligands to preserve their integrity and to improve their biocompatibility. Various ligands have already been examined to date for this purpose, such as citrate ions[132], poly-ethylene glycol (PEG),[133,134,135] undecane-thiols and amine derivatives,[136] DNA strands[137] as well as uncoated GNPs as references.[138] Indeed PEG-based ligands have been often considered for applications in imaging and therapy[139,140]

because of their high stability, biocompatibility, low cytotoxicity, and interesting antibacterial activity.[141,142]

The morphology of AuNPs can be modulated by the chemical nature of the organic coating. For instance, thiol-terminated monomethoxy PEG ligands have been considered for synthesizing gold nanostructures with different shapes (gold spherical nanoparticles GNPs, nanospikes GNSs and nanorods GNRs) around 50nm (Figure 2.12).[143] The use of other synthesis ligands can yield branched nanoparticles by maximizing the surface to volume ratio and leading to star polyhedral gold nanocrystals or nanostars.[144] For instance, the influence of alkylamine ligands has been demonstrated several times on the morphology of gold nanostars.[145,146,147] A long chain amine ligand promotes rounded nanostars whereas shorter chain amine favors pointed nanoclusters.[145]

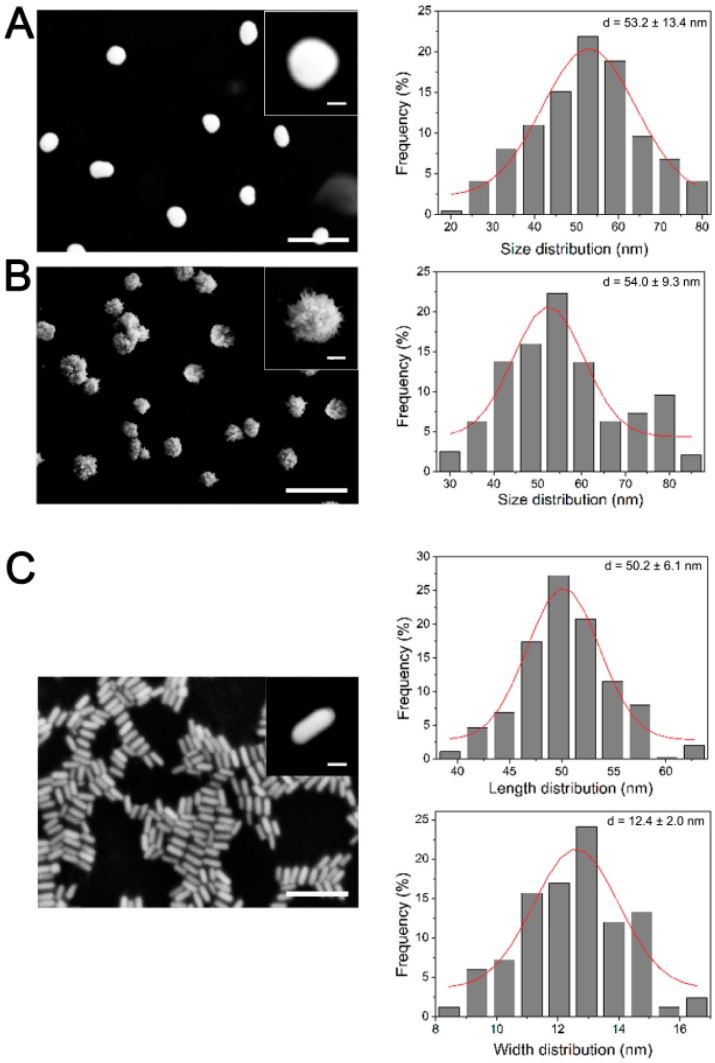

Figure 2.12. *(left) SEM images of gold spherical nanoparticles GNPs (A), nanospikes GNSs (B) and nanorods GNRs (C) and their size distribution histograms (right). This figure was taken from reference [143].*

The grafting density of the ligands can be evaluated precisely experimentally.[148,149,150] According to the models, it decreases with the diameter of the nanoparticle and the ligand molecular weight. As shown in Figure 2.13 (a), for small AuNPs (below 5 nm), grafting densities exceed 1.6 chains/nm^2.[149] Moreover, for short chain ligand (below 1000 g/mol), the densities become larger than 2.5 chains/nm^2 (see Figure 2.13 (b)) (3.2-3.9 chains/nm^2

for specific PEG ligands[148,150]). The molecular weights and number of ligands on the AuNPs have also a significant influence on their orientations around gold,[150,151] giving rise to a transition from disorganized "mushroom" orientations to more rigid "brush" configurations.

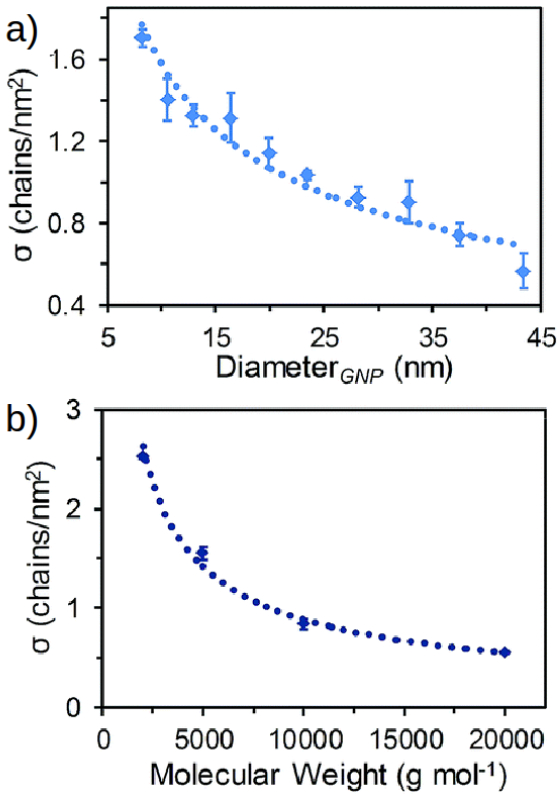

Figure 2.13. *Evolution of the grafting density of SH-PEG ligands on AuNPs against a) diameter of AuNPs and b) ligands molecular weight. This figure was adapted from the reference [149].*

Regarding the theoretical models of coated AuNPs, classical molecular dynamics is one possibility to describe the coordination of alkane-thiols and PEG ligands.[152,153,154] According to these models, the thickness of the coating is only weakly dependent on the surface ligand density, whereas the degree of water penetration in the coating increases for a smaller number of attached ligands. Hybrid approaches combining force-field

molecular dynamics simulations, CGMD and DFT allow the investigation of bicomponent self-assembled monolayers (SAM) on gold.[155,156] To describe more accurately the SAM energetics, DFT calculations are mainly performed on extended model gold surfaces.[155,156,157] For the isolated adsorption of dehydrogenated PEG on Au(111), (100), (110) surfaces, the adsorption energies are -89, -186 and -209 $kJ.mol^{-1}$, respectively with the PBE GGA functional.[156] SAMs composed of mercaptododecanoic acid and PEG-amide alkylthiol ligands chemisorbed on Au(111) have been optimized at the DFT-D3 level with adsorption strength of -3.48 and -4.15 eV per chain, respectively,[155] in agreement with previous theoretical studies.[158,159] This strong value has been found also from DFT models of Au_{38} subnanocluster with several dehydrogenated ethanethiol ligands $Au_{38}(C_2H_5S)_N$ (4.6 eV for one molecule at the local density approximation (LDA) level with SIESTA code).[161] Other calculations for methylthiolate adsorption on Au_{20} subnanocluster show a more moderate stability for non-dissociative chemisorption (-1.16 eV per molecule at the PBE-D2 level with SIESTA code).[161] According to the energy decomposition analysis of SAMs composed of alkylthiol ligands adsorbed on Au(111),[155] the adsorption is dominated by dispersion forces (60% of adsorption energy) and by the binding between the ligands and the gold surface (70% in average; the interchain attractive contribution being twice weaker). These results are confirmed by other DFT studies for SAM consisting of dodecanethiol and terphenylthiol ligands on Au111.[157]

2.3.4 Endocytosis of PEGylated AuNPs

The mechanisms of AuNPs internalizations by cancer cells (endocytosis) is still unclear, despite several studies have shown that internalized AuNPs are able to produce more ROS to induce cell apoptosis and necrosis.[162,163,164] At the cell scale, the pathways of endocytosis can be either investigated experimentally by optical and microscopic techniques.[137] or modeled theoretically by coarse-grained molecular dynamics (CGMD) simulations.[165] At the molecular scale, the interaction modes between naked or coated

AuNPs with membrane lipidic bilayers can also be described by atomistic classical force-fields or CGMD.[166] Among the key factors influencing endocytosis, the morphology and the size of AuNPs are of prime importance.

According to recent measurements,[143] the cellular uptake is increased in the order of gold spherical nanoparticles (GNPs) > nanospikes (GNSs) > nanorods (GNRs) (see Figure 2.12 for the structures) in agreement with previous measurements[167] and dissipative particle dynamics (DPD) simulations.[168] All the PEGylated AuNPs induce enhanced cancerous cell death rates upon X-ray irradiation. However, sensitization enhancement ratios determined by the amount of internalized gold atoms have been found larger for spherical GNPs than other shapes, thus showing the impact of nanoparticle morphology on cancer radiotherapy. At larger sizes (80-90 nm) or alternate shapes, other uptake measurements have shown different trends between PEGylated gold nanotriangles (nanoprisms), nanorods and nanostars.[169,170] CGMD simulations of water-solvated AuNPs with various shapes in the range 2-10 nm demonstrate also alternative conclusions for the cellular uptake efficiency.[171] In particular, DPD simulations show that the anisotropy of a copolymer coating improves the cell penetration, with a maximum uptake for Janus-type nanoparticles.[172] PEG-functionalized dithiolane ligands terminated by either methoxy or carboxy group have been used to synthesize AuNPs in the range 2.4-89 nm.[173] Up to 16 nm, these AuNPs have been found to localize in the cell nucleus, whereas larger NPs have not entered the cell and have been located at their periphery.

From a mechanistic point of view, experimental ESEM/TEM and theoretical CGMD approaches[137] have recently shown that the cellular uptake occurs through the ligand exchange at the nanoparticle/membrane interface. The physisorbed ligands on the nanoparticle surface have a larger ability to exchange with membrane lipidic molecules depending on their adsorption affinity and chain length. In these experiments, AuNPs typically aggregate into an ordered monolayer on the lipid bilayers, hence affecting the cell membrane integrity, the uptake efficiency, and the endocytosis pathways. For

PEGylated AuNPs, the measurements of height and diameter demonstrate their lower propensity to agglomerate at the interface with the membrane and lower capacity to internalize with respect to citrate ligands and DNA strands.

The chemical nature of the PEG-based ligands (varying with alkyl chains, length and pH) and their surface grafting density have also a significant impact on the endocytosis. PEGylated AuNPs terminated with long alkyl chains (up to C_{18}) present larger cell uptake than classical PEG coronas,[174] while smaller chains presenting two thiol functions can reduce the uptake as the surface coverage increases.[175] The pH-reversible cell affinity and photothermal therapeutic efficiency have been measured by synthesizing PEGylated mixed-charge gold nanostars.[176] By tuning the pH gradient around neutrality with mixed ammonium/carboxylate terminal functions, the authors have demonstrated the concomitant higher uptake for ammonium enriched gold nanostars.

Due to the difficulty to observe experimentally the interaction between the nanoparticle and the cell membrane,[166] a few theoretical studies based on DPD,[168,172] CGMD[177] and on free energy calculation continuum models[178] have been reported to model these interfaces approximatively.

2.4 Limits of the State-of-the-art and Objectives of My Thesis

Although AuNPs have been proven as promising radiosensitizers since the last two decades, there are only very few clinical trials that combine radiotherapy with AuNPs.[95,89,179] Several properties of AuNPs such as size, shape and functionalization, and the impact on radiosensitization are still poorly understood. To date, there is a lack of studies at the atomic scale describing the effect of chemical and biological environment on the relative stability of AuNPs, before the irradiation takes place.

As exposed in section 2.2.4, the stability of AuNPs in model conditions (vacuum) as a function of size and morphology is still an open question although experimental

measurements and theoretical studies are compared as much as possible. This will be discussed in Chapter 4 and the stability order of AuNPs in the range 0.9-3.4 nm will be tackled by using three theoretical descriptors.

Before describing the photocatalytic processes of water radiolysis at the atomic scale, a first understanding of the stability and the competitive forms of AuNPs in the biological natural environment is required. Therefore, the morphology, structure, and energetics of AuNPs in contact with liquid water will be examined in Chapter 5. In particular, an explicit static or atomistic model describing the interaction of water monomers and solvation shells (first solvation shell around the nanoparticle) with gold nanoparticles in the range 1−2 nm will be presented. We aim to probe the water effect on AuNPs morphology and size as a first model describing the influence of the biological environment. In particular, we will examine, in a comprehensive and systematic study, the adsorption energetics of water, especially for decahedral gold shapes, a competitive form which has been rarely considered in the theoretical literature at the DFT level to date. To this end, in the framework of LABEX PRIMES, we propose to generate DFT-based electrostatic potentials and provide them to our collaborators at IPNL, so that these parameters will be incorporated into their Monte-Carlo simulation code for a better estimation of free radicals in the presence of AuNPs.

In the previous sections 2.2.6 and 2.2.7, we have shown that although numerous experimental studies have investigated the shape of PEGylated AuNPs, only few information is available today regarding the relationship between the PEG coating and the nanoparticle stability, the impact of the PEG coating on the uptake ability of AuNPs and the radiosensitization and associated radiolysis mechanisms. For instance, an accurate description of the stability depending on the size and the morphology is missing for gold nanoclusters around 1 nm, where the fluxionality is predominant. Moreover, the concomitant role of water (biological environment) on this stability, its localization around the nanoparticle and its synergy with the PEG corona, are also poorly understood

at this atomic scale, although water radiolysis promoted by AuNPs is a key element of radiotherapy. Regarding the help of theory, as previously exposed, DFT studies explore mainly the interaction between PEG and alkanethiol-based molecules with Au extended surfaces (a relevant model for really large nanoparticle facets). To date the organic coating of dry or hydrated PEGylated AuNPs has not been modeled accurately for nanoclusters. In Chapter 6, we will then explore the influence of PEGylation, the grafted ligand density and the simultaneous hydration on the stability of gold nanoparticles (1.1-1.3 nm). Our objective is the determination of the role of the PEG ligand on the nanoparticle stability and on the confinement of water molecules at the proximity of gold, in order to discuss the cellular uptake of the AuNPs and water radiolysis for therapeutic applications.

In this thesis, we will also try to bridge the gap between the theoretical description of nanomaterials for radiotherapy applications with the modeling of the DNA damages caused by the IR, once the ROS have been generated. The characterization of DNA lesions structures is crucial to understand the possible mechanisms leading to mutagenesis and carcinogenesis. Indeed, the structural information of DNA lesions allow the quantification of the induced distortion, and their impact on processing by repair enzymes. Classical molecular dynamics (MD) simulations can describe in detail the dynamics of these systems that are often difficult to access by experimental methods, due to the difficulty to isolate such complex lesions and the small involved length and time scales. In Chapter 7, we will present our works based on MD simulations to study the structural and dynamical properties of trilysine peptide interacting with a trioligonucleotide TGT and with the same TGT motif embedded within an 15-bp oligonucleotide. A mechanistic pathway after one-electron oxidation of the central guanine is proposed at the DFT level. Finally, by using MD simulations coupled with free energy methods, the repair rate of different cyclobutane pyrimidine dimers (T<>T, T<>C, C<>T, C<>C) will be rationalized, and the recognition of the four lesions by the DDB2 protein moiety will be analyzed precisely at the atomic level.

References

1. Bray, F., Ferlay, J., Soerjomataram, I., Siegel, R. L., Torre, L. A., Jemal, A. Global cancer statistics 2018: GLOBOCAN estimates of incidence and mortality worldwide for 36 cancers in 185 countries. *CA: a cancer journal for clinicians*, **2018**, 68(6), 394-424.

2. Hoeijmakers, J. H. Genome maintenance mechanisms for preventing cancer. *Nature*, **2001**, 411(6835), 366.

3. Watson, J. D., Crick, F.H.C. A structure for deoxyribose nucleic acid, *Nature*, **1953**, 171, 737-738.

4. User: Sponk. Comparison of a single-stranded RNA and a double-stranded DNA with their corresponding nucleobases. [Online; accessed 2015-08-05]. Mar. 2010.
5. Davey, C. A., Sargent, D. F., Luger, K., Maeder, A. W., & Richmond, T. J. Solvent mediated interactions in the structure of the nucleosome core particle at 1.9 Å resolution. *Journal of molecular biology*, **2002**, 319(5), 1097-1113.

6. Lindahl T., Barnes D. Repair of endogenous DNA damage. *Cold Spring Harb Symp Quant Biol* **2000**, 65, 127–133.

7. Dexheimer, T. S. DNA repair pathways and mechanisms. *In DNA repair of cancer stem cells, Springer, Dordrecht*. **2013**, 19-32.

8. De Bont, R., & Van Larebeke, N. Endogenous DNA damage in humans: a review of quantitative data. *Mutagenesis*, **2014**, 19(3), 169-185.

9. Schärer, O. D. Chemistry and biology of DNA repair. *Angewandte Chemie International Edition*, **2003**, 42(26), 2946-2974.

10. Qi, Y., Spong, M. C., Nam, K., Banerjee, A., Jiralerspong, S., Karplus, M., & Verdine, G. L. Encounter and extrusion of an intrahelical lesion by a DNA repair enzyme. *Nature*, **2009**, 462(7274), 762.

11. Boiteux, S., Guillet, M. Abasic sites in DNA: repair and biological consequences in Saccharomyces cerevisiae. *DNA repair*, **2004**, 3(1), 1-12.

12. Loeb, L. A., Preston, B. D. Mutagenesis by apurinic/apyrimidinic sites. *Annual review of genetics*, **1986**, 20(1), 201-230.

13. Gates, K. S. An overview of chemical processes that damage cellular DNA: spontaneous hydrolysis, alkylation, and reactions with radicals. *Chemical research in toxicology*, **2009**, 22(11), 1747-1760.

14. Barker, S., Weinfeld, M., Zheng, J., Li, L., & Murray, D. (2005). Identification of mammalian proteins cross-linked to DNA by ionizing radiation. *Journal of Biological Chemistry*, *280*(40), 33826-33838.

15. Kow, Y. W. Repair of deaminated bases in DNA. *Free Radical Biology and Medicine*, **2002**, 33(7), 886-893.

16. Miller-Fleming, L., Olin-Sandoval, V., Campbell, K., & Ralser, M. Remaining mysteries of molecular biology: the role of polyamines in the cell. *Journal of molecular biology*, **2015**, 427(21), 3389-3406.

17. Pegg, A. E. Functions of Polyamines in Mammals. *Journal of Biological Chemistry* 291, **2016**, 14904–14912.

18. Michael, A. J. Polyamines in eukaryotes, bacteria, and archaea. *Journal of Biological Chemistry,* **2018**, 291(29), 14896-14903.

19. Feuerstein, B. G., Williams, L. D., Basu, H. S., and Marton, L. J. Implications and concepts of polyamine-nucleic acid interactions. *Journal of Cellular Biochemistry,* **1991**, 46, 37–47.

20. Minois, N., Carmona-Gutierrez, D., Madeo, F. Polyamines in aging and disease. *Aging (Albany NY),* **2011**, 3(8), 716.

21. Gosule, L. C., and Schellman, J. A. (1978) DNA condensation with polyamines: I. Spectroscopic studies. Journal of Molecular Biology 121, 311 – 326.

22. Tretyakova, N. Y., Groehler, A., and Ji, S. DNA-Protein Cross-Links: Formation, Structural Identities, and Biological Outcomes. *Accounts of Chemical Research*, **2015**, 48, 1631– 1644.

23. Bai, J., Zhang, Y., Xi, Z., Greenberg, M. M., and Zhou, C. Oxidation of 8-Oxo-7,8- dihydro-2-deoxyguanosine Leads to Substantial DNA-Histone Cross-Links within Nucle- osome Core Particles. *Chemical Research in Toxicology,* **2018**, 31, 1364–1372.

24. Esparza, D., Mincitar, J., Tran, N., Ramos, A., Miller, K., & Stemp, E. (2016). Chemical and Biochemical Stability of Guanine Lysine Crosslinks Formed by Guanine Oxidation. The FASEB Journal, 30(1_supplement), 1050-2.

25. Stingele, J., Bellelli, R., Boulton, S. J. Mechanisms of DNA–protein crosslink repair. *Nature Reviews Molecular Cell Biology*, **2017**, 18(9), 563.

26. Silerme, S., Bobyk, L., Taverna-Porro, M., Cuier, C., Saint-Pierre, C., Ravanat, J. L. DNA-polyamine cross-links generated upon one electron oxidation of DNA. *Chemical research in toxicology*, **2014**, 27(6), 1011-1018.

27. Perrier, S., Hau, J., Gasparutto, D., Cadet, J., Favier, A., and Ravanat, J.-L. Characterization of Lysine-Guanine Cross-Links upon One-Electron Oxidation of a Guanine-Containing Oligonucleotide in the Presence of a Trilysine Peptide. *Journal of the American Chemical Society*, **2014**, 128, 5703–5710, PMID: 16637637.

28. Xu, X., Muller, J. G., Ye, Y., and Burrows, C. J. DNA-Protein Cross-links between Guanine and Lysine Depend on the Mechanism of Oxidation for Formation of C5 Vs C8 Guanosine Adducts. *Journal of the American Chemical Society,* **2008**, 130, 703–709.

29. Cadet J., Douki T., Gasparutto D., Ravanat J.-L. Oxidative damage to DNA: formation, measurements and biochemical features *Mut. Res.,* **2003**, 531, 5-23.

30. Thapa, B., Munk, B. H., Burrows, C. J., and Schlegel, H. B. Computational Study of the Radical Mediated Mechanism of the Formation of C8, C5, and C4 Guanine:Lysine Adducts in the Presence of the Benzophenone Photosensitizer. *Chemical Research in Toxicology,* **2016**, 29, 1396–1409.

31. Uvaydov, Y., Geacintov, N. E., and Shafirovich, V. Generation of guanine amino acid cross-links by a free radical combination mechanism. *Phys. Chem. Chem. Phys.*, **2014**, 16, 11729–11736.
32. Bishnu, T., H., M. B., J., B. C., and Bernhard, S. H. Computational Study of Oxidation of Guanine by Singlet Oxygen (•1g) and Formation of Guanine: Lysine Cross-Links. *Chemistry A European Journal* 23, 5804–5813.
33. Adhikary, A., Kumar, A., Becker, D., and Sevilla, M. D. The Guanine Cation Radical: Investigation of Deprotonation States by ESR and DFT. *The Journal of Physical Chemistry B*, **2006**, 110, 24171–24180, PMID: 17125389.
34. Lomax, M. E., Folkes, L. K., O'neill, P. Biological consequences of radiation-induced DNA damage: relevance to radiotherapy. *Clinical oncology*, **2013**, 25(10), 578-585.
35. Khanna, K. K., & Jackson, S. P. DNA double-strand breaks: signaling, repair and the cancer connection. *Nature genetics*, **2001**, 27(3), 247.
36. Ikehata, H., Ono,T. The Mechanisms of UV Mutagenesis. *J. Radiat. Res*., **2011**, 52, 115–125.
37. Rünger,T.M. and Kappes,U.P. Mechanisms of mutation formation with long-wave ultraviolet light (UVA). *Photodermatol. Photoimmunol. Photomed.*, **2008**, 24, 2–10.
38. Cadet,J., Mouret,S., Ravanat,J.L. and Douki,T. Photoinduced damage to cellular DNA: Direct and photosensitized reactions. *Photochem. Photobiol.*, **2012**, 88, 1048–1065.

39. Cadet,J., Douki,T. and Ravanat,J.L.Oxidatively generated damage to cellular DNA by UVB and UVA radiation. *Photochem. Photobiol.*, **2015**, 91, 140–155.

40. Drouin, R., Therrien, J.P. UVB-induced Cyclobutane Pyrimidine Dimer Frequency Correlates with Skin Cancer Mutational Hotspots in p53. *Photochem. Photobiol.*, **1997**, 66, 719–726.

41. Sage, E., Lamolet, B., Brulay, E., Moustacchi, E., Chteauneuf, A., Drobetsky, E.A. Mutagenic specificity of solar UV light in nucleotide excision repair-deficient rodent cells. *Proc. Natl. Acad. Sci. U. S. A.*, **1996**, 93, 176–180.

42. Sage,E. Distribution and repair of photolesions in DNA: Genetic consequences and the role of sequence context. Photochem. Photobiol., 1993, 57, 163–174.

43. Pfeifer, G.P., You,Y.-H., Besaratinia, A. Mutations induced by ultraviolet light. Fundam. *Mol. Mech. Mutagen.*, **2005**, 571, 19–31.

44. Gustavsson, T., Improta, R., Markovitsi, D. DNA/RNA: Building blocks of life under UV irradiation. *J. Phys. Chem. Lett.*, **2010**, 1, 2025–2030.

45. Bhagavan, N.V., Ha,C.-E. Structure and Properties of DNA Photoproducts. *In Essentials of Medical Biochemistry. CRC Press*, **2015**, 381–400.

46. Cadet, J., Mouret, S., Ravanat, J.L., Douki, T. Photoinduced damage to cellular DNA: Direct and photosensitized reactions. *In Photochemistry and Photobiology. Blackwell Publishing Ltd*, **2012**, 88, 1048–1065.

47. Cadet, J., Sage, E., Douki, T. Ultraviolet radiation-mediated damage to cellular DNA. *Mut. Res. Fund. Mol. Mec. Mut.*, **2005**, 571, 3–17.

48. Banyasz, A., Douki, T., Improta, R., Gustavsson, T., Onidas, D., Vayá, I., Perron, M., Markovitsi, D. Electronic excited states responsible for dimer formation upon UV absorption directly by thymine strands: Joint experimental and theoretical study. *J. Am. Chem. Soc.*, **2012**, 134, 14834–14845.

49. Rauer, C., Nogueira, J.J., Marquetand, P. González, L. Cyclobutane Thymine Photodimerization Mechanism Revealed by Nonadiabatic Molecular Dynamics. *J. Am. Chem. Soc.*, **2016**, 138, 15911–15916.

50. Epe, B. DNA damage spectra induced by photosensitization. *Photochem. Photobiol. Sci.*, **2012**, 11, 98–106.

51. Cuquerella, M.C., Lhiaubet-Vallet, V., Cadet, J. Miranda, M.A. Benzophenone photosensitized DNA damage. *Acc. Chem. Res.*, **2012**, 45, 1558–1570.

52. Dumont, E., Wibowo, M., Roca-Sanjuán, D., Garavelli, M., Assfeld, X., Monari, A. Resolving the benzophenone DNA-photosensitization mechanism at QM/MM level. *J. Phys. Chem. Lett*., **2015**, 6, 576–580.

53. Sinha, R.P., Häder, D.-P. UV-induced DNA damage and repair: a review. *Photochem. Photobiol. Sci.*, **2002**, 1, 225–236.

54. Kim, J-K, Patel, D., Choi, B-S Contrasting structural impacts induced by cis-syn cyclobutane dimer and (6–4) adducts in DNA duplex decamers: Implication in mutagenesis and repair activity. *Photochem. Photobiol.*, **1995**, 62, 44–50.

55. Kim, J. -K., Choi, B-S The Solution Structure of DNA Duplex-Decamer Containing the (6-4) Photoproduct of Thymidylyl (3′→5′)Thymidine by NMR and Relaxation Matrix Refinement. *Eur. J. Biochem.*, **1995**, 228, 849–854.

56. Jing, Y., Kao, J.F.-L., Taylor, J.S. Thermodynamic and base-pairing studies of matched and mismatched DNA dodecamer duplexes containing cis-syn, (6-4) and Dewar photoproducts of TT. *Nucleic Acids Res.*, **1998**, 26, 3845–3853.

57. Fujiwara, Y., Iwai, S. hermodynamic studies of the hybridization properties of photolesions in DNA. *Biochemistry*, **1997**, 36, 1544–1550.

58. Park, C.J., Lee, J.H., Choi,B.S. Functional insights gained from structural analyses of DNA duplexes that contain UV-damaged photoproducts. *Photochem. Photobiol.*, **2007**, 83, 187–195.

59. Dehez, F., Gattuso, H., Bignon, E., Morell, C., Dumont, E., Monari, A. Conformational polymorphism or structural invariance in DNA photoinduced lesions: implications for repair rates. *Nucleic Acids Res.*, **2017**, 45, 3654–3662.

60. Sedletska,Y., Radicella, J.P., Sage, E. Replication fork collapse is a major cause of the high mutation frequency at three-base lesion clusters. *Nucleic Acids Res.*, **2013**, 41, 9339–9348.

61. Lee, J.H., Choi, Y.J., Choi, B.S. Solution structure of the DNA decamer duplex containing a 3’-T x T basepair of the cis-syn cyclobutane pyrimidine dimer: implication for the mutagenic property of the cis-syn dimer. *Nucleic Acids Res.*, **2000**, 28, 1794–1801.

62. Johnson, R.E., Haracska, L., Prakash, S., Prakash, L. Role of DNA polymerase eta in the bypass of a (6-4) TT photoproduct. *Mol. Cell. Biol.*, **2001**, 21, 3558–63.

63. Pfeifer, G.P. Formation and Processing of UV Photoproducts: Effects of DNA Sequence and Chromatin Environment. *Photochem. Photobiol.*, **1997**, 65, 270–283.

64. Mouret, S., Charveron, M., Favier, A., Cadet, J., Douki, T. Differential repair of UVB-induced cyclobutane pyrimidine dimers in cultured human skin cells and whole human skin. *DNA Repair (Amst).*, **2008**, 7, 704–712.

65. Ziegler, A., Leffell, D.J., Kunala, S., Sharma, H.W., Gailani, M., Simon, J.A., Halperin, A.J., Baden, H.P., Shapiro, P.E., Bale, A.E. Mutation hotspots due to sunlight in the p53 gene of nonmelanoma skin cancers. *Proc. Natl. Acad. Sci. U. S. A.*, **1993**, 90, 4216–20.

66. Brash, D.E., Rudolph, J.A., Simon, J.A., Lin, A., McKenna, G.J., Baden, H.P., Halperin, A.J., Pontén, J. A role for sunlight in skin cancer: UV-induced p53 mutations in squamous cell carcinoma. *Proc. Natl. Acad. Sci. U. S. A.*, **1991**, 88, 10124–8.

67. Lawrence, C.W., Gibbs, P.E.M., Borden, A., Horsfall, M.J., Kilbey, B.J. Mutagenesis induced by single UV photoproducts in E. coli and yeast. *Mutat. Res. Toxicol.*, **1993**, 299, 157–163.

68. Taylor, J.S. Unraveling the Molecular Pathway from Sunlight to Skin Cancer. *Acc. Chem. Res.*, **1994**, 27, 76–82.

69. Urruticoechea, A., Alemany, R., Balart, J., Villanueva, A., Viñals, F., Capella, G. Recent advances in cancer therapy: an overview. *Current pharmaceutical design*, **2010**, 16(1), 3-10.
70. Chabner, B. A., & Roberts Jr, T. G. (2005). Chemotherapy and the war on cancer. *Nature Reviews Cancer*, *5*(1), 65.

71. Laprise-Pelletier, M.; Simao, T.; Fortin, M.-A. Gold nanoparticles in radiotherapy and recent progress in nanobrachytherapy. *Adv. Healthcare Mater.* **2018**, 7, 1701460.

72. Cheng, L., Wang, C., Feng, L., Yang, K., Liu, Z. Functional nanomaterials for phototherapies of cancer. *Chemical reviews*, **2014**, 114(21), 10869-10939.

73. Agostinis, P., Berg, K., Cengel, K. A., Foster, T. H., Girotti, A. W., Gollnick, S. O., Stephen, M.H, Hamblin, M.R, Juzeniene, A., Kessel, D., Moan, J., Mroz, P., Nowis, D., Piette, J., Korbelik, M. Photodynamic therapy of cancer: an update. *CA: a cancer journal for clinicians*, **2011**, 61(4), 250-281.

74. Huang, Y., Luo, Y., Zheng, W., Chen, T. Rational design of cancer-targeted BSA protein nanoparticles as radiosensitizer to overcome cancer radioresistance. ACS applied materials & interfaces, 2014, 6(21), 19217-19228.

75. Wang, H., Mu, X., He, H., & Zhang, X. D. Cancer radiosensitizers. *Trends in pharmacological sciences*, **2018**, 39(1), 24-48.

76. Schürmann, R., Vogel, S., Ebel, K., & Bald, I. The Physico-Chemical Basis of DNA Radiosensitization: Implications for Cancer Radiation Therapy. *Chemistry–A European Journal*, **2018,** 24, 10271

77. Hainfeld, J. F.; Slatkin, D. N.; Smilowitz, H. M. The Use of Gold Nanoparticles to Enhance Radiotherapy in Mice. *Phys. Med. Biol.* **2004**, 49(18), 309.

78. Bobyk, L., Edouard, M., Deman, P., Vautrin, M., Pernet-Gallay, K., Delaroche, J., Adam, J-F., Estève, H., Ravanat, J-L., Elleaume, H. Photoactivation of gold nanoparticles for glioma treatment. *Nanomedicine: Nanotechnology, Biology and Medicine*, **2013**, 9(7), 1089-1097.

79. Xu, R.; Ma, J.; Sun, X.; Chen, Z.; Jiang, X.; Guo, Z.; Huang, L.; Li, Y.; Wang, M.; Wang, C. Ag nanoparticles sensitize IR-induced killing of cancer cells. *Cell Res.*, **2009**, 19, 1031–1034.

80. Detappe, A., Kunjachan, S., Rottmann, J., Robar, J., Tsiamas, P., Korideck, H., Tillement, O., Berbeco, R. AGuIX nanoparticles as a promising platform for image-guided radiation therapy. *Cancer nanotechnology*, **2015**, 6(1), 4.

81. Le Duc, G., Miladi, I., Alric, C., Mowat, P., Bräuer-Krisch, E., Bouchet, A., ... & Epicier, T. Toward an image-guided microbeam radiation therapy using gadolinium-based nanoparticles. *ACS nano*, **2011**, *5*(12), 9566-9574.

82. Carter, J. D., Cheng, N. N., Qu, Y., Suarez, G. D., & Guo, T. Nanoscale energy deposition by X-ray absorbing nanostructures. *The Journal of Physical Chemistry B*, **2007**, 111, 11622-11625.

83. Porcel, E., Liehn, S., Remita, H., Usami, N., Kobayashi, K., Furusawa, Y., Le Sech, C., Lacombe, S. Platinum nanoparticles: a promising material for future cancer therapy? *Nanotechnology*, **2010**, 21(8), 085103.

84. Le Goas, M., Paquirissamy, A., Gargouri, D., Fadda, G., Testard, F., Aymes-Chodur, C., Renault, J. P. Irradiation Effects on Polymer-Grafted Gold Nanoparticles for Cancer Therapy. *ACS Applied Bio Materials*, **2018**, 2(1), 144-1546.

85. Deng, J., Xu, S., Hu, W., Xun, X., Zheng, L., & Su, M. Tumor targeted, stealthy and degradable bismuth nanoparticles for enhanced X-ray radiation therapy of breast cancer. *Biomaterials*, **2018**, *54*, 24-33.

86. Kobayashi, K., Usami, N., Porcel, E., Lacombe, S., & Le Sech, C. Enhancement of radiation effect by heavy elements. *Mutation Research/Reviews in Mutation Research*, **2010**, 704(1-3),, 123-131.

87. Coulter, J. A., Hyland, W. B., Nicol, J., Currell, F. J. Radiosensitising nanoparticles as novel cancer therapeutics—pipe dream or realistic prospect? *Clinical Oncology*, **2013**, 25(10), 593-603.

88. Huang, X., El-Sayed, M. A. Gold nanoparticles: optical properties and implementations in cancer diagnosis and photothermal therapy. *Journal of advanced research*, **2010**, 1(1), 13-28.

89. Rancoule, C., Magné, N., Vallard, A., Guy, J. B., Rodriguez-Lafrasse, C., Deutsch, E., Chargari, C. Nanoparticles in radiation oncology: From bench-side to bedside. *Cancer letters*, **2016**, 375(2), 256-262.

90. Kobayashi, K.; Usami, N.; Porcel, E.; Lacombe, S.; Le Sech, C. Enhancement of radiation effect by heavy elements. *Mutation Research,* **2010**, 704 (1-3), 123-131.

91. Peukert, D.; Kempson, I.; Douglass, M.; Bezak, E. Metallic nanoparticle radiosensitisation of ion radiotherapy: a review. *Physica Medica,* **2018**, 47, 121-128.

92. Fang, J., Nakamura, H., & Maeda, H. The EPR effect: unique features of tumor blood vessels for drug delivery, factors involved, and limitations and augmentation of the effect. *Advanced drug delivery reviews*, **2011**, 63(3), 136-151.

93. Henderson, L.; Neumann, O.; Kaffes, C.; Zhang, R.; Marangoni, V.; Ravoori, M. K.; Kundra, V.; Bankson, J.; Nordlander, P.; Halas, N. J. Routes to potentially safer T1 magnetic resonance imaging contrast in a compact plasmonic nanoparticle with enhanced fluorescence. *ACS Nano* **2018**, 12 (8), 8214-8223.

94. Gilles, M.; Brun, E.; Sicard-Roselli, C. Gold nanoparticles functionalization notably decreases radiosensitization through hydroxyl radical production under ionizing radiation, *Colloids and Surfaces B: Biointerfaces* **2014**, 123, 770-777.

95. Brun, E.; Sicard-Roselli, C. Actual questions raised by nanoparticle radiosensitization. *Radiation Physics and Chemistry* **2016**, 128, 134-142.

96. Her, S.; Jaffray, D. A.; Allen, C. Gold nanoparticles for applications in cancer radiotherapy: Mechanisms and recent advancements. *Advanced Drug Delivery Reviews* **2017**, 109, 84-101.

97. Misawa, M., & Takahashi, J. Generation of reactive oxygen species induced by gold nanoparticles under x-ray and UV Irradiations. *Nanomedicine: Nanotechnology, Biology and Medicine*, **2011**, 7(5), 604-614.

98. Zhang, X. D., Luo, Z., Chen, J., Shen, X., Song, S., Sun, Y., Fan, F., Leong, D. T.,Xie, J. Ultrasmall Au10−12 (SG)10−12 nanomolecules for high tumor specificity and cancer radiotherapy. *Advanced materials*, **2014**, 26(26), 4565-4568.

99. Baletto, F. (2018). Structural properties of sub nanometer metallic clusters. Journal of Physics: Condensed Matter.

100. Zhang, X. D., Chen, J., Luo, Z., Wu, D., Shen, X., Song, S. S., ... & Fan, S. Enhanced Tumor Accumulation of Sub-2 nm Gold Nanoclusters for Cancer Radiation Therapy. *Advanced healthcare materials*, **2014**, 3(1), 133-141.

101. Baletto, F.; Ferrando, R.; Fortunelli, A.; Montalenti, F.; Mottet, C. Crossover among structural motifs in transition and noble-metal clusters. *J. Chem. Phys.* **2002**, 116(9), 3856-3863.

102. Baletto, F.; Ferrando, R. Structural properties of nanoclusters: Energetic, thermodynamic, and kinetic effects. *Rev. Mod. Phys.* **2005**, 77(1), 371.

103. Häberlen, O. D.; Chung, S.-C.; Stener, M.; Rösch, N. From clusters to bulk: a relativistic density functional investigation on a series of gold clusters Au n, n=6,…,147. *J. Chem. Phys.* **1997**, 106, 5189-5201.

104. Ferrando, R.; Fortunelli, A.; Rossi, G. Quantum effects on the structure of pure and binary metallic nanoclusters. *Phys. Rev. B* **2005**, 72, 085449-1,9.

105. Logsdail, A. J.; Li, Z. Y.; Johnston, R. L. Faceting preferences for AuN and PdN nanoclusters with high-symmetry motifs. *Phys. Chem. Chem. Phys.* **2013**, 15, 8392-8400.

106. Li, H.; Li, L.; Pedersen, A.; Gao, Y.; Khetrapal, N.; Jónsson, H.; Zeng, X. C. Magic-number gold nanoclusters with diameters from 1 to 3.5 nm: Relative stability and catalytic activity for CO oxidation. *Nano Lett.* ***2015***, 15(1), 682-688.

107. Tarrat, N.; Rapacioli, M.; Cuny , J.; Morillo, J.; Heully, J.-L.; Spiegelman, F. Global optimization of neutral and charged 20- and 55-atom silver and gold clusters at the DFTB level. *Computational and Theoretical Chemistry* **2017**, 1107, 102–114.

108. Tarrat, N.; Rapacioli, M.; Spiegelman F. Au147 nanoparticles: ordered or amorphous? *J. Chem. Phys.* **2018**, 148, 204308.

109. Rahm, J. M.; Erhart, P. Beyond Magic Numbers: Atomic Scale Equilibrium Nanoparticle Shapes for Any Size. *Nano Lett.* **2017**, 17(9), 5775-5781.

110. Cleveland, C. L.; Landman, U.; Schaaff, T. G.; Shafigullin, M. N.; Stephens, P. W.; Whetten, R. L. Structural Evolution of Smaller Gold Nanocrystals: The Truncated Decahedral Motif. *Phys. Rev. Lett.* **1997**, 79, 1873.

111. Vankayala, R.; Kuo, C.-L.; Nuthalapati, K.; Chiang, C.-S.; Hwang, K.-C. Nucleus-Targeting Gold Nanoclusters for Simultaneous In Vivo Fluorescence Imaging, Gene Delivery, and NIR-Light Activated Photodynamic Therapy. *Advanced Functional Materials*, **2015**, 25, 5934-5945.

112. Koga, K.; Takeo, H.; Ikeda, T.; Ohshima, K.-I. In situ grazing-incidence x-ray-diffraction and electron-microscopic studies of small gold clusters. *Phys. Rev. B,* **1998**, 57, 4053.

113. Koga, K.; Ikeshoji, T.; Sugawara, K.-I. Size- and Temperature-Dependent Structural Transitions in Gold Nanoparticles. *Phys. Rev. Lett*. **2004**, 92, 115507.

114. Li, Z. Y.; Young, N. P.; Di Vece, M.; Palomba, S.; Palmer, R. E.; Bleloch, A. L.; Curley, B. C.; Johnston, R. L.; Jiang, J.; Yuan, J. Three-dimensional atomic-scale structure of size-selected gold nanoclusters. *Nature* **2008**, 451, 46-48.

115. Foster, D. M.; Ferrando, R.; Palmer, R. E. Experimental determination of the energy difference between competing isomers of deposited, size-selected gold nanoclusters. *Nature Communications* **2018**, 9, 1323.

116. Plant, S. R.; Cao, L.; Palmer, R. E. Atomic Structure Control of Size-Selected Gold Nanoclusters during Formation. *J. Am. Chem. Soc.* **2014**, 136, 7559-7562.

117. Barnard, Amanda S., et al. "Nanogold: a quantitative phase map." *ACS nano* 3.6 (2009): 1431-1436.

118. Haume, K., Rosa, S., Grellet, S., Śmiałek, M. A., Butterworth, K. T., Solov'yov, A. V., ... & Mason, N. J. Gold nanoparticles for cancer radiotherapy: a review. *Cancer nanotechnology*, **2016**, 7(1), 8.

119. Gervais, B.; Beuve, M.; Olivera, G.H.; Galassi, M.E.; Rivarola, R.D. Production of HO2 and O2 by multiple ionization in water radiolysis by swift carbon ions. *Chem. Phys. Lett.* **2005**, 410 (4-6), 330-334.

120. Gervais, B.; Beuve, M.; Olivera, G.H.; Galassi, M.E. Numerical simulation of multiple ionization and high LET effects in liquid water radiolysis. *Radiat. Phys. Chem.* **2006**, 75 (4), 493-513.

121. Meng, S.; Wang, E. G.; Gao, S. Water adsorption on metal surfaces: a general picture from density functional theory studies. *Phys. Rev. B* **2004**, 69, 195404-1,13.

122. Phatak, A. A.; Delglass, W. N.; Ribeiro, F. H.; Schneider, W. F. Density functional theory comparison of water dissociation steps on Cu, Au, Ni, Pd and Pt. *J. Phys. Chem. C* **2009**, 113, 7269-7276.

123. Nadler, R.; Sanz, J. F. Effect of dispersion correction on the Au (1 1 1)-H2O interface: a first-principles study. *J. Chem. Phys.* **2012**, 137(11), 114709.

124. Carrasco, J.; Klimes, J.; Michaelides, A. The role of van der Waals forces in water adsorption on metals. *J. Chem. Phys.* **2013**, 138, 024708-1,9.

125. Berg, A.; Peter, C.; Johnston, K. Evaluation and Optimization of Interface Force Fields for Water on Gold Surfaces. *J. Chem. Theory Comput.* **2017**, 13(11), 5610-5623.

126. Lin, X.; Groß, A. First-principles study of the water structure on flat and stepped gold surfaces. *Surf. Sci.* **2012**, 606, 886-891.

127. Xue, Y. Water monomer interaction with gold nanoclusters from van der Waals density functional theory. *J. Chem. Phys.* **2012**, 136(2), 024702

128. de Morais, R. F.; Kerber, T.; Calle-Vallejo, F.; Sautet, P.; Loffreda, D. Capturing solvation effects at a liquid/nanoparticle interface by Ab Initio molecular dynamics: Pt201 immersed in water. *Small* **2016**, 12(38), 5312-5319.

129. Ju, S.-P. A molecular dynamics simulation of the adsorption of water molecules surrounding an Au nanoparticle. *J. Chem. Phys.* **2005**, 122, 094718-1,6.

130. Chang, C. I.; Lee, W. J.; Young, T. F.; Ju, S. P.; Chang, C. W.; Chen, H. L.; Chang, J. G. Adsorption mechanism of water molecules surrounding Au nanoparticles of different sizes. *J. Chem. Phys.* **2008**, 128(15), 154703.

131. Zhu, B.; Xu, Z.; Wang, C.; Gao, Y. Shape evolution of metal nanoparticles in water vapor environment. *Nano Lett.* **2016**, 16(4), 2628-2632.

132. Brun, E., Sanche, L., & Sicard-Roselli, C. Parameters governing gold nanoparticle X-ray radiosensitization of DNA in solution. *Colloids and surfaces B: Biointerfaces*, **2009**, *72*(1), 128-134.

133. Liu, C. J., Wang, C. H., Chen, S. T., Chen, H. H., Leng, W. H., Chien, C. C., ... & Hsiao, M. (2010). Enhancement of cell radiation sensitivity by pegylated gold nanoparticles. Physics in Medicine & Biology, 55(4), 931.

134. Zhang, X. D., Wu, D., Shen, X., Chen, J., Sun, Y. M., Liu, P. X., & Liang, X. J. (2012). Size-dependent radiosensitization of PEG-coated gold nanoparticles for cancer radiation therapy. *Biomaterials*, *33*(27), 6408-6419.

135. Gilles, M., Brun, E., & Sicard-Roselli, C. (2014). Gold nanoparticles functionalization notably decreases radiosensitization through hydroxyl radical production under ionizing radiation. Colloids and Surfaces B: Biointerfaces, 123, 770-777.

136. Xiao, F., Zheng, Y., Cloutier, P., He, Y., Hunting, D., & Sanche, L. (2011). On the role of low-energy electrons in the radiosensitization of DNA by gold nanoparticles. Nanotechnology, 22(46), 465101.

137. Wang, X., Wang, X., Bai, X., Yan, L., Liu, T., Wang, M., ... & Chen, C. (2018). Nanoparticle Ligand Exchange and Its Effects at the Nanoparticle–Cell Membrane Interface. Nano letters, 19(1), 8-18.

138. Rahman, W. N., Bishara, N., Ackerly, T., He, C. F., Jackson, P., Wong, C., ... & Geso, M. (2009). Enhancement of radiation effects by gold nanoparticles for superficial radiation therapy. Nanomedicine: Nanotechnology, Biology and Medicine, 5(2), 136-142.

139. Jokerst, J. V., Lobovkina, T., Zare, R. N., & Gambhir, S. S. (2011). Nanoparticle PEGylation for imaging and therapy. Nanomedicine, 6(4), 715-728.

140. Suk, J. S., Xu, Q., Kim, N., Hanes, J., & Ensign, L. M. (2016). PEGylation as a strategy for improving nanoparticle-based drug and gene delivery. Advanced drug delivery reviews, 99, 28-51.

141. Reznickova, A., Slepicka, P., Slavikova, N., Staszek, M., & Svorcik, V. (2017). Preparation, aging and temperature stability of PEGylated gold

nanoparticles. Colloids and Surfaces A: Physicochemical and Engineering Aspects, 523, 91-97.

142. Reznickova, A., Slavikova, N., Kolska, Z., Kolarova, K., Belinova, T., Kalbacova, M. H., ... & Svorcik, V. (2019). PEGylated gold nanoparticles: Stability, cytotoxicity and antibacterial activity. Colloids and Surfaces A: Physicochemical and Engineering Aspects, 560, 26-34.

143. Ma, N., Wu, F. G., Zhang, X., Jiang, Y. W., Jia, H. R., Wang, H. Y., Jia, H. R., Li, Y.H., Liu, P.,Gu, N., Chen, Z. Shape-dependent radiosensitization effect of gold nanostructures in cancer radiotherapy: comparison of gold nanoparticles, nanospikes, and nanorods. ACS applied materials &interfaces, 2017, 9(15), 13037-13048.

144. Burt, J. L., Elechiguerra, J. L., Reyes-Gasga, J., Montejano-Carrizales, J. M., & Jose-Yacaman, M. (2005). Beyond Archimedean solids: star polyhedral gold nanocrystals. *Journal of crystal growth*, *285*(4), 681-691.

145. Bazán-Díaz, L., Mendoza-Cruz, R., Velázquez-Salazar, J. J., Plascencia-Villa, G., Romeu, D., Reyes-Gasga, J., ... & Guisbiers, G. (2015). Gold–copper nanostars as photo-thermal agents: synthesis and advanced electron microscopy characterization. Nanoscale, 7(48), 20734-20742.

146. Niu, W., Chua, Y. A. A., Zhang, W., Huang, H., & Lu, X. (2015). Highly symmetric gold nanostars: crystallographic control and surface-enhanced Raman scattering property. Journal of the American Chemical Society, 137(33), 10460-10463.

147. Ahmad, N., Wang, G., Nelayah, J., Ricolleau, C., & Alloyeau, D. (2017). Exploring the formation of symmetric gold nanostars by liquid-cell transmission electron microscopy. Nano letters, 17(7), 4194-4201.

148. Benoit, D. N., Zhu, H., Lilierose, M. H., Verm, R. A., Ali, N., Morrison, A. N., ... & Colvin, V. L. (2012). Measuring the grafting density of nanoparticles in solution by analytical ultracentrifugation and total organic carbon analysis. Analytical chemistry, 84(21), 9238-9245.

149. Lu, J., Xue, Y., Shi, R., Kang, J., Zhao, C. Y., Zhang, N. N., ... & Liu, K. (2019). A non-sacrificial method for the quantification of poly (ethylene glycol) grafting density on gold nanoparticles for applications in nanomedicine. Chemical science, 10(7), 2067-2074.

150. Rahme, K., Chen, L., Hobbs, R. G., Morris, M. A., O'Driscoll, C., & Holmes, J. D. (2013). PEGylated gold nanoparticles: polymer quantification as a function of PEG lengths and nanoparticle dimensions. Rsc Advances, 3(17), 6085-6094.

151. Liu, H., Doane, T. L., Cheng, Y., Lu, F., Srinivasan, S., Zhu, J. J., & Burda, C. (2015). Control of surface ligand density on PEGylated gold nanoparticles for optimized cancer cell uptake. Particle & Particle Systems Characterization, 32(2), 197-204.

152. Lane, J. M. D., & Grest, G. S. (2010). Spontaneous asymmetry of coated spherical nanoparticles in solution and at liquid-vapor interfaces. Physical review letters, 104(23), 235501.

153. Jiménez, A., Sarsa, A., Blázquez, M., & Pineda, T. (2010). A molecular dynamics study of the surfactant surface density of alkanethiol self-assembled monolayers on gold nanoparticles as a function of the radius. The Journal of Physical Chemistry C, 114(49), 21309-21314.

154. Haume, K., Mason, N. J., & Solov’yov, A. V. (2016). Modeling of nanoparticle coatings for medical applications. The European Physical Journal D, 70(9), 181.

155. Meena, S. K., Goldmann, C., Nassoko, D., Seydou, M., Marchandier, T., Moldovan, S., ... & Portehault, D. (2017). Nanophase segregation of self-assembled monolayers on gold nanoparticles. ACS nano, 11(7), 7371-7381.

156. Gao, H. M., Liu, H., Qian, H. J., Jiao, G. S., & Lu, Z. Y. (2018). Multiscale simulations of ligand adsorption and exchange on gold nanoparticles. Physical Chemistry Chemical Physics, 20(3), 1381-1394.

157. Goldmann, C., Ribot, F., Peiretti, L. F., Quaino, P., Tielens, F., Sanchez, C., ... & Portehault, D. (2017). Quantified binding scale of competing ligands at the surface of gold nanoparticles: The role of entropy and intermolecular forces. Small, 13(20), 1604028.

158. Carro, P., Torrelles, X., & Salvarezza, R. C. (2014). A novel model for the (√ 3×√ 3) R 30° alkanethiolate–Au (111) phase based on alkanethiolate–Au adatom complexes. Physical Chemistry Chemical Physics, 16(35), 19017-19023.

159. Fajín, J. L., Teixeira, F., Gomes, J. R., & Cordeiro, M. N. D. (2016). Effect of van der Waals interactions in the DFT description of self-assembled monolayers of thiols on gold. In 9th Congress on Electronic Structure: Principles and Applications (ESPA 2014) (pp. 127-139). Springer, Berlin, Heidelberg.

160. Cuadrado, R., Puerta, J. M., Soria, F., & Cerdá, J. I. (2013). A first principles study of thiol-capped Au nanoparticles: Structural, electronic, and magnetic properties as a function of thiol coverage. The Journal of chemical physics, 139(3), 034319.

161. Ting, E. C., Popa, T., & Paci, I. (2016). Surface-site reactivity in small-molecule adsorption: A theoretical study of thiol binding on multi-coordinated gold clusters. Beilstein journal of nanotechnology, 7(1), 53-61.

162. Chithrani, D. B., Jelveh, S., Jalali, F., van Prooijen, M., Allen, C., Bristow, R. G., ... & Jaffray, D. A. Gold nanoparticles as radiation sensitizers in cancer therapy. *Radiation research*, **2010**, 173(6), 719-728.

163. Janic, B., Liu, F., Bobbitt, K-R., Brown, S., Chetty, J., Mao, G., Movsas, B., Wen, N., Cellular Uptake and Radio-sensitization Effect of Small Gold Nanoparticles in MCF-7 Breast Cancer Cells, *J Nanomed Nanotechno*l **2018**, Vol 9(3): 499

164. Burger, N., Biswas, A., Barzan, D., Kirchner, A., Hosser, H., Hausmann, M., ... & Veldwijk, M. R. A method for the efficient cellular uptake and retention of small modified gold nanoparticles for the radiosensitization of cells. *Nanomedicine: Nanotechnology, Biology and Medicine*, **2014**, 10(6), 1365-1373.

165. Zhang, S., Gao, H., & Bao, G. Physical principles of nanoparticle cellular endocytosis. *ACS nano*, **2015**, 9(9), 8655-8671.

166. Manning, M. D., Kwansa, A. L., Oweida, T., Peerless, J. S., Singh, A., & Yingling, Y. G. Progress in ligand design for monolayer-protected nanoparticles for nanobio interfaces. *Biointerphases*, **2018**, 13(6), 06D502.

167. Wang, Y., Black, K. C., Luehmann, H., Li, W., Zhang, Y., Cai, X., ... & Li, Z. Y. Comparison study of gold nanohexapods, nanorods, and nanocages for photothermal cancer treatment. *ACS nano*, **2013**, 7(3), 2068-2077.

168. Li, Y., Kröger, M., & Liu, W. K. Shape effect in cellular uptake of PEGylated nanoparticles: comparison between sphere, rod, cube and disk. *Nanoscale*, **2015**, 7(40), 16631-16646.

169. Xie, X., Liao, J., Shao, X., Li, Q., & Lin, Y. The effect of shape on cellular uptake of gold nanoparticles in the forms of stars, rods, and triangles. *Scientific reports*, **2017**, 7(1), 3827.

170. Ma, X., Cheng, Y., Huang, Y., Tian, Y., Wang, S., & Chen, Y. PEGylated gold nanoprisms for photothermal therapy at low laser power density. *RSC Advances*, **2015**, 5(99), 81682-81688.

171. Lunnoo, T., Assawakhajornsak, J., & Puangmali, T. In Silico Study of Gold Nanoparticle Uptake into a Mammalian Cell: Interplay of Size, Shape, Surface Charge, and Aggregation. *The Journal of Physical Chemistry C*, **2019**, 123(6), 3801-3810.

172. Liu, Y., Peng, B., Sohrabi, S., & Liu, Y. The Configuration of Copolymer Ligands on Nanoparticles Affects Adhesion and Uptake. *Langmuir*, **2016**, 32(39), 10136-10143.

173. Oh, E., Delehanty, J. B., Sapsford, K. E., Susumu, K., Goswami, R., Blanco-Canosa, J. B., ... & Goering, P. L. Cellular uptake and fate of PEGylated gold nanoparticles is dependent on both cell-penetration peptides and particle size. *ACS nano*, **2011**, 5(8), 6434-6448.

174. Ho, L. W. C., Yung, W. Y., Sy, K. H. S., Li, H. Y., Choi, C. K. K., Leung, K. C. F., ... & Choi, C. H. J. Effect of alkylation on the cellular uptake of polyethylene glycol-coated gold nanoparticles. *ACS nano*, **2017**, 11(6), 6085-6101.

175. Van Haute, D., Liu, A. T., & Berlin, J. M. Coating metal nanoparticle surfaces with small organic molecules can reduce nonspecific cell uptake. *ACS nano*, **2018**, 12(1), 117-127.

176. Wang, S., Teng, Z., Huang, P., Liu, D., Liu, Y., Tian, Y., ... & Lu, G. Reversibly Extracellular pH Controlled Cellular Uptake and Photothermal Therapy by PEGylated Mixed-Charge Gold Nanostars. *Small*, **2015,** 11(15), 1801-1810.

177. Lunnoo, T., Assawakhajornsak, J., & Puangmali, T. In Silico Study of Gold Nanoparticle Uptake into a Mammalian Cell: Interplay of Size, Shape, Surface Charge, and Aggregation. *The Journal of Physical Chemistry C*, **2019**, 123(6), 3801-3810.

178. Van Lehn, R. C., Atukorale, P. U., Carney, R. P., Yang, Y. S., Stellacci, F., Irvine, D. J., & Alexander-Katz, A. Effect of particle diameter and surface composition on the spontaneous fusion of monolayer-protected gold nanoparticles with lipid bilayers. *Nano letters*, **2013**, 13(9), 4060-4067.

179. Cui, L., Her, S., Borst, G. R., Bristow, R. G., Jaffray, D. A., & Allen, C. Radiosensitization by gold nanoparticles: Will they ever make it to the clinic?. *Radiotherapy and Oncology*, **2017**, 124(3), 344-356.

Chapter 3: Methodology

3.1 Introduction

Theoretical modeling has known significant advances over the last decades and is becoming an essential approach to investigate many chemical, physical and biological properties at the atomic level. Furthermore, as computers continue to increase in speed and capacity, larger and more complex three-dimensional structures can be studied. In practice, there are two main approaches to compute the total electronic energy of a system at an accurate level: Quantum Mechanics (QM), also named *ab initio* or wavefunction theory (WFT) methods, which is based on the numerical solution of the Schrödinger equation and density functional theory (DFT) based on the solution of Kohn-Sham equations. Molecular Mechanics (MM) is another approach (low level of accuracy regarding energetics) which is based on Newtonian mechanics, relying on the harmonic approximation. In this thesis, we use DFT to calculate the electronic structures of gold metallic nanoparticles (up to 1000 atoms) and explicit solvent MD simulations (MM-based) to simulate the dynamics behavior of DNA and protein (up to 30000 atoms). This chapter is devoted to present the theoretical background and methodologies used in this thesis. The basic principals of quantum mechanics (Schrödinger equation and Born-Oppenheimer approximation) is given is section 3.2. In section 3.3, a brief introduction of DFT and a description of VASP program is given. In section 3.4, the basis of classical molecular dynamics method is presented.

3.2 Schrödinger Equation and Born-Oppenheimer Approximation

Computational methods applied to calculate the electronic structure of many-body systems is based on the resolution of the time-independent, non relativistic Schrödinger equation, presented in equation 3.1:

$$\hat{H}\Psi = E\Psi \quad \text{[Eq 3.1]}$$

where $\hat{H}$ is the Hamiltonian operator, Ψ is the multi-electron wave function describing the quantum state of the system and E is its energy. For a system with *n* electrons and *M* nuclei, the Hamiltonian can be decomposed in different components:

$$\hat{H} = \hat{T}_e + \hat{V}_{eN} + \hat{V}_{ee} + \hat{T}_N + \hat{V}_{NN}$$

$$= -\sum_{i}^{electrons} \frac{\Delta_i}{2} - \sum_{i}^{elec.} \sum_{k}^{nuclei} \frac{Z_k}{r_{ik}} + \sum_{i}^{elec.} \sum_{j>i}^{elec.} \frac{1}{r_{ij}} + \sum_{k} \sum_{l>k} \frac{Z_k Z_l}{R_{kl}} - \sum_{k}^{nucl.} \frac{\Delta_k}{2 M_k} \quad \text{[Eq 3.2]}$$

where $\hat{T}_e$ and $\hat{T}_N$ represent the kinetic energy of the electrons and nuclei, respectively, $\hat{V}_{eN}$ stands for electron-nuclei attractive electrostatic interaction , $\hat{V}_{ee}$ for the electron-electron repulsion , and the last term $\hat{V}_{NN}$ for the nuclei-nuclei repulsion.

Solving this equation is incredibly complex due to the coupling between electrons and nuclei. However according to the the *Born-Oppenheimer* (BO) approximation[1], the electron mass is roughly a factor of 1000 smaller thann the one of the nuclei, and the electrons are moving much faster than the nuclei. The wave function of the nuclei is neglected, so only the Hamiltonian related to electrons is considered. Despite this first step in the simplification of the problem, the Schrödinger equation can not be solved analytically, and additional approximations have to be introduced. In this context, Hartree-Fock (HF) theory[2] is proposed in 1928 to describing the total wave function as a Slater determinant. However this approach does not take into account the electronic correlation (the correlation energy which is defined as the difference between the HF energy and exact energy) and thus can lead to a wrong description of chemical bonding and reactivity.

3.3 Density Functional Theory

Density Functional Theory (DFT) is a widely used approach to solve the many-body Schrödinger equation. DFT is based on two theorems. The first theorem introduced by Hohenberg and Kohn[3] in 1964 states that the energy of the ground state of an electronic system is a unique functional of the electron density *ρ(r)*. This means that the ground state electron density determines the Hamiltonian $\hat{H}$, which determines the set of solutions/states $\{\Psi_i\}$, which determines all the properties of the system. Meanwhile, according to the second theorem, introduced by Kohn and Sham,[4] the exact electron density is the one which minimizes the energy functional and it can be obtained from the variational principle which involves only the density. The ground-state energy according to this theorem is separated into four distinct parts:

$$E[\rho(\vec{r})] = T_e^{KS}[\rho(\vec{r})] + E_H[\rho(\vec{r})] + E_{ext}[\rho(\vec{r})] + E_{xc}[\rho(\vec{r})] \quad \text{[Eq 3.3]}$$

where $T_e^{KS}[\rho(\vec{r})]$ is the electronic kinetic energy, $E_H[\rho(\vec{r})]$ is the energy resulting from electronic repulsion, $E_{ext}[\rho(\vec{r})]$ is the energy of attraction between electrons and nuclei and $E_{xc}[\rho(\vec{r})]$ is the exchange-correlation energy account for the quantum-chemical interaction between the electrons.

3.3.1 Exchange-Correlation Functional

The only unknown in the Kohn-Sham theorem is the exact form of the exchange-correlation function $E_{xc}[\rho(\vec{r})]$. However there several approximations for $E_{xc}[\rho(\vec{r})]$ such as the local density approximation (LDA)[5] and the generalized gradient approximation (GGA)[6]. LDA is a class of exchange-correlation functional which depends only on the local values of the electronic density based on the homogeneous electron gas model. The energy is written as :

$$E_{XC}^{LDA}[\rho(r)] = \int \rho(r)\epsilon_{XC}(\rho(r))\,dr \quad \text{[Eq 3.4]}$$

where ϵ_{XC} is the exchange-correlation energy per electron for an homogeneous electron gas of density $\rho(r)$. GGA includes a gradient expansion of the density as an additional variable at the same coordinate in order to represent better the inhomogeneous electron density.

$$E_{XC}^{GGA}[\rho(r)] = \int \rho(r)\epsilon_{XC}(\rho(r))\,dr + \int F_{XC}[\rho(r), \nabla\rho(r)] \quad \text{[Eq 3.5]}$$

Several GGA functionals are available such as Becke[7], Perdew and Wang (PW91)[8] and Perdew, Burke and Enzerhof (PBE)[9,10]. In this thesis, we use PBE functionals for all the DFT calculations.

LDA and GGA are the first two classes of exchange-correlation functionals present in the Jacob's ladder[11], a metaphor proposed to classify different levels of approximation, as illustrated in Figure 3.1. Climbing the ladder means that the sophistication of the exchange-correlation functional and kinetic energy operator increases and more accurate predictions are expected.

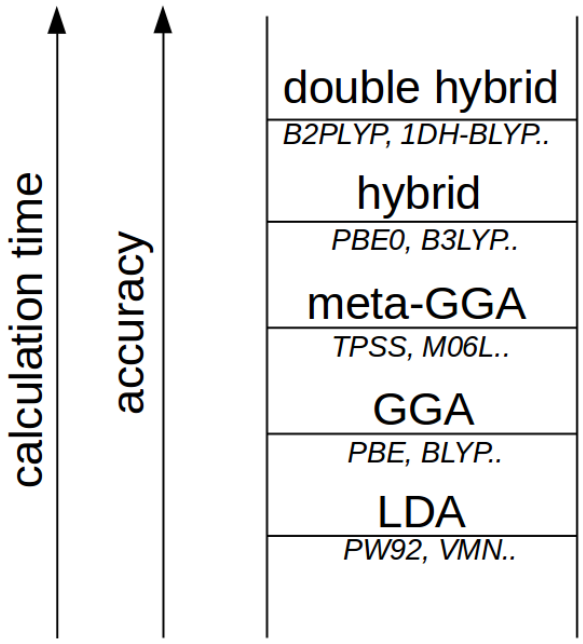

Figure 3.1. *Schematic representation of Jacob's ladder of the exchange-correlation approximation. The five generation of functionals are sorted by accuracy and calculation time. Examples of functionals are given in italic.*

3.3.2 Dispersion Correction

At the standard LDA and GGA levels in DFT, London dispersion or van der Waals (vdW) weak interactions are not described yet. Dispersion is a long-range, weak interaction coming from the response of electrons in one region to instantaneous charge density fluctuations in another one.[12] Indeed, dispersion force is particularly important since it can contribute significantly to the stability of weakly bonded systems such as adsorption of water on metallic surface or nanoparticles. However, standard DFT exchange correlation functionals (LDA, GGA or hybrid) often fail to provide a proper description of the asymptotic behavior of dispersion interactions. Several dispersion corrections have been proposed in order to improve the overall accuracy of GGA functionals. For instance, DFT-D3[13,14,15], optB86b-vdW[16,17], and dDsC[18,19].

In the DFT-D3 approach proposed by Grimme, the total electronic energy is given by:

$$E_{DFT-D3} = E_{DFT} + E_{disp} \quad \text{[Eq 3.6]}$$

where the dispersion energy E_{disp} is calculated as :

$$E_{disp} = -\frac{1}{2}\sum_{i=1}^{N_{at}}\sum_{j=1}^{N_{at}}\sum_{L}\left(f_{d,6}\frac{C_{6ij}}{r_{ij,L}^{6}} + f_{d,8}\frac{C_{8ij}}{r_{ij,L}^{8}}\right) \quad \text{[Eq 3.7]}$$

The dispersion coefficient C_{6ij} is adjusted on the basis of local geometry (coordination number) around atoms i and j. Two fitting forms of $f_{d,n}$ can be used: zero damping[20] and Becke-Johnson damping[21]. Zero damping method is expressed as :

$$f_{d,n}(r_{ij}) = \frac{S_n}{1 + 6\left(r_{ij}/\left(SR,n\,R_{oij}\right)\right)^{-\alpha n}} \quad \text{[Eq 3.8]}$$

Becke-Jonson damping is expressed as:

$$f_{d,n}(r_{ij}) = \frac{S_n r_{ij}^{n}}{r_{ij}^{n} + \left(\alpha_1 R_{oij} + \alpha_2\right)^{-n}} \quad \text{[Eq 3.9]}$$

In order to choose the best dispersion corrected functional able to improve the description of the electronic properties of gold systems (bulk, nanoparticle etc) with respect to GGA functionals, we have compared optB86b-vdW, dDsC and DFT-D3 functionals with zero damping or Becke-Johnson damping on their ability to reproduce bulk property. The cohesion energy of gold bulk calculated with different functionals against the NKPTS (number of K-points) is evaluated in Figure 3.2. The value of ΔE_{coh} for all the functionals becomes constant starting from NKPTS=50. ΔE_{coh} of gold bulk calculated with DFT-D3 (zero damping) functional (-3.695 eV/atom) is the closest one to the experimental value, follow by DFT-D3 (Becke-Johnson damping) (-3.657 eV/atom) and opt-B86b (-3.605 eV/atom). ΔE_{coh} calculated with dDsC functional (-3.424 eV/atom) is very far from experimental value. Based on this analysis, we have thus chosen DFT-D3 functional with zero damping for all the DFT calculations of gold nanoparticles.

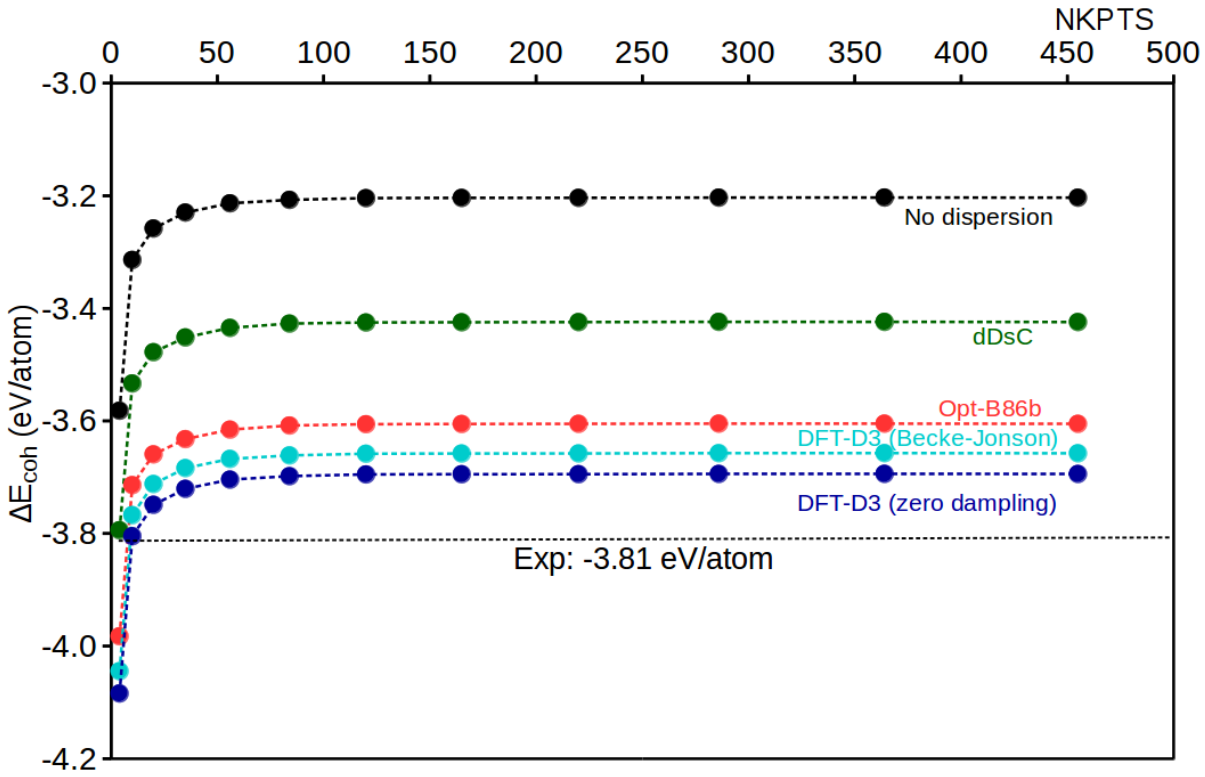

Figure 3.2. *Cohesion energy of gold bulk* ΔE_{coh} in *eV/atom against the number of K-points. The reference (no dispersion) and the experimental bulk value (-3.81 eV/atom) is also given.*

3.3.3 VASP Program

For all the DFT calculations performed in this thesis, the Vienna ab initio Simulation Package (VASP)[22,23,24] developped by G.Kresse and J. Furthmüller is used. This code applied DFT to treat systems with periodic boundary conditions (nuclei and electrons are translated in the three directions of the space defined by the vectors of the elementary pattern). In this tridimensional periodic system, VASP uses Bloch theorem[29] for expending the Kohn-Sham wave function. This theorem states that the electronic wave function can be written in the form of a plane wave phase factor:

$$\Psi_{i\vec{k}}(r) = e^{i\vec{k}r} u_{i\vec{k}}(r) \quad \text{[Eq 3.10]}$$

where $\vec{k}$ is a vector of the reciprocal space, e^{ikr} is the phase equivalent to the equation of plan wave and $u_{i\vec{k}}(r)$ is a periodic function associated with a band (or 'energy level' for periodic system). The electronic properties are calculated in the first Brillouin zone thanks to Fourier transform techniques. Within the Kohn-Sham method applied to periodic systems, the number of $\vec{k}$ vectors times the set of monoelectronic equations need to be solved. However, this is impossible if the number of $\vec{k}$ vectors is infinite. Monkhorst-Park[25] approach is proposed in this context to sample the Brillouin zone at special sets of k-points. A plane-wave energy cut-off is also introduced in the calculations in order to reduce the basis set to a finite size. This value is fixed at 400 eV because of the regular pseudo-potential of atomic oxygen. The pseudo-potentials which are used for the description of the electron-ion interactions, is approximated using the projector augmented-wave (PAW) method.[26] The precision of the calculations is set to "normal" and the total electronic energy convergence criterion is set to 10^{-6} eV. Geometry optimization is performed using the conjugate-gradient algorithm, with a threshold of 10^{-2} eV.Å^{-1} for the residual forces acting on the nuclei.

3.4 Classical Molecular Dynamics Calculations

3.4.1 Force Fields

In molecular mechanics, the total energy of the system can be described by mathematical expressions of potential, which are called force fields. Three force fields commonly used for the simulations of protein and DNA biomolecules are CHARMM[30] (Chemistry at HARvard Molecular Mechanics), GROMOS[31] and AMBER[32] (Assisted Model Buildingwith Energy Refinement). The latter force field has been used in this thesis, since

specific corrections for DNA backbone important at the microsecond range have been proposed for the parm99 force field. It can be written as:

$$E_{tot} = \sum_{bond} K_r (r - r_{eq})^2 + \sum_{angles} K_\theta (\theta - \theta_{eq})^2 + \sum_{dihedral} (\frac{V_n}{2})[1 + \cos(n\phi) - \gamma] + \sum_{i<j} [\frac{A_{ij}}{R_{ij}^{12}} - \frac{B_{ij}}{R_{ij}^{6}} + \frac{q_i q_j}{\epsilon R_{ij}}]$$

[Eq. 3.11]

The total energy (E_{tot}) is the sum of bonded (bonds, angles, dihedrals and improper dihedrals) and non-bonded (Coulomb and van der Waals) components. In this equation, the first two terms describe the covalent-bond stretching and angle bending by using harmonic functions; K_r and K_θ correspond to the force of the energetic penalty imposed for deviations of the bond length and angle from the defined minimum energy positions. Torsional potentials for valence angles are described with a multiplicity *n* and a phase *δ*; A and B are non bonded atoms, with van der Waals interactions described by Lennard-Jones potential (the repulsion term is represented by the R^{-12} and the dispersion by the R^{-6} part of the potential). The electrostatic interactions are described by a charge-charge interaction-term (Coulombic potentials).

The parameterization is based on experimental and/or high-level quantum mechanical calculations. In Chapter 7, we use the parm99 force field with bsc1 corrections[33] for the simulations of DNA. The parameter of DNA lesions have been generated with antechamber and parmcheck subprograms of AMBER, and atom point charges can be computed using the RESP[34] protocol. ff14SB[35] force field is chosen to describe protein and TIP3P[36] model to describe the water environment.

3.4.2 Molecular Dynamics Simulations

First introduced by Alder and Wainwright[27] in the late 50s and their first application to a protein[28] in 1976, molecular dynamics (MD) simulations have become a popular and powerful approach nowadays to study the biological system at atomic level. MD simulations calculate the relative positions of the atoms at small interval of time (1fs, see

later), thus the behavior of atoms over a longer time scale can be predicted. This can be achieved by integrating the Newton's equations of motion (Eq. 3.12) iteratively.

$$F_i = m_i a_i = m_i \frac{d^2 r_i}{dt^2} \quad \text{[Eq. 3.12]}$$

where m_i is the mass of atom i and a_i is the acceleration resulting from the force F_i acting on atom i.

In order to numerically solve equation 3.12, standard Taylor series can be used to calculate the position after a short time interval Δt. Various numerical algorithms have been proposed for integrating the equations of motion, such as Verlet algorithm, the velocity Verlet algorithm and the Beeman's algorithm. Among them, Verlet algorithm and its leap-frog alternative are the most widely used which propagates the atomic positions r_i and velocity V_i at half-time step from time t to $t+\Delta t$:

$$v_i\left(t + \frac{\Delta t}{2}\right) = v_i\left(t - \frac{\Delta t}{2} + a_i(t).dt\right) \quad \text{[Eq. 3.13]}$$

Then the atomic positions are calculated as:

$$r_i(t + \Delta t) = r_i(t) + v_i \frac{\Delta t}{2}.\Delta t \quad \text{[Eq. 3.14]}$$

To avoid instability of the integration, a time step Δt should not be larger than the fastest molecular movements (1fs of bond vibrations involving hydrogen atoms in the solute). In Amber, SHAKE[37] algorithm is applied to freeze X-H vibrations, thus this allow the use of Δt to speed up the calculations. SHAKE algorithm can also combined with Hydrogen Mass Repartionning[38] (HMR). The idea is to repartition the mass of heavy atoms into the bonded hydrogen atoms in order to slow the highest-frequency motions of the macromolecule, the time step of the simulation can be increased by a factor of 2.

3.4.3 General Procedure for Running MD Simulations

Many packages are available for running MD simulations with the most popular being: AMBER, CHARMM, GROMACS and NAMD. In general, the simulation procedure can be divided into five steps: preparation, minimization, heating, equilibration, and production. The starting coordinates of the system can be obtained in the databases of experimental crystal or NMR structures in Protein Data Bank (PDB). For isolated oligonucleotides, NAB molecular manipulation package (available in AMBER) is developed to facilitate their construction. Then, a topology file which contains all the information required to define the molecule within the simulation (for instance, the bond lengths, bond angles, partial charges and atom masses etc...) is prepared. The next step consists in solvating the system in a water box (explicitly or implicitly), and adding salt ions to neutralize the system and mimic a physiological environment. Various shapes of water box can be used such as cubic, rhombic, sphere, and truncated octahedron. These solvation boxes however, would present undesired boundary effects due to their finite dimensions. This can be avoided by using a larger solvation box and simulating in periodic boundary conditions (PBC). Since PBC is used, a cut-off must be employed for long-range interactions to prevent self-interactions between atoms' images from one box to the other. Particle-Mesh-Ewald[39] method is used at the same time to treat the long-range electrostatic interaction. Now, minimization step is needed to ensure there are no steric clashes after the addition of hydrogens and solvent molecules. After minimization, the system is brought up to the temperature of interest (usually at 300K in physiological conditions). The heating run is performed slowly for short periods of time. Langevin thermostat is used in our simulations in order to control heating and to ensure that the average temperature is the desired one during the remaining simulation steps. Equilibration step is then performed to ensure the system is in a stable state, which mean that the energy and temperature should remain stable. At this stage, the system is ready

for the production run. The simulation time can be up to nano/micro-seconds, depending on the system size and computational resources available.

3.4.4 Free Energy Calculations

Classical MD simulations have prove very helpful and efficient to sample well the regions with low potential energy configuration spaces. However, the regions of higher energy are sampled rarely and can be overlooked. To overcome the drawback of MD simulations, free energy calculations can be performed by adding biases to enforce the sampling of a transition between two states and thus allow to overcome high energy barriers. Different algorithms have been developed to sample such rare events such as umbrella sampling (US)[40], metadynamics[41], and extended adaptive biasing force (eABF)[42,43]. Recently, meta-ABF[44] algorithms have been proposed to cross the free-energy barriers by incorporating a history-dependent potential term in the eABF method. The combination of metadynamics and eABF in this algorithm improve significantly the sampling efficiency and convergence rate, with the simulation time also much shorter compared with other importance-sampling algorithms. Meta-ADF has been used by our colleagues from Nancy to calculate the free energy of base flipping in Chapter 7.

References

1. M. Born, J. R. Oppenheimer, *Ann. Der Physik* **1927**, 84, 457.
2. Hartree, D. R. (1928, January). The wave mechanics of an atom with a non-Coulomb central field. Part I. Theory and methods. In Mathematical Proceedings of the Cambridge Philosophical Society (Vol. 24, No. 1, pp. 89-110). Cambridge University Press.
3. Hohenberg, P., & Kohn, W. Inhomogeneous electron gas. *Physical review*, **1964**, *136*(3B), B864.
4. Kohn, W., & Sham, L. J. Self-consistent equations including exchange and correlation effects. *Physical review*, **1965**, 140(4A), A1133.
5. Ceperley, D. M., & Alder, B. J. Ground state of the electron gas by a stochastic method. *Physical Review Letters*, **1980**, 45(7), 566.
6. Perdew, J. P., & Yue, W. Accurate and simple density functional for the electronic exchange energy: Generalized gradient approximation. *Physical review B*, **1986**, 33(12), 8800.
7. Becke, A. D. Density-functional exchange-energy approximation with correct asymptotic behavior. *Physical review A*, **1998**, 38(6), 3098.
8. Perdew, J. P., & Wang, Y. Accurate and simple analytic representation of the electron-gas correlation energy. *Physical Review B*, **1992**, 45(23), 13244.
9. Perdew, J. P., Burke, K., & Ernzerhof, M. Generalized gradient approximation made simple. *Physical review letters*, **1996**, 77(18), 3865.
10. Burke, K., Perdew, J. P., & Ernzerhof, M. Generalized Gradient Approximation Made Simple, *Phys. ReV. Lett*, **1996**, 78, 1396.

11. Perdew, J. P., & Schmidt, K. Jacob's ladder of density functional approximations for the exchange-correlation energy. *AIP Conference Proceedings*, **2001**, 577, 1, 1-20.

12. Klimeš, J., & Michaelides, A. Perspective: Advances and challenges in treating van der Waals dispersion forces in density functional theory. *The Journal of chemical physics*, **2012**, *137*(12), 120901.

13. Grimme, S. Semiempirical GGA-type density functional constructed with a long-range dispersion correction. *Journal of computational chemistry*, **2006**, 27(15), 1787-1799.

14. Grimme, S., Antony, J., Ehrlich, S., & Krieg, H. A consistent and accurate ab initio parametrization of density functional dispersion correction (DFT-D) for the 94 elements H-Pu. *The Journal of chemical physics*, **2010**, 132(15), 154104.

15. S. Grimme, S. Ehrlich, and L. Goerigk, ``Effect of the damping function in dispersion corrected density functional theory", *J. Comp. Chem.* **2011**, 32, 1456.

16. Lee, K., Murray, É. D., Kong, L., Lundqvist, B. I., & Langreth, D. C. Higher-accuracy van der Waals density functional. *Physical Review B*, **2010**, 82(8), 081101.

17. Klimeš, J., Bowler, D. R., & Michaelides, A. Chemical accuracy for the van der Waals density functional. *Journal of Physics: Condensed Matter*, **2009**, 22(2), 022201.

18. S. N. Steinmann, and C. Corminboeuf, ``Comprehensive benchmarking of a density-dependent dispersion correction", *J. Chem. Theory Comput.*, **2011**, **7**, 3567.

19. S. N. Steinmann, and C. Corminboeuf, ``A generalized-gradient approximation exchange hole model for dispersion coefficients", *J. Chem. Phys.*, **2011**, 134, 044117.

20. Chai, J.; Head-Gordon, M. Long-Range Corrected Hybrid Density Functionals with Damped Atom-Atom Dispersion Corrections. *Phys. Chem. Chem. Phys.*, **2008**, 10, 6615−6620.

21. Johnson, E. R.; Becke, A. D. A Post-Hartree-Fock Model of Intermolecular Interactions.*J. Chem. Phys.*, **2005**, 123, 024101.

22. G. Kresse and J. Hafner. Ab initio molecular dynamics for liquid metals. *Phys. Rev. B*, **1993**, 47, 558–561.

23. G. Kresse and J. Furthmüller. Efficiency of ab-initio total energy calculations for metals and semiconductors using a plane-wave basis set. *Comp. Mat. Sci.*, **1996**, 6, 15–50.

24. G. Kresse and J. Furthmüller. Efficient iterative schemes for ab initio total-energy calculations using a plane-wave basis set. *Phys. Rev. B*, **1996**, 54, 11169–11186.

25. H. J. Monkhorst and J. D. Pack. Special points for brillouin-zone integrations. *Physical Review B*, **1976**, 13(12):5188–5192.

26. G. Kresse and D. Joubert. From ultrasoft pseudopotentials to the projector augmented-wave method. *Phys. Rev. B*, **1999**, 59:1758–1775.

27. Alder, B. J., & Wainwright, T. E. Studies in molecular dynamics. I. General method. *The Journal of Chemical Physics*, **1959**, 31(2), 459-466.

28. McCammon, J. A., Gelin, B. R., Karplus, M., & WOLYNES, P. G. The hinge-bending mode in lysozyme. *Nature*, **1976**, 262(5566), 325.

29. Bloch, F. Über die quantenmechanik der elektronen in kristallgittern. Zeitschrift für *Physik A Hadrons and Nuclei*, **1929**, 52(7), 555-600.

30. Brooks, B. R.; Bruccoleri, R. E.; Olafson, B. D.; States, D. J.; Swaminathan, S.; Karplus, M. J. CHARMM: A program for macromolecular energy, minimization, and dynamics calculations *J. Comput. Chem.*, **1983**, 4, 187.

31. Schmid, N., Eichenberger, A. P., Choutko, A., Riniker, S., Winger, M., Mark, A. E., & van Gunsteren, W. F. Definition and testing of the GROMOS force-field versions 54A7 and 54B7. *European biophysics journal*, **2011**, *40*(7), 843.

32. Cornell, W. D., Cieplak, P., Bayly, C. I., Gould, I. R., Merz, K. M., Ferguson, D. M., ... & Kollman, P. A. A second generation force field for the simulation of proteins, nucleic acids, and organic molecules. *Journal of the American Chemical Society*, **1995**, *117*(19), 5179-5197.

33. Ivan Ivani, Pablo D Dans, Agnes Noy, Alberto Pérez, Ignacio Faustino, Adam Hospital, Jürgen Walther, Pau Andrio, Ramon Goñi, Alexandra Balaceanu, et al.Parmbsc1: a refined force field for DNA simulations. *Nature methods*, **2016**, 13(1):55–58.

34. Wang, J., Cieplak, P. and Kollman, P.A. How well does a restrained electrostatic potential (RESP) model perform in calculating conformational energies of organic and biological molecules? *J. Comput. Chem.*, **2000**, 21, 1049–1074.

35. Maier, J. A., Martinez, C., Kasavajhala, K., Wickstrom, L., Hauser, K. E., & Simmerling, C. ff14SB: improving the accuracy of protein side chain and backbone parameters from ff99SB. *Journal of chemical theory and computation*, **2015**, 11(8), 3696-3713.

36. Mark, P., & Nilsson, L. Structure and dynamics of the TIP3P, SPC, and SPC/E water models at 298 K. *The Journal of Physical Chemistry A*, **2001**, 105(43), 9954-9960.

37. Ryckaert, J. P., Ciccotti, G., & Berendsen, H. J. Numerical integration of the cartesian equations of motion of a system with constraints: molecular dynamics of n-alkanes. *Journal of computational physics*, **1977**, *23*(3), 327-341.

38. Hopkins, C. W., Le Grand, S., Walker, R. C., & Roitberg, A. E. Long-time-step molecular dynamics through hydrogen mass repartitioning. *Journal of chemical theory and computation*, **2015**, 11(4), 1864-1874.

39. Abdulnour Toukmaji, Celeste Sagui, John Board, and Tom Darden. Efficient particle-mesh ewald based approach to fixed and induced dipolar interactions. *The Journal of chemical physics*, **2000**, 113(24):10913–10927.

40. Torrie, G. M.; Valleau, J. P. Nonphysical sampling distributionsin Monte Carlo free-energy estimation: Umbrella sampling. *J. Comput.Phys.* **1977**, 23(2), 187−199.

41. Barducci, A.; Bonomi, M.; Parrinello, M. Metadynamics. WIRES *Comput. Mol. Sci.* **2011**,1(5), 826−843.

42. Darve, E.; Pohorille, A. Calculating free energies using average force. *J. Chem. Phys.*, **2001**, 115(20), 9169−9183.

43. Comer, J.; Gumbart, J. C.; Hénin, J.; Lelièvre, T.; Pohorille, A.; Chipot, C. The adaptive biasing force method: Everything you alwayswanted to know but were afraid to ask. *J. Phys. Chem. B* **2015**,119(3),1129−1151.

44. Fu, H., Zhang, H., Chen, H., Shao, X., Chipot, C., & Cai, W. Zooming across the Free-Energy Landscape: Shaving Barriers, and Flooding Valleys. *The journal of physical chemistry letters*, **2018**, *9*(16), 4738-4745.

Chapter 4: Structure and Stability of AuNPs

4.1 Introduction

Before we investigate the effect of chemical (PEG) and biological (water) environment on the relative stability of the competitive morphologies of AuNPs, it is important to have a fundamental understanding of those isolated AuNPs models in vacuum. In Chapter 2, we have shown that the question of the most stable shapes according to the size of the NP is debatable.[1,2,3,4,5] Most of the theoretical studies available in the literature are based on simulations using effective semi-empirical potential and global optimization methods to explore the potential energy surface and to identify the global minimum of nanoparticle structures. Those based on *ab initio* calculations are relatively scarce due to computational cost. Consequently, the choice of the theoretical methods as well as the parameters used to develop into the semi-empirical potentials result in different conclusions. Furthermore, even though the two most common descriptors, normalized cohesion energy and excess energy, have been used extensively in the theoretical community to compare the relative stability of metallic NPs, their reliability and their ability to predict the trends observed experimentally are still questioned. One of the key issue is the fact that they are not observables, that one can compare directly with experiments.

In this chapter, we propose to investigate AuNPs stability as a function of size and morphology by using DFT calculations including dispersion forces. Our Heuristic approach offers a good compromise in terms of accuracy and computational cost. A set of nanoclusters with six different morphologies is selected and optimized in the range 0.9-3.4 nm. The relative stability of the optimized structures is then compared by using cohesive energy, excess energy and a new descriptor introduced in this thesis, nanoparticle surface energy. Our DFT results are compared with available measurements.

4.2 Methodology

DFT calculations (spin restricted) of Au NPs were performed by using the VASP code[6,7,8] version 5.3.5. PBE[9] with Grimme's D3[10] semi-empirical dispersion corrected functional (zero-damping formalism) was considered to describe electronic exchange and correlation at the generalized gradient approximation with van der Waals interactions. The core-electrons were described by the projector-augmented wave (PAW) pseudo-potentials[11] (11 valence electrons per Au atom), and valence electrons were expanded in plane waves with a kinetic cut-off energy of 400 eV. All the Au NPs were modeled in a cubic box of 5×5×5 nm^3 with a Γ-point only approach for the k-point mesh and related Brillouin zone. For the Au bulk, the fcc crystalline structure was described by using a k-point grid of 17×17×17. In the geometry optimizations, the Au NPs structures were relaxed completely with 10^{-6} eV for the convergence of the total electronic energy and -0.01 $eV.Å^{-1}$ for the minimization of the residual forces on the nuclei. A Methfessel-Paxton smearing was used for the calculation of the total electronic energy.

4.3 NP Models and Optimal Structures

The objective of this chapter is the determination of competitive morphologies in the range of sizes accessible by DFT calculations, from 0.9 to 3.4 nm. In Figure 4.1, the polyhedra considered in this study are defined, including the three key octahedral, icosahedral and decahedral symmetries according to the literature.[3,4] Truncated Octahedra (to) and Cubotahedra (cubo) are both face-centered cubic (FCC) crystal, the rest being multiple twinned FCC crystallites with I_h [icosahedra (ico)] and D_h symmetry [Ino-decahedra (ino), regular decahedra (deca) and Marks-decahedra (marks)]. Decahedra and icosahedra contain only {111} facets, while the other morphologies contain both {111} and {100} facets, as shown in Figure 4.1. The structures of AuNPs that are considered in our work exhibit magic number and are known to be more abundant than others non-magic number sturctures.[12] Ino-decahedra (ino), icosahedra (ico) and cubotahedra (cubo)

are three close-packed isomers composed of the same magic number (Au_{55}, Au_{147}, Au_{309}, Au_{561}, and Au_{923}) and form complete symmetrical structures. Truncated octahedra can be regular (rto) (Au_{38}, $Au_{201,}$ Au_{586}) or irregular (ito) (Au_{79}, Au_{116}, $Au_{314,}$ $Au_{405,}$ $Au_{807\ and}$ Au_{976}) depending on the hexagonal facets as shown in Figure 4.1 (regular meaning having the same length of edges). Please also note that in the case of Marks-decahedron, a concave shape with twin boundaries introduced by Marks,[13] there are two possibilites to build the NPs (Please see Figure 4.7 for all the optimized structures): by either removing the five corner atoms of the regular decahedra shape to build the {110} re-entrant facet (Au_{49}, $Au_{100,}$ $Au_{176,}$ Au_{282}, Au_{423}, Au_{604} and Au_{830}), or using theses latter structures and truncate all the atoms of the edges in order to create square facets on the nanoparticles (Au_{75}, $Au_{146,}$ $Au_{176,}$ Au_{247}, Au_{383}, Au_{559} and Au_{780}). A summary of the six AuNPs morphology and the information of these NP facets are indicated in Figure 4.1 and Table 4.1 while all the optimal structures of the considered 44 NPs are displayed in Figures 4.2- 4.7.

AuNP	$\mathbf{N_F}$	$\mathbf{N_{HF}}$	$\mathbf{N_{S(R)F}}$	$\mathbf{N_{TF}}$	$\mathbf{N_{PF}}$	$\mathbf{N_v}$	$\mathbf{N_e}$
Truncated octahedron (to)	14	8	6	0	0	24	36
Ino-decahedron (ino)	15	0	5	10	0	12	25
Icosahedron (ico)	20	0	0	20	0	12	30
Cubotahedron (cubo)	14	8	6	0	0	12	24
Decahedron (deca)	10	0	0	10	0	7	15
Marks-decahedron (marks)	15	0	5	0	10	32	50

Table 4.1*. For each morphology, the total number of facets N_F, the total number of hexagonal N_{HF}, square or rectangular $N_{S(R)F}$, triangular $N_{TF,}$ pentagonal N_{PF} facets, the total number of vertices N_v, and edges Ne are given.*

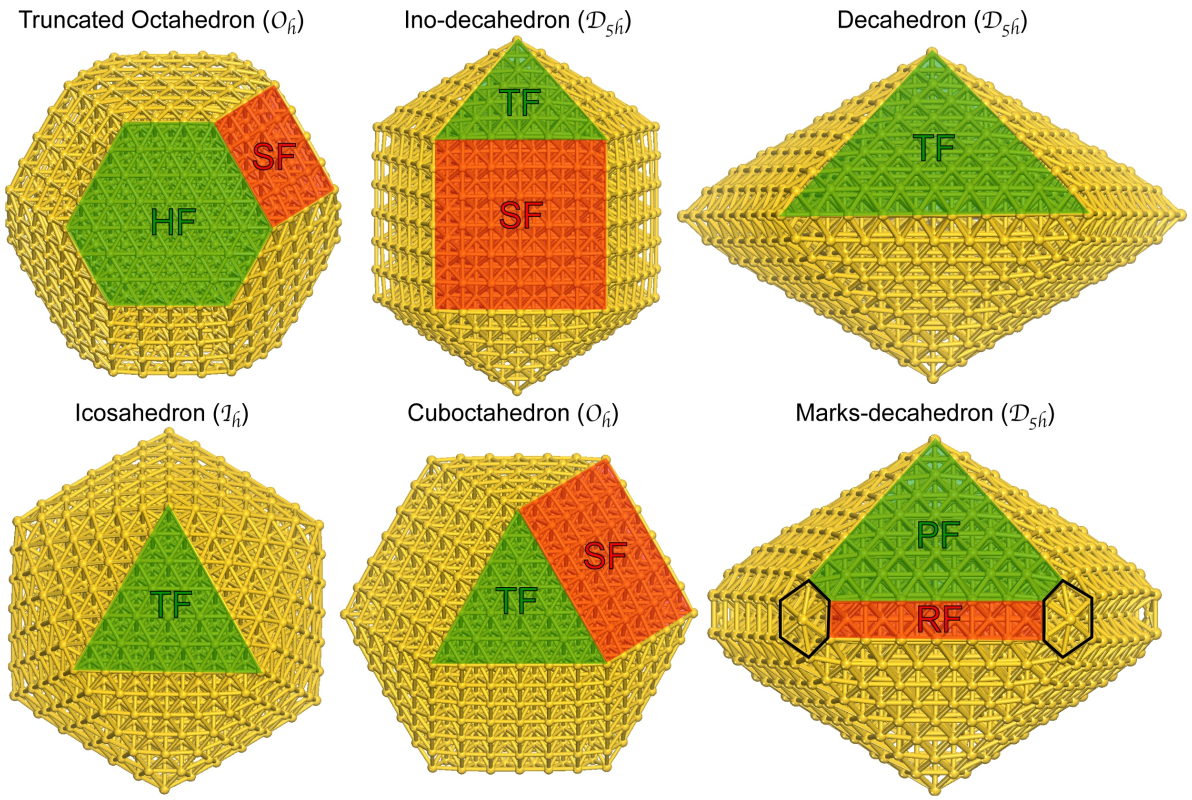

Figure 4.1. *Definition of the considered Au NP morphologies in the range of 0.9-3.4 nm (44 NPs): Truncated octahedra (to), cuboctahedra (cubo), ino-decahedra (ino), and Marks decahedra (marks) are composed of mixed facets [hexagonal (HF), triangular (TF), pentagonal (PF) with square (SF) or rectangular (RF) facets], whereas decahedra (deca) and icosahedra (ico) present only triangular facets (TF).*

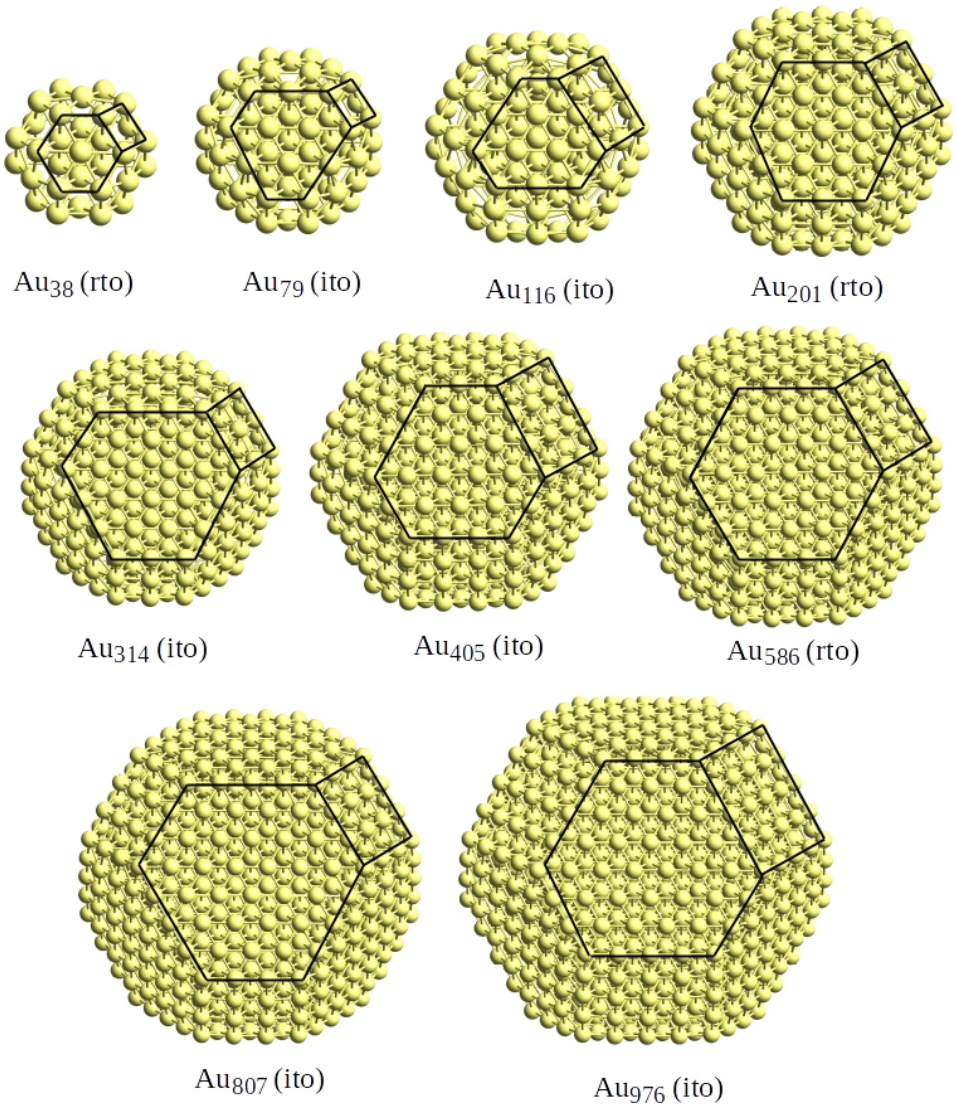

Figure 4.2. *Optimized structures of regular (rto) and irregular (ito) truncated octahedral Au NPs in the range 0.9-3.4 nm.*

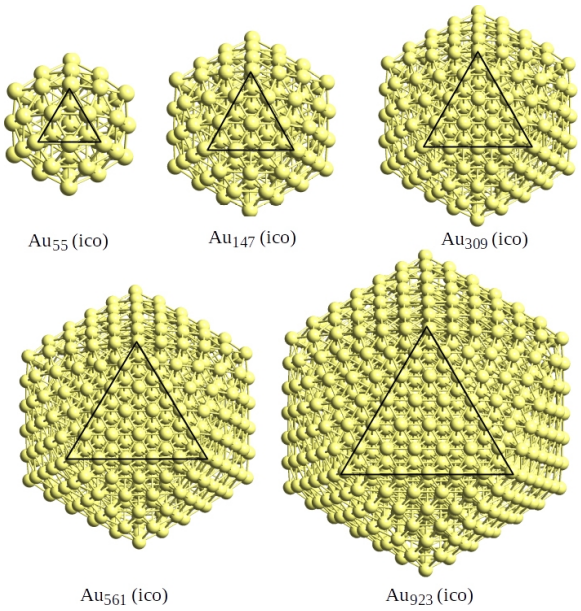

Figure 4.3. *Optimized structures of icosahedral Au NPs in the range 0.9-3.4 nm.*

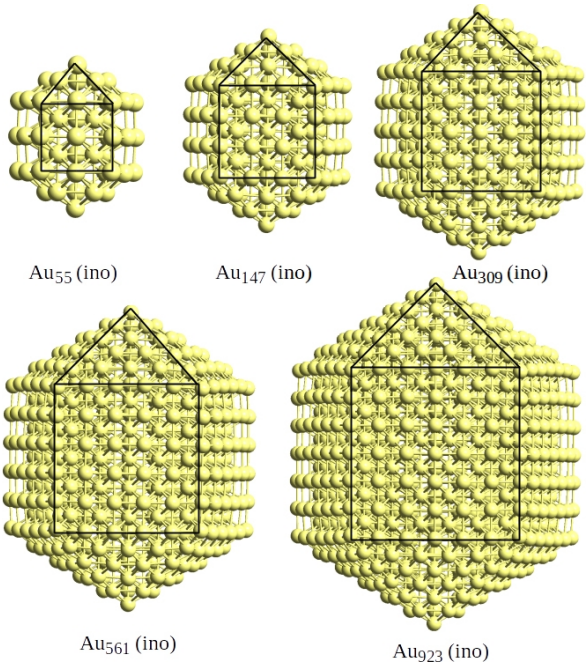

Figure 4.4. *Optimized structures of ino-decahedral Au NPs in the range 0.9-3.4 nm.*

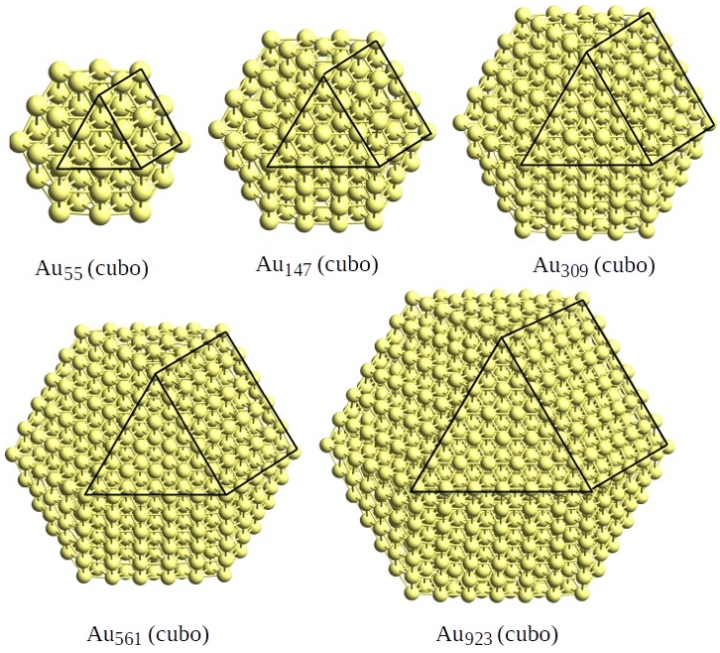

Figure 4.5. *Optimized structures of cuboctahedral Au NPs in the range 0.9-3.4 nm.*

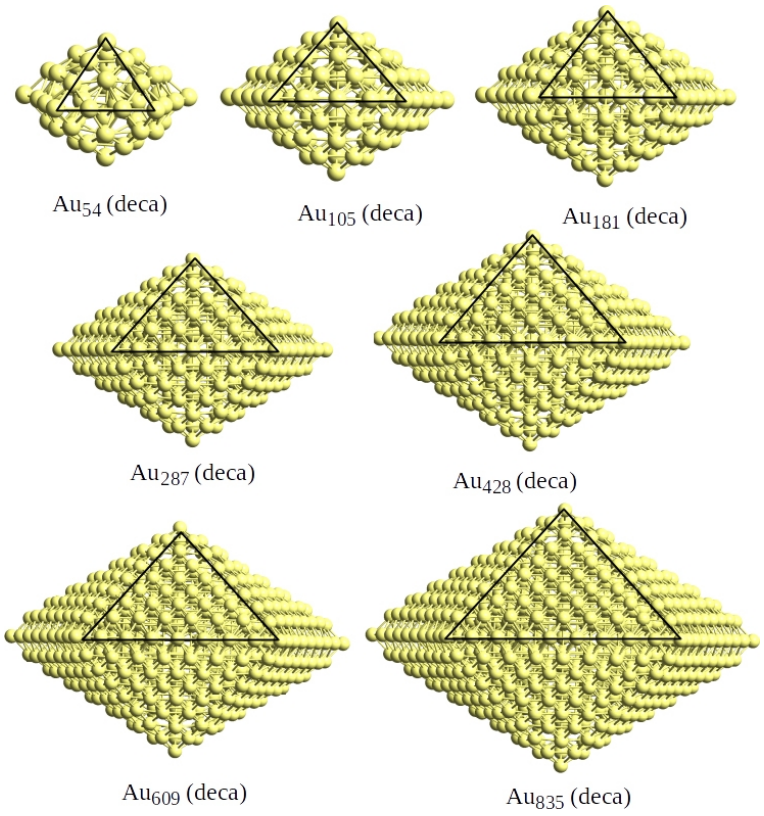

Figure 4.6. *Optimized structures of regular decahedral Au NPs in the range 0.9-3.4 nm.*

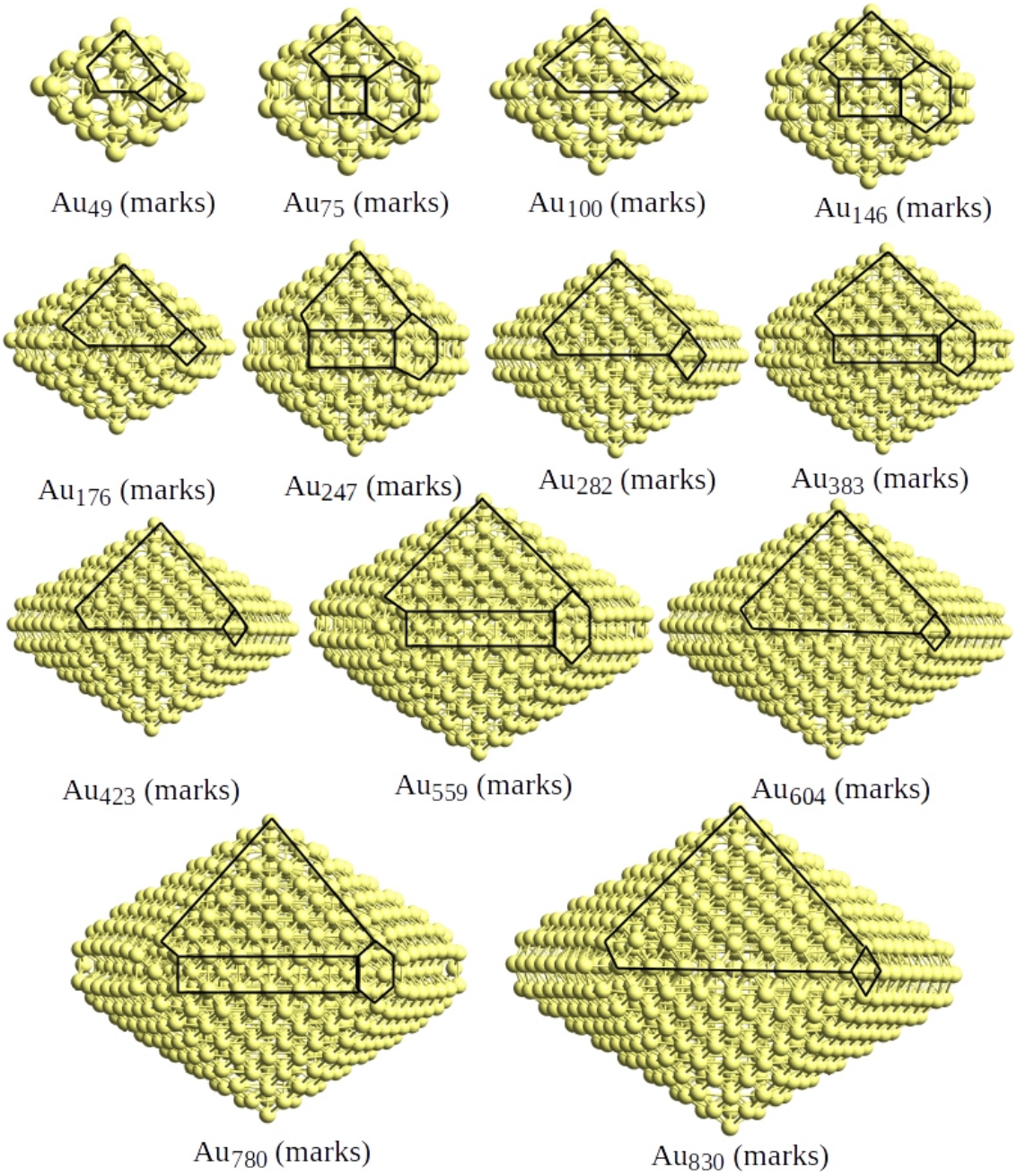

Figure 4.7. *Optimized structures of Marks-decahedral Au NPs in the range 0.9-3.4 nm.*

4.4 Results and Discussion

After geometry optimizations of theses NPs at DFT-D3 level of calculation, we will use three descriptors: normalized cohesion energy, excess energy and our proposed nanoparticle surface energy to compare the relative stability of AuNPs according to morphology and size.

4.4.1 Cohesion Energy Analysis

The cohesion energy per Au atom (E_{coh}) is defined as follows:

$$\Delta E_{coh} = \frac{E_{tot}(AuNP) - N_{Au} * E_{tot}(Au_{iso})}{N_{Au}} \quad \text{[Eq. 4.1]}$$

where N_{Au} is the total number of Au atoms in Au NP, $E_{tot}(AuNP)$ being the total electronic energy of the relaxed nanocluster and $E_{tot}(Au_{iso})$ being the total electronic energy of an isolated gold atom. The cohesion energy can be further decomposed empirically into four additive terms, where each term corresponds to the different contributions to the NP energetics coming from the positions of atoms[14] :

$$E_{coh} = a N + b N^{2/3} + c N^{1/3} + d \quad \text{[Eq. 4.2]}$$

The first term $(a N)$ corresponds to volume contribution (internal strain), $b N^{2/3}$ represents contribution from facets, $c N^{1/3}$ and d from the edges and vertices, respectively. Since we normalize the cohesive energy by the total number of atoms of AuNP in order to determine its evolutions against N, both sides of Eq. 4.2 is divided by N and give:

$$E_{coh}/N = a + b N^{-1/3} + c N^{-2/3} + d N^{-1} \quad \text{[Eq. 4.3]}$$

This equation show that the normalized cohesion energy is roughly proportional to the largest term $N^{-1/3}$. This gives:

$$\Delta E_{coh} = \left\langle E_{facets}^{surf} \right\rangle * N^{-1/3} + \Delta E_{coh}^{\infty}(bulk) \quad \text{[Eq. 4.4]}$$

The slope $\left\langle E_{facets}^{surf} \right\rangle$ (eV) can be identified as the average facet surface energy of the NP (including center, edge and corner atoms) and the offset $\Delta E_{coh}^{\infty}(bulk)$ (eV) as the cohesion energy extrapolated for the bulk (infinite value of N). Figure 4.8 plots the cohesion energy of the NP in vacuum against $N^{-1/3}$. For each polyhedral family among the six key shapes exposed in Figure 4.1, we have quantified the slopes and the offsets of the linear laws obtained in the range 0.9-3.4 nm (38-976 atoms).

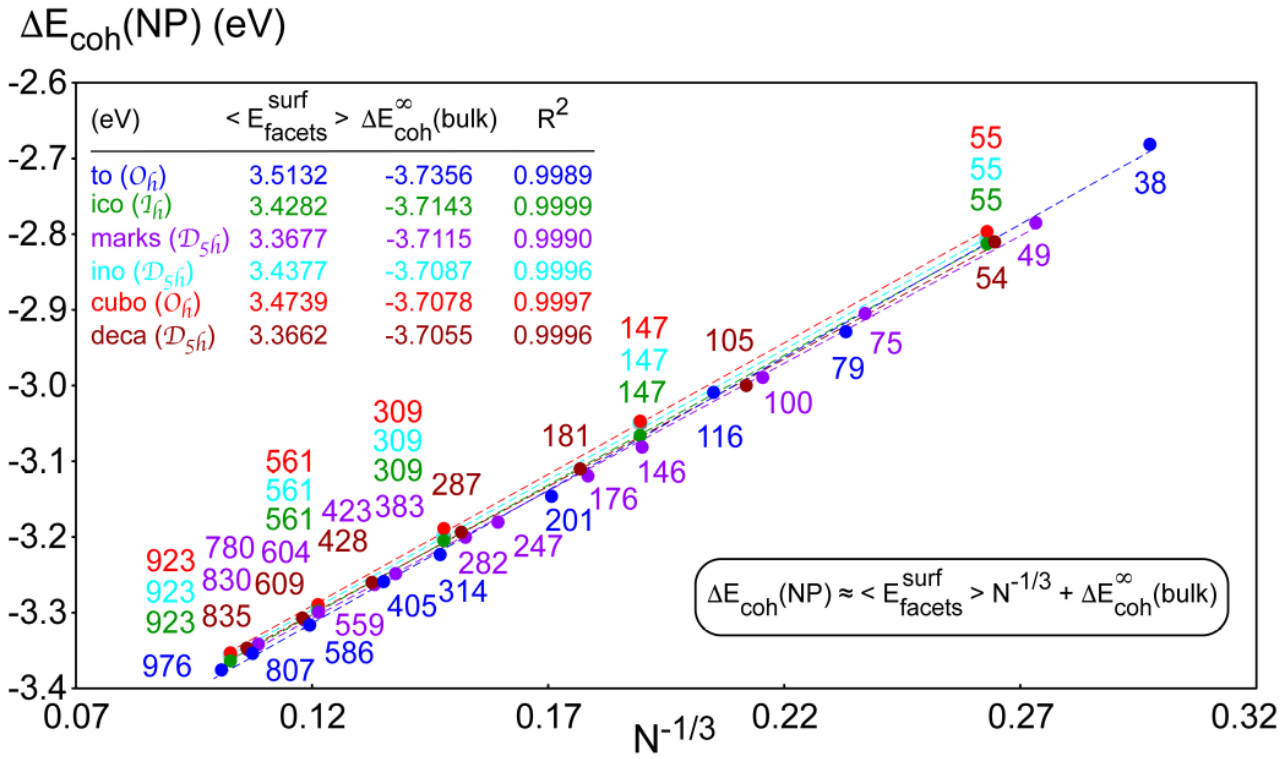

Figure 4.8. *Normalized cohesion energy per atom ΔE_{coh} (NP) (eV) diagram against $N^{-1/3}$, where N is the number of Au atoms in the NP. The parameters (slope, offset and R^2) of the linear regressions are defined in the equation 4.4. The six different families of the NPs are reported with different colors defined in the inset where the parameters of the linear regression for each shape family are exposed (the stability for each family being captured in average by the values of the offsets).*

The corresponding R^2 of the linear regression for the six AuNPs are larger than 0.9990, showing that the linear laws used in our studies are meaningful. The obtained offsets are close to the calculated bulk cohesion energy (-3.695 eV/atom) in good agreement with experiment (-3.81 eV/atom). Our linear models are in better agreement with experiments of previous DFT work[2] (-3.285 eV for the icosahedra with the TPSS functional). However, they differ slightly from one polyhedral family to another one because the examined range of NP size is limited (below 3.4 nm). The truncated octahedral NPs have the most stable offset (-3.736 eV/atom). This is expected since it exhibits the bulk fcc crystallinity and have a good surface/volume ratio. They compete with icosahedra and Marks-decahedra with bulk cohesion energy of -3.714 eV/atom and -3.711 eV/atom, respectively. In contrast, the decahedral NPs (regular and Marks) show the minimal facet surface energies (3.367 eV). This is expected because these polyhedra exhibit mainly large (111)-facet type. Then come the icosahedra with small (111)-facet type (3.428 eV in this work, whereas 2.478 eV was proposed previously[2]). The NPs having the highest average facet surface energy are truncated octahedra, ino-decahedra, and cuboctahedra because they possess large (100)-facet type, well-known to be less stable than (111) type.

4.4.2 Excess Energy Analysis

In addition, we propose to compare the trends coming from the cohesion energy with those resulting from the calculation of excess energy (ΔE_{exc}) introduced by *Baletto et al*,[3,4] a relevant descriptor which separates more clearly the nanoparticle stability. The formula of excess energy per atom is the following one :

$$\Delta E_{exc} = \frac{E_{tot}(AuNP) - N_{Au} * E_{tot}(Au_{bulk})}{N^{2/3}} \quad \text{[Eq. 4.5]}$$

where $E_{tot}(AuNP)$ is the total electronic energy of the Au NP, N_{Au} is the total number of Au atoms in Au NP and $E_{tot}(Au_{bulk})$ being the total electronic energy of gold bulk (1 atom in the primitive cell). The energetic balance between the Au NP and the bulk is similar to a surface energy. $N^{2/3}$ is the normalization constant chosen empirically to take into account the proportion of surface Au atoms with respect to the core Au atoms.

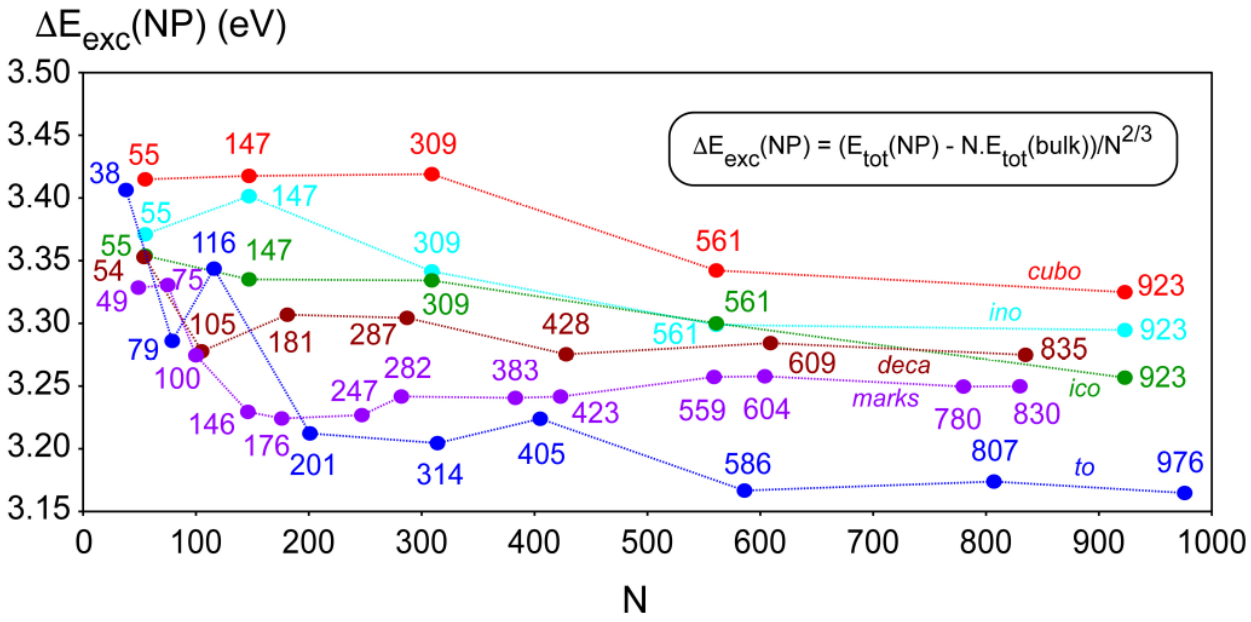

Figure 4.9. *Excess energy ΔE_{exc} (NP) (eV) diagram against the number N of Au atoms in the NP according to the Equation 4.5 .The six different families of the NPs are reported with different colors , with the same definition shown in Figure 4.8.*

In Figure 4.9, the calculations show that two shapes compete in the range of 0.9-1.8 nm (38 to 201 atoms): truncated octahedral and decahedral (regular and Marks); the Au_{55} icosahedron is also competitive. Above 1.8 nm (201 atoms), the variation is more monotonous and the truncated octahedra become really more stable than the other polyhedra. At 3.4 nm (about 1000 atoms), they predominate while the Marks-decahedra and icosahedra are minority. Cuboctahedron is always metastable according to this

descriptor. Our picture differs from previous systematic studies based on global optimization methods, effective semiempirical potentials, and Monte Carlo simulations concluding that decahedral shapes are either majority or equivalent in stability to truncated octahedral forms.[1,3,4,5] In addition, the stability of icosahedra tends to slightly increase with the NP size, in contrast with these previous studies. Our global trends are in better agreement with a previous study based on simulations obtained with the Sutton-Chen potential[16] and they also support in part the recent DFT study examining a set of Au NPs with the TPSS functional.[2] Several experimental studies based on HAADF-STEM measurements have been reported for the determination of the structure of gold nanoclusters especially for particular size 309[28],561[29], and 923[30]atoms. (See chapter 3 for experimental STEM images). The reported images in these publications show the preference of defective decahedral and face-centered cubic forms with respect to icosahedral shape. Our DFT results based on excess energy support these conclusions because truncated octahedral and Marks-decahedral forms are found more stable than the icosahedral shape above 300 atoms.

4.4.3 Surface Energy Analysis

Up to date, most of the descriptor used to compare the relative stability of NP are either based on cohesive energy or excess energy. According to Ferrando *et al*, the stability of nanoparticles depends on their crystallinity and surface energy effects.[15] However, surface energy effects can be captured by another descriptor, named nanoparticle surface energy (Γ), which is not so well addressed in the literature, neither experimentally nor theoretically. Experimental determination of surface free energy is rather challenging especially for small metallic NP. To our knowledge, the experimental nanoparticle surface energy has been reported only for copper[17], silver[18] , gold[19,20] and bimetallic copper-gold nanoparticles.[20] Depending on the experimental approach and the way the evaporation

data are fitted, the nanoparticle surface energy can vary significantly (see for example ref 19 for the comparison of AuNP surface energy reported in the literature). We will only focus our analysis on mesurements where Γ is calculated based on Kelvin equation[21] which relates the equilibrium vapor pressure to surface curvature. In fact in the Kelvin equation Γ is the only free parameter to be extracted from the fitted slope, so the experimentalists conclude to a better reliability for the corresponding measurements. Thus according to ref [17, 18 and 20] , the surface energy obtained by fitting the Kelvin equation for copper, silver, and gold are 1.70±0.03, 1.13, and 1.12±0.03 J/m^2, respectively. Theses measurements also showed that from one NP to another one, Γ does not change much and poorly depend on the size. These available experimental measurements are crucial in order to validate theoretical approaches. Indeed, there exist a lot of thermodynamics models mostly developed, on Tolman length[22] to predict the NP surface energy.[23,24,25] According to their calculations on different AuNP morphologies, cuboctahedral clusters show a slightly higher Γ than the icosahedra in the case of the smaller clusters ($Au_{309}$and Au_{923}).[24] Γ for icosahedral shape increases significantly as the size increases, in contrast to regular cuboctahedral and truncated octahedral AuNP.[25] However in these thermodynamic models, their NP structures are not optimized at DFT level, meaning that the surface relaxation depending on NP size and morphology is not determined explicitly at an *ab initio* level. So, the ability and accuracy of these thermodynamic models to predict the experiment values are still under debate.

In this section, we propose to estimate the nanoparticle surface energy with the structures of AuNPs being optimized at DFT-D3 level of calculation. The surface energy (Γ) is defined as the reversible work per unit area involved in creating a new surface at constant temperature, volume, and total number of moles.[26] It is calculated as follows (in J/m^2):

$$\Gamma = \frac{E_{tot}(AuNP) - N_{Au} * E_{tot}(Au_{bulk})}{A} \quad \text{[Eq. 4.6]}$$

where $E_{tot}(AuNP)$ is the total electronic energy of the optimized Au NP, N_{Au} is the total number of Au atoms in Au NP, $E_{tot}(Au_{bulk})$ being the total electronic energy of gold fcc bulk, and Λ being the surface area of the corrresponding relaxed AuNP. The latter is calculated using the average Au-Au distance of the NP outer-shell ($\widehat{d_{surf}}(Au-Au)$) and the analytical formula of the surface area of different morphologies [27] is given in Table 4.2.

Au NP	Λ
Regular truncated octahedron (to)	$(6+12\sqrt{3})(nd)^2$
Ino-decahedron (ino)	$5(nd)^2(1+\sqrt{3}/2)$
Icosahedron (ico)	$(5\sqrt{3})(nd)^2$
Cubotahedron (cubo)	$(6+2\sqrt{3})(nd)^2$
Decahedron (deca)	$(5/2)(\sqrt{3})(nd)^2$
Defective decahedron (def)	$10[((n-1)^2 d^2\sqrt{(3)})/4]+10(2d(n-1)-d)d\sqrt{(3)}/4+10(d^2/2)$
Marks decahedron (marks)	$10[((n-1)^2 d^2\sqrt{(3)})/4]+10(2d(n-1)-d)d\sqrt{(3)}/4$ $+5([(n-1)d-d]^2)+5d^2(4\sqrt{(2)})+10(d^2/2)$

Table 4.2. *Analytical formula used to calculate the surface area of Au NPs. nd is the length of edge and d is the average distance of the NP outer shell.*

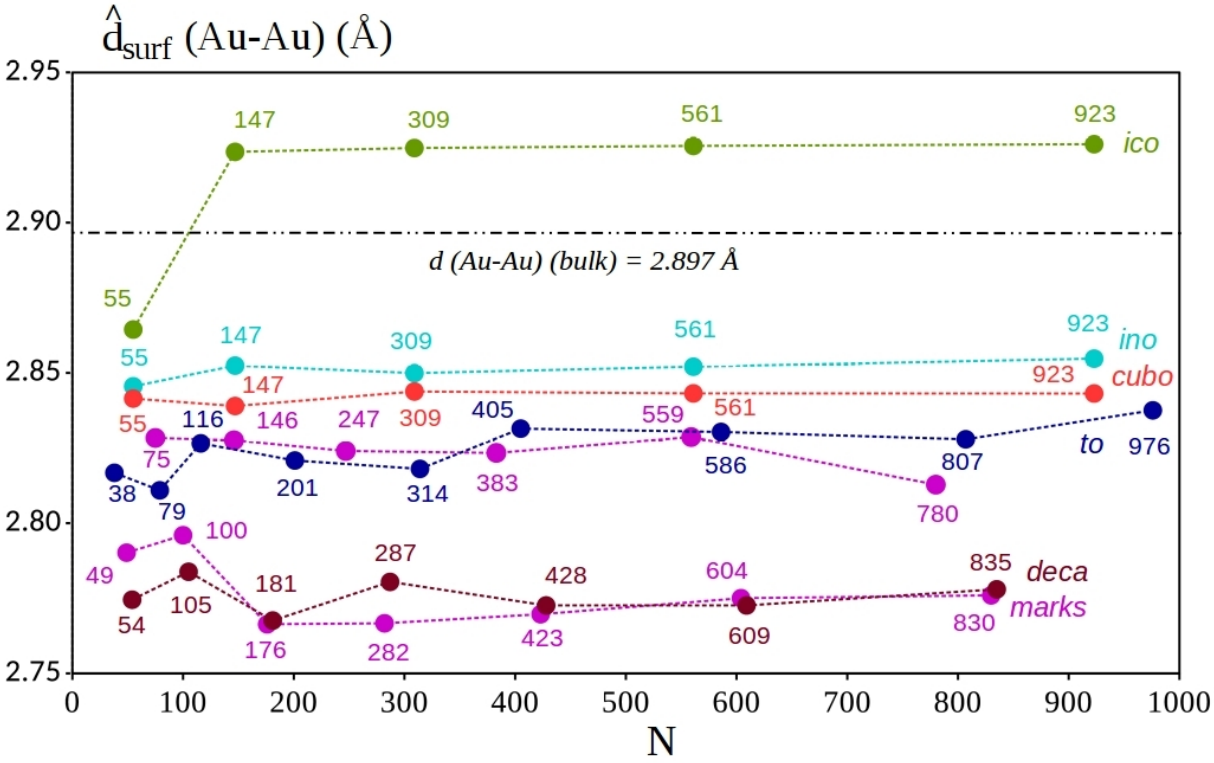

Figure 4.10. *Evolution of the average surface Au-Au distance (* $\widehat{d_{surf}(Au-Au)}$ *) in Å against the number of Au atoms N. The six different families of the NPs are reported with different colors , with the same definition shown in Figure 4.8.*

The average surface distance ($\widehat{d_{surf}(Au-Au)}$) against the number of atoms is plotted in Figure 4.10. In general, this value does not vary much when the size increases. The Au-Au distance of the bulk, calculated at the same level is also given (2.897 Å). After relaxation of the AuNP, the average surface distances for all the Au NPs become significantly shorter with respect to the bulk value, meaning that there is a systematic contraction of the NP volume, with exception of isocahedral shape starting from Au_{147}, where the distance becomes longer and being constant at ≈2.920 Å. This shows that the icosahedra, being the most spherical shape with 20 equivalent {111} triangular facets

exhibit a unique surface property compared to others polyhedra. The average surface distance of ino-decahedra, and to a less extent cuboctahedra, are very closed to the bulk value. Decahedra and Marks-decahedra present the most dramatic shortening of the Au-Au distance, with the average distance fluctuating around 2.75 Å.

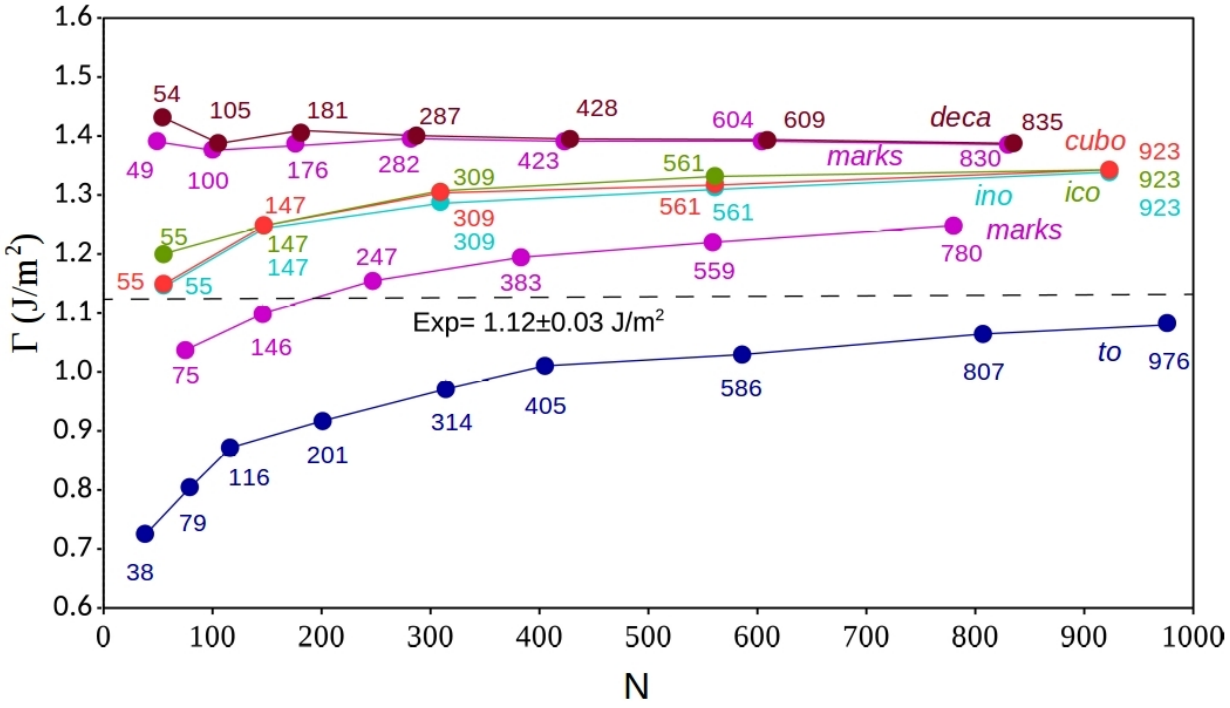

Figure 4.11. *Surface energy Γ (J/m²) diagram against the number N of Au atoms. The six different families of the NPs are reported with different colors, with the same definition as Figure 4.8. The experimental surface energy from ref [20] is given for comparison.*

Once the average Au-Au distance in the outer shell is calculated on the basis of the relaxed geometries, the surface area (Λ) can be evaluated to estimate the surface energy (Γ) of the nanocluster. The results are presented in Figure 4.11. Please note that we are comparing six morphologies with different symmetries and crystallinities, but the reference of the surface energy for all AuNPs is the one calculated for fcc-based bulk.

As a matter of fact, Au bulk structures related to D_h and I_h symmetries do not exist. Hence, in the following, we can only compare the stability trends of Γ of AuNP having the same crystallinity.

A general remark is that the NP surface energies do not vary much and it tend rapidly to an asymptotic value when the size increases, in fair agreement with a recent experiment that shows that the nanoparticle surface energy is independent of size.[20] According to this descriptor, truncated octahedron is more stable than cuboctahedron in the range 0.9 – 3.4 nm, the surface energy varies from 0.726 to 1.083 J/m^2. The value of the biggest explored size of truncated octahedra (Au_{976}) is very close to the experimental value (1.12 ± 0.03 J/ m^2),[20] showing that our estimation of nanoparticle surface energy at DFT-D3 level is very predictive. The surface energy shows that cuboctahedra which are always the least stable polyhedral according to cohesive energy and excess energy analyses, become competitive energetically with other morphologies (icosahedral and ino-decahedral). This clarifies the analysis of the proportion of competitive structural isomers at Au_{561} proposed experimentally by HAADF STEM images, where fcc cubotahedra is more stable than decahedra and icosahedra.[29] Then, the absolute stability of Marks decahedra is separated into two trends: the family of NPs containing mixed pentagonal, rectangular, and re-entrance facets (Au_{75}, $Au_{146,}$ $Au_{176,}$ Au_{247}, Au_{383}, Au_{559} and Au_{780}) being more stable than the one containing only pentagonal and re-entrance facets (Au_{49}, $Au_{100,}$ $Au_{176,}$ Au_{282}, Au_{423}, Au_{604} and Au_{830}). The Γ of the first family of Marks decahedra is also very close to the experimental value of 1.12 ± 0.03 J/m^2, (from 1.037 to 1.248 J/m²). Regular decahedra and second family of Marks decadera are the least stable NPs with the highest surface energy (from 1.431 to 1.388 J/m²) .

4.5 Conclusion

In this chapter, we have compared in a systematic way, the stability of a set of AuNPs in the range 0.9-3.4 nm using three descriptors: cohesive energy, excess energy, and nanoparticle surface energy. All the Au NP structures were fully relaxed at DFT-D3 level. Our calculations highlight the importance of the computational method (choice of the exchange-correlation functional and dispersion forces), and the need of accurate parametrization for mesoscale Monte-Carlo simulations aiming to evaluate precisely the relative stability of AuNPs. On the one hand, cohesion energy and excess energy which are the two mostly used theoretical descriptors to explore the NP stability, provide different stability trends at the same level of comparison or calculation, thus opening the question about their predictive ability. On the other hand, these two descriptors are not observable, in contrast to calculated nanoparticle surface energy which can be compared straightforwardly with experiments. In this context, we proposed to extend the discussion related to the relative stabilities of Au NPs by introducing nanoparticle surface energy at DFT with D3 dispersion correction level. This functional reproduces quite accurately the measurements, so the nanoparticle surface energy descriptor is relevant to predict precisely energetics and geometrical properties (areas) of AuNPs. The general asymptotic convergence of the properties (average Au-Au length and energies) of the AuNPs demonstrated in this chapter is an indication of our ability to extrapolate easily the chemical and physical properties of these NPs at larger size (above 3.4 nm), and open exciting perspectives for developing in the future much faster ab initio-based global optimization methods aiming to probe the absolute stability of AuNPs with an improved accuracy.

References

1. Logsdail, A. J.; Li, Z. Y.; Johnston, R. L. Faceting preferences for AuN and PdN nanoclusters with high-symmetry motifs. *Phys. Chem. Chem. Phys.* **2013**, 15, 8392-8400.

2. Li, H.; Li, L.; Pedersen, A.; Gao, Y.; Khetrapal, N.; Jónsson, H.; Zeng, X. C. Magic-number gold nanoclusters with diameters from 1 to 3.5 nm: Relative stability and catalytic activity for CO oxidation. *Nano Lett.* ***2015***, 15(1), 682-688.

3. Baletto, F.; Ferrando, R.; Fortunelli, A.; Montalenti, F.; Mottet, C. Crossover among structural motifs in transition and noble-metal clusters. *J. Chem. Phys.* **2002**, 116(9), 3856-3863.

4. Baletto, F.; Ferrando, R. Structural properties of nanoclusters: Energetic, thermodynamic, and kinetic effects. *Rev. Mod. Phys.,* **2005**, 77(1), 371.

5. Rahm, J. M.; Erhart, P. Beyond Magic Numbers: Atomic Scale Equilibrium Nanoparticle Shapes for Any Size. *Nano Lett.*, **2017**, 17(9), 5775-5781.

6. Kresse, G.; Hafner, J. Ab initio Molecular Dynamics for Liquid Metals. *Phys. Rev. B* **1993**, 47, 558. DOI: 10.1103/PhysRevB.47.558.

7. Kresse, G.; Furthmüller, J. Efficiency of Ab-initio Total Energy Calculations for Metals and Semiconductors Using a Plane-wave Basis Set. Comput. Mat. Sci. 1996, 6, 15-50.

8. Kresse, G.; Furthmüller, J. Efficient Iterative Schemes for Ab-initio Total-energy Calculations Using a Plane-wave Basis Set. *Phys. Rev. B* **1996**, 54, 11169.

9. Perdew, J. P.; Burke, K.; Ernzerhof, M. Generalized Gradient Approximation Made Simple. *Phys. Rev. Lett.* **1996**, 77, 3865. DOI: 10.1103/PhysRevLett.77.3865.

10. Grimme, S.; Antony, J.; Ehrlich, S.; Krieg, H. A consistent and accurate ab initio parametrization of density functional dispersion correction (DFT-D) for the 94 elements H-Pu. *J. Chem. Phys.* **2010**, 132, 154104.

11. Kresse, G.; Joubert, D. From Ultrasoft Pseudopotentials to the Projector Augmented-wave Method. *Phys. Rev. B* **1999**, 59, 1758.

12. Teo, B. K., & Sloane, N. J. A. Magic numbers in polygonal and polyhedral clusters. *Inorganic Chemistry*, **1985**, 24(26), 4545-4558.

13. Marks, L. D. Modified Wulff constructions for twinned particles. *Journal of Crystal Growth*, **1983**, 61(3), 556-566.

14. Uppenbrink, J., & Wales, D. J. Structure and energetics of model metal clusters. *The Journal of chemical physics*, **1992**, 96(11), 8520-8534.

15. Ferrando, R., Jellinek, J., & Johnston, R. L. (2008). Nanoalloys: from theory to applications of alloy clusters and nanoparticles. Chemical reviews, 108(3), 845-910.

16. Wang, B.; Liu, M.; Wang, Y.; Chen, X. Structures and energetics of silver and gold nanoparticles. *J. Phys. Chem. C.* **2011**, 115(23), 11374-11381.

17. Gozzi, D., Tomellini, M., Lazzarini, L., Latini, A. High-temperature determination of surface free energy of copper nanoparticles. *The Journal of Physical Chemistry C*, **2010**, 114(28), 12117-12124.

18. Nanda, K. K., Maisels, A., Kruis, F. E., Fissan, H., Stappert, S. Higher surface energy of free nanoparticles. *Physical review letters*, **2003**, 91(10), 106102.

19. Nanda, K. K., Maisels, A., & Kruis, F. E. Surface tension and sintering of free gold nanoparticles. *The Journal of Physical Chemistry C*, **2008**, 112(35), 13488-13491.

20. Chmielewski, A., Nelayah, J., Amara, H., Creuze, J., Alloyeau, D., Wang, G., & Ricolleau, C. Direct Measurement of the Surface Energy of Bimetallic Nanoparticles: Evidence of Vegard's Rulelike Dependence. *Physical review letters*, **2018**, 120(2), 025901.

21. Skinner, L. M., & Sambles, J. R. The Kelvin equation—a review. *Journal of Aerosol Science*, **1972**, 3(3), 199-210.

22. Tolman, R. C. Consideration of the Gibbs theory of surface tension. *The journal of chemical physics*, **1948**, 16(8), 758-774.

23. Nanda, K. K. Liquid-drop model for the surface energy of nanoparticles. *Physics Letters A*, **2012**, 376(19), 1647-1649.

24. Ali, S., Myasnichenko, V. S., Neyts, E. C. Size-dependent strain and surface energies of gold nanoclusters. *Physical Chemistry Chemical Physics*, **2016**, 18(2), 792-800.

25. Molleman, B., Hiemstra, T. Size and shape dependency of the surface energy of metallic nanoparticles: unifying the atomic and thermodynamic approaches. *Physical Chemistry Chemical Physics*, **2018**, 20(31), 20575-20587.

26. Ouyang, G., Wang, C. X., Yang, G. W. Surface energy of nanostructural materials with negative curvature and related size effects. *Chemical reviews*, **2009**, *109*(9), 4221-4247.

27. Baletto, F. Structural properties of sub nanometer metallic clusters. *Journal of Physics: Condensed Matter*. **2018**

28. Li, Z. Y.; Young, N. P.; Di Vece, M.; Palomba, S.; Palmer, R. E.; Bleloch, A. L.; Curley, B. C.; Johnston, R. L.; Jiang, J.; Yuan, J. Three-dimensional atomic-scale structure of size-selected gold nanoclusters. *Nature* **2008**, 451, 46-48.

29. Foster, D. M.; Ferrando, R.; Palmer, R. E. Experimental determination of the energy difference between competing isomers of deposited, size-selected gold nanoclusters. *Nature Communications* **2018**, 9, 1323.

30. Plant, S. R.; Cao, L.; Palmer, R. E. Atomic Structure Control of Size-Selected Gold Nanoclusters during Formation. *J. Am. Chem. Soc.* **2014**, 136, 7559-7562.

Chapter 5: Stability of AuNPs Covered by Water Monoshells

5.1 Introduction

In the context of AuNP-enchanced radiotherapy, water which is considered as a model of the biological natural environment, plays undoubtedly a key role. Indeed, the interaction of water with ionizing radiation in the presence of AuNPs generates a huge amount of free radicals through the reaction of water radiolysis. Those radicals interact aggressively with DNA (indirect damage) and produce more DNA lesions, and concomitantly they induce cell death and lead to a better performance of radiotherapy. The generation of free radicals and the initial physico-chemical process upon irradiation of AuNPs can be investigated theoretically by using nanodosimetric Monte-Carlo simulations. However, the interaction of water with AuNPs before irradiation as a function of size and morphology is still poorly understood at the atomic level with first-principle methods. In the literature a few theoretical studies have been devoted to the adsorption properties of water on gold nanoclusters, but for clusters of very small size (less than 20 atoms). Above 1 nm, the available theoretical data is scarce, and even rare for the adsorption of a complete shell of water molecules interacting with AuNPs.

In this chapter, we use DFT-D3 calculations to model the water/AuNP interface with an explicit atomistic model. We aim to rationalize the interaction between water molecules and AuNP as a function of the nanoparticle morphology and size. Calculations have been performed to explore the adsorption structures and energetics of water molecules on AuNPs, from single adsorption to a shell of water molecules. Then once the optimized geometries and adsorption energetics of AuNPs in contact with water have been understood, the electrostatic potential of the solvated gold nanoparticles are calculated, aiming to improve the parametrization of the Monte-Carlo simulations in collaboration with Michael Beuve and Floriane Poignant (IPNL).

5.2 Methodology

DFT calculations (spin restricted) of AuNPs and water adsorption have been performed by using the VASP code, version 5.3.5. PBE with Grimme's D3 semi-empirical dispersion corrected functional (zero-damping formalism) has been considered to describe electronic exchange and correlation at the generalized gradient approximation with van der Waals interactions. The core-electrons were described by the projector-augmented wave (PAW) pseudo-potentials (11 valence electrons per Au atom), and valence electrons were expanded in plane waves with a kinetic cut-off energy of 400 eV. All the AuNPs were modeled in a cubic box of 5×5×5 nm^3 with a -point only approach for the k-point mesh and related Brillouin zone. In the geometry optimizations, the Au NPs and water adsorption structures were relaxed completely with 10^{-6} eV for the convergence of the total electronic energy and -0.01 $eV.Å^{-1}$ for the minimization of the residual forces on the nuclei. A Methfessel-Paxton smearing was used for the calculation of the total electronic energy.

5.3 Isolated Water Adsorption

In the following, we have evaluated the adsorption energetics of one water molecule on AuNPs for two cases: In the first case, the morphology of the NP is kept constant (truncated octahedron), with an explored wide range of size from 0.9 to 3.4 nm. In the second case, the adsorption of water monomer is performed on four morphologies of AuNPs in a more restricted range of size: truncated octahedra, inodecahedra, icosahedra and regular decahedra, in the range 0.9-1.8 nm.

The adsorption energy of one water monomer on the various Au NPs is expressed as follows:

$$\Delta E_{ads} = E_{tot}\left(AuNP - H_2O\right) - E_{tot}\left(AuNP\right) - E_{tot}\left(H_2O\right) \quad \text{[Eq. 5.1]}$$

where $E_{tot}(AuNP-H_2O)$ is the total electronic energy of the complete relaxed system (water monomer adsorbed on the Au NP) , $E_{tot}(AuNP)$ being the total electronic energy of the isolated relaxed AuNP (with a starting guess for the geometry optimization being the deformed Au structure in presence of water) and $E_{tot}(H_2O)$ being the total electronic energy of the isolated relaxed water molecule.

Energy decomposition analyses (EDAs) are performed to understand the impact of water adsorption and solvation on adsorption energetics. Two different EDAs are developed and discussed throughout this chapter. First, the adsorption energy can be decomposed into pure GGA PBE contribution ΔE_{cov} (eV) and dispersion D3 semi-empirical corrective term (ΔE_{disp}) (eV):

$$\Delta E_{ads} = \Delta E_{cov} + \Delta E_{disp} \quad \text{[Eq. 5.2]}$$

Second, the adsorption energy can be decomposed into interaction and deformation terms[1]:

$$\Delta E_{ads} = \Delta E_{defo}(AuNP) + \Delta E_{defo}(H_2O) + \Delta E_{inte}(H_2O-Au) \quad \text{[Eq. 5.3]}$$

The interaction energy represents the energy associated with the formation of the chemical bond between Au and water (Au-O in our case), while the deformation energy is the cost needed to distort the geometry for both interacting species. Such EDA have been used for the past 30 years for quantifying different contributions to chemical bonding of molecular systems.[1,2]

5.3.1 Adsorption on Truncated Octahedra (0.9 – 3.4 nm)

In the following section, we have studied the adsorption strength of one water molecule on nine truncated octahedra AuNPs as a function of the NP size. Referring to our previous chapter, we showed that in general, the most stable morphologies in the range 0.9-3.4 nm is the *fcc* truncated octahedra, on the basis of the analysis three theoretical

descriptors. For this reason, we have chosen first this morphology to investigate the adsorption properties of water monomer on AuNPs, from Au_{38} to Au_{976}.

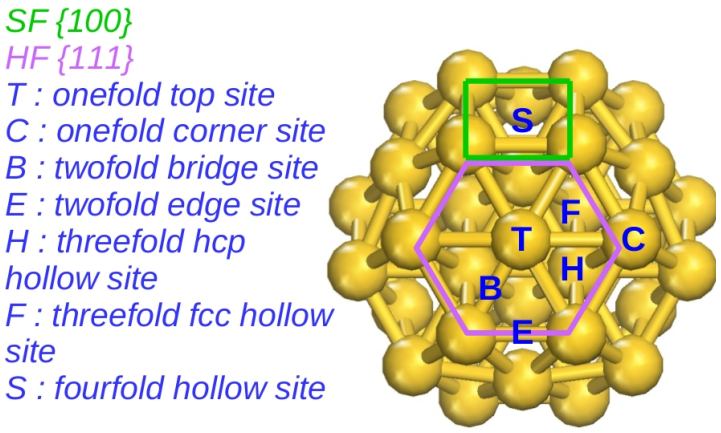

Figure 5.1. *Definition of all the possible adsorption sites for* Au_{38}.

For Au_{38} , all the possible top, bridge, fcc and hcp threefold hollow sites have been considered as shown in Figure 5.1 (considering the non-equivalent positions depending on their location : corners, edges and {111} or {100} facets). After the geometry optimizations, the bridge and hollow adsorption forms have all diffused to top positions. Hence, since these two latter sites have been found unstable, in the following only the optimal top adsorption structures will be presented for all the Au nanoclusters, with an exception of Au_{807} and Au_{976}, where we have only considered the adsorption at the corner due to computational cost.

The structures of the most favorable adsorption site for truncated octahedra and the corresponding adsorption energy is presented in Figure 5.2, while all the metastable adsorption forms are presented in Appendix A (Figures A.1- A.7). The analysis shows that for truncated octahedron, in the range of 0.9-3.4 nm, the most competitive adsorption sites for water molecule are located essentially at the corners of hexagonal {111} facets (lowest coordination number for truncated octahedron), except for Au_{116} (at the center of square {100} facet), and Au_{314} (at the edge of hexagonal {111} facet). In this range of size, the adsorption strength of water monomer on AuNP is moderate, and varies from -

0.337eV (Au_{79}) to -0.462 eV (Au_{116}). Starting from Au_{807}, the adsorption energy becomes constant at -0.348 eV. The most stable adsorption site belongs to Au_{116} (ΔE_{ads} = -0.462 eV). In all cases, the water monomer adsorbs in a flat form parallel to the NP facets with a quite long Au-O distance (2.446 - 2.625 Å).

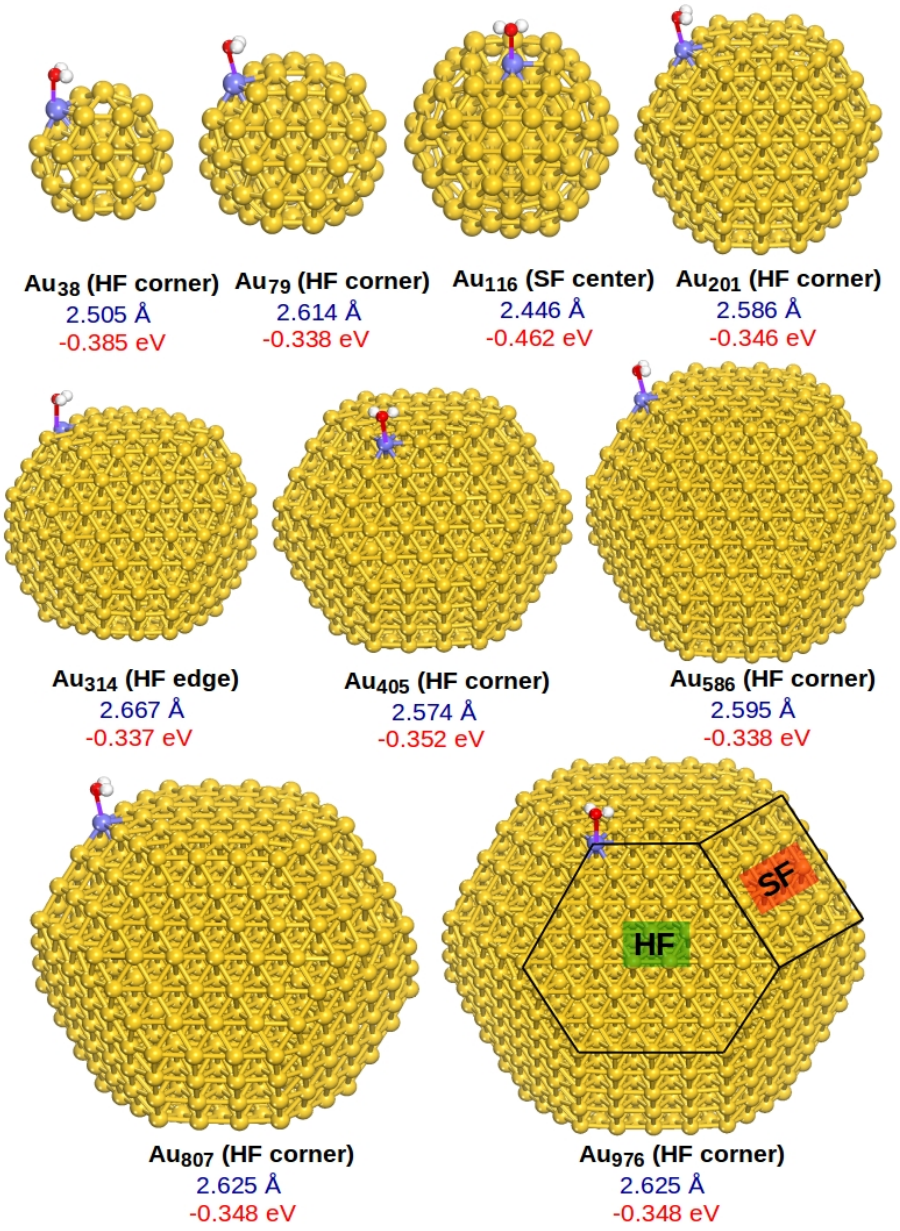

Figure 5.2. *Optimized adsorption structures of a water monomer on nine different truncated octahedra AuNPs, in the range of 0.9-3.4 nm. HF and SF correspond to hexagonal and square facet, respectively. The definitions of the H_2O adsorption site are given inside parenthesis. The Au-O bond distances are reported in Å (blue characters), whereas the adsorption energies in eV (red characters).*

The energy decomposition analysis (EDA) is performed based on the most favorable adsorption structure from Au_{38} to $Au_{976.}$ Firstly, the adsorption energy can be decomposed into the sum of pure GGA PBE energy (ΔE_{cov}) and the dispersive energy (ΔE_{disp}) . The evolution of these energies against the size of truncated octahedra is plotted in Figure 5.3. In all cases, the covalence contribution is predominance in the adsorption energy (60% belongs to ΔE_{cov}, approximatively), except for Au_{314} where dispersion contributes to half of the ΔE_{ads}. Both pure GGA (-0.210 eV) and dispersion (-0.254 eV) energy for Au_{116} are the largest one in the range 0.9 -3.4 nm, and concomitantly lead to the strongest adsorption energy. The stronger dispersion energy found for water adsorbed on Au_{116} can be explained from the adsorption site in Figure 5.2, where the water monomer is located at the center of the square facet (larger van der Waals force contributions between water and gold compared to the adsorption at edges or corners). Secondly, the adsorption energy is decomposed into interaction energy between the water monomer and AuNP (ΔE_{int} AuNP...H_2O), and the energy of deformation of AuNP (ΔE_{def} AuNP) and also of the water (ΔE_{def} H_2O) . According to Figure 5.3, the two latter contributions are negligible for the truncated octahedra due to the small geometry distortions associated upon chemisorption (ΔE_{def} AuNP is slightly positive for Au_{38} and Au_{116} but the contribution is very weak). The interaction energy between the two systems, in other words the chemical bonding “Au-O” capture almost the trend of adsorption energy.

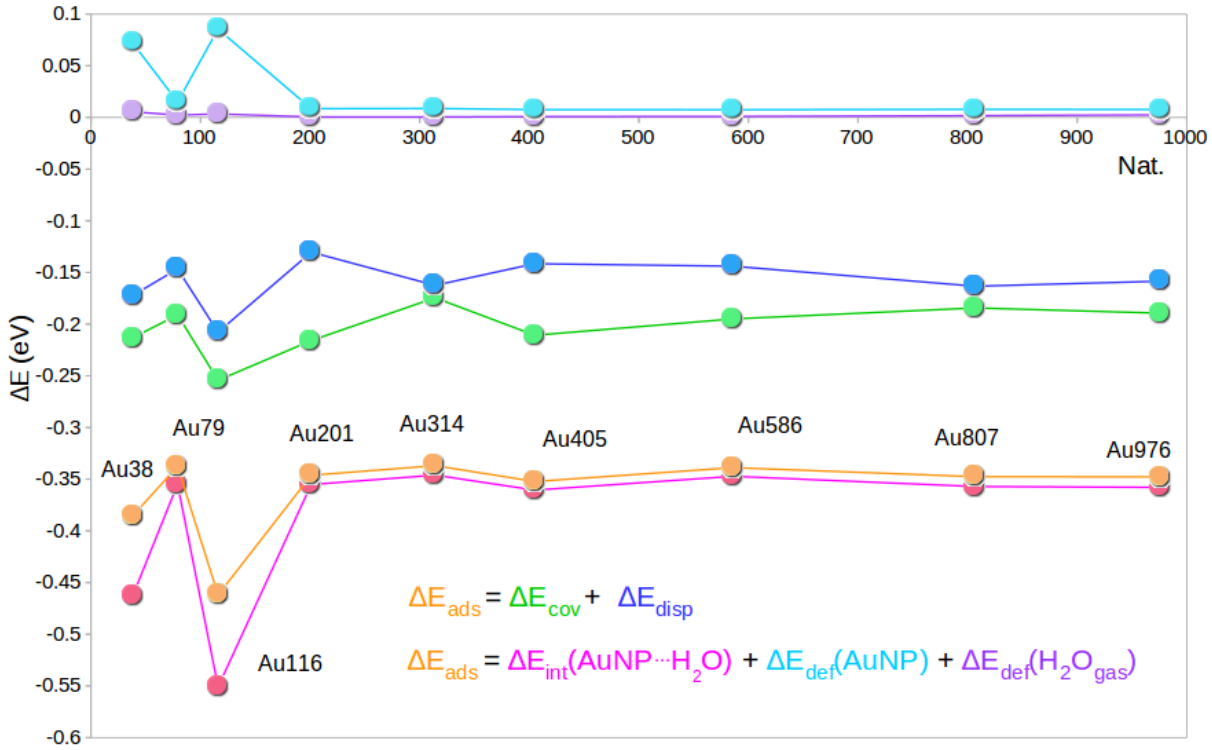

Figure 5.3. *Energy decomposition analysis of adsorption energy* ΔE_{ads} *for water monomer on truncated octahedron, from* Au_{38} *to* Au_{976}*. The equations of EDA are given and the definition of the different contributions is given in different colors.*

5.2.2 Adsorption on Icosahedral, Decahedral and Octahedral Morphologies (0.9-1.8 nm)

In the second step, we have examined the adsorption properties of a water molecule on different competitive gold polyhedra with different morphologies in the range of 0.9-1.8 nm. A set of 9 nanoclusters has been defined as follows. The truncated octahedra Au_{38}, Au_{79}, and Au_{201} from the previous analysis have been selected for comparison. In addition, regular decahedra Au_{54} and Au_{105} and other metastable shapes such as icosahedra and ino-decahedra (Au_{55} and Au_{147}) have also been considered to explore the impact of

water adsorption on their metastability. Because of the large computational cost required to optimize the water solvation shell examined on, the biggest cluster considered is Au_{201}. In Figure 5.4, for each of the 9 nanocluster, the most stable adsorption structures have been reported (including adsorption energetics, Au-O distance and site), while all the metastable adsorption forms are presented in Appendix A (Figure A.8- A.13).

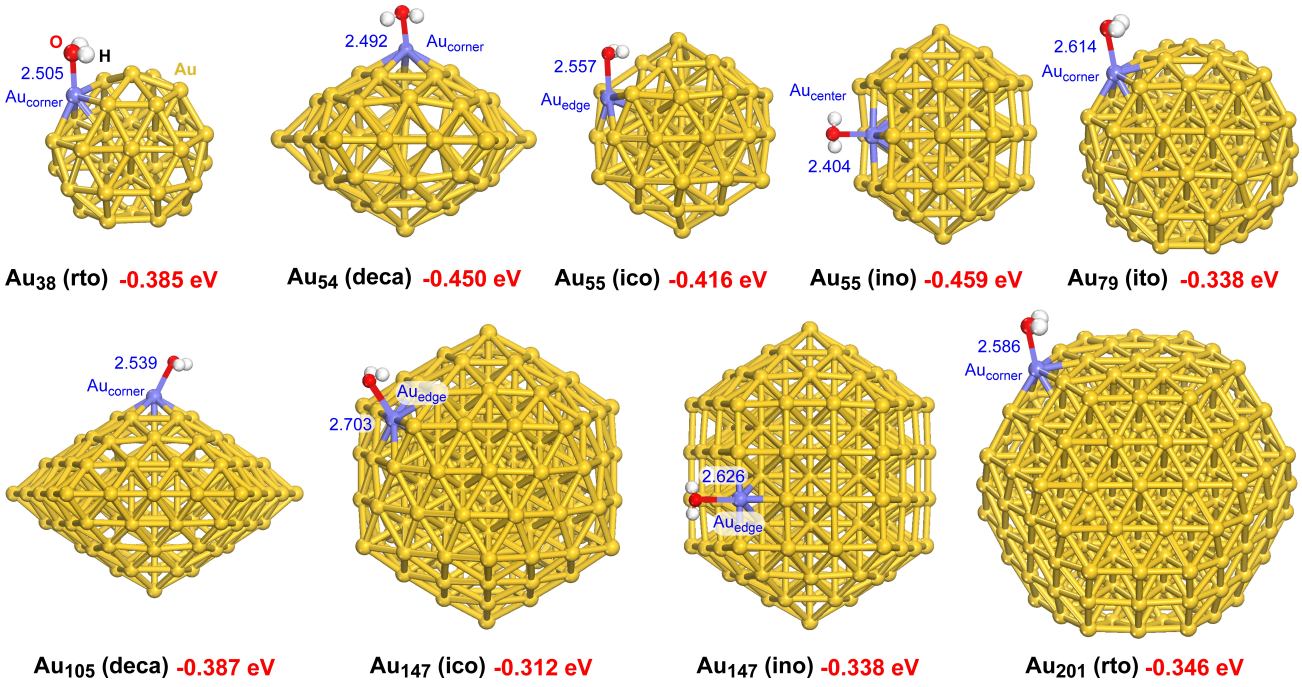

Figure 5.4. *Optimized adsorption structures of a water monomer on nine different Au NPs in the range of 0.9-1.8 nm, including four competitive morphologies : regular and irregular truncated octahedron (rto and ito, respectively), icosahedron (ico), ino-decahedron (ino) and decahedron (deca). The definitions of colors for atoms are given, as well as the location of the surface Au adsorption site with the following possibilities: corner, edge, facet center. The Au-O bond distances are reported in Å (blue characters), whereas the adsorption energies in eV (red characters).*

As shown in Figure 5.4, as the size of the NP increases, the adsorption site changes (although the adsorption at a corner remains the majority) and the evolution of the adsorption energy is not monotonous, with values in a narrow range: from -0.31 to -0.46 eV. Our results agree with previous DFT values proposed on Au small clusters[4]and Au(111).[5,6] The adsorption of a water molecule is thus a weak chemisorption with a quite long Au-O distance in the range 2.40-2.63 Å. This is consistent with the weak deformation of Au NPs after adsorption. To quantify this, an energy decomposition analysis of adsorption energetics is also proposed in Figure 5.5 and Figure 5.6.

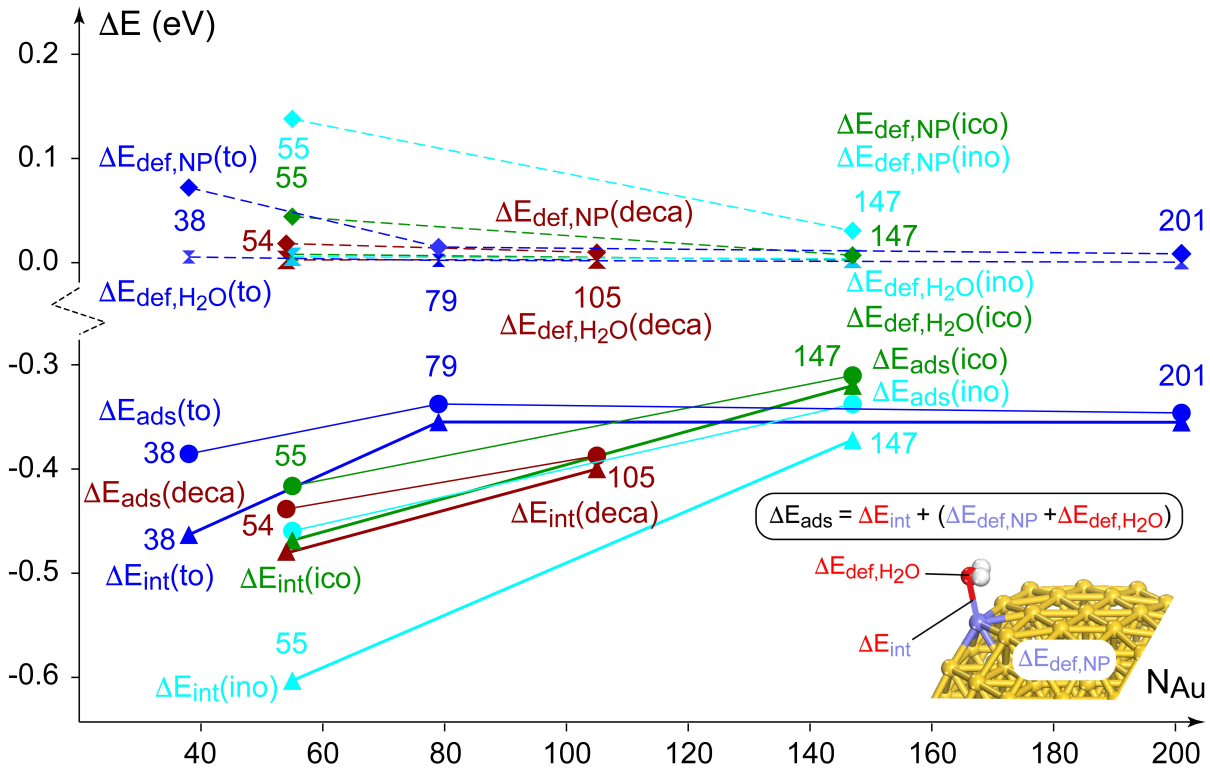

Figure 5.5: *Energy diagram against the number of Au atoms in the NPs, showing the energy decomposition analysis (EDA) of the adsorption energy (ΔE_{ads}, eV) of water monomer on nine different Au clusters with four different shapes (defined by specific colors) in the range of 0.9-1.8 nm (see Figure 2 for the optimal adsorption structures). ΔE_{ads} is expressed in the equation as the sum of the pure binding energy between Au NP and water (ΔE_{int}, energy gain), the deformation energy of water between optimal isolated situation and the geometry in the adsorption form ($\Delta E_{def,H2O}$, energy cost), and the equivalent deformation energy of Au NP ($\Delta E_{def,NP}$, energy cost).*

According to this analysis (Figure 5.5), the deformation energy of the Au NPs is positive and weak in general for all the shapes in 0.01-0.14 eV range. In parallel, the deformation energy of the water monomer is also positive and close to zero (below 8 meV). This means that the non monotonous trend of adsorption energy is mainly

captured by the interaction energy between the Au cluster and water (same trend observed in the case of adsorption on truncated octahedra 0.9-3.4 nm). Moreover, this interaction, which corresponds to the chemical bonding between both partners, is the strongest one (-0.6 eV) for the ino-decahedral NPs and for the icosahedral shape at least for small size (-0.47 eV). For truncated octahedra and decahedra, the chemical bonding is quite weaker (from -0.32 to -0.47 eV) and it varies less with the cluster size.

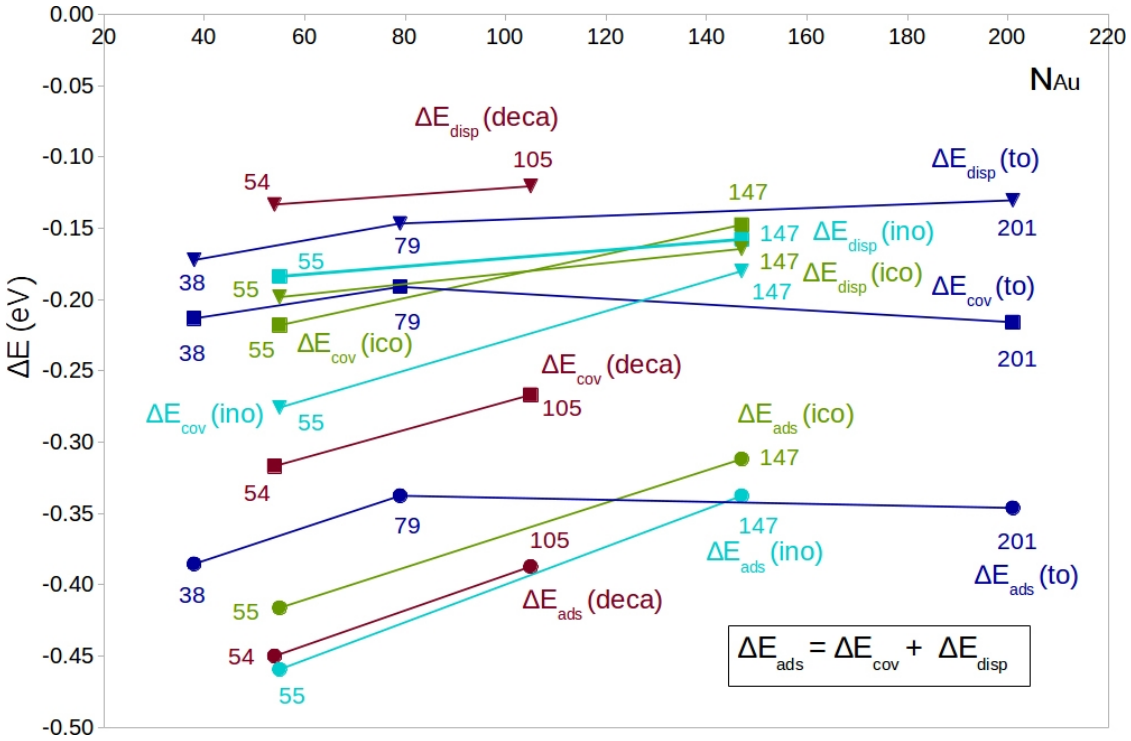

Figure 5.6. *Energy decomposition analysis (EDA) of adsorption energy* ΔE_{ads} *for water monomers on Au NPs.* ΔE_{ads} *(points in circle) is defined as the sum of pure GGA PBE ("covalence") energy* ΔE_{cov} *(points in square) and dispersion energy* ΔE_{disp} *(points in triangle). These energies for truncated octahedral, icosahedra, ino-decahedra and decahedra are differentiated by blue, green, cyan, and brown color, respectively.*

Then, the adsorption energy ΔE_{ads} (eV) of each water monomer on the 9 different Au nanoclusters (0.9-1.8 nm) has been decomposed into pure DFT GGA PBE term, noted

ΔE_{cov} (eV) and dispersion D3 semi-empirical corrective term, named ΔE_{disp} (eV), as shown in Figure 5.6. As a preliminary remark, in the decomposition energy model, the two components are systematically negative and thus stabilizing. They are equivalent in proportion in the range 30-60% for dispersion and 40-70% for the pure GGA PBE term ("covalence"). Both of them globally capture the trends of the adsorption energy.

5.4 Water Monoshells Adsorbed on AuNPs (0.9-1.8 nm)

On the basis of the best adsorption structures of water monomers on the Au NPs, we then propose to explore the interaction of a complete shell of water molecules around the metallic clusters by a static approach. The starting geometries of these solvation shells come from an additive principle assuming that the coadsorption of the best sites is an optimal choice for maximizing the overall stability of the solvated nanocluster. This means that, for the various NPs, all the equivalent sites corresponding to the best adsorption form of monomers are occupied by water molecules. Then, to complete the solvation shells, metastable adsorption sites were considered in such a way that a network of flat co-physisorbed and co-chemisorbed water molecules is built up through hydrogen bonds with reasonable distances (longer than 1.8 Å). Thus, because all the molecules were initially coplanar with respect to one facet, no arbitrary choice related to H-up/H-down configuration has been considered by construction. This starting choice was also guided by a previous molecular dynamics study of immersed Au clusters (13, 55 and 147) in water, showing that the hydrogen bonding of water molecules is arranged in a two-dimensional structure for Au_{55} and Au_{147}.[7]

In the following, all the structures of solvated AuNP and the adsorption energies are illustrated in section 5.3.1, nanoparticle structural deformation induced by water monoshells are presented in section 5.3.2, whereas details of the total number of water molecules per NP, the numbers of chemisorbed and physisorbed molecules, and analyses of hydrogen bonds are presented in section 5.3.3.

5.4.1 Adsorption Structures and Energetics

The normalized adsorption energy per water molecule in the monoshell is defined as follows:

$$\Delta E_{ads} = \frac{E_{tot}\left(AuNP - N\,H_2O\right) - E_{tot}\left(AuNP\right) - N\,H_2O * E_{tot}\left(H_2O\right)}{N_{H2O}} \quad \text{[Eq. 5.4]}$$

where $E_{tot}\left(AuNP - N\,H_2O\right)$ is the total electronic energy of the complete relaxed system (water monoshell adsorbed on the Au NP), $E_{tot}\left(AuNP\right)$ being the total electronic energy of the isolated relaxed AuNP (with a starting guess for the geometry optimization being the deformed Au structure in presence of water) and $E_{tot}\left(H_2O\right)$ being the total electronic energy of the isolated relaxed water molecule. N_{H2O} is the total number of water molecules in the monoshells.

The surface coverage of water is addressed in Figure 5.7, with the ratio of chemisorbed and physisorbed molecules. When the size of the NP increases, this coverage decreases in average progressively from 0.44 to 0.23 ML with two exceptions at sizes 55 and 147 for icosahedral (0.40 ML) and ino-decahedral (0.31 ML) shapes. In a concomitant way, the number of chemisorbed molecules decreases in favor of physisorbed water (the ratio decreasing in average from 0.27 to 0.15), again with two exceptions for Au_{55} (0.28) and Au_{147} (0.22). At the largest size (Au_{201}), the calculated coverage of 0.23 ML is smaller than the one proposed previously (0.29 ML) for an explicit liquid water/Pt_{201} interface investigated by ab initio molecular dynamics at 350 K.[8] Our result for Au with a static approach is thus reasonable because the chemical bonding on Au_{201} (-0.35 eV) is almost twice weaker than the one found on Pt_{201} (-0.54 eV). For the two exceptions of larger coverage of chemisorbed water on Au_{55} and Au_{147} (icosahedra and ino-decahedra), this is only a direct consequence of the stronger interaction energy or chemical bonding discussed before, not the fact that these clusters would present more stable adsorption sites in number.

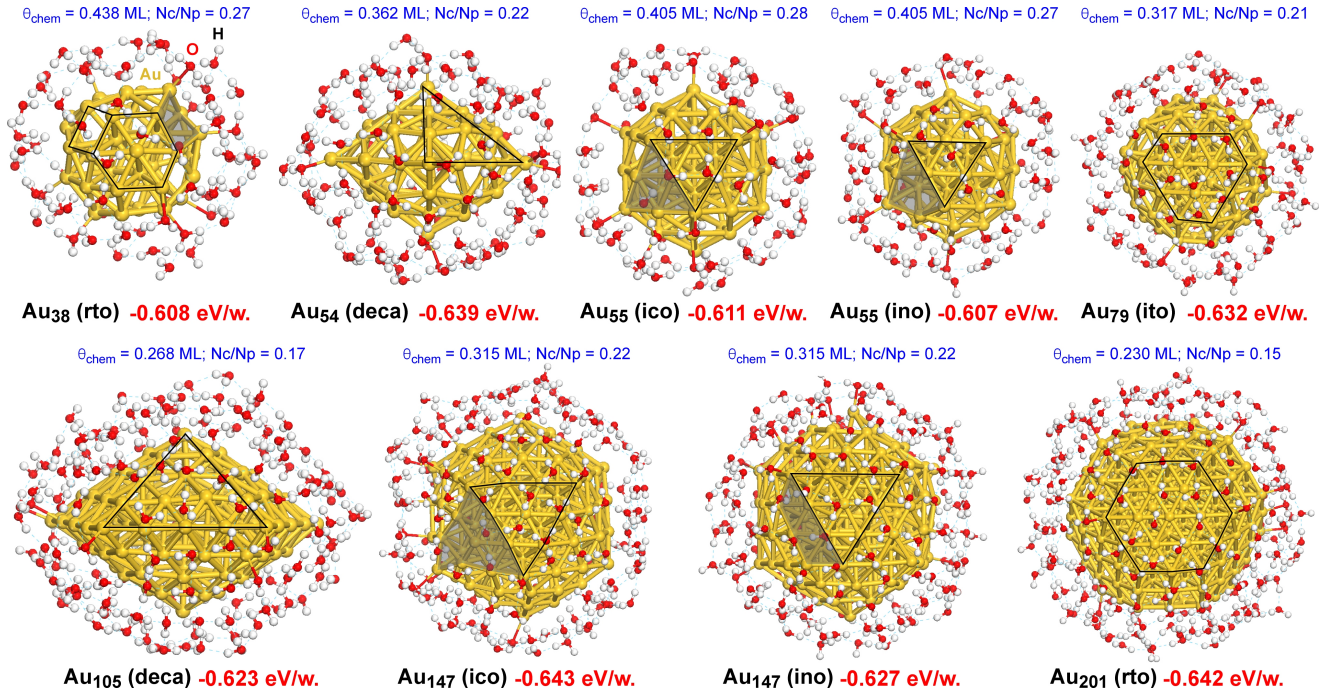

Figure 5.7. *Optimized adsorption structures of a shell of water molecules on nine different Au NPs in the range 0.9-1.8 nm, including four competitive morphologies: regular and irregular truncated octahedron (rto and ito, respectively), icosahedron (ico), ino-decahedron (ino) and decahedron (deca). The definitions of colors for atoms are given. The adsorption energies in eV per water molecule in total are reported (red), as well as the surface coverage of chemisorbed water molecules in ML (monolayer) and the ratio Nc/Np between chemisorbed water (Nc) and physisorbed water (Np). The complex network of hydrogen bonds is also marked by light gray dotted lines. The strongly distorted facets of icosahedral (and transformed ino-decahedral) shapes are drawn with full gray areas for* Au_{55} *and* Au_{147}*.*

At first glance, these optimal structures are relatively homogeneous regarding the distribution of chemisorbed and physisorbed water and as a function of the NP size; however, no clear arrangement appears, in agreement with a previous MD study.[7] In

addition, the solvation shells are quite spherical around the Au NPs, thus meaning that the average interaction between each water molecule and the cluster should not vary much. This can be seen with the average adsorption energy per water (from -0.607 to -0.643 eV/water), which does not change much against the nanocluster size (see Eq. 5.4 for the definition). This contrasts with the adsorption of the monomer discussed before. The adsorption energy per water is in average 70% stronger for the solvation shell with respect to the isolated adsorption. According to the optimal geometries, this gain is certainly not due to a strengthening of chemisorbed water but rather to the formation of chemical bonds between the molecules (hydrogen bonds). See section 5.3.3 for a detailed analysis of the hydrogen bonds.

Considering now the impact of the water solvation shells on the geometry of the Au NPs after the geometry optimizations, deformations of the clusters are observed in Figure 5.7, even for the most stable case in vacuum, such as Au_{38}, Au_{54}, Au_{79}. This effect is also seen for the less stable icosahedra Au_{55} and Au_{147}. A quantitative analysis of the structural deformation of the nanoparticle outershells upon water adsorption is addressed in section 5.3.2. Moreover, the metastable ino-decahedra Au_{55} and Au_{147} in vacuum are transformed into corresponding icosahedra through the interaction with the water shells. This original result is counterintuitive because water chemisorption on Au is quite weak as reported before, and HAADF-STEM images show that gold icosahedral nanoclusters in model operating conditions (in the range 1-3 nm) transform into decahedral structures.[14,15,16]However, the increase of the chemical bond with water obtained for these clusters and the concomitant increase of chemisorbed water coverage discussed previously allow us to explain the origins of such a remarkable phenomenon. Then in this study we demonstrate that water, standing for a model of the biological environment, may have a significant impact on the morphology of metastable NP shapes, although the intrinsic interaction with water is relatively weak.

5.4.2 Nanoparticle Structure : Induced Deformation by Water Monoshells

In order to evaluate the influence of the water monoshells on the structure of the Au nanoparticles, we introduce the roundness degree S of the nanocluster as follows :

$$S = \frac{R^{min}}{R^{max}} \quad \text{[Eq. 5.5]}$$

where R^{min} (and R^{max}) are the minimal (maximal) radius (Å) from the nanoparticle center to the nanocluster relaxed outer shell (after geometry optimization with or without water monoshells). This roundness degree is essentially a positive value in the range [0;1] (dimensionless) : the closer to 1 meaning an optimized nanoparticle outershell approaching the geometry of a sphere; the closer to 0 meaning an outershell approaching the geometry of an ellipsoid.

In order to quantify the influence of the adsorption of the water monoshells on the Au nanoparticle structures, we have calculated the variation of the roundness degree ΔS on the basis of the optimized nanocluster outershells with and without the presence of water. The corresponding variation is thus defined as follows :

$$\Delta S = S_{AuNP-NH2O} - S_{AuNP} \quad \text{[Eq. 5.6]}$$

where $S_{AuNP-NH2O}$ and S_{AuNP} are the roundness degrees with and without water monoshells, respectively. When ΔS is positive, the water monoshell has induced a significant geometric deformation of the nanocluster outershell from its symmetric structure in vacuum toward a globally rounder shape. At the opposite, when ΔS is negative, the resulting geometric deformation of the nanocluster outershell upon water adsorption is a stretching of the initial symmetric structure along the largest symmetry axis of the nanoparticle. When ΔS is close to zero, the nanocluster may have been slightly distorted upon water adsorption, however, in average, the deformation is negligible.

All the corresponding results have been exposed in Table 5.1 and Figure 5.8. As a first remark (see Figure 5.8), the influence of the adsorption of water monoshells on the nanocluster shape tends to decrease progressively with the size of the nanoparticle. From a general standpoint, the majority of the Au clusters have undergone a slight stretching of their structures (negative ΔS). Among the nine nanoclusters, only two of them have become rounder (Au_{38} (rto) and Au_{55} (ino), with positive ΔS) and two other ones have not been distorted significantly in average (Au_{54} (deca) and Au_{147} (ino), with ΔS being almost zero).

In the case of Au_{55} (ino) and Au_{147} (ino) with the presence of the water monoshells, the final and relaxed metallic geometries (icosahedral shape) are different from the clean initial structures (ino-decahedral shapes). This morphology change is captured in the calculation of ΔS . For Au_{55} (ino), the change of morphology from ino-decahedral to icosahedral shape induced by the water monoshell explains the positive value of ΔS (the nanocluster being rounder). For Au_{147} (ino), this phenomenon is similar to a lesser extent.

Nanocluster	Au_{38} (rto)	Au_{54} (deca)	Au_{55} (ico)	Au_{55} (ino)	Au_{79} (ito)	Au_{105} (deca)	Au_{147} (ico)	Au_{147} (ino)	Au_{201} (rto)
$R^{min}_{AuNP-NH2O}$ (Å)	3.882	4.008	4.645	4.704	5.267	5.101	6.657	6.765	7.201
$R^{max}_{AuNP-NH2O}$ (Å)	5.784	6.896	5.727	5.570	6.464	9.339	8.421	8.816	8.982
$S_{AuNP-NH2O}$	0.671	0.581	0.811	0.845	0.815	0.546	0.790	0.767	0.802
R^{min}_{AuNP} (Å)	3.653	3.990	4.810	4.203	5.356	5.244	6.870	6.497	7.329
R^{max}_{AuNP} (Å)	5.769	6.900	5.441	5.678	6.424	9.213	8.291	8.570	8.855
S_{AuNP}	0.633	0.578	0.884	0.740	0.833	0.569	0.828	0.728	0.827
ΔS	0.038	0.003	-0.073	0.104	-0.019	-0.023	-0.038	0.009	-0.026

Table 5.1. *Surface atom to center distance analysis: minimal* $R^{min}_{AuNP-NH2O}$ *and maximal* $R^{max}_{AuNP-NH2O}$ *radii (Å) from center to surface atom of solvated Au nanoparticles ("AuNP-NH2O"), minimal* R^{min}_{AuNP} *and maximal* R^{max}_{AuNP} *radii (Å) from center to surface atom of naked Au NP, roundness degree of solvated* $S_{AuNP-NH2O}$ *and naked AuNP* S_{AuNP} *, and the variation of roundness degree* ΔS *with and without water (dimensionless).*

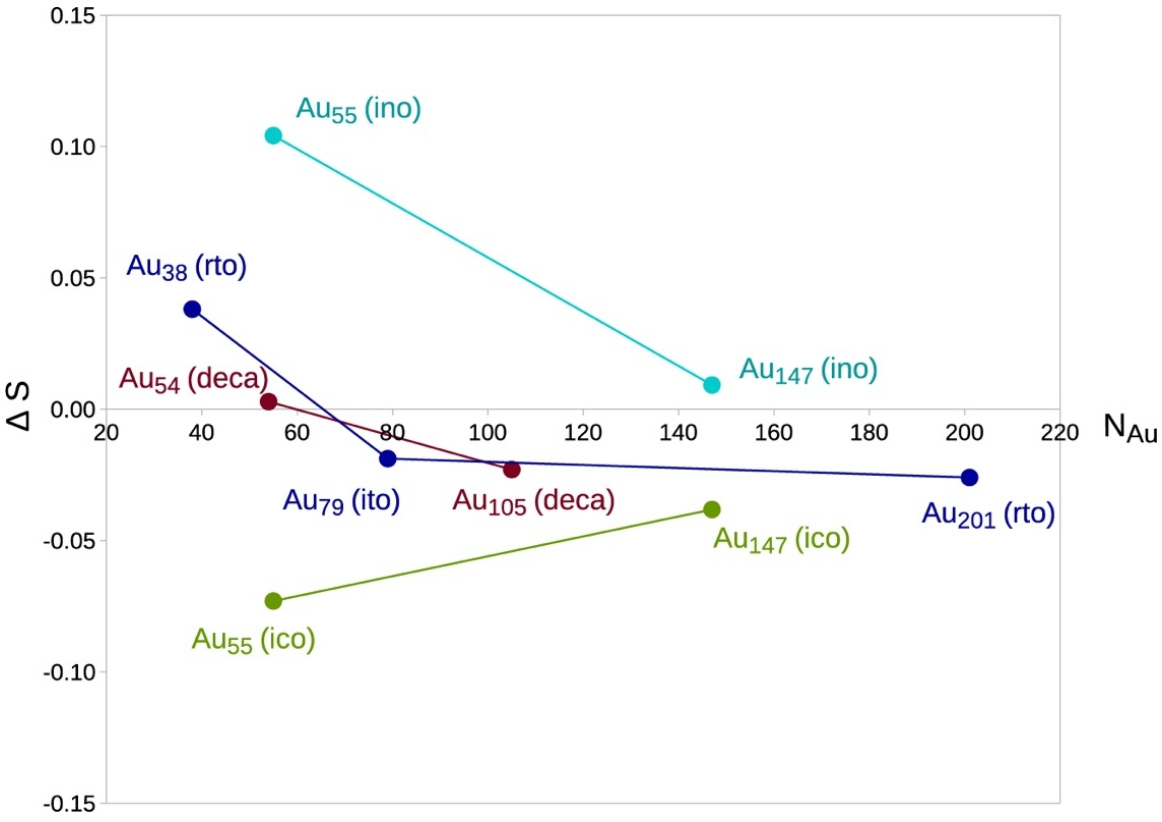

***Figure 5.8**. Evolution of the variation of the roundness degree ΔS (dimensionless) upon water adsorption (monoshells) as a function of the number of Au atoms (N_{Au}) present in the nine considered nanoparticles.*

5.4.3 Hydrogen Bonding Model

In this section, a theoretical model is developed to evaluate the part of the total hydrogen bond energy in the adsorption energy of water molecules surrounding the Au nanoclusters.

In our additive model, the total coadsorption energy ΔE_{coads}^{tot} for N_{H2O} water molecules present in the monoshell surrounding the Au NP is expressed following the additive model :

$$\Delta E_{coads}^{tot} = \Delta E_{deform}^{tot} + N_{chem}^{H2O}\,\Delta E_{\mathrm{int},chem}^{1\,H2O,best} + N_{phys}^{H2O}\,\Delta E_{\mathrm{int},phys}^{1\,H2O,best} + \Delta E_{\mathrm{int},H2O-H2O}^{tot} + N.A. \quad \text{[Eq. 5.7]}$$

where ΔE_{deform}^{tot} is the total deformation energy of Au NP and water molecules induced by the adsorption process, $\Delta E_{\mathrm{int},chem}^{1\,H2O,best}$ being the interaction energy of one water monomer chemisorbed on Au NP (best chemisorption structure), $\Delta E_{\mathrm{int},phys}^{1\,H2O,best}$ being the interaction energy of one water monomer physisorbed on Au NP (best physisorption structure), $\Delta E_{\mathrm{int},H2O-H2O}^{tot}$ being the total interaction energy between water molecules in the monoshell, N_{chem}^{H2O} being the total number of chemisorbed water molecules, N_{phys}^{H2O} being the total number of physisorbed water molecules and N.A. being the non-additivity of the model.

The first approximation is the neglect of the non-additivity of the model. The second one is that the total interaction energy between the water molecules is identified as the total hydrogen bonding energy:

$$\Delta E_{\mathrm{int},H2O-H2O}^{tot} \approx \Delta E_{HB}^{tot} \quad \text{[Eq. 5.8]}$$

The last approximation is that the sum of total deformation energy and the interaction energy of chemisorbed and physisorbed molecules in the monoshell is expressed as N_{H2O} times the interaction energy of one chemisorbed water monomer (best chemisorption form) on the Au NP:

$$N_{H2O}\,\Delta E_{ads}^{1\,H2O,best} \approx \Delta E_{deform}^{tot} + N_{chem}^{H2O}\,\Delta E_{\mathrm{int},chem}^{1\,H2O,best} + N_{phys}^{H2O}\,\Delta E_{\mathrm{int},phys}^{1\,H2O,best} \quad \text{[Eq. 5.9]}$$

This means that chemisorbed and physisorbed molecules are initially not differentiated. As a consequence, the total coadsorption energy reads:

$$\Delta E_{coads}^{tot} = N_{H2O}\,\Delta E_{ads}^{1H2O,best} + \Delta E_{HB}^{tot} \quad \text{[Eq. 5.10]}$$

Hence in our model, the total hydrogen bonding energy between water molecules in the adsorbed monoshell is calculated according to the following formula and associated Figure 5.22:

$$\Delta E_{HB}^{tot} = E_{tot,OPT}^{NH2O,GEO2} - \left(N_{chem}^{H2O}\,E_{tot,OPT}^{1H2O,GEO1} + N_{phys}^{H2O}\,E_{tot,OPT}^{1H2O,GEO3} + \left(1 - N_{chem}^{H2O}\right)E_{tot,SPE}^{1AuX,GEO1}\right) \quad \text{[Eq. 5.11]}$$

where $E_{tot,OPT}^{NH2O,GEO2}$ is the total electronic energy of the complete relaxed system (water monoshell and Au_X) noted "OPT.GEO2 $E_{tot,OPT}^{1H2O,GEO1}$ ", being the total electronic energy of the best chemisorption form of one water monomer on Au_X, noted "OPT.GEO1", $E_{tot,OPT}^{1H2O,GEO3}$ being the total electronic energy of the optimized isolated water molecule in gas phase, noted "OPT.GEO3", and $E_{tot,SPE}^{1AuX,GEO1}$ being the total electronic energy of the deformed and isolated Au_X nanocluster (without water) in the geometry "OPT.GEO1" (single point energy calculation noted "SPE.GEO1"). This means that physisorption is neglected in our approximated model.

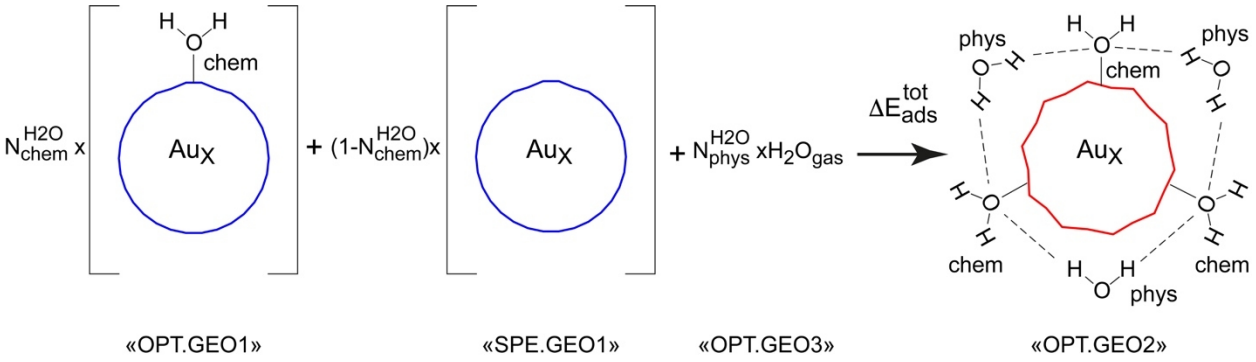

Figure 5.9. *Hydrogen bonding model for the water monoshells decorating the various Au nanoclusters (X atoms, X being 38, 54, 55, 79, 105, 147, 201). OPT.GEO1 is the optimal geometry of the water monomer chemisorbed on the* Au_X *nanocluster (best chemisorption form). SPE.GEO1 is the same geometry of OPT.GEO1 used to calculate the energy of the isolated and deformed* Au_X *nanocluster (single point energy). OPT.GEO2 is the optimal geometry of the water monoshell surrounding the* Au_X *nanocluster. OPT.GEO3 is the optimized isolated water molecule in gas phase.* N_{chem}^{H2O} *and* N_{phys}^{H2O} *are the numbers of chemisorbed and physisorbed water molecules, respectively.*

The hydrogen bond energy is then derived by normalizing the total hydrogen bonding energy by the number of water molecules:

$$E_{HB} = \frac{\Delta E_{HB}^{tot}}{N_{H2O}} \quad \text{[Eq. 5.12]}$$

The number of hydrogen bonds per water molecule in the monoshell is finally evaluated by dividing the normalized hydrogen energy E_{HB} by the water dimerization energy $E_{H2Odimer}^{gas}$ calculated for two water molecules in the gas phase (-0.256 eV at the PBE-D3 level):

$$N_{HB} = \frac{E_{HB}}{E_{H2Odimer}^{gas}} \quad \text{[Eq. 5.13]}$$

All these results are exposed in the Table 5.2.

Nanocluster	Au_{38} (rto)	Au_{54} (deca)	Au_{55} (ico)	Au_{55} (ino)	Au_{79} (ito)	Au_{105} (deca)	Au_{147} (ico)	Au_{147} (ino)	Au_{201} (rto)
N_{H2O}	65	96	77	79	110	148	160	158	212
N_{chem}^{H2O}	14	17	17	17	19	22	29	29	28
N_{phys}^{H2O}	51	79	60	62	91	126	131	129	184
$\Delta E_{ads}^{1H2O,best}$ (eV)	-0.385	-0.399	-0.416	-0.459	-0.338	-0.387	-0.310	-0.338	-0.346
ΔE_{coads}^{tot} (eV/ H_2O)	-0.608	-0.639	-0.611	-0.607	-0.632	-0.623	-0.643	-0.627	-0.642
E_{HB} (eV/ H_2O)	-0.516	-0.566	-0.509	-0.489	-0.571	-0.564	-0.585	-0.572	-0.595
N_{HB}	2.181	2.388	2.151	2.063	2.412	2.381	2.469	2.417	2.512

Table 5.2. *Hydrogen bonding model for water monoshells on Au NPs : total number of water molecules* N_{H2O} *, number of chemisorbed* N_{chem}^{H2O} *and physisorbed* N_{phys}^{H2O} *water molecules, adsorption energy of best chemisorption form for water monomer* $\Delta E_{ads}^{1H2O,best}$ *, normalized coadsorption energy per water molecule in the monoshell* ΔE_{coads}^{tot} *, hydrogen bonding energy per water molecule* E_{HB} *and number of hydrogen bonds per water in the monoshell* N_{HB} *.*

In fact, on the basis of the energetic models presented above, the adsorption energy per water of the solvation shell is mainly due to the formation of two hydrogen bonds in average (from -0.49 to -0.59 eV/water depending on the NP size), the rest being the interaction energy between water and gold (around -0.1 eV/water). In the case of Au

NPs, the formation of the water shell occurs at the detriment of chemisorption, because the latter is rather weak. Hence, for Au NPs in the 0.8-1.9 nm range, both the stability of the solvation shell (-0.6 eV/water) and the average number of formed hydrogen bonds (golden rule of 2) are remarkably independent of the NP size and morphology. By comparison, in bulk water, the cohesion energy per water molecule is known from experiments (-9.9 kcal/mol or -0.429 eV/water).[9] In addition, the two-body contribution of the dissociation energy of water dimers benchmarked by coupled cluster calculations on configurations extracted from ab initio molecular dynamics simulations of liquid water has been evaluated to be -0.137 eV (while it is -0.221 eV at equilibrium in the gas phase).[10] This means that the maximum number of hydrogen bonds per water molecule in bulk liquid can be estimated to be 3.13 bonds, considering that only hydrogen bonding contributes to the cohesion energy in the liquid. This assumption agrees with previous experimental measurements from neutron diffraction[11] (3.58 hydrogen bonds per water molecule) and with a Car-Parrinello molecular dynamics simulation study[12](3.48 hydrogen bonds per water molecule). Hence, we found a decrease of the number of hydrogen bonds in our solvation shells (“onion peel”) around Au NPs (from 2.06 to 2.51 hydrogen bonds per water, see Table 5.2) by comparison with bulk water, in fair agreement with a previous MD study.[13]

5.5 Analysis of Electrostatic Potential

In this section, the electrostatic potential V(x,y,z) for solvated AuNPs is calculated, in order to evaluate the impact of solvation on AuNP and to provide these parameters obtained at *ab initio* level *for* our collaborators M. Beuve and F. Poignant. This potential is calculated at any point (x,y,z) of the 3D supercell considered in our study. In order to analyse more easily the results, an average electrostatic potential ($\widehat{V_z}$) is integrated along the Z axis of the 3D 5×5×5 nm^3 box (this axis is chosen in such a way that the layers of the Au NP are perpendicular to it, as well as the adsorption structure of water monomers):

$$\widehat{V_z} = \int_0^z V(x,y,z)\,dxdy \quad \text{[Eq. 5.14]}$$

This choice of representation enables a separation of the contributions coming from the water molecule.

Several Au clusters with four morphologies: truncated octahedra Au_{38}, Au_{79} and Au_{201}, decahedra Au_{54}, icodechadera Au_{55} and icosahedra Au_{55} were selected for analyses. In Figure 5.10, the average electrostatic potential is plotted for three systems: clean AuNP in vacuum (curves in black), AuNP with one chemisorbed water molecule (curves in blue), and AuNP with on shell of water molecules (curves in green). The correspondence of the average electrostatic potential with the atomic plane for Au_{38} (rto) is presented in Figure 5.11, all the others analysis of AuNPs are presented in Appendix B (Figure B.1 -B.5).

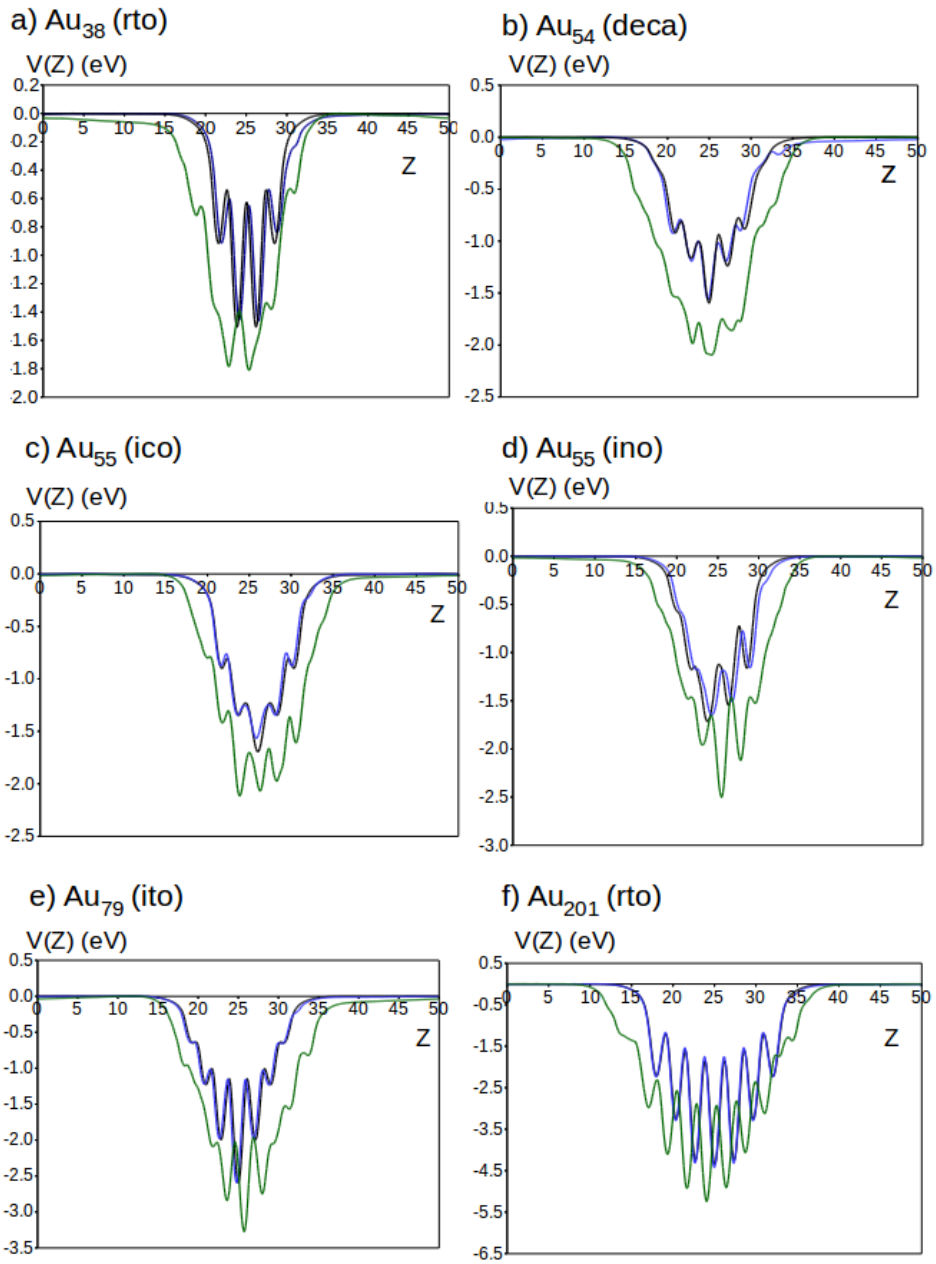

Figure 5.10. *Average electrostatic potential [V(Z)] in eV along the direction of Z axis is plotted for the naked AuNP (in black), AuNP with isolated water adsorption (in blue) and AuNPs with adsorption of one shell of water molecules (in green).*

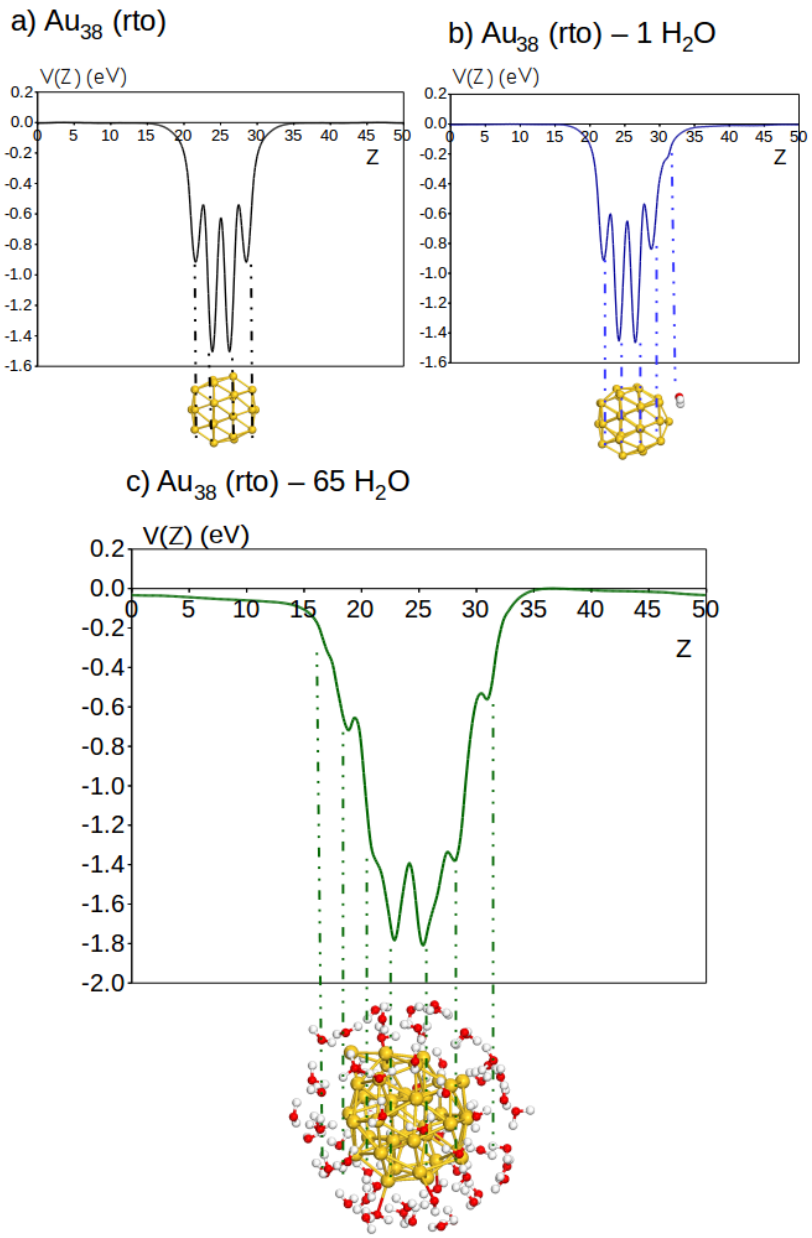

Figure 5.11. *Average electrostatic potential [V(Z)] in eV along the direction of Z axis and its corresponding with the atomic plane of for the case of Au38 (rto) is plotted for the a) naked NP , b) NP with isolated water adsorption and c) NP with adsorption of one shell of water molecules.*

Figure 5.10 showed that the curve of the is complexe and different depending on the atomic plane of AuNP. The evolution of for the naked AuNP and with the isolated water adsorption are almost identical for all cases, showing that the perturbation upon the adsorption of one water molecule on the potential energy of AuNPs is negligible. On the other hand, when the AuNPs are saturated coated by with monoshells of water molecules, the extent along Z of the average electrostatic potential increases and the osscilation of potential become wider in dimension along axis Z, due to the expansion and the deformation of the nanocluster in response to the adsorption of these water monoshells. The overall shape of the curves become more complexe in presence of water monoshells and less in correspondence with the Au atomic layers since the electrostatic information coming from water is added in the total calculated value. In order to separate the contributions of the Au cluster and water systematically, a radial integration of the electrostatic potential would surely be more convenient.

5.6 Conclusion

In this chapter, we have investigated the impact of water adsorption on an extensive set of AuNP morphologies. The study of isolated adsorption of one water molecule on AuNP in the range 0.9-3.4 nm shows that the most stable adsorption forms are similar (corners and edges) regardless of the nanoparticle shape and size, although the adsorption strength differs significantly. When a complete and explicit water solvation shell interacts with gold nanoclusters, metastable in vacuum and presenting a predominance of {100} square facets (ino-decahedra Au_{55} and Au_{147}), these nanoparticles are found unstable and transform into the closest morphologies exhibiting mainly {111} triangular facets and symmetries. The corresponding adsorption strength per water molecule becomes independent of shape and size and is enhanced by the formation of two hydrogen bonds on average. Our DFT work opens promising perspectives for a reparametrization of semiempirical potentials and global optimization methods aiming to describe the relative stability between ino-decahedra and icosahedra in interaction with a water solvation shell at larger NP size. In particular, this would allow the study of Au_{309}, Au_{561}, and Au_{923}, both with static and dynamic approaches for Au/water interfaces, and this would show whether the water solvation still induces the transformation between metastable morphologies at larger NP size. Extracted from our DFT models, the average electrostatic potential coming from AuNP in interaction with water molecules are key parameters for future theoretical developments related to radiochemistry in collaboration with colleagues from Institut de Physique Nucléaire in Lyon.

References

1. Calle-Vallejo, F., Sautet, P., & Loffreda, D. Understanding adsorption-induced effects on platinum nanoparticles: an energy-decomposition analysis. *The journal of physical chemistry letters*, **2014** , 5(18), 3120-3124.
2. Kitaura, K.; Morokuma, K. A New Energy Decomposition Scheme for Molecular Interactions within the Hartree-Fock Approximation. *Int. J. Quantum Chem.* **1976**, 10, 325−340.
3. Umeyama, H.; Morokuma, K. The Origin of Hydrogen Bonding. An Energy Decomposition Study. *J. Am. Chem. Soc.* **1977**, 99, 1316−1332.
4. Xue, Y. Water monomer interaction with gold nanoclusters from van der Waals density functional theory. *J. Chem. Phys.* **2012**, 136(2), 024702.
5. Nadler, R.; Sanz, J. F. Effect of dispersion correction on the Au (1 1 1)-H2O interface: a first-principles study. *J. Chem. Phys.* **2012**, 137(11).
6. Carrasco, J.; Klimes, J.; Michaelides, A. The role of van der Waals forces in water adsorption on metals. *J. Chem. Phys.* **2013**, 138, 024708-1,9.
7. Chang, C. I.; Lee, W. J.; Young, T. F.; Ju, S. P.; Chang, C. W.; Chen, H. L.; Chang, J. G. Adsorption mechanism of water molecules surrounding Au nanoparticles of different sizes. *J. Chem. Phys.* **2008**, 128(15), 154703.
8. de Morais, R. F.; Kerber, T.; Calle-Vallejo, F.; Sautet, P.; Loffreda, D. Capturing solvation effects at a liquid/nanoparticle interface by Ab Initio molecular dynamics: Pt201 immersed in water. *Small* **2016**, 12(38), 5312-5319.
9. Levitt, M.; Hirschberg, M.; Sharon, R.; Laidig, K. E.; Daggett, V. Calibration and testing of a water model for simulation of the molecular dynamics of proteins and nucleic acids in solution *J. Phys. Chem. B* **1997**, 101, 5051-5061.

10. Santra, B.; Michaelides, A.; Scheffler, M. Coupled cluster benchmarks of water monomers and dimers extracted from density-functional theory liquid water: the importance of monomer deformations *J. Chem. Phys.* **2009**, 131, 124509-1,9.

11. Soper, A. K.; Bruni, F.; Ricci, M. A. Site–site pair correlation functions of water from 25 to 400 °C: Revised analysis of new and old diffraction data. *J. Chem. Phys.* **1997**, 106, 247.

12. Guardia, E.; Skarmoutsos, I.; Masia, M. Hydrogen Bonding and Related Properties in Liquid Water: A Car–Parrinello Molecular Dynamics Simulation Study. *J. Phys. Chem. B* **2015**, 119 (29), 8926-8938.

13. Ju, S.-P. A molecular dynamics simulation of the adsorption of water molecules surrounding an Au nanoparticle. *J. Chem. Phys.* **2005**, 122, 094718-1,6.

14. Li, Z. Y.; Young, N. P.; Di Vece, M.; Palomba, S.; Palmer, R. E.; Bleloch, A. L.; Curley, B. C.; Johnston, R. L.; Jiang, J.; Yuan, J. Three-dimensional atomic-scale structure of size-selected gold nanoclusters. *Nature* **2008**, 451, 46-48.

15. Foster, D. M.; Ferrando, R.; Palmer, R. E. Experimental determination of the energy difference between competing isomers of deposited, size-selected gold nanoclusters. *Nature Communications* **2018**, 9, 1323.

16. Plant, S. R.; Cao, L.; Palmer, R. E. Atomic Structure Control of Size-Selected Gold Nanoclusters during Formation. *J. Am. Chem. Soc.* **2014**, 136, 7559-7562.

Chapter 6 : PEGylation of Hydrated Gold Nanoparticles

6.1 Introduction

In the previous chapter, we have studied the interaction of water molecules with AuNPs without the presence of the synthesis coating. However, AuNPs for biomedical applications are usually synthesized in the presence of organic ligands. Complex organic coatings on the particle surface prevent the sintering of AuNPs and shield them from the biological environment, the required time to reach the targeted cancerous cells. In this context, hydrophilic polyethylene-glycol (PEG) is an excellent choice of ligand as PEG coatings have been shown to increase blood circulation time and reduce toxicity of AuNPs.[1] Nevertheless, despite their widespread use in experiments, there is a current lack of theoretical models able to describe the relative stability of AuNPs in the simultaneous presence of hydration and PEGylation. Moreover, the role of PEG ligands on the water radiolysis and generation of radical species is poorly described in the literature.

In this chapter, we aim to model the PEGylation of AuNPs at the DFT level, first by considering the adsorption of one PEG ligand, and then by decorating the nanoparticles with coadsorbed ligands approaching saturation at the surface. In a further step, the model is hydrated by a large number of explicit water molecules which are mainly in interaction with PEG ligands, through hydrogen bonds. An energy decomposition model is proposed to evaluate the adsorption strength between one PEG ligand and AuNPs at various conditions (isolated PEG adsorption, ligand saturation, hydration effect) and to determine energetics of the hydrogen bonds. Finally, the relationship between the adsorption strength and the cellular uptake of AuNPs as a function of morphology is discussed.

6.2 Methodology

Spin-restricted DFT calculations of PEGylated and hydrated GNPs were performed by using the VASP package, version 5.3.5. PBE with Grimme's D3 semi-empirical dispersion corrected functional (zero-damping formalism) was considered to describe electronic exchange and correlation at the generalized gradient approximation (GGA) with van der Waals interactions. The core-electrons were described by the projector-augmented wave (PAW) pseudo-potentials (11 valence electrons per Au atom), and valence electrons were expanded in plane waves with a kinetic cut-off energy of 400 eV. All the GNPs were modeled in a cubic box of 5×5×5 nm^3 with a Γ-point only approach for the k-point mesh and related Brillouin zone. In the geometry optimizations of the complete systems, the coadsorption structures of PEG and water on GNPs were relaxed completely with 10^{-6} eV for the convergence of the total electronic energy and -0.01 $eV.Å^{-1}$ for the minimization of the residual forces on the nuclei. A Methfessel-Paxton smearing was used for the calculation of the total electronic energy.

6.3 Choice of AuNPs and PEG Model

The first important step in the study is the selection of the gold nanoclusters to build the organic monolayers of PEGylated systems. According to the measurements, depending on the choice of the synthesis ligand and the size, GNPs may have several competitive morphologies including nanospheres, nanostars (nanospikes), nanorods, nanotriangles and nanoprisms. In order to tackle the discussion of the internalization of the GNPs and the ligand exchange with the membrane which has been recently proposed,[2] our choice in this work is to elaborate DFT models of gold nanospheres, nanospikes and nanorods. Due to the inherent limit of 3D models (5 nm × 5 nm × 5 nm), the size of the gold

nanoclusters will then be considered in the range 1.1-1.3 nm. Although small, these nanoclusters are not far from the explored experimental range (2.4-89 nm).[3]

In Chapter 4, we shown that five typical morphologies are competitive in vacuum in the range 1- 3.4nm: Marks-decahedral, regular decahedral, icosahedral, ino-decahedral and regular/irregular truncated octahedral shapes. In this chapter these morphologies are described by Au_{49} (marks), Au_{54} (deca), Au_{55} (ico), Au_{55} (ino) and Au_{79} (ito), respectively. By looking at the relative stability order provided by the normalized cohesion energy of the nanocluster per Au atom, the trend is the following one in vacuum: Au_{79} (ito) > Au_{55} (ico) > Au_{55} (ino) > Au_{54} (deca) > Au_{49} (marks). In the fluxional regime considered here, these highly symmetric polyhedral forms may not be the most stable ones for each size, as previously demonstrated from global optimization methods and semi-empirical potentials.[4,5]

The choice of the PEG ligand length is also strongly determined by the restraints of the supercell size. In order to keep a reasonable vacuum space between GNPs decorated by an organic coating and their equivalent periodic images (in the range 1.8-3.2 nm), two ethylene glycol units (2 EG) have been considered in the PEG ligands, leading to trans-conformer molecules (see Figure 6.15 in Section 6.4.4) of length 1.6 nm and weight 166 Da (much lower than the molecular weights usually employed in radiotherapeutic experiments ranging from 50 to 200 EG units).

Regarding the grafting moiety, thiol functions -SH are hydrogenated in all our models for the following reasons: (1) gold nanoclusters in the fluxional regime (around 1 nm) may be strongly affected by the surrounding environment in terms of stability and shape (see for instance the influence of water solvation in Chapter 5), thus strongly bound dehydrogenated PEG ligands may induce totally amorphous shapes for which there will be no possibility to establish relationships between morphology and ligand exchange; (2) from recent measurements, the mechanism of endocytosis has been explained by the exchange of physisorbed ligands between GNPs and the cell membrane,[2] thus the

interaction between the PEG ligand and the nanoparticle has to be moderate; (3) a recent theoretical study demonstrates that long alkyl chain thiols mainly adsorb molecularly (-SH) on Au adatom deposited on Au(111) (-1.54 eV at the PBE-D3 level with VASP code), at the opposite of short alkyl chain thiols which adsorb dissociatively (-S-).[6] Concerning the second terminal function, -COOH moiety is chosen to correspond to experimental synthesis ligands.[2]

6.4 Energy Decomposition Analysis Model

In the following section, EDA models are presented for an isolated adsorbed PEG molecule (Eqs. 6.1-6.6), for monoshells of PEGylated AuNPs (Eqs. 6.7-6.18, Figures 6.1-6.2) and for monoshells of hydrated PEGylated AuNPs (Eqs. 6.19-6.49, Figures 6.3-6.14). Definitions of coadsorption energies, several normalizations, covalence and dispersion energies, deformation and various interaction energies are also given.

6.4.1/ Isolated adsorption of a PEG molecule

The adsorption energy ΔE_{ads} for one PEG molecule reported on Table 6.1 of section 6.5 is defined as follows:

$$\Delta E_{ads} = E_{tot}(AuNP-1\,PEG) - E_{tot}(AuNP) - E_{tot}(PEG) \quad \text{[Eq. 6.1]}$$

with $E_{tot}(AuNP-1\,PEG)$ being the total electronic energy of the adsorption structure of one PEG molecule on AuNPs, $E_{tot}(AuNP)$ being the total electronic energy of the isolated relaxed AuNP (with a starting guess for the geometry optimization being the deformed AuNP in the presence of the PEG ligand), and $E_{tot}(PEG)$ being the total electronic energy of the isolated relaxed PEG molecule.

6.4.1.1/ Decomposition in pure GGA and dispersion energies

The adsorption energy of one PEG molecule can be decomposed into pure GGA PBE contribution (covalence) ΔE_{cov} (eV) and dispersion D3 semi-empirical corrective term (ΔE_{disp}) (eV):

$$\Delta E_{ads} = \Delta E_{cov} + \Delta E_{disp} \quad \text{[Eq. 6.2]}$$

6.4.1.2/ Decomposition in deformation and interaction energies

The adsorption energy ΔE_{ads} for one PEG molecule can be decomposed in deformation energies of AuNP and of PEG, and in interaction energy between AuNP and PEG (chemical bonding) :

$$\Delta E_{ads} = \Delta E_{\text{def}}(AuNP) + \Delta E_{\text{def}}(PEG) + \Delta E_{\text{int}}(PEG - Au) \quad \text{[Eq. 6.3]}$$

where the deformation energies read :

$$\Delta E_{\text{def}}(AuNP) = E_{tot}(AuNP/@) - E_{tot}(AuNP) \quad \text{[Eq. 6.4]}$$

$$\Delta E_{\text{def}}(PEG) = E_{tot}(PEG/@) - E_{tot}(PEG) \quad \text{[Eq. 6.5]}$$

with $E_{tot}(AuNP/@)$ and $E_{tot}(PEG/@)$ being the total electronic energies of AuNP and PEG molecule calculated in the optimal geometry of the complete relaxed system noted “@”, respectively.

The interaction energy between AuNP and the PEG molecule is then:

$$\Delta E_{\text{int}}(PEG - Au) = E_{tot}(AuNP - 1\,PEG) - \left(E_{tot}(AuNP/@) + E_{tot}(PEG/@)\right) \quad \text{[Eq. 6.6]}$$

6.4.2/ Monoshells of PEGylated AuNPs

The normalized coadsorption energy ΔE_{coads} per chemisorbed PEG molecule presented on the Table 6.2 of section 6.6 is defined as follows:

$$\Delta E_{coads}^{tot} = N_{chem}^{PEG} \times \Delta E_{coads} = E_{tot}(AuNP - xPEG) - E_{tot}(AuNP) - x\, E_{tot}(PEG) \quad \text{[Eq. 6.7]}$$

with, ΔE_{coads}^{tot} being the total coadsorption energy of PEG molecules (eV), $E_{tot}(AuNP - xPEG)$ being the total electronic energy of the complete optimized system (PEG monoshell adsorbed on AuNP), $E_{tot}(AuNP)$ being the total electronic energy of the isolated relaxed AuNP (with a starting guess for the geometry optimization being the deformed AuNP in the presence of PEG monoshell), $E_{tot}(PEG)$ being the total electronic energy of one isolated relaxed PEG molecule, *x* and N_{chem}^{PEG} being the total numbers of PEG ligands and of chemisorbed PEG molecules, respectively.

6.4.2.1/ Decomposition in pure GGA and dispersion energies

The normalized coadsorption energy per PEG molecule $\widetilde{\Delta E_{coads}}$ can be decomposed into normalized pure GGA PBE contribution ΔE_{cov} (eV/PEG) and dispersion D3 semi-empirical corrective term (ΔE_{disp}) (eV/PEG):

$$\widetilde{\Delta E_{coads}} = \Delta E_{coads}^{tot} / x = \Delta E_{cov} + \Delta E_{disp} \quad \text{[Eq. 6.8]}$$

6.4.2.2/ Decomposition in deformation and interaction energies

The total coadsorption energy ΔE_{coads}^{tot} can be decomposed in total deformation energies of AuNP $\Delta E_{\mathrm{def}}^{tot}(AuNP)$ and of *x* PEG molecules $\Delta E_{\mathrm{def}}^{tot}(xPEG)$, and in total interaction energy $\Delta E_{\mathrm{int}}^{tot}(2B)(xPEG - Au)$ between two subsystems (noted “2B”): AuNP and *x* PEG molecules (chemical bonding) :

$$\Delta E_{coads}^{tot} = \Delta E_{\mathrm{def}}^{tot}(AuNP) + \Delta E_{\mathrm{int+def}}^{tot}(xPEG) + \Delta E_{\mathrm{int}}^{tot}(2B)(xPEG - Au) \quad \text{[Eq. 6.9]}$$

where the deformation energies read :

$$\Delta E_{\mathrm{def}}^{tot}(AuNP) = E_{tot}(AuNP/@) - E_{tot}(AuNP) \quad \text{[Eq. 6.10]}$$

$$\Delta E_{\mathrm{int+def}}^{tot}(xPEG) = E_{tot}(xPEG/@) - xE_{tot}(PEG) \quad \text{[Eq. 6.11]}$$

with $E_{tot}(AuNP/@)$ and $E_{tot}(xPEG/@)$, being the total electronic energies of AuNP and *x* PEG molecules calculated in the optimal geometry of the complete relaxed system noted "@", respectively. In the case of *x* PEG, the deformation energy includes also the interaction energy between the PEG molecules, since the reference is the isolated relaxed gas phase system (one PEG in the supercell).

The total interaction energy between AuNP and *x* PEG molecules is :

$$\Delta E_{\text{int}}^{tot}(2\,B)(xPEG-Au)=E_{tot}(AuNP-xPEG)-\left(E_{tot}(AuNP/@)+E_{tot}(xPEG/@)\right) \quad \text{[Eq. 6.12]}$$

By normalizing per chemisorbed PEG ligand, the average interaction energy between one PEG and AuNP as exposed in Table 6.2 can then be derived as follows:

$$\Delta E_{\text{int}}(PEG-Au)=\left(\Delta E_{\text{int}}^{tot}(2\,B)(xPEG-Au)\right)/N_{chem} \quad \text{[Eq. 6.13]}$$

This interaction energy is also illustrated hereafter in Figure 6.1.

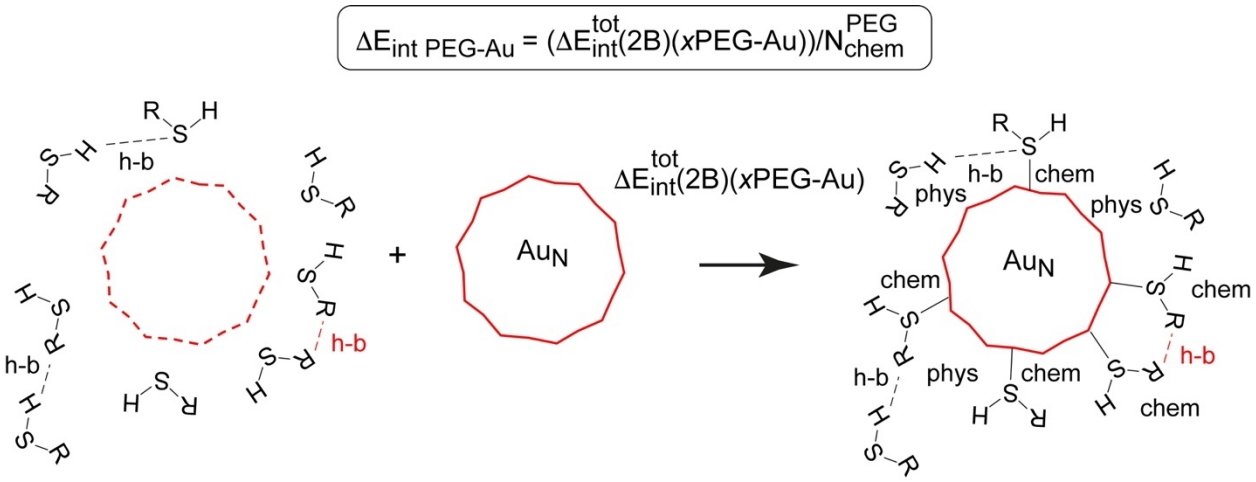

Figure 6.1. *Definition of the normalized interaction energy between AuNP and PEG ligands.*

Alternatively, the total interaction energy $\Delta E_{\text{int}}^{tot}(MB)(xPEG-Au)$ between AuNP and *x* PEG molecules considered separately (not in one subsystem) can be expressed also as follows :

$$\Delta E_{\text{int}}^{tot}(MB)(xPEG-Au)=E_{tot}(AuNP-xPEG)-\left(E_{tot}(AuNP/@)+\sum_{i=1}^{x}\left(E_{tot}(PEG_i/@)\right)\right)$$ [Eq.6.14]

with $E_{tot}(PEG_i/@)$ being the total electronic energy of one PEG molecule belonging to the shell composed of *x* PEG ligands, calculated in the optimal geometry of the complete relaxed system noted "@".

The total interaction energy between PEG molecules belonging to the family of *x* PEG ligands is then derived as follows :

$$\Delta E_{\text{int}}^{tot}(PEG-PEG)=E_{tot}(xPEG/@)-\sum_{i=1}^{x}\left(E_{tot}(PEG_i/@)\right)$$ [Eq. 6.15]

By combining Eqs. 6.12 and 6.15, one can write easily:

$$\Delta E_{\text{int}}^{tot}(MB)(xPEG-Au)=\Delta E_{\text{int}}^{tot}(2B)(xPEG-Au)+\Delta E_{\text{int}}^{tot}(PEG-PEG)$$ [Eq. 6.16]

Furthermore, by combining Eqs. 6.11 and 6.12, one can define the interaction energy between *x* PEG ligands and AuNP including the deformation energy of *x* PEG :

$$\Delta E_{\text{def+int}}^{tot}(MB)(xPEG-Au)=\Delta E_{\text{int+def}}^{tot}(PEG-PEG)+\Delta E_{\text{int}}^{tot}(2B)(xPEG-Au)$$

$$=E_{tot}(AuNP-xPEG)-\left(E_{tot}(AuNP/@)+xE_{tot}(PEG)\right)$$ [Eq. 6.17]

Finally, the normalized interaction and deformation energy per PEG molecule (given in Table 6.2 and illustrated in Figure 6.2) is obtained as follows:

$$\Delta E_{\text{def+int}}(PEG-PEG)=\Delta E_{\text{def+int}}^{tot}(PEG-PEG)/x$$ [Eq. 6.18]

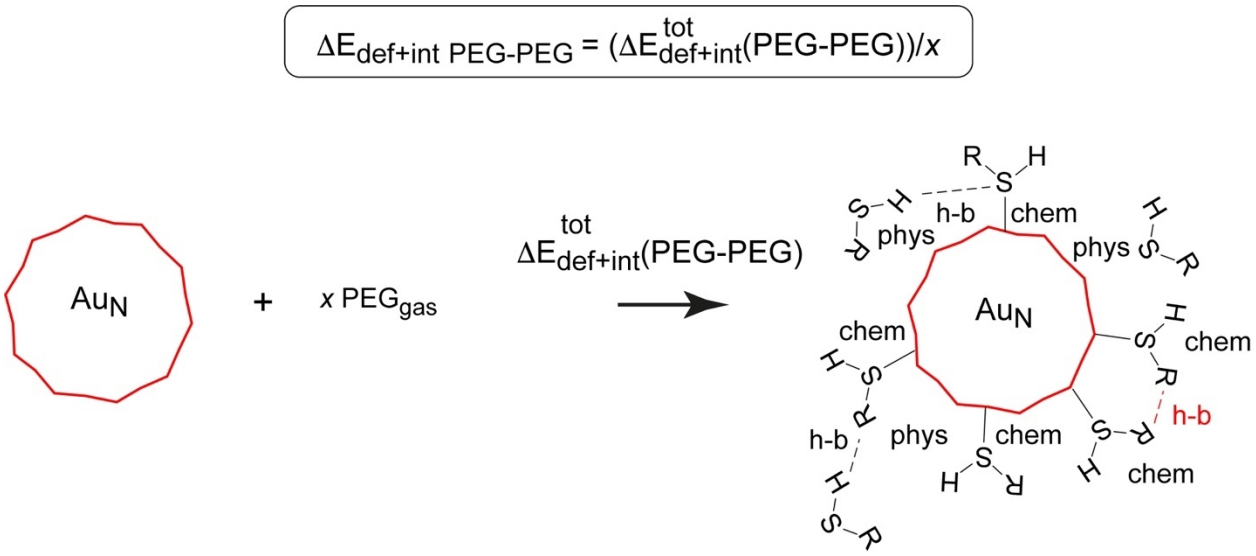

Figure 6.2. *Definition of the normalized interaction energy (including deformation energy) between PEG ligands.*

6.4.3/ Monoshells of hydrated PEGylated AuNPs

The normalized coadsorption energy ΔE_{coads} per chemisorbed PEG molecule addressed on Table 6.3 of section 6.7 is defined as follows:

$$\Delta E_{coads}^{tot} = N_{chem}^{PEG} \Delta E_{coads} = E_{tot}\left(AuNP/xPEG/y\,H_2O\right) - E_{tot}\left(AuNP\right) - x\,E_{tot}\left(PEG\right) - y\,E_{tot}\left(H_2O\right)$$

[Eq. 6.19]

with $E_{tot}\left(AuNP/xPEG/y\,H_2O\right)$ being the total electronic energy of the complete relaxed system (hydrated PEGylated AuNP), $E_{tot}\left(AuNP\right)$ being the total electronic energy of the isolated relaxed AuNP (with a starting guess for the geometry optimization being the deformed AuNP in the presence of hydrated PEGylated monoshells), *x* being the total number of PEG molecules, $E_{tot}\left(PEG\right)$ being the total electronic energy of one isolated relaxed PEG molecule, *y* being the total number of water molecules,

$E_{tot}(H_2O)$ being the total electronic energy of one isolated relaxed water molecule, and N_{chem}^{PEG} being the total number of chemisorbed PEG ligands.

6.4.3.1/ Decomposition in pure GGA and dispersion energies

The normalized coadsorption energy per PEG molecule $\widetilde{\Delta E_{coads}}$ can be decomposed into normalized pure GGA PBE contribution (covalence) ΔE_{cov} (eV/PEG) and dispersion D3 semi-empirical corrective term (ΔE_{disp}) (eV/PEG):

$$\widetilde{\Delta E_{coads}} = \Delta E_{coads}^{tot} / x = \Delta E_{cov} + \Delta E_{disp} \quad \text{[Eq. 6.20]}$$

6.4.3.2/ Decomposition in deformation and interaction energies

The total coadsorption energy ΔE_{coads}^{tot} can be decomposed in total deformation energies of AuNP $\Delta E_{\text{def}}^{tot}(AuNP)$, of x PEG molecules $\Delta E_{\text{def}}^{tot}(xPEG)$, of y H_2O molecules $\Delta E_{\text{def}}^{tot}(y\,H_2O)$ and in total interaction energy $\Delta E_{\text{int}}^{tot}(3\,B)(AuNP/xPEG/y\,H_2O)$ between three subsystems (noted "3B" for "three-body"): AuNP, x PEG and y H_2O molecules (chemical bondings) :

$$\Delta E_{coads}^{tot} = \Delta E_{\text{def}}^{tot}(AuNP) + \Delta E_{\text{int+def}}^{tot}(xPEG) + \Delta E_{\text{int+def}}^{tot}(y\,H_2O) + \Delta E_{\text{int}}^{tot}(3\,B)(AuNP/xPEG/y\,H_2O)$$

[Eq. 6.21]

where the deformation energies read :

$$\Delta E_{\text{def}}^{tot}(AuNP) = E_{tot}(AuNP/@) - E_{tot}(AuNP) \quad \text{[Eq. 6.22]}$$

$$\Delta E_{\text{int+def}}^{tot}(xPEG) = E_{tot}(xPEG/@) - xE_{tot}(PEG) \quad \text{[Eq. 6.23]}$$

$$\Delta E_{\text{int+def}}^{tot}(y\,H_2O) = E_{tot}(y\,H_2O/@) - yE_{tot}(H_2O) \quad \text{[Eq. 6.24]}$$

with $E_{tot}(AuNP/@)$, $E_{tot}(xPEG/@)$ and $E_{tot}(y\,H_2O/@)$, being the total electronic energies of AuNP, x PEG and y H_2O molecules calculated in the optimal geometry of the complete relaxed system noted "@", respectively. In the case of x PEG

(y H_2O), the deformation energy includes also the interaction energy between the PEG (H_2O) molecules, since the reference is the isolated relaxed gas phase system (one PEG or one H_2O in the supercell).

The total interaction energy $\Delta E_{\text{int}}^{tot}(3B)(AuNP/xPEG/y\,H_2O)$ between the three subsystems AuNP, *x* PEG and y H_2O molecules is calculated as follows :

$$\Delta E_{\text{int}}^{tot}(3B)(AuNP/xPEG/y\,H_2O)=E_{tot}(AuNP/xPEG/y\,H_2O)-\left(E_{tot}(AuNP/@)+E_{tot}(xPEG/@)+E_{tot}(y\,H_2O/@)\right)$$

[Eq. 6.25]

The total interaction energy between AuNP and *x* PEG molecules is :

$$\Delta E_{\text{int}}^{tot}(2B)(xPEG-Au)=E_{tot}(AuNP-xPEG/@)-\left(E_{tot}(AuNP/@)+E_{tot}(xPEG/@)\right)$$

[Eq. 6.26]

where $E_{tot}(AuNP-xPEG/@)$ is the total electronic energy of the subsystem AuNP with *x* PEG ligands in the frozen geometry of the complete relaxed system.

By normalizing per chemisorbed PEG ligand, the average interaction energy between one PEG and AuNP (as exposed in Table 6.3 and depicted in Figure 6.3) can then be derived as follows:

$$\Delta E_{\text{int}}(PEG-Au)=\left(\Delta E_{\text{int}}^{tot}(2B)(xPEG-Au)\right)/N_{chem}^{PEG} \quad \text{[Eq. 6.27]}$$

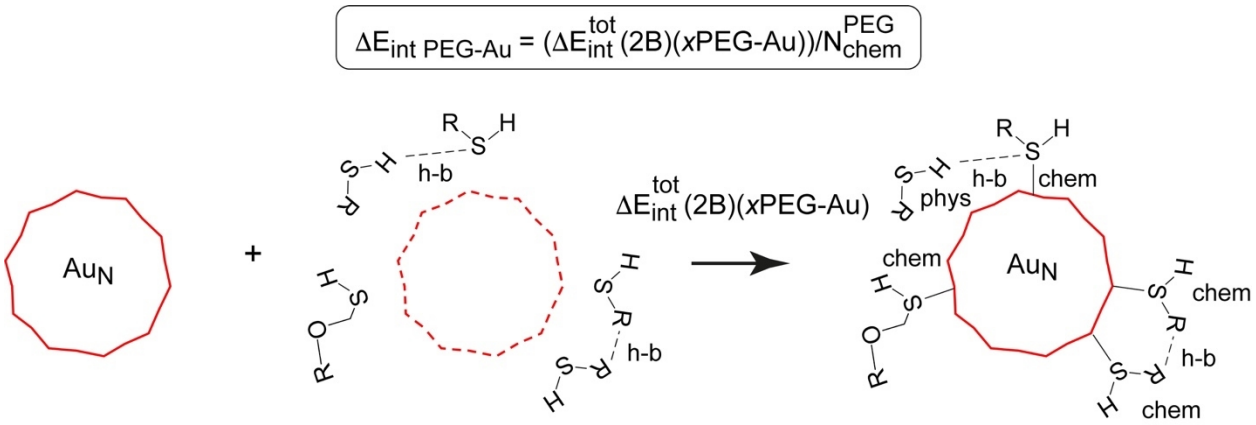

Figure 6.3. *Definition of the normalized interaction energy between AuNP and PEG ligands.*

This total interaction energy between AuNP and *x* PEG can also be evaluated in the presence of *y* H_2O hydrating the PEG coating:

$$\Delta E_{\text{int}}^{tot}(2\,B)\left(xPEG\,,y\,H_2O-Au\right)=E_{tot}\left(AuNP/xPEG/y\,H_2O\right)-\left(E_{tot}\left(AuNP/@\right)+E_{tot}\left(xPEG\,,y\,H_2O/@\right)\right)$$

[Eq. 6.28]

where $E_{tot}\left(xPEG\,,y\,H_2O/@\right)$ is the total electronic energy of the frozen geometry of *x* PEG and *y* H_2O molecules taken from the complete relaxed system, noted "@".

By normalizing per chemisorbed PEG ligand, the average interaction energy between one hydrated PEG and AuNP (as reported on Table 6.3 and illustrated in Figure 6.4) can also be derived as follows:

$$\Delta E_{\text{int}}\left(\left(PEG+H_2O\right)-Au\right)=\left(\Delta E_{\text{int}}^{tot}(2\,B)\left(xPEG\,,yH_2O-Au\right)\right)/N_{chem}^{PEG}$$ [Eq. 6.29]

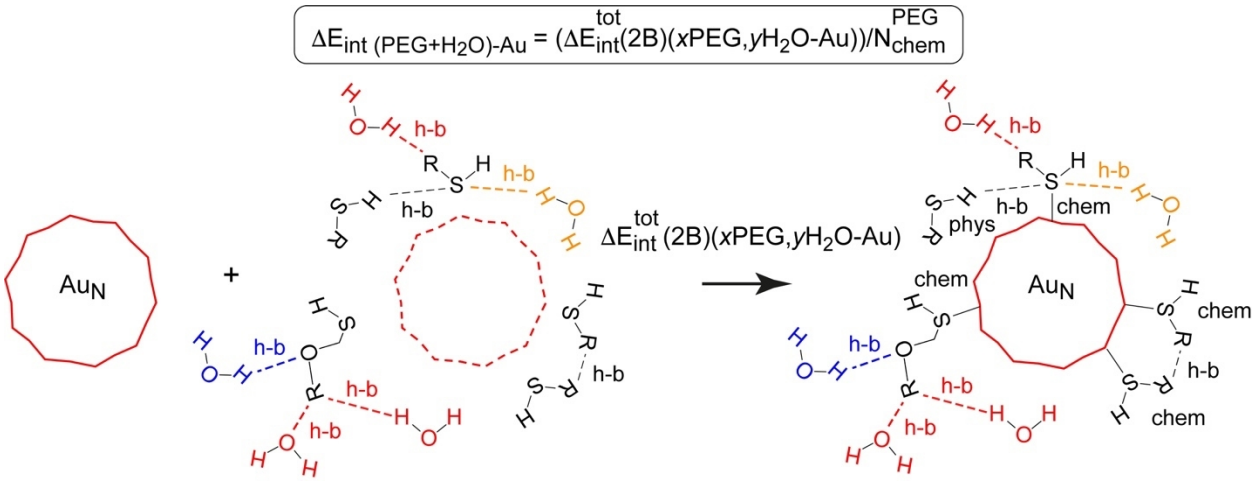

Figure 6.4. *Definition of the normalized interaction energy between AuNP and PEG ligands, in the presence of the hydrated shell.*

In the same way of the interaction between AuNP and *x* PEG, the total interaction energy between AuNP and *y* H_2O molecules is expressed easily :

$$\Delta E_{\text{int}}^{tot}(2\,B)\left(y\,H_2O-Au\right)=E_{tot}\left(AuNP-yH_2O/@\right)-\left(E_{tot}\left(AuNP/@\right)+E_{tot}\left(yH_2O/@\right)\right) \quad [\text{Eq.6.30}]$$

where $E_{tot}\left(AuNP-yH_2O/@\right)$ is the total electronic energy of the subsystem AuNP with *y* H_2O molecules in the frozen geometry of the complete relaxed system.

By normalizing per H_2O molecule, the average interaction energy between one water molecule and AuNP (as given in Table 6.3 of section 6.7 and depicted in Figure 6.5) is then obtained :

$$\Delta E_{\text{int}}\left(H_2O-Au\right)=\left(\Delta E_{\text{int}}^{tot}(2\,B)\left(y\,H_2O-Au\right)\right)/y \quad [\text{Eq. 6.31}]$$

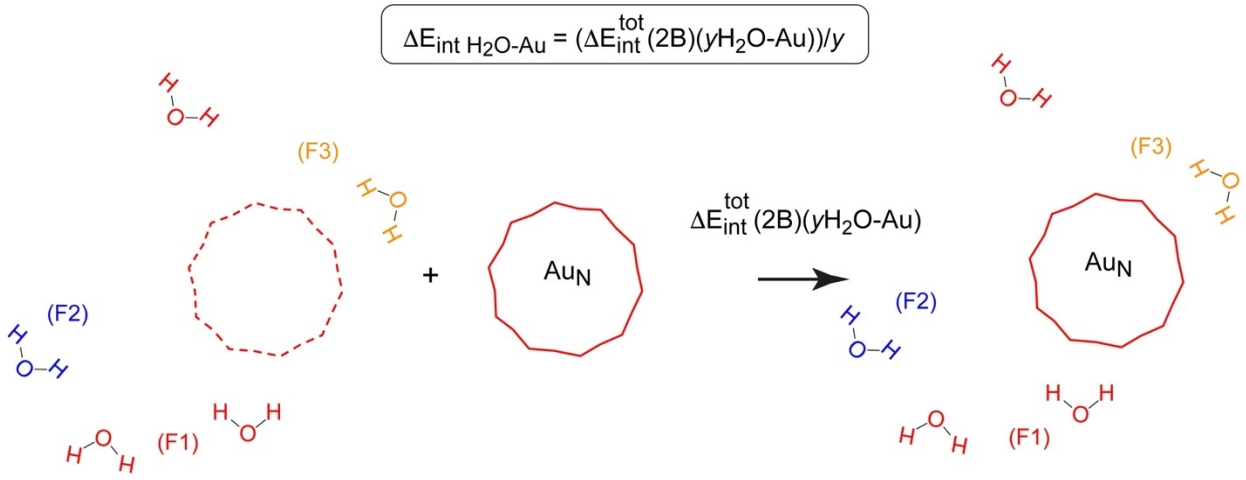

Figure 6.5. *Definition of the normalized interaction energy between AuNP and water molecules.*

By following Eqs. 6.26 and 6.30, the total interaction energy between *x* PEG and *y* H_2O molecules reads:

$$\Delta E_{\text{int}}^{tot}(2B)(xPEG-y\,H_2O)=E_{tot}(xPEG-yH_2O/@)-\left(E_{tot}(xPEG/@)+E_{tot}(yH_2O/@)\right) \quad \text{[Eq. 6.32]}$$

where $E_{tot}(xPEG-yH_2O/@)$ is the total electronic energy of the subsystem *x* PEG with *y* H_2O molecules in the frozen geometry of the complete relaxed system. In this latter equation, there is no Au in the energetic balance.

There are two ways of normalization for the latter interaction energy : by either H_2O or PEG molecule. This leads to two additional respective formulas derived hereafter and presented in Table 6.3 for the values and illustrated in Figure 6.6:

$$\Delta E_{\text{int}}(PEG-H_2O)=\left(\Delta E_{\text{int}}^{tot}(2B)(xPEG-y\,H_2O)\right)/y \quad \text{[Eq. 6.33]}$$

$$\Delta E_{\text{int}}(PEG-H_2O)=\left(\Delta E_{\text{int}}^{tot}(2B)(xPEG-y\,H_2O)\right)/x \quad \text{[Eq. 6.34]}$$

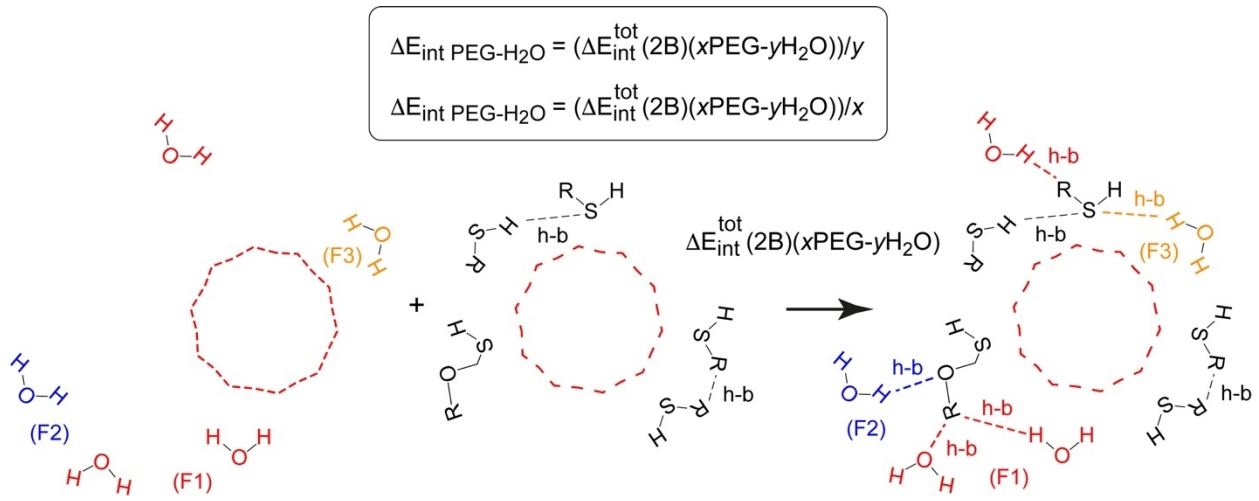

Figure 6.6. *Definition of the normalized interaction energy (two different normalizations) between x PEG ligands and y H_2O molecules.*

There exists a relationship between the "3B" interaction energy and some of the "2B" terms defined hereabove. By combining Eqs. 6.25 with 6.26 and 6.30, one can derive:

$$\Delta E_{\text{int}}^{tot}(3B)\left(AuNP/xPEG/y\,H_2O\right)-\left(\Delta E_{\text{int}}^{tot}(2B)(xPEG-Au)+\Delta E_{\text{int}}^{tot}(2B)\left(y\,H_2O-Au\right)\right)$$

$$=\left(E_{tot}\left(AuNP/xPEG/y\,H_2O\right)+E_{tot}\left(AuNP/@\right)\right)-\left(E_{tot}\left(AuNP-xPEG/@\right)+E_{tot}\left(AuNP-yH_2O/@\right)\right)$$

[Eq. 6.35]

The latter term in Eq. 6.35 is equivalent to interaction energy calculated between *x* PEG and *y* H_2O molecules, but in presence of AuNP, all of them calculated in the frozen geometries extracted from the complete relaxed system. This energy is defined as $\widetilde{\Delta E_{\text{int}}^{tot}(2B)}(xPEG-y\,H_2O)$. This leads to the complete equation linking the "3B" term with "2B" ones:

$$\Delta E_{\text{int}}^{tot}(3B)(AuNP/xPEG/y\,H_2O)=\Delta E_{\text{int}}^{tot}(2B)(xPEG-Au)+\Delta E_{\text{int}}^{tot}(2B)(y\,H_2O-Au)+\widetilde{\Delta E_{\text{int}}^{tot}(2B)}(xPEG-y\,H_2O)$$

[Eq. 6.36]

Alternatively, the total interaction energy $\Delta E_{\text{int}}^{tot}(MB)(xPEG-y\,H_2O)$ between x PEG and y H_2O molecules, all considered separately (not in two subsystems), can be expressed also as follows :

$$\Delta E_{\text{int}}^{tot}(MB)(xPEG-y\,H_2O)=E_{tot}(xPEG-y\,H_2O/@)-\left(\sum_{i=1}^{x}\left(E_{tot}(PEG_i/@)\right)+\sum_{j=1}^{y}\left(E_{tot}(H_2O_j/@)\right)\right)$$

[Eq. 6.37]

with $E_{tot}(PEG_i/@)$ and $E_{tot}(H_2O_j/@)$ being respectively the total electronic energies of one PEG molecule belonging to the shell composed of x PEG ligands, and of one water molecule belonging to the shell composed of y H_2O molecules, all calculated in the optimal geometry of the complete relaxed system noted "@".

The total interaction energy between PEG molecules belonging to the family of x PEG ligands is then derived as follows :

$$\Delta E_{\text{int}}^{tot}(PEG-PEG)=E_{tot}(xPEG/@)-\sum_{i=1}^{x}\left(E_{tot}(PEG_i/@)\right)$$ [Eq. 6.38]

And the total interaction energy between H_2O molecules belonging to the family of y H_2O is obtained in a similar way:

$$\Delta E_{\text{int}}^{tot}(H_2O-H_2O)=E_{tot}(y\,H_2O/@)-\sum_{j=1}^{y}\left(E_{tot}(H_2O_j/@)\right)$$ [Eq. 6.39]

By combining Eqs. 6.32 with 6.38 and 6.39, one can then write:

$$\Delta E_{\text{int}}^{tot}(MB)(xPEG-y\,H_2O)=\Delta E_{\text{int}}^{tot}(2B)(xPEG-y\,H_2O)+\Delta E_{\text{int}}^{tot}(PEG-PEG)+\Delta E_{\text{int}}^{tot}(H_2O-H_2O)$$

[Eq. 6.40]

Moreover, by combining Eqs. 6.23, 6.24 and 6.32, one can define the interaction energy between *x* PEG and *y* H_2O molecules including the deformation energies of *x* PEG and *y* H_2O:

$$\Delta E^{tot}_{\text{int+def}}(MB)(xPEG-y\,H_2O)=\Delta E^{tot}_{\text{int+def}}(PEG-PEG)+\Delta E^{tot}_{\text{int+def}}(H_2O-H_2O)+\Delta E^{tot}_{\text{int}}(2B)(xPEG-y\,H_2O)$$

[Eq. 6.41]

In addtion, the normalized interaction and deformation energies per PEG and per water molecule (given in Table 6.3 and depicted in Figures 6.7 and 6.8) are obtained as follows:

$$\Delta E_{\text{def+int}}(PEG-PEG)=\Delta E^{tot}_{\text{def+int}}(PEG-PEG)/x \quad \text{[Eq. 6.42]}$$

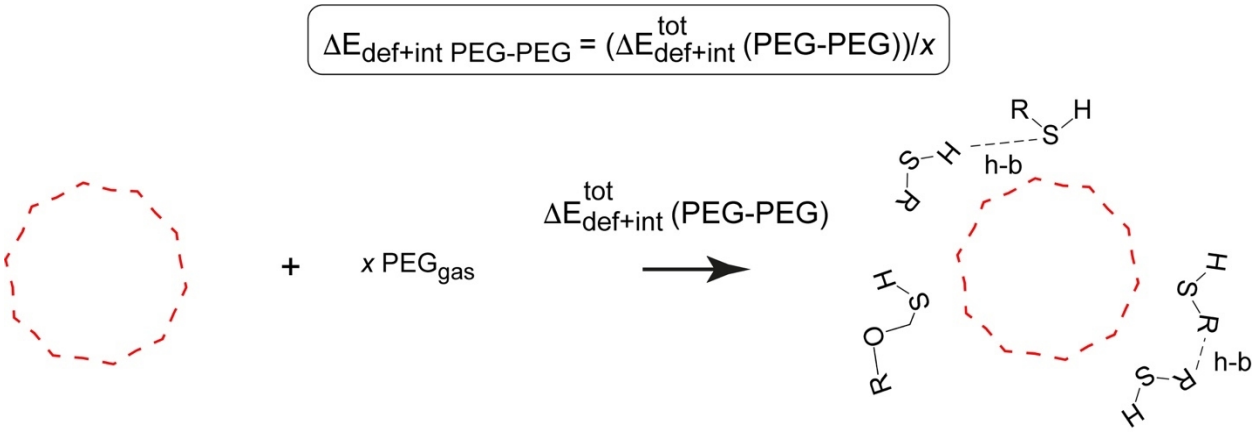

Figure 6.7. *Definition of the normalized interaction energy (including deformation energy) between PEG ligands.*

$$\Delta E_{\text{def+int}}(H_2O-H_2O)=\Delta E^{tot}_{\text{def+int}}(H_2O-H_2O)/y \quad \text{[Eq. 6.43]}$$

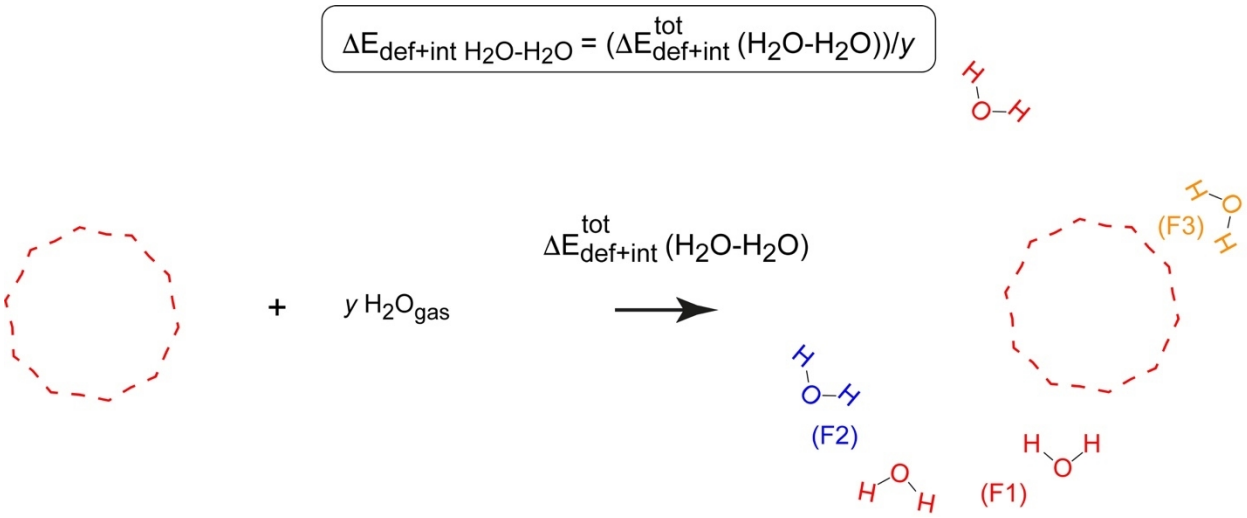

Figure 6.8. *Definition of the normalized interaction energy (including deformation energy) between H_2O molecules.*

A last decomposition is considered by separating the family of y H_2O molecules belonging to the hydration shell to three subsystems: water molecules in interaction (F1) with the -COOH moieties of the PEG ligands, (F2) with the oxygen atoms of the ethylene glycol chains and (F3) with the -SH groups (see Figure 6.28).

With these definitions, the interaction energies between x PEG ligands and H_2O molecules of each family normalized by the corresponding number of water molecules y_1 for (F1), y_2 for (F2) and y_3 for (F3) ($y = y_1 + y_2 + y_3$) can then be easily derived (as given in Table 6.3 and illustrated in Figures 6.9, 6.10 and 6.11):

$$\Delta E_{\text{int}}\left(xPEG-y_1H_2O\right)=\left(E_{tot}\left(xPEG-y_1H_2O/@\right)-\left(E_{tot}\left(xPEG/@\right)+E_{tot}\left(y_1H_2O/@\right)\right)\right)/y_1$$

[Eq. 6.44]

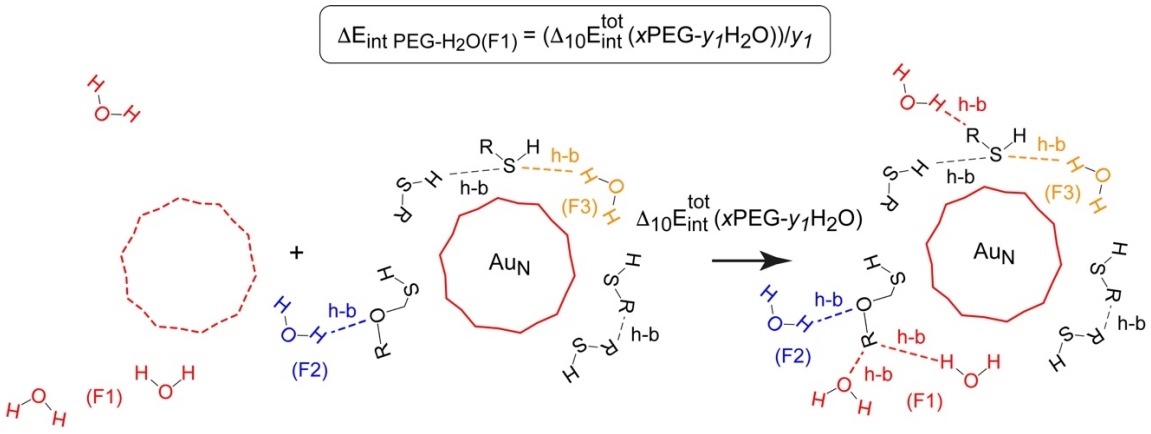

Figure 6.9. *Definition of the normalized interaction energy between x PEG ligands and y_1 H_2O molecules belonging to family (F1).*

$$\Delta E_{\text{int}}\left(xPEG-y_2H_2O\right)=\left(E_{tot}\left(xPEG-y_2H_2O/@\right)-\left(E_{tot}\left(xPEG/@\right)+E_{tot}\left(y_2H_2O/@\right)\right)\right)/y_2$$

[Eq. 6.45]

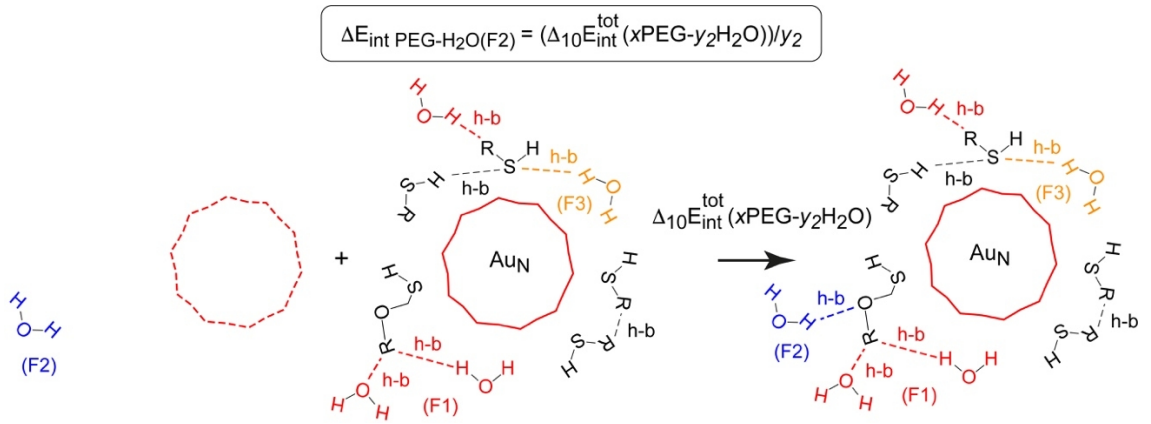

Figure 6.10. *Definition of the normalized interaction energy between x PEG ligands and y_2 H_2O molecules belonging to family (F2).*

$$\Delta E_{\text{int}}\left(xPEG-y_3H_2O\right)=\left(E_{tot}\left(xPEG-y_3H_2O/@\right)-\left(E_{tot}\left(xPEG/@\right)+E_{tot}\left(y_3H_2O/@\right)\right)\right)/y_3$$

[Eq. 6.46]

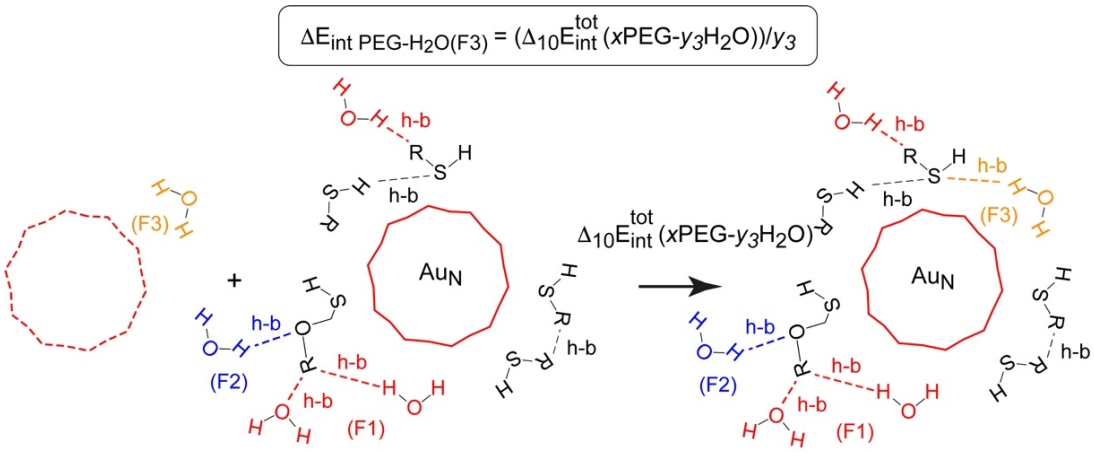

Figure 6.11. *Definition of the normalized interaction energy between x PEG ligands and* y_3 H_2O *molecules belonging to family (F3).*

Similarly, the interaction energies between AuNP and the water molecules of each family can be expressed with the following formulas (addressed in Table 6.3 and depicted in Figures 6.12, 6.13 and 6.14):

$$\Delta E_{\text{int}}\left(y_1H_2O-Au\right)=\left(E_{tot}\left(AuNP-y_1H_2O/@\right)-\left(E_{tot}\left(AuNP/@\right)+E_{tot}\left(y_1H_2O/@\right)\right)\right)/y_1$$

[Eq. 6.47]

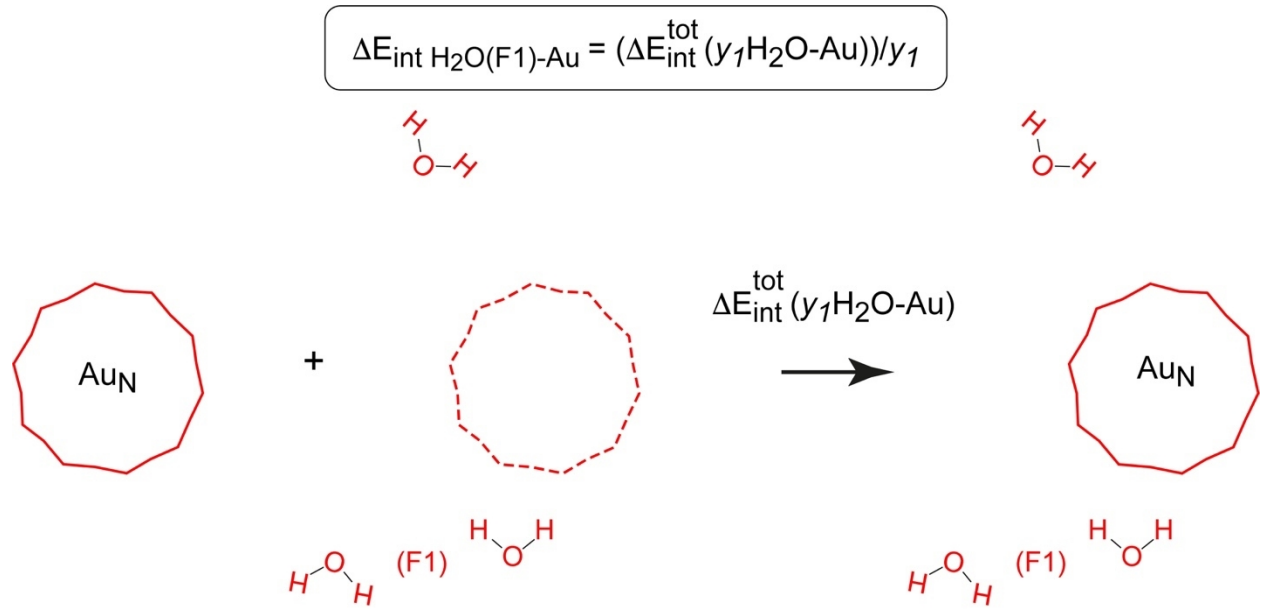

Figure 6.12. *Definition of the normalized interaction energy between AuNP and y_1 H_2O molecules belonging to family (F1).*

$$\Delta E_{\text{int}}\left(y_2 H_2O - Au\right) = \left(E_{tot}\left(AuNP - y_2 H_2O/@\right) - \left(E_{tot}\left(AuNP/@\right) + E_{tot}\left(y_2 H_2O/@\right)\right)\right)/y_2 \qquad \text{[Eq. 6.48]}$$

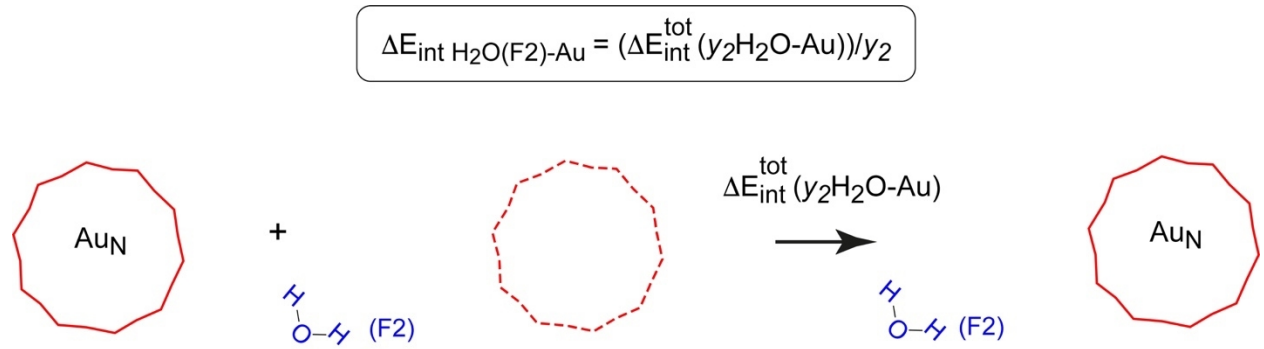

Figure 6.13. *Definition of the normalized interaction energy between AuNP and y_2 H_2O molecules belonging to family (F2).*

$$\Delta E_{\text{int}}\left(y_3 H_2O - Au\right) = \left(E_{tot}\left(AuNP - y_3 H_2O/@\right) - \left(E_{tot}\left(AuNP/@\right) + E_{tot}\left(y_3 H_2O/@\right)\right)\right)/y_3 \quad \text{[Eq. 6.49]}$$

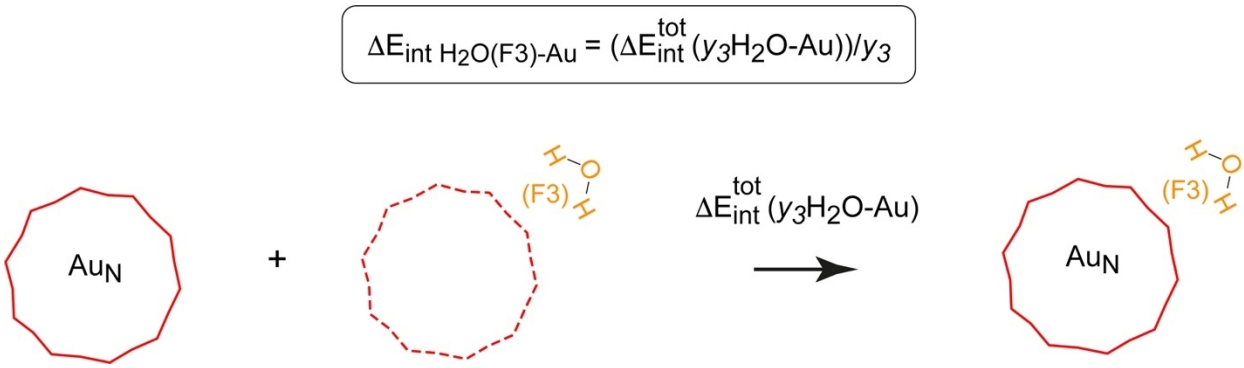

Figure 6.14. *Definition of the normalized interaction energy between AuNP and y3 H2O molecules belonging to family (F3).*

6.4.4/ Gas phase PEG-H 2 O dimers and hydrogen bond analysis of hydrated PEGylated GNPs

In the following section, the optimized structures and related energetics are exposed for gas phase dimers between one PEG and one water molecules (see Figure 6.15). The dimerization occurs mainly through hydrogen bonds between PEG and water. Since the PEG presents four oxygen atoms in our chosen ligand, several competitive configurations have been found during the geometry optimizations, while the water molecule interacts with -COOH, ethylene glycol (EG) units and -SH moieties. The most stable dimer corresponds to an interaction between the water molecule and the PEG through a hydrogen bond with the oxygen atom of the EG unit closer to -SH group (-0.339 eV). The dimer resulting from the interaction between water and PEG via a hydrogen bond with the sulphur atom of -SH moiety is metastable with a competitive dimerization energy of -0.304 eV. The configuration associated with two hydrogen bonds between water and -COOH terminal group of the PEG is slightly less favorable (-0.29 eV).

The number of hydrogen bonds between PEG and H_2O in the case of the hydrated PEGylated GNPs are evaluated by dividing the average interaction energy between PEG and H_2O (normalized per PEG or per water) by the dimerization energy of the most stable configuration between one PEG and one water (dimer2) as follows:

$$N_{HB} = \frac{\Delta E_{\text{int PEG-H2O}}}{\Delta E_{dimer\,2}} \quad \text{[Eq. 6.50]}$$

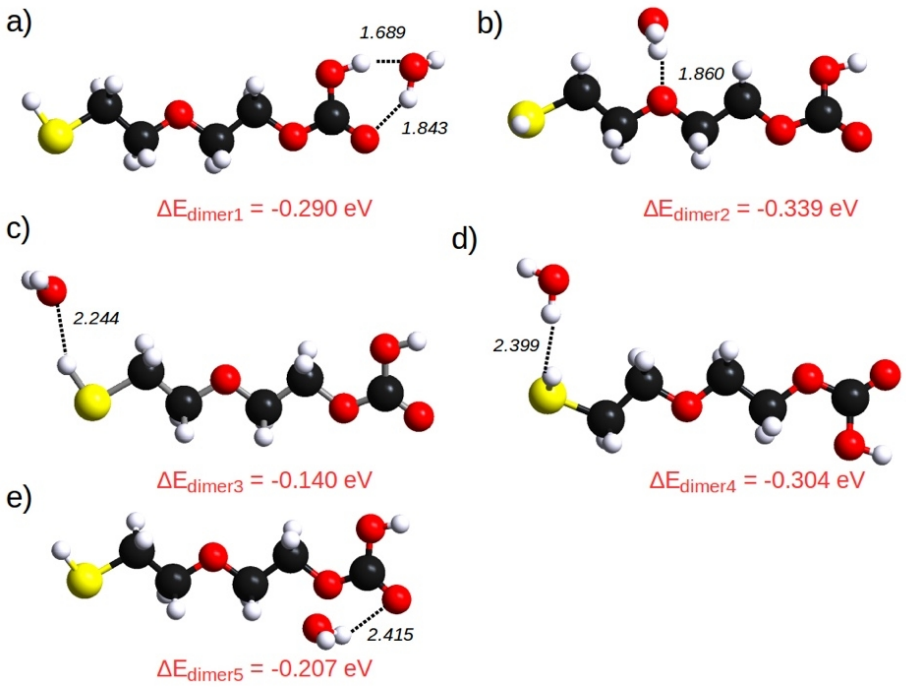

Figure 6.15. *Optimal dimerization structures between one PEG and one water molecules. The hydrogen bonds are marked with dotted black lines and the corresponding distances are expressed in Å. The dimerization energies are reported as well in eV.*

6.5 Various DFT models of PEGylated AuNPs

6.5.1 Isolated PEG Adsorption

Before considering the monoshells of PEG ligands surrounding the Au nanoclusters, the most stable adsorption forms have to be investigated for each shape and size. In Figure 6.16 and Table 6.1, the key results of the best adsorption structures of isolated PEG on the five Au nanoclusters (PBE-D3 level of calculation) have been reported. All the optimized stable and metastable forms are presented in figure 6.17-6.21, with adsorption energies (the percentage of dispersion is being indicated in parentheses in each case) and key distances. All the top sites including corner, edge and facet have been considered for adsorption.

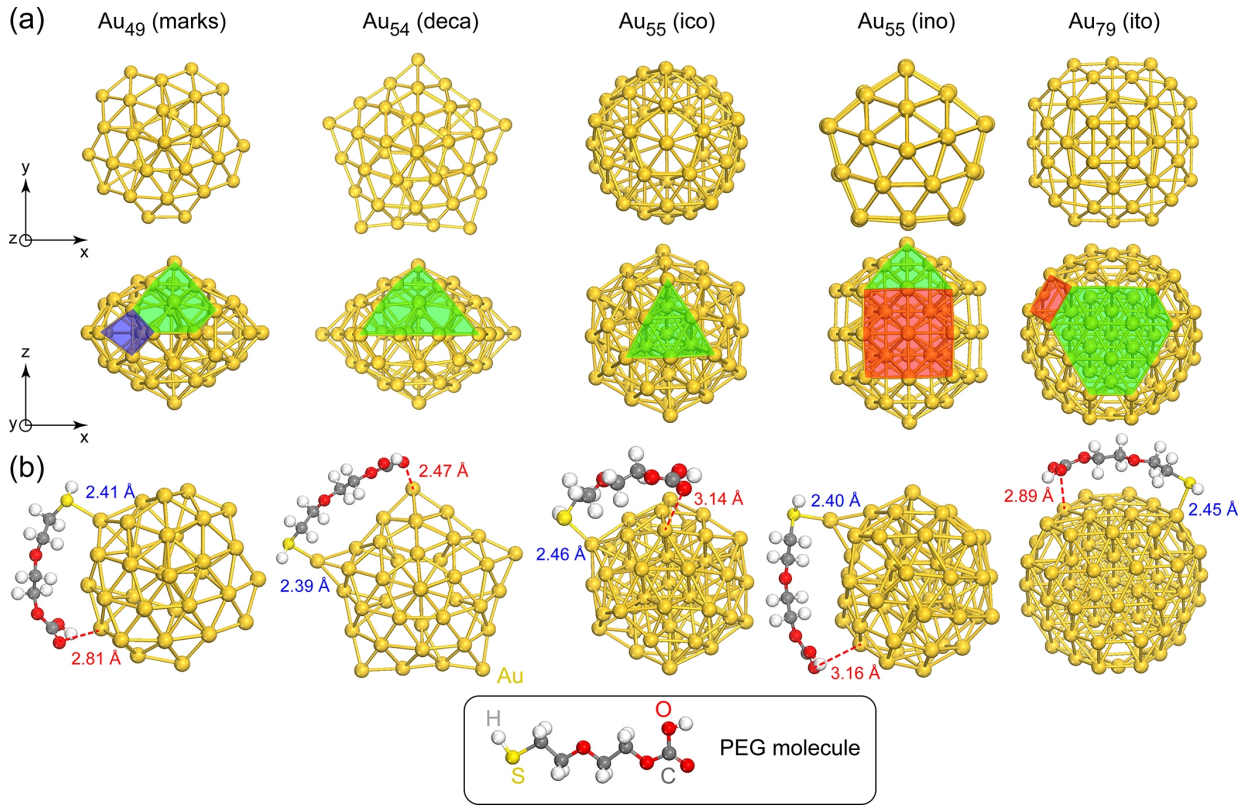

Figure 6.16. *(a) Top and laterals views of optimized clean Au nanoclusters in the range 1.1-1.3 nm with five different morphologies : defective (concave) Marks decahedral (marks) Au_{49}, regular decahedral (deca) Au_{54}, icosahedral (ico) Au_{55}, ino-decahedral (ino) Au_{55} and irregular truncated octahedral (ito) Au_{79}. The facet types are marked with colored areas: green for (111)-type (triangle, pentagon or hexagon), red for (100)-type (square) and blue for (110)-type (concavity). (b) Best and optimized adsorption structures of one PEG molecule (composed of two ethylene glycol units, thiol and carboxy terminal groups) on the five Au nanoclusters. The adsorption occurs mainly through simultaneous chemical bonds between -SH or -COOH moieties and Au kink and edge atoms, following an $\eta_2\mu_2$ form. -SH group binds via the S atom, while -COOH through the -C=O carbonyl bond. The colors of atom types are defined and will be kept in all the figures.*

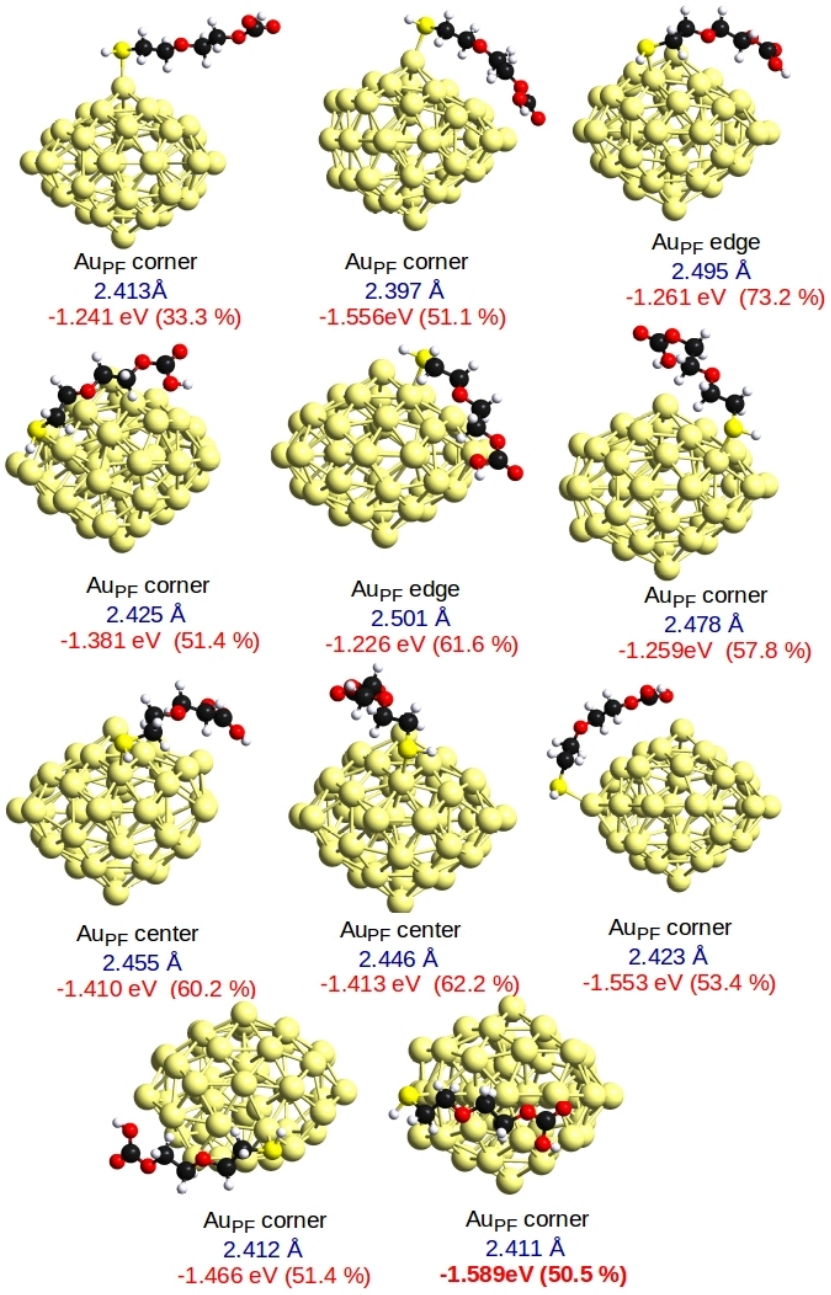

Figure 6.17. *Optimized adsorption structures of one PEG molecule on different top adsorption sites of Au_{49} (marks) (PF meaning pentagonal facet). The Au-S bond distances are reported in blue characters (Å), whereas the adsorption energies in red characters (eV) (the most stable structure with bold characters).*

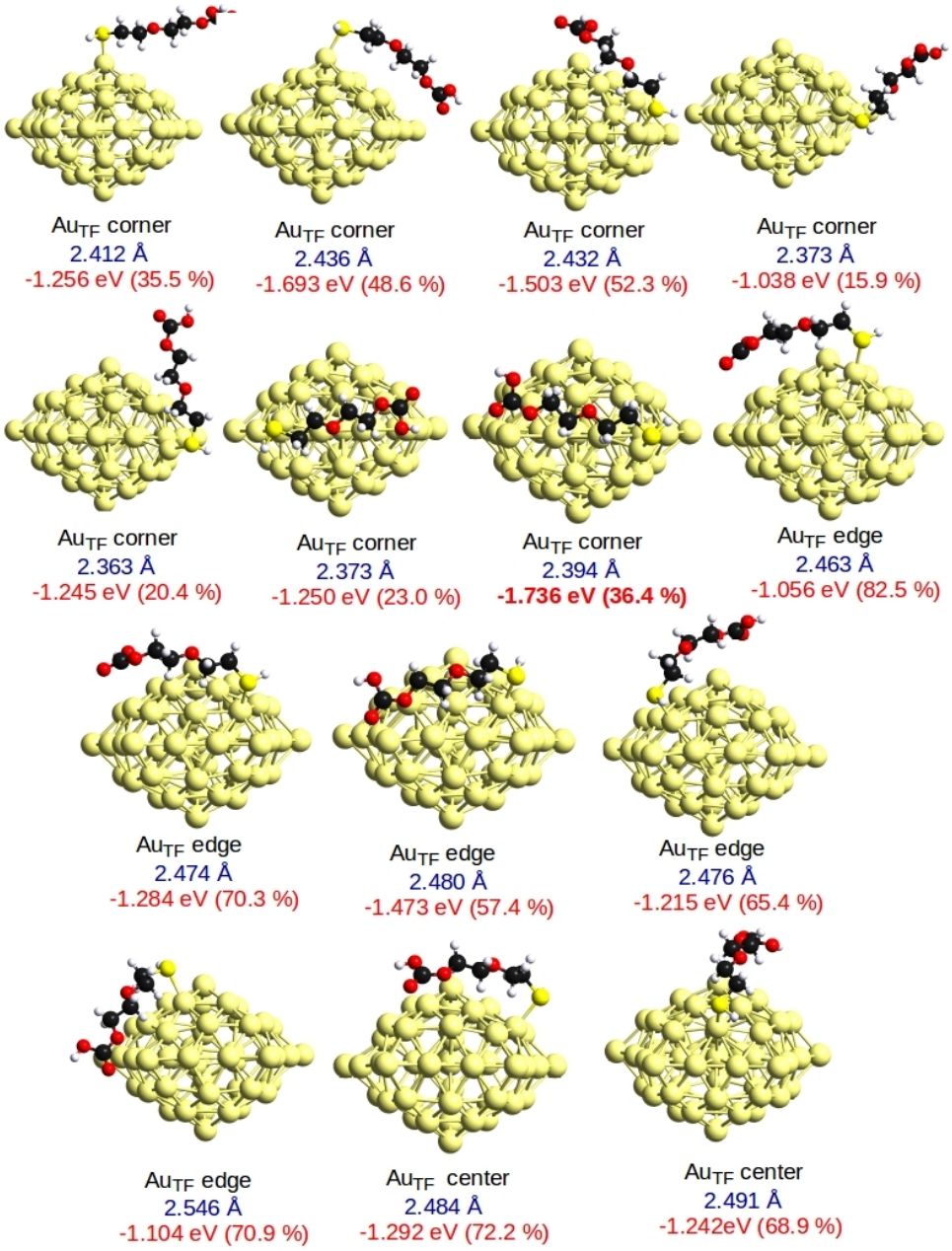

Figure 6.18. *Optimized adsorption structures of one PEG molecule on different top adsorption sites of Au54 (deca) (TF meaning triangular facet). The Au-S bond distances are reported in blue characters (Å), whereas the adsorption energies in red characters (eV) (the most stable structure with bold characters).*

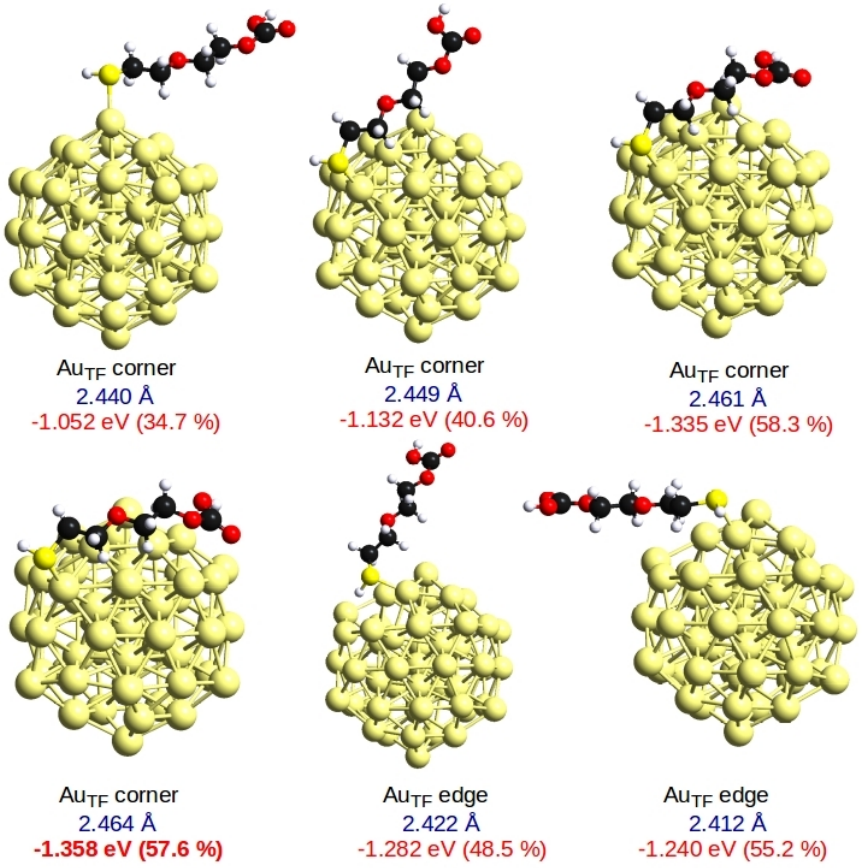

Figure 6.19. *Optimized adsorption structures of one PEG molecule on different top adsorption sites of Au55 (ico) (TF meaning triangular facet). The Au-S bond distances are reported in blue characters (Å), whereas the adsorption energies in red characters (eV) (the most stable structure with bold characters).*

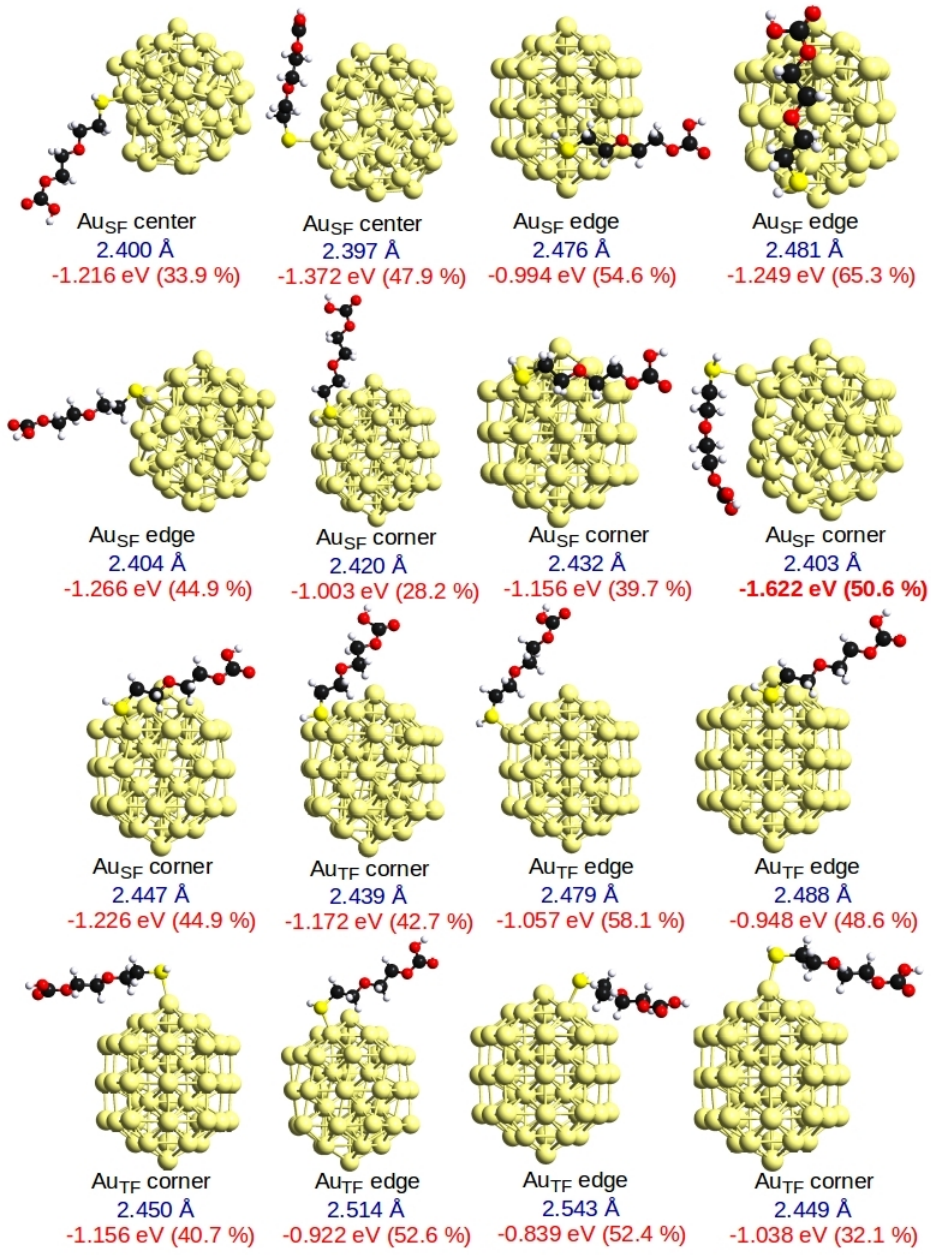

Figure 6.20. *Optimized adsorption structures of one PEG molecule on different top adsorption sites of Au55 (ino) (SF and TF meaning square and triangular facet, respectively). The Au-S bond distances are reported in blue characters (Å), whereas the adsorption energies in red characters (eV) (the most stable structure with bold characters).*

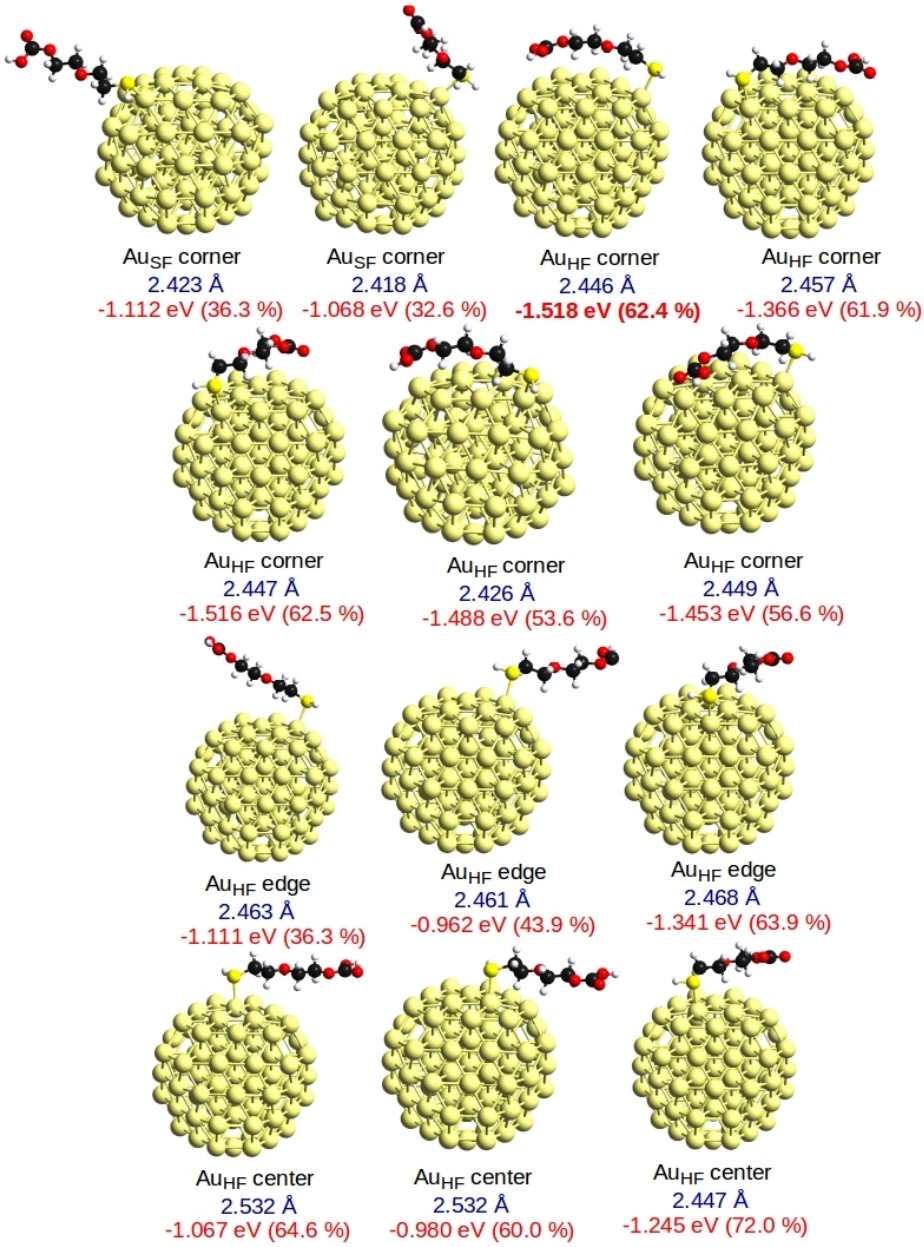

Figure 6.21. *Optimized adsorption structures of one PEG molecule on different top adsorption sites of Au79 (ito) (SF and HF meaning square and hexagonal facet, respectively). The Au-S bond distances are reported in blue characters (Å), whereas the adsorption energies in red characters (eV) (the most stable structure with bold characters).*

Due to the terminal -SH and -COOH moieties of PEG and the various adsorption sites on Au nanoclusters (kink, edge, facet), there exist many adsorption structures. Since S atom is more strongly bound to Au(111) than COOH,[7] the adsorption of PEG on Au nanoclusters has been built mainly through -SH moiety (with a short distance in the range 2.39-2.46 Å, see Figure 6.16 b). However, for isolated chemisorption, an additional stabilizing interaction between -COOH (via -C=O) and Au is obtained in all cases (with a longer distance in the range 2.47-3.16 Å).

According to the best adsorption structures, SH terminal group is always bound on a nanoparticle kink, while COOH moiety can interact with a nanoparticle kink or an edge. The most stable adsorption form is found on Au_{54} (deca) (-1.736 eV, Table 6.1), for which the distortion of the gold nanocluster is significant with an extraction of the interacting Au kink atom from its epitaxial position and a beginning of stellation for the nanoparticle (Figure 6.16 b). The adsorption strength magnitude (1.358-1.736 eV) is compatible with previous theoretical works for alkane-thiols on Au_{20} (-1.16 eV) and Au(111) (-1.54 eV).[6,8] The adsorption of PEG on Au_{55} (ino) is the second best form (-1.623 eV) which results in a strong deformation of the nanorod shape (ino-decahedron) where the (100) facets transform into (111)-type orientations (icosahedron), see Figure 6.16 b. In this latter case, the extraction of the kink interacting Au atom is as spectacular as the one discussed before for Au_{54} (deca). For the three other Au nanoclusters, the adsorption energy is weaker and the gold shape resembles the initial symmetric morphology.

1 PEG	Au_{49} (marks)	Au_{54} (deca)	Au_{55} (ico)	Au_{55} (ino)	Au_{79} (ito)
Grafting density	0.20	0.19	0.16	0.15	0.08
ΔE_{ads}	-1.589	-1.736	-1.358	-1.623	-1.519
ΔE_{disp}	-0.802	-0.632	-0.783	-0.822	-0.948
ΔE_{cov}	-0.787	-1.104	-0.575	-0.801	-0.571
$\Delta E_{def\ AuNP}$	0.044	0.045	0.043	0.057	0.066
$\Delta E_{def\ PEG}$	0.178	0.093	0.125	0.076	0.098
$\Delta E_{int\ PEG\text{-}Au}$	-1.810	-1.874	-1.526	-1.756	-1.683

Table 6.1. *Grafting densities (molec.nm^{-2}) and adsorption energetics of the most stable structures for one PEG molecule on five Au nanoclusters (Figure 6.16). Adsorption energy ΔE_{ads} (eV), decomposed into dispersion ΔE_{disp} (eV) and pure GGA ΔE_{cov} (eV) contributions, or into deformation energy of Au, $\Delta E_{def\ AuNP}$, of PEG, $\Delta E_{def\ PEG}$ (eV) and interaction energy between PEG and Au, $\Delta E_{int\ PEG\text{-}Au}$ (eV) (chemical bonding).*

Due to the simultaneous bonds between the two terminal functions and gold, the PEG ligand tends to bend over the Au nanocluster, in order to optimize the van der Waals forces. This can be understood by the energy decomposition of the adsorption energy into pure-GGA (covalence) and dispersion energetic terms (Table 6.1 and Eq. 6.2). The dispersion energy is predominant over pure-GGA contribution, except for the most stable PEG-Au nanocluster (Au_{54} (deca)). In this latter case, the stabilizing effect of the beginning of nanocluster stellation results in a pure-GGA term almost twice larger (-1.104 eV) than the dispersion energy (-0.63 eV). An alternative way to analyze the trend of adsorption energies is their decomposition into destabilizing (positive) deformation energies (PEG ligand and Au nanocluster) and stabilizing (negative) interaction energies between PEG and Au (chemical bonding). The adsorption energy is essentially due to the chemical bonding between PEG and Au (from -1.874 to -1.526 eV), although its variation does not capture really the one of the adsorption strength. The minority deformation energies are negligible for Au clusters and more significant for PEG, especially on Au_{49}

(marks) (0.178 eV) and Au_{55} (ico) (0.125 eV) where the chain bending is the largest one. For the deformation of Au, the energetic terms are also weak for Au_{54} (deca) and Au_{55} (ino), although the geometric distortion is large with respect to the initial symmetric clusters. These deformation energies have been calculated from the optimal deformed Au nanoclusters (those obtained from adsorption forms). Indeed, those distorted particles are more stable than their equivalent symmetric shapes. The deformation of AuNPs structures upon adsorption are presented later in section 6.5.4.

6.5.2 Monoshells of PEGylated AuNPs

Once the most stable chemisorption forms of one PEG molecule are known, the organic coating composed of monoshells of PEG ligands surrounding GNPs can be built more easily. In the next step, the five typical morphologies of Au nanoclusters have been decorated by a surface density of PEG molecules approaching saturation (Figure 6.22). Due to the difference of surface area and accessible surface Au atoms between all these clusters, the molecule surface (grafting) density varies from one cluster to another one. The explored range is 2.7-5.1 molec.nm^{-2} (Table 6.2), in fair agreement with the litterature.[9,10,11] Although the molecule surface density changes significantly, the surface coverage normalized to the number of surface Au atoms, is equivalent for all the GNPs, in the range 0.40-0.45 ML (less than half monolayer).

In order to reach a complete monoshell of ligands on GNPs, the clusters have been decorated by maximizing the best adsorption forms found previously for isolated PEG, and by completing the organic coating with metastable structures. The optimal PEG monoshells on GNPs have been addressed in Figure 6.22 and corresponding energetics in Table 6.2. From a geometrical point of view, the PEGylated GNPs exhibit different ligand organization from one cluster to another one. In the case of the decahedral shapes (Au_{49} (marks) and Au_{54} (deca)), the ligand arrangements are more symmetric “brushed-type”

(Figure 6.22 a,b), whereas the icosahedral and octahedral clusters (Au_{55} (ico) and Au_{79} (ito)) are decorated by a more disordered "bushy-type" coating (Figure 6.22 c,d,e).

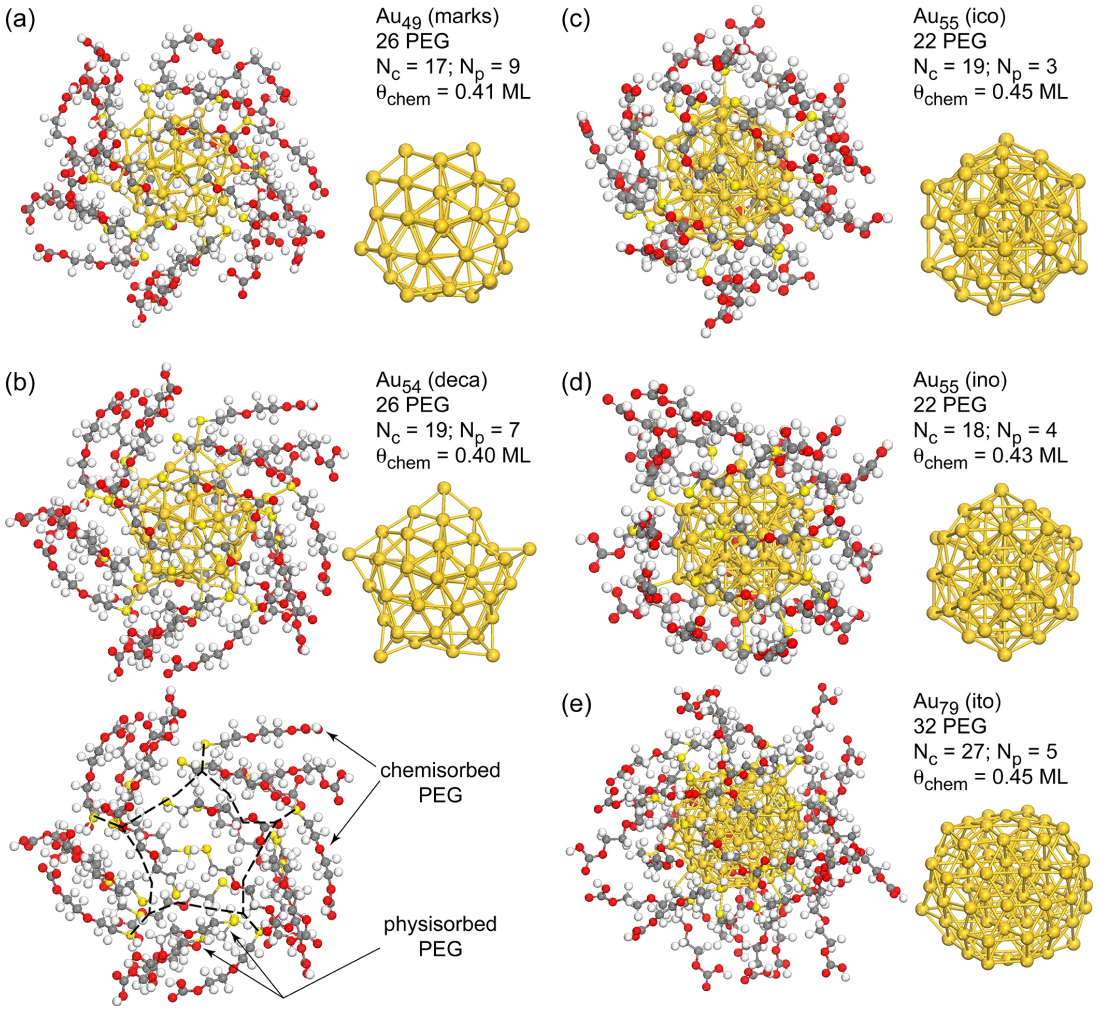

Figure 6.22. *Optimized PEGylated Au nanoclusters with monoshells of adsorbed molecules close to saturation : (a) Marks-decahedral Au_{49}, (b) stellated decahedral Au_{54}, (c) icosahedral Au_{55}, (d) initially ino-decahedral Au_{55} (transformed into icosahedral Au_{55}) and (e) irregular truncated octahedral Au_{79}. Distorted geometries of Au clusters (without PEG) are also presented. For each system the numbers of PEG ligands in the organic coating, of chemisorbed (N_c) and physisorbed (N_p) molecules, the surface coverage* θ_{chem}

related to chemisorbates (ML = monolayer) are mentioned. The stellation (Au_{54}) results in a more organized coating ("brushed-type"), whereas non symmetric deformation (Au_{49}, Au_{55} and Au_{79}) induces disordered monoshells ("bushy-type").

PEG_{sat}	Au_{49} (marks)	Au_{54} (deca)	Au_{55} (ico)	Au_{55} (ino)	Au_{79} (ito)
Grafting density	5.09	4.87	3.44	3.24	2.66
ΔE_{coads} (/PEG_{chem})	-1.933	-1.719	-1.565	-1.569	-1.471
ΔE_{disp} (/PEG_{tot})	-0.754	-0.780	-0.815	-0.791	-0.783
ΔE_{cov} (/PEG_{tot})	-1.180	-0.938	-0.750	-0.778	-0.689
$\Delta E_{int\ PEG\text{-}Au}$ (/PEG_{chem})	-1.269	-1.200	-1.092	-1.224	-1.053
$\Delta E_{def\ AuNP}$ (non normalized)	1.851	2.362	0.884	2.205	2.479
$\Delta E_{def+int\ PEG\text{-}PEG}$ (/PEG_{tot})	-0.506	-0.470	-0.449	-0.382	-0.430

Table 6.2. *Grafting densities (molec.nm^{-2}) and adsorption energetics of the PEGylated SAMs on five Au nanoclusters (Figure 6.22). Coadsorption energy ΔE_{coads} (eV per chemisorbed PEG), decomposed into dispersion ΔE_{disp} (eV per PEG ligand) and pure GGA ΔE_{cov} (eV per PEG ligand) contributions, or into deformation energy of Au, $\Delta E_{def\ AuNP}$ (non normalized), of PEG summed with the PEG-PEG intermolecular interaction energy, $\Delta E_{def+int\ PEG\text{-}PEG}$ (eV per PEG ligand) and into interaction energy between PEG and Au, $\Delta E_{int\ PEG\text{-}Au}$ (eV per chemisorbed PEG).*

The deformation of the metallic nanoclusters has significantly increased with respect to the isolated adsorption. In the case of Au_{55} (ino), the nanorod initial morphology of ino-

decahedron is entirely lost in favor of an icosahedron (Figure 6.22 d). In addition, the stellation induced by the PEG coating on Au_{54} (deca) is remarkably strong (Figure 6.22 b). The PEG ligands separate during the geometry optimizations in two different adsorption families : majority chemisorbed molecules bound through -SH groups to gold and minority physisorbed ligands inside the organic coating bound with other ligands via hydrogen bonds and van der Waals interactions (Figure 6.22 b). The hydrogen bonds can also stabilize cochemisorbed PEG molecules and help the brushed configuration as depicted in Figure 6.22b for Au_{54} (deca).

From an energetic standpoint (Table 6.2), the coadsorption energy per PEG molecule of the PEGylated GNPs is globally similar to the previous adsorption energy values for isolated chemisorption. However, it can be either larger (Au_{49} (marks) and Au_{55} (ico)) or smaller (Au_{54} (deca), Au_{55} (ino) and Au_{79} (ito)) due to the lateral interactions between ligands (lateral effect) and the competition for interacting with the electronic density of gold nanoclusters (coverage effect). For the case of Au_{55} (ino) and (ico), the coadsorption energy per PEG is identical since the ino-decahedron is transformed into icosahedron as explained before. Likewise the isolated system, this energy can be decomposed into pure GGA and dispersion energy terms. Close to ligand saturation, the dispersion energy is slightly more stabilizing than the pure GGA contribution, except, once again, for the systems having the largest coadsorption energy (Au_{49} (marks) and Au_{54} (deca)).

According to the energy decomposition analysis (EDA) in terms of deformation and interaction energies, the interaction energy between PEG and Au nanoclusters per PEG ligand (Eq. 6.13 and Figure 6.1) is globally weakened in the monoshells by comparison with the isolated adsorption (from -1.053 to -1.269 eV). This is clearly a coverage effect linked to the competition between the molecules (gold atoms sharing their electronic density). Surprisingly, the deformation energy of the Au clusters is very large (from 0.884 to 2.479 eV). In order to maximize the interaction with the PEGylated monoshell, all the gold atoms in the cluster undergo a significant deformation with respect to their initial

symmetric positions (Figure 6.22). This means that the distorted geometry of Au in the optimal structures including the PEG ligands is not stable anymore, at the opposite of the isolated chemisorption. The distortion of these clusters is maximal for Au_{54} (deca) (2.362 eV) and Au_{79} (ito) (2.479 eV). In the case of Au_{54} (deca), a stellated cluster is obtained with the five corners of the pentagonal structure extracted from their initial symmetric positions. The global energetic loss coming from the concomitant weakened PEG-Au interaction energy and increased Au deformation energy is balanced by the stabilizing intermolecular interaction energy between the PEG ligands (from-0.382 to -0.506 eV per molecule). This energetic term (Eq. 6.18 and Figure 6.2) is the resulting contribution of weak destabilizing PEG deformation energy and significantly stabilizing dispersion forces and hydrogen bonds between molecules. Hence the apparently unstable stellation (in vacuum) and other deformations of gold structure are promoted by the monoshells of PEG ligands, especially by the lateral molecular interactions.

6.5.3 Hydration of PEGylated AuNPs

In order to further approach realistic conditions for GNPs in the context of radiotherapy, the consideration of the chemical environment of synthesis protecting the metallic nanoparticle (PEGylation) is not enough. The presence of water as a first model of the biological environment is required. Hence in the following, the coadsorption of PEG and water molecules at the surface of gold clusters is described, as well as the solvation of GNPs through the interaction of water molecules with PEG chains.

The corresponding models have been built starting from the optimized monoshells of PEGylated GNPs exposed before, where a large number of water molecules have been positioned around the PEG adsorbates (in average 2 water per PEG chain according to the available free space) through hydrogen bonds and a small number of water molecules have been coadsorbed with PEG (around 10), through oxygen-Au bonds, each time there was enough free space at the surface of the Au nanoclusters. Hence, since PEG

adsorption energy is by far larger than water value, the possibility of expelling PEG by water has not been considered. This leads finally to a water/PEG ratio in the range 2.2-2.4 in the hydrated PEGylated GNP structures. In order to keep the analysis as complete as possible, each of the three typical morphologies (decahedral, icosahedral and octahedral) has been retained by solvating the stellated Au_{54} (deca) GNP (interesting for experiments) and the more spherical Au_{55} (ico) and Au_{79} (ito) stable GNPs. The optimal structures and associated energetic analysis are reported on Figure 6.23 and Table 6.3.

Figure 6.23. *Optimized hydrated and PEGylated Au nanoclusters with monoshells of coadsorbed molecules close to saturation : (a) stellated decahedral Au_{54}, (b) icosahedral Au_{55} and (c) irregular truncated octahedral Au_{79}. Distorted geometries of Au clusters (without the hydrated coating) are also presented. For each system the numbers of PEG ligands and H_2O molecules in the organic coating are mentioned, as well as the number of chemisorbed (N_c) and physisorbed (N_p) PEG and the surface coverage θ_{chem} related to chemisorbed PEG (ML). The hydration of the PEGylated monoshell tends to increase the disordering in the coating of the stellated Au_{54} cluster.*

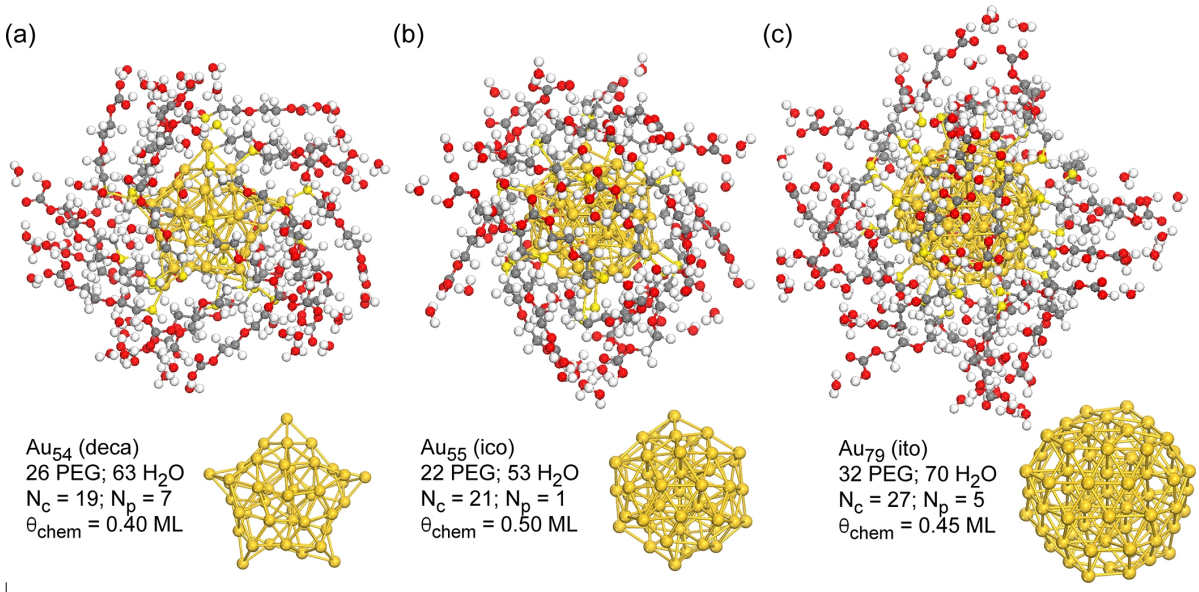

At the structural level, the solvation by water has not changed much the surface coverage of the PEGylated coating, although in the case of Au_{55} (ico), two physisorbed ligands are now chemisorbed. In addition, the large deformation of gold geometry and in particular the stellation obtained for Au_{54} (deca), are also weakly perturbed by water. Water molecules interacting with PEG chains through hydrogen bonds are mainly kept in their building positions, although some of them have relaxed by multiplying hydrogen bonds between themselves, between two PEG chains and also with -COOH moieties (two hydrogen bonds per COOH). These latter water molecules have hindered the direct hydrogen bonding between PEG chains through -COOH; a stabilizing interaction previously found for the non-hydrated PEGylated GNPs. A consequence for Au_{54} (deca) is a disordering in the well-organized "brushed-type" configuration of the organic coating. Initially coadsorbed water molecules on Au nanoclusters have all desorbed during the geometry optimizations. In their physisorbed state, they interact with PEG ligands through hydrogen bonds with either -SH or -C_2H_4-O- groups. Most of these molecules are positioned in a "H-down type" adsorption mode pointing toward Au facets.

Regarding energertics (Table 6.3), the coadsorption energy per chemisorbed PEG for hydrated PEGylated GNPs is globally larger (from -2.88 eV to -3.767 eV) than the values calculated before without water (Table 6.2). This gain is in part due to the significant number of stabilizing additional hydrogen bonds provided by water solvation. This strengthening is also visible on the pure GGA contribution to the coadsorption energy which is now predominant with respect to the dispersion term, as shown in Table 6.3, by comparison with the previous non-hydrated PEGylated GNPs. By decomposing the coadsorption energy in terms of deformation and interaction energies between the three partners (Au, PEG and H_2O), the first remark is related to the equivalent large distortion energy of the metal in the range 1.357-2.122 eV, and the negligible summed deformation and interaction energy for PEG and water alone. For PEG ligands, this is correlated to the cleavage of the hydrogen bonding between -COOH moieties, while for water, this result means that the majority of the molecules form hydrogen bonds with PEG chains (not with themselves), as demonstrated by the interaction energy between H_2O and PEG (from -0.581 to 0.668 eV in average per water molecule, corresponding to 1.71-1.97 hydrogen bonds, or from -1.270 to -1.618 eV in average per PEG, corresponding to 4.3-5.6 hydrogen bonds (Eq. 6.50 and Figure 6.15).

Regarding the interaction energy between water and gold, the calculated values are close to zero and negative, thus meaning that water interacting with gold is physisorbed. For the interaction energy between PEG molecule and Au nanocluster, a positive effect of water solvation is found since they are increased (from -0.94 to -1.14 eV) with respect to the non hydrated cases (from -1.09 to -1.20 eV).

PEG_{sat}-H_2O	Au_{54} (deca)	Au_{55} (ico)	Au_{79} (ito)
ΔE_{coads} (/PEG_{chem})	-3.767	-2.880	-3.138
ΔE_{disp} (/PEG_{tot})	-1.030	-1.050	-1.007
ΔE_{cov} (/PEG_{tot})	-1.722	-1.701	-1.542
$\Delta E_{def\ AuNP}$ (sans norm)	2.122	1.357	1.953
$\Delta E_{int\ (PEG+H2O)-Au}$ (/PEG_{chem})	-1.340	-1.110	-1.147
$\Delta E_{int\ PEG-Au}$ (/PEG_{chem})	-1.114	-0.940	-0.951
$\Delta E_{int\ H2O-Au}$ (/H_2O_{tot})	-0.042	-0.040	-0.039
$\Delta E_{def+int\ PEG-PEG}$ (/PEG_{tot})	-0.033	-0.089	-0.153
$\Delta E_{int\ PEG-H2O}$ (/H_2O_{tot})	-0.736	-0.680	-0.656
$\Delta E_{int\ PEG-H2O}$ (/PEG_{tot})	-1.783	-1.637	-1.436
$\Delta E_{def+int\ H2O-H2O}$ (/H_2O_{tot})	-0.084	-0.078	-0.100
$\Delta E_{int\ PEG-H2O(F1)}$ (/$H_2O(F_1)$)	-0.735	-0.689	-0.673
$\Delta E_{int\ PEG-H2O(F2)}$ (/$H_2O(F_2)$)	-0.905	-0.904	-1.107
$\Delta E_{int\ PEG-H2O(F3)}$ (/$H_2O(F_3)$)	-0.716	-0.817	-0.930
$\Delta E_{int\ H2O(F1)-Au}$ (/$H_2O(F_1)$)	-0.004	-0.029	-0.022
$\Delta E_{int\ H2O(F2)-Au}$ (/$H_2O(F_2)$)	-0.217	-0.162	-0.096
$\Delta E_{int\ H2O(F3)-Au}$ (/$H_2O(F_3)$)	-0.235	-0.108	-0.173

Table 6.3. *Adsorption energetics of the PEGylated and hydrated SAMs on three Au nanoclusters (Figure 3). Coadsorption energy* ΔE_{coads} *(eV per chemisorbed PEG), decomposed into dispersion* ΔE_{disp} *(eV per PEG) and pure GGA* ΔE_{cov} *(eV per PEG) contributions. Second decomposition into deformation energy of Au,* $\Delta E_{def\ AuNP}$ *(non normalized), of PEG summed with the PEG-PEG interaction energy,* $\Delta E_{def+int\ PEG\text{-}PEG}$ *(eV per PEG), of* H_2O *summed with* H_2O-H_2O *interaction energy, (eV per* H_2O*), and into several interaction energies : between hydrated PEG and Au,* $\Delta E_{int\ (PEG+H2O)\text{-}Au}$ *(eV per chemisorbed PEG), between PEG and Au,* $\Delta E_{int\ PEG\text{-}Au}$ *(eV per chemisorbed PEG), between* H_2O *and Au,* $\Delta E_{int\ H2O\text{-}Au}$ *(eV per* H_2O*), between PEG and* H_2O*,* $\Delta E_{int\ PEH\text{-}H2O}$ *(eV per* H_2O *or per PEG). The interaction between PEG and* H_2O *is also decomposed according to three different families (F1, F2, F3) of water molecules hydrating the organic coating (Figure 5). Same thing for the interaction between* H_2O *(F1, F2, F3) and Au.*

6.5.4 Deformation of AuNPs Structures Upon Adsorption & Roundness Degree Analysis

In the following section, the energetics and geometrical properties of the relaxed uncoated GNPs coming from the adsorbed systems are presented. In Figure 6.24, the structures corresponding to the most stable uncoated GNPs after geometry optimizations have been addressed. In the case of the isolated PEG adsorption, there are many possibilities for considering a starting geometry for each nanoparticle (Au_{49} (marks), Au_{54} (deca), Au_{55} (ico), Au_{55} (ino) and Au_{79} (ito)). They come from the various possibilities of stable and metastable adsorption forms reported in section 6.5.1. In the analysis presented here, only the most stable clean GNPs are discussed. For the cases corresponding to monoshells of PEG molecules and for the ones associated with hydrated and PEGylated

configurations, there is only one possibility (in our study) to optimize the uncoated GNPs after adsorption.

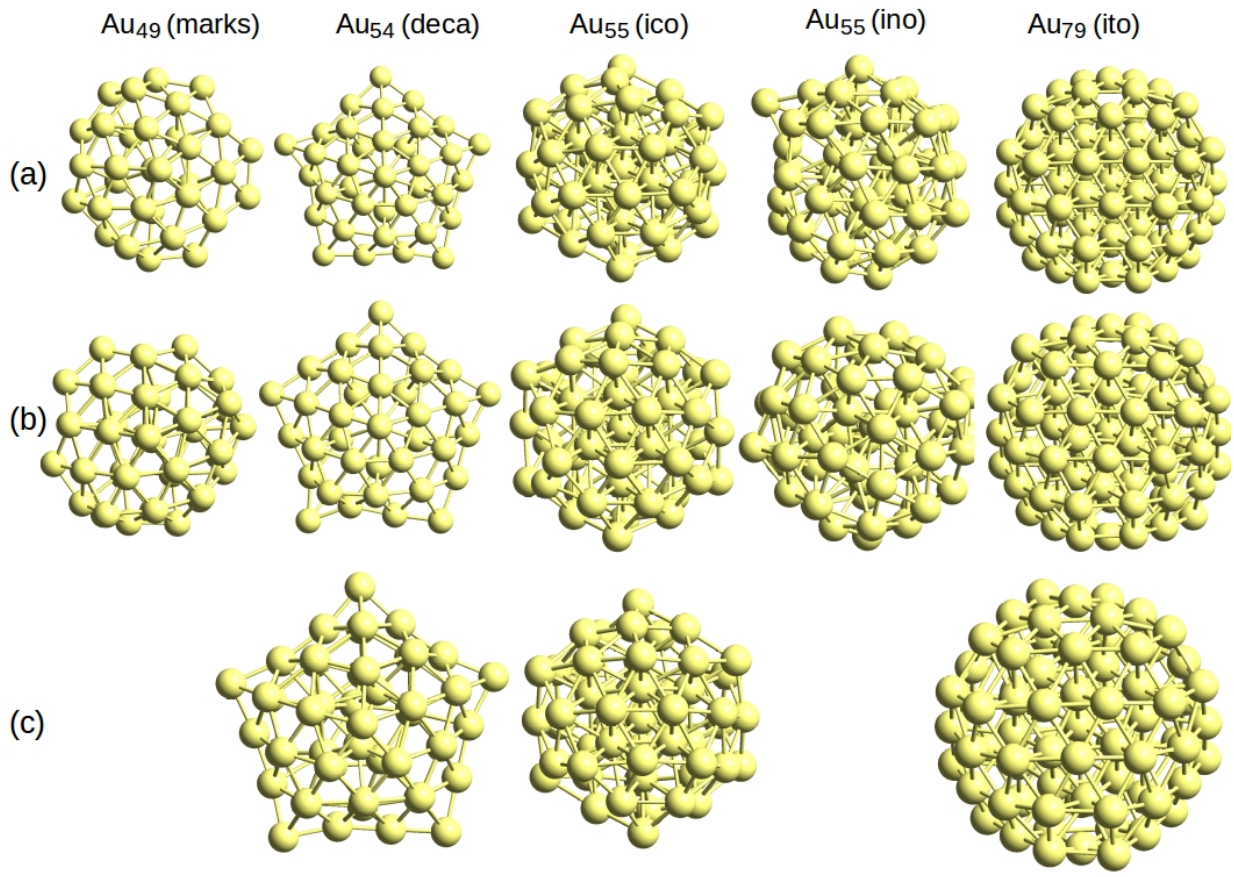

Figure 6.24. *Optimized structures of uncoated GNPs for Au49 (marks), Au54 (deca), Au55 (ico), Au55 (ino) and Au79 (ito) related to (a) isolated PEG adsorption, (b) monoshells of adsorbed PEG molecules and (c) hydrated and PEGylated coatings. The initial geometries for the optimizations are those coming from the relaxed adsorption structures.*

Regarding the induced deformation after geometry optimization, we note that Au_{54} (deca) becomes stellated upon PEGylation. According to Figure 6.25, the average cohesion energy per atom shows that this stellation is stabilizing, except for the hydrated PEGylated case, for which the distortion is too large. Au_{55} (ico) is always slightly deformed by the presence of the chemical environment (PEG and/or H_2O) (same conclusion for Au_{49} (marks)). This deformation is stabilizing as shown in Figure 6.25. In the case of Au_{55} (ino), the chemical environment systematically causes the transformation of the nanocluster into a distorted Au_{55} icosahedral shape. Finally, for Au_{79} (ito), the deformation of the cluster is negligible upon adsorption of PEG and/or H_2O. This results in a quasi-identical cohesion energy per atom, as shown in Figure 6.25.

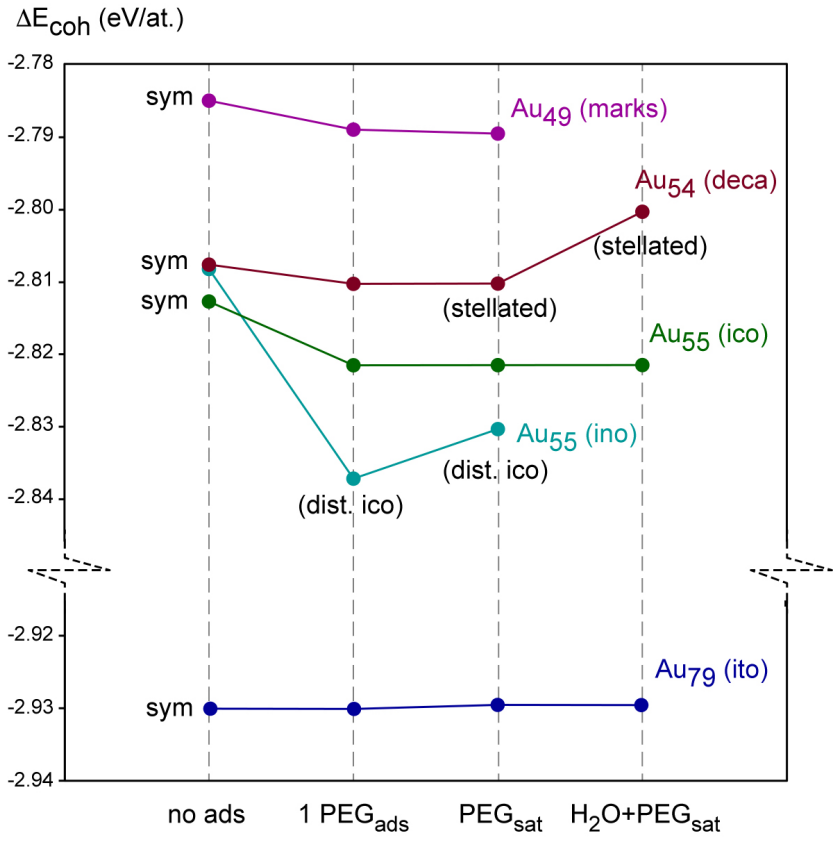

Figure 6.25. *Stability diagram of optimal GNPs against the chemical environment for the initial starting structures. The cohesion energy ΔE_{coh} per atom (eV/at.) has been plotted*

for optimized Au_{49} (marks), Au_{54} (deca), Au_{55} (ico), Au_{55} (ino) and Au_{79} (ito) clean nanoclusters in various conditions for the starting geometries of the optimizations : no adsorption (highly symmetric clusters), one isolated PEG molecule, saturation of PEG adsorbates and hydrated PEGylated monoshells.

In order to evaluate the influence of the PEGylation and hydration on the structure of AuNPs, we introduce the roundness degree S of the nanocluster as follows and likewise in Chapter 5:

$$S = \frac{R^{min}}{R^{max}} \quad \text{[Eq. 6.51]}$$

where R^{min} (and R^{max}) are the minimal (maximal) radius (Å) from the nanoparticle center to the nanocluster relaxed outer shell (after geometry optimization with or without chemical environment). This roundness degree is essentially a positive value in the range [0;1] (dimensionless) : the closer to 1 meaning an optimized nanoparticle outershell approaching the geometry of a sphere; the closer to 0 meaning an outershell approaching the geometry of an ellipsoid.

In order to quantify the influence of the adsorption of the PEG molecules and their hydration on the AuNP structures, we have calculated the variation of the roundness degree ΔS on the basis of the optimized nanocluster outershells with and without the presence of PEG adsorbates (with or without water). The corresponding variation is thus defined as follows depending on the chemical environment :

$$\Delta S = S_{AuNP-1PEG} - S_{AuNP} \quad \text{[Eq. 6.52]}$$

$$\Delta S = S_{AuNP-xPEG} - S_{AuNP-1PEG} \quad \text{[Eq. 6.53]}$$

$$\Delta S = S_{AuNP-xPEG-yH2O} - S_{AuNP-xPEG} \quad \text{[Eq. 6.54]}$$

where $S_{AuNP-xPEG-yH2O}$, $S_{AuNP-xPEG}$, $S_{AuNP-1PEG}$, and S_{AuNP} are the roundness degrees for the complete hydrated PEGylated systems, the saturated PEGylated

structures, the isolated PEG adsorption case and the clean GNP, respectively. When ΔS is positive, the variation of the chemical environment (PEG and/or H_2O) has induced a significant geometric deformation of the nanocluster outershell from its symmetric structure toward a globally rounder shape. At the opposite, when ΔS is negative, the resulting geometric deformation of the nanocluster outershell upon PEGylation and/or hydration is a stretching of the initial symmetric structure along a specific direction (adsorption axis). When ΔS is close to zero, the nanocluster may have been slightly distorted upon PEG and/or H_2O adsorption, however, in average, the deformation is negligible.

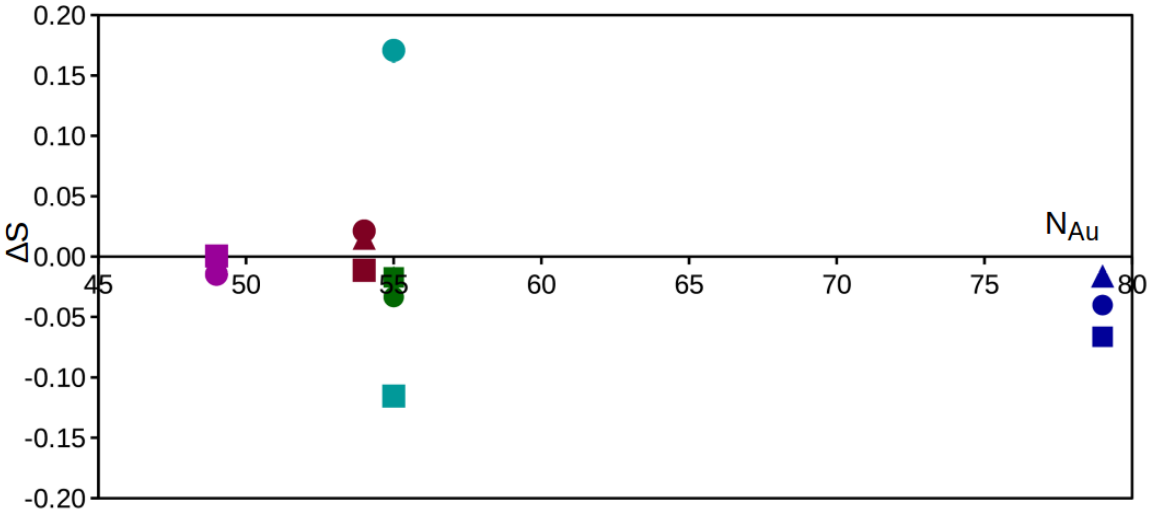

Figure 6.26. *Analysis of roundness degree variation (ΔS) of AuNPs. squares mean ΔS upon isolated PEG adsorption; circles ΔS upon adsorption of PEG monolayer; triangles ΔS upon coadsorption of PEG-H_2O monolayer. The colors in purple, marron, green, cyan and blue correspond to Au_{49} (marks), Au_{54} (deca), Au_{55} (ico), Au_{55} (ino), and Au_{79} (ito), respectively.*

The corresponding results are exposed in Figure 6.26 hereafter. Most of the nanoclusters are weakly perturbed by the chemical environment in terms of variation of roundness degree, except for Au_{55} (ino) with either isolated PEG adsorption ($\Delta S << 0$), due a significant distortion of the cluster along the adsorption axis (Figure 6.24), or with a monoshell of PEG molecules, due to the transformation of its ino-decahedral shape in favor of a distorted icosahedral form ($\Delta S >> 0$).

6.6 Discussion

Once the structural and energetic properties of hydrated and PEGylated GNPs have been described, the next steps are the understanding of the role of the PEG ligand on the stability and the morphology of Au nanoclusters and the determination of the relationship between the coated GNP stability and their use in radiotherapy.

According to the energetic analysis of hydrated PEGylated GNPs, PEG ligands promote the stellation of regular decahedral shape (Au_{54} (deca)). In order to quantify this result and to compare the overall stability of all the coated GNPs, another energetic descriptor is introduced to evaluate the absolute stability of each system. This corresponds to the formation energy obtained by generating the Au nanocluster from isolated Au atoms and by coadsorbing PEG molecules in an aqueous environment (Figure 6.27). This formation energy normalized by the relaxed surface areas of the Au clusters becomes unitary (formation surface energy Γ_{form}).

In Figure 6.27, the absolute stability of all the coated GNPs is then plotted against the molecule surface density calculated by dividing the number of adsorbed PEG ligands by the nanoparticle area. According to this new analysis, the stellated decahedral-based Au_{54} cluster is by far the most stable one in all the considered cases (isolated PEG adsorption, Figure 6.27 a, non hydrated and hydrated PEG coadsorption, Figure 6.27 b). From a more general standpoint, the intrinsic stability of the cluster increases almost linearly with the molecule surface density, and inversely with respect to the nanoparticle size. The

predicted stability order is the following one: Au_{54} (deca) > Au_{55} (ico) > Au_{79} (ito). This counter-intuitive trend is just the opposite of the one calculated in vacuum. The case of Au_{49} (marks) is an exception with respect to this trend in term of size. This is explained by the decrease of the nanocluster area related to the presence of concavities (defects in the Marks-decahedral shape) by comparison with Au_{54} (deca), thus inducing an increase of the molecule surface density. In addition, the number of PEG ligands is constant also due to the defects which do not allow to adsorb more molecules. Hence the stellation process can be linked to a stabilizing structuring ligand effect, since this strongly distorted morphology is unstable in vacuum as explained before. The energy loss related to this metallic deformation is compensated by a small weakening of the interaction energy between PEG and Au and also by a significant stabilizing contribution of the lateral intermolecular interactions (hydrogen bonds). This analysis agrees with experiments showing the high propensity of gold nanoparticles to stabilize in nanostar and nanospike shape.[12,13,14]

Regarding Au_{55} (ico) and Au_{79} (ito) (our models of spherical GNPs), the PEG ligands (hydrated or not) globally keep the shape of the nanoclusters also observed experimentally,[12,13] although they are less stable than the stellated Au_{54} (deca) system. Concerning Au_{55} (ino) (our model of nanorod), the PEGylation has a strong destabilizing effect on this metastable morphology since it transforms into icosahedral shape at this size, in agreement with previous results obtained with a water solvation shell (see Chapter 5).

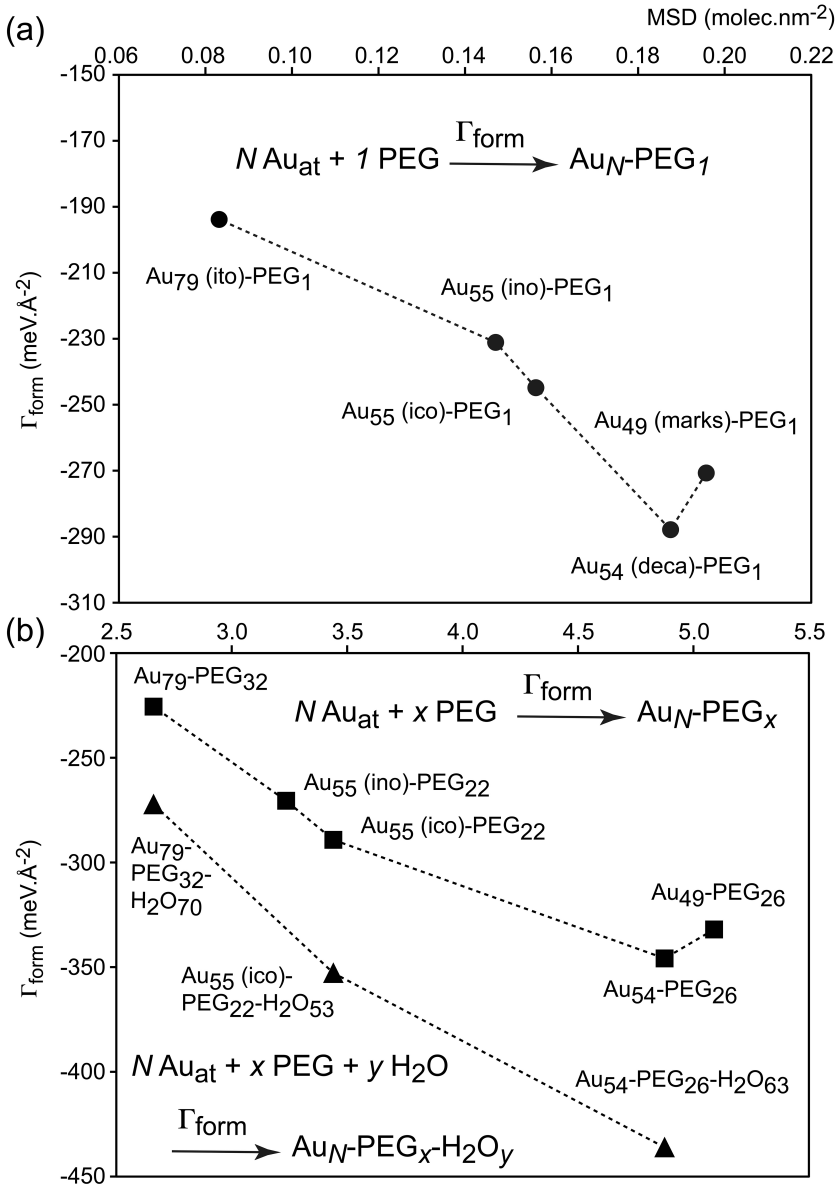

Figure 6.27. *Formation energy* Γ_{form} *expressed in surface energy per particle unit area (meV.Å*$^{-2}$*) of GNPs plotted against the PEG molecule surface density (MSD) (molec.nm*$^{-2}$*). (a) Isolated adsorption of a PEG on five typical Au nanoclusters. (b) (top) PEGylated GNPs (SAM) for the five Au clusters and (bottom) hydrated PEGylated GNPs for the three competitive shapes. The chemical equations are indicated for the corresponding definitions of* Γ_{form}*.*

A relationship between the stability of GNPs and their ability to internalize in the cell (endocytosis) for radiotherapeutic applications can be established since the cellular uptake has been recently correlated with the ligand exchange at the nanoparticle/membrane interface.[2] The physisorbed ligands on the nanoparticle surface can be exchanged more easily with lipidic molecules depending on the adsorption affinity and ligand size. According to other measurements,[12] the cellular uptake varies with the nanoparticle morphology and increases in the order of nanospheres > nanospikes > nanorods. By assuming that the ligand exchange is driving the internalization, an explanation of the change of the uptake performance can be proposed on the basis of our theoretical study, at least for spherical and starred GNPs, since our model of nanorod is unstable at the nanometer size. The energy cost to desorb one ligand from the GNPs can be evaluated by the opposite of the coadsorption energy per PEG ligand, in case of a non-activated process. This energy cost is a good approximation of the ligand exchange with the lipidic membrane since the final state (ligand grafted on the membrane) does not really depend on the nature of the GNP. For non-hydrated GNPs (Table 6.2), the coadsorption energy is the largest one for the stellated Au_{54} (deca) system (-1.719 eV), then come the more spherical systems Au_{55} (ico) and Au_{79} (ito) (-1.565 and -1.471 eV, respectively). Hence the energy cost to desorb one PEG ligand is maximal for the starred Au_{54} (deca) GNP, thus meaning that the ligand exchange will be easier for the more spherical Au_{55} (ico) and Au_{79} (ito) GNPs. As a consequence, according to our analysis at the nanometer scale for gold, the cellular uptake will then be larger for more spherical morphologies such as icosahedral (Au_{55}) and octahedral (Au_{79}) shapes than for the stellated decahedral one (Au_{54}).

Looking at the EDA for non hydrated GNPs (Table 6.2), the reason for the increase of coadsorption energy in the case of Au_{54} (deca) (larger energy cost for exchange) is the larger interaction energy between one PEG ligand and Au (-1.20 eV) with respect to the two other nanoclusters Au_{55} (ico) and Au_{79} (ito) (-1.092 and -1.053 eV, respectively). This theoretical result agrees with measurements[12] and brings a first element of explanation. In

the case of hydrated and PEGylated GNPs (Table 6.3), the trend is identical with systematically larger coadsorption energies (-3.767 eV for Au_{54} while -2.88 and -3.138 eV for Au_{55} and Au_{79}, respectively) and interaction energies between PEG and Au (-1.34 eV for Au_{54} while -1.11 and -0.95eV for Au_{55} and Au_{79}, respectively), by comparison with the previous case, due to a stabilizing solvation effect. The corresponding energy costs are large since in our energetic balance for calculating the coadsorption energy does not include the solvation effect for the references (isolated water and isolated PEG molecules which are considered in the gas phase). The interaction energy (around -1 eV) calculated between PEG and Au (effective chemical bonding without the environment) is more realistic for evaluating the ligand exchange cost.

The concept of physisorbed ligand (less bound to the GNPs) evoked experimentally[2] is not straightforward. Inside the organic coating, all the PEG molecules are not equivalent as explained in the previous section. In the case of Au_{54} (deca), there is a marked difference between chemisorbed PEG ligands at the spikes of the stellated nanocluster (more outside the ligand monoshell or at its periphery) and the other ones, either physisorbed (lying inside the coating with no direct interaction with Au) or chemisorbed on Au inside the organic coating. A detailed analysis of the ligand extraction (Table 6.4) indicates that the energy cost to remove one chemisorbed PEG molecule at the spike of the stellated GNP is however smaller than the one related to a physisorbed PEG lying in the organic coating. Due to all the possible stabilizing interactions (Table 6.3) associated with one PEG ligand (PEG-PEG, PEG-H_2O, PEG-Au), the concept of physisorption should be used cautiously. The ligand extraction energy analysis (Table 6.4) also supports the trends previously discussed for the relative order of interaction energies between PEG and Au.

PEG_{sat}-H_2O	Au_{54} (deca)	Au_{55} (ico)	Au_{79} (ito)
ΔE_{lee} (PEG_{chem})	2.705	2.680	2.310
ΔE_{lee} (PEG_{phys})	3.139	2.786	2.382

Table 6.4. *Ligand extraction energy ΔE_{lee} (eV) related to the removal of one physisorbed or chemisorbed PEG molecule from the hydrated PEGylated GNPs. These energies are endothermic and obtained by single point energy calculations of the complete systems with a missing ligand.*

Although the PEG organic layer is relatively dense, a few water molecules are stabilized inside the coating according to our DFT calculations (Figure 6.23). The ratio between H_2O and PEG molecules increases slightly (from 2.19 to 2.42) with the GNP absolute stabilization (from Au_{79} to Au_{54} (Figure 6.27) and the simultaneous ordering of the ligand monoshell (from "bushy" to "brushed-type"). This stabilizing effect leading to the confinement of a few water molecules at the proximity of the Au nanocluster is quantified by the EDA in terms of interaction energy between adsorbed PEG ligand and H_2O, bonded mainly through hydrogen bonds (Table 6.3).

By defining three subgroups of water molecules in interaction with PEG ligands in the organic layer, depending on the type of hydrogen bonding and location all along the PEG chains, a remarkable trend results from the analysis of interaction energies between PEG and H_2O. The first and majority family of water molecules (F1) interact with the -COOH terminal groups of PEG ligands by two asymmetric hydrogen bonds (Figure 6.28). These molecules are located at the periphery of the organic coating, mostly outside the organic coating, thus explaining the zero interaction with Au clusters (Table 6.3). The average interaction energy between H_2O(F1) and PEG is moderate (-0.735, -0.689 and -0.673eV per water for Au_{54} (deca), Au_{55} (ico) and Au_{79} (ito), respectively) and close to the same energetic term calculated for all the water molecules. However, this interaction energy

increases significantly when water diffuses inside the organic layer to interact with the oxygen atoms of the ethylene glycol chains (see the interaction energy between H_2O(F2) and PEG, from -0.904 and -1.107 eV per water). This means that the PEGylation can promote also the diffusion of water inside the organic coating progressively. This analysis is also supported by the stability of PEG-H_2O gas phase dimers through hydrogen bonds (Figure 6.15). When water molecules approach the surface of the nanoparticle, they position in a "H-down"-type configuration because of the stabilizing interaction between water (F2) or (F3) with Au (from -0.096 to -0.235 eV per water of each family). For the stellated Au_{54} cluster, the further diffusion closer to the metal (via a hydrogen bonding with the thiol group) is also possible although the interaction energy (between H_2O(F3) and PEG, -0.716 eV per water) is slightly weaker than the value at the periphery of the PEG chains (-0.735 eV per water). At the opposite, for the more spherical Au_{55} icosahedral GNP, which has a larger propensity to internalize the targeted cell, the interaction energy (between H_2O(F3) and PEG, -0.817 eV per water) is again larger than the one calculated outside the ligand monoshell (-0.689 eV per water).

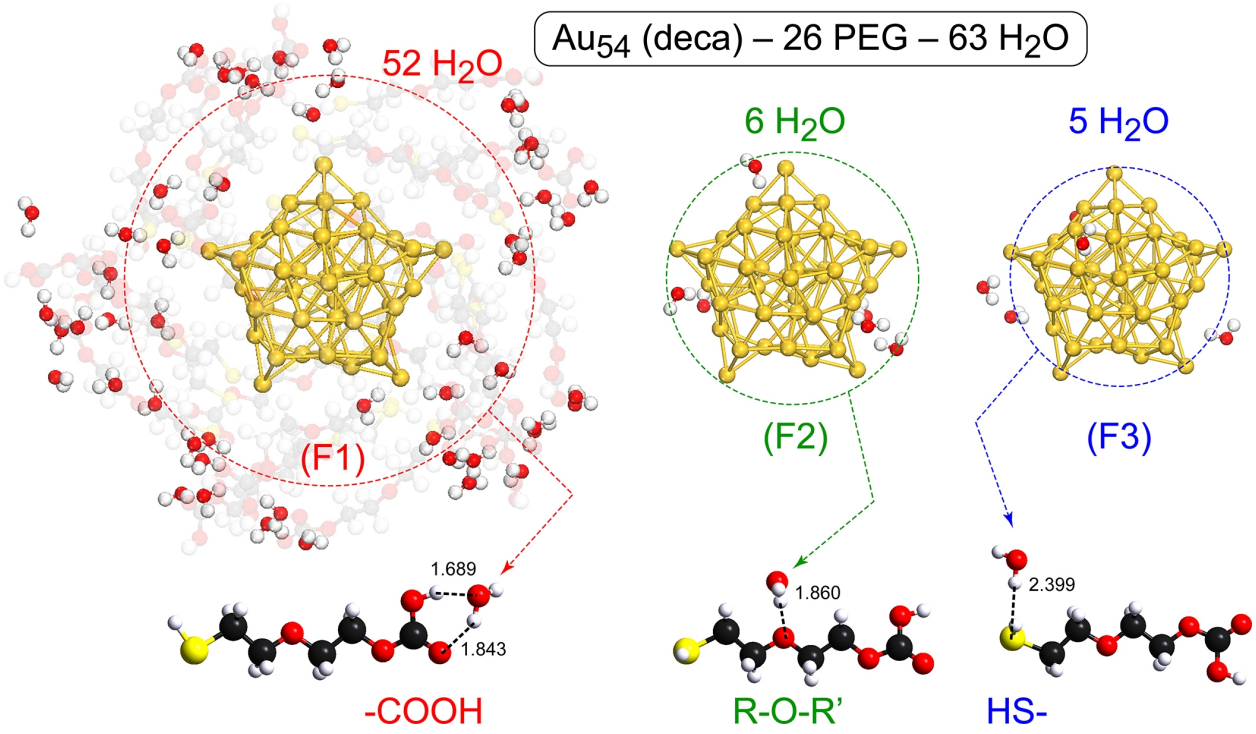

Figure 6.28. *Three families (F1, F2, F3) of water molecules (63 in total) hydrating the optimized PEGylated coating (26 PEG molecules) of the stellated Au_{54} decahedral cluster. F1 family (52 molecules) corresponds to water interacting with the carboxylic ending group of PEG ligands at the periphery of the GNP; F2 family (6 molecules) is related to water interacting with the oxygen atoms of ethylene glycol in the PEG; F3 family (5 molecules) gathers water interacting with thiol moiety in the ligands.*

As a consequence, the PEGylation promotes the confinement of water molecules at the vicinity of gold, especially for the spherical morphologies which exhibit the largest ability to exchange ligands with the membrane and penetrate the cell. This last result opens the discussion of the location of water molecules around the GNPs at the moment of the X-ray irradiation during the radiotherapeutic treatment. Due to their higher stability and vicinity toward the metallic particle, confined water molecules belonging to families (F2) and (F3) can be considered as good candidates for photoexcitation and radiolysis. In fact, the proximity to Au should enhance the photocatalytic activity and the homolytic dissociation of water leading to •OH and •H radical species. Moreover, these species confined inside the PEG chains could also be stabilized by interacting with either dehydrogenated thiol group or the oxygen atoms of the EG moiety. In this perspective, the PEG chains would ensure a dual role by promoting the confinement of water close to gold, and stabilizing concomitantly H• and OH• reactive oxygen species inside the coating, far enough from the biological environment and liquid water, thus avoiding an immediate reverse recombination.

6.7 Conclusion

The PEGylation of several sizes and morphologies of gold nanoparticles has been explored on the basis of density functional theory calculations in the range 1.1-1.3 nm. The role of the PEG chains on the stability and on the shape of the nanoparticle has been discussed in terms of structural and energetic elements.

The stellation of the decahedral nanocluster Au_{54} has been demonstrated and explained by the particular stability of the PEG ligands through stabilizing interactions energies between PEG and Au and between PEG chains (hydrogen bonds). These interactions compensate the large deformation energy required to distort the geometry of the nanocluster. The promoter effect of PEGylation on the starred morphology is also preserved when the gold nanoparticles are hydrated. In this case, the multiple stabilizing interactions between water molecules and PEG chains (mainly via hydrogen bonds) explain the stellation.

A relation could have been established between the stability of the coated gold clusters and their uptake inside the cell. Due to the larger stability of the PEG chains in the case of the stellated hydrated and PEGylated Au_{54} cluster, the energy cost to exchange a PEG ligand with the membrane is expected to be higher than the one predicted for more spherical icosahedral Au_{55} and truncated octahedral Au_{79} clusters. In absolute value, these latter spherical nanoparticles are less stable than the starred Au_{54} cluster in this mixed chemical and biological environment, in favor of a higher propensity to be internalized in the cell. This counterintuitive result is in fair agreement with measurements provided for much larger gold aggregates.

Finally, the stabilized confinement of a few water molecules close to gold has been shown and explained by a second promoter effect of the PEG chains which tend to form stronger hydrogen bonds with water inside the organic coating than outside. This remarkable property of the hydrated PEGylated layer surrounding gold questions the role

of the water confinement on the radiolysis and the generation of reactive oxygen species, in the context of radiotherapy.

References

1. Jokerst, J. V., Lobovkina, T., Zare, R. N., & Gambhir, S. S. Nanoparticle PEGylation for imaging and therapy. *Nanomedicine*, **2011**, 6(4), 715-728.

2. Wang, X., Wang, X., Bai, X., Yan, L., Liu, T., Wang, M., ... & Chen, C. Nanoparticle Ligand Exchange and Its Effects at the Nanoparticle–Cell Membrane Interface. *Nano letters*, **2018**, *19*(1), 8-18.

3. Oh, E., Delehanty, J. B., Sapsford, K. E., Susumu, K., Goswami, R., Blanco-Canosa, J. B., ... & Goering, P. L. Cellular uptake and fate of PEGylated gold nanoparticles is dependent on both cell-penetration peptides and particle size. *ACS nano*, **2011**, 5(8), 6434-6448.

4. Häberlen, O. D.; Chung, S.-C.; Stener, M.; Rösch, N. From clusters to bulk: a relativistic density functional investigation on a series of gold clusters Au n, n = 6,⋯,147. *J. Chem. Phys.* **1997**, 106, 5189– 5201.

5. Ferrando, R.; Fortunelli, A.; Rossi, G. Quantum effects on the structure of pure and binary metallic nanoclusters. Phys. Rev. B: Condens. *Matter Mater. Phys.* **2005**, 72, 085449, DOI: 10.1103/PhysRevB.72.085449.

6. Guesmi, H., Luque, N. B., Santos, E., & Tielens, F. Does the S− H Bond Always Break after Adsorption of an Alkylthiol on Au (111)?. *Chemistry–A European Journal*, **2017**, 23(6), 1402-1408.

7. Santiago-Rodriguez, Y., Herron, J. A., Curet-Arana, M. C., & Mavrikakis, M. Atomic and molecular adsorption on Au (111). *Surface Science*, **2014**, 627, 57-69.

8. Elvis C. M. Ting, Tatiana Popa and Irina Paci, Surface-site reactivity in small-molecule adsorption: A theoretical study of thiol binding on multi-coordinated gold clusters, Beilstein *J. Nanotechnol.* **2016**, 7, 53–61.

9. Santosh Kumar Meena, Claire Goldmann, Douga Nassoko, Mahamadou Seydou, Thomas Marchandier, Simona Moldovan, Ovidiu Ersen, François Ribot, Corinne Chanéac, Clément Sanchez, David Portehault, Frederik Tielens, and Marialore Sulpizi, Nanophase Segregation of Self-Assembled Monolayers on Gold Nanoparticles, *ACS Nano* **2017**, 11, 7371−7381.

10. Denise N. Benoit, Huiguang Zhu, Michael H. Lilierose, Raymond A. Verm, Naushaba Ali, Adam N. Morrison, John D. Fortner, Carolina Avendano, and Vicki L. Colvin, Measuring the Grafting Density of Nanoparticles in Solution by Analytical Ultracentrifugation and Total Organic Carbon Analysis, *Analytical Chemistry*, vol. 84, **2012**, 9238−9245.

11. Jun Lu,a Yao Xue, Rui Shi, Jing Kang, Chao-Yang Zhao, Ning-Ning Zhang, Chun-Yu Wang, Zhong-Yuan Lu and Kun Liu , A non-sacrificial method for the quantification of poly(ethylene glycol) grafting density on gold nanoparticles for applications in nanomedicine, *Chem. Sci.*, **2019**, 10,2067.

12. Ma, N., Wu, F. G., Zhang, X., Jiang, Y. W., Jia, H. R., Wang, H. Y., Jia, H. R., Li, Y.H., Liu, P., Gu, N., Chen, Z. Shape-dependent radiosensitization effect of gold nanostructures in cancer radiotherapy: comparison of gold nanoparticles, nanospikes, and nanorods. *ACS applied materials & interfaces*, **2017**, 9(15), 13037-13048. DOI: 10.1021/acsami.7b01112

13. Justin L. Burta, Jose L. Elechiguerraa, Jose Reyes-Gasga, J. Martin Montejano-Carrizalesc, Miguel Jose-Yacaman, Beyond Archimedean solids: Star polyhedral gold nanocrystals, *Journal of Crystal Growth,* **2005,** 285 681–691.

14. J. M. Cabrera-Trujillo*, J. M. Montejano-Carrizales, J. L. Rodrı´guez-Lo´pez, W. Zhang, J. J. Vela´zquez-Salazar, and M. Jose´-Yacama´n, Nucleation and Growth of Stellated Gold Clusters: Experimental Synthesis and Theoretical Study, *J. Phys. Chem. C* **2010**, 114, 21051–21060.

Chapter 7: Formation and Repair of DNA Lesions

7.1 Introduction

In previous Chapters 4-6, a significant advance has been reported on the theoretical modeling of AuNPs in the context of radiotherapy for cancer treatment. On the basis of DFT models of AuNPs in the range 0.9-3.4 nm, several models have been proposed to describe the stability and the morphology of AuNPs decorated by an organic coating composed of a monolayer of hydrated PEG ligands (around 1 nm). The confinement of a few water molecules inside the organic shell has opened an interesting discussion related to water radiolysis promoted by AuNPs. The description of the reaction pathways and associated mechanism of such a photo-excited process exceeds the scope of the present work since other theoretical methodologies (TDDFT for instance) would be required to explore these properties in a relevant and accurate way. Hence the keys explaining the generation of reactive oxygen species at the proximity of AuNPs will not be given in the context of this thesis. However, first theoretical models of formation and repair of DNA lesions occurring also at the atomic scale can be explored once the radical species have been produced and have diffused from the nanoparticle to another part of the targeted cells (nuclei and DNA). This will be the subject of the last and following chapter of results of this PhD manuscript.

In radiotherapy, ionizing radiation (IR) is used to generate reactive oxygen species (ROS) and induce clustered of DNA lesions of the exposed tumor tissues, leading to apoptosis or necrosis. On the other hand, exposure to IR or the radiation coming from sunlight can be harmful to normal tissues since it cause genetic modifications and promotes carcinogenesis if the DNA lesions are not repaired. Recently, DNA-polyamines cross-links caused by oxidation of hydroxyl radical or singlet oxygen have been characterized in cellular DNA[1], opening the question of the chemical pathway leading to these deleterious lesions. In a recent work, we have characterized owing to classical all-atom molecular dynamics (MD) the interaction between a 16-bp oligonucleotide and three short, most prevalent natural polyamines (putrescine, spermine and spermidine). In

particular, we reported a good correlation of binding free energies between isothermal titration calorimetry (ITC) measurements[2] and our MD simulations. This work has been done in collaboration with Dr. Emmanuelle Bignon and has been published in *Chemistry–A European Journal*.[10] In this chapter, we extend our simulations to propose representative structures for the association pattern between the tris-lysine peptide KKK and i) the trinucleotide TGT and ii) the 15-bp self-complementary oligonucleotide whose sequence d(GCGCGCTGTCGCGCG). In collaboration with Dr. Antonio Monari from University of Lorraine, we also corroborate a mechanistic pathway involving a fast deprotonation of the guanine radical cation followed by hydrogen transfer from the ammonium leaving as a result a nitrogen reactive species that can subsequently cross-link with guanine.

On the other hand, cyclobutane pyrimidine dimers (CPDs), a typical UVB-induced DNA lesion, can formed in four bipyrimidine sequences: T<>T, T<>C, C<>T, C<>C; indeed, due to the strand orientation, C<>T and T<>C are not equivalent. HPLC-mass spectrometry revealed that the fours CPDs are not repaired at the same rate, T<>T are removed more slowly than those containing cytosine.[3] Together with our collaborators from University of Lorraine, we have investigated the dynamic behavior of an oligonucleotide containing the four different CPDs in order to rationalize the experimental observed repair rate by using MD simulations. Specifically, the interaction between a damaged DNA strand and the nucleotide excision repair enzyme DDB1/DDB2, responsible for photolesions recognition is considered. The flipping of CPD lesions from intra-helical to an extra-helical position with or without the presence of repaired enzyme is examined by using the combined metadynamics and extended adaptive biasing force method (meta-eABF). In this project, I have been implied in a first assessment of the collective variable for the extrusion angle, which turns out to be a delicate one. I spend one-month stay in Nancy in March 2018 to become familiar with NAMD and explicit free energy calculations. The MD simulations and free energy calculations are mainly performed by Cecilia Hognon using the local computing

resources of the LPCT Laboratory, I stayed in touch with her when she was re-running the series of MD simulations.

7.2 Methodology

7.2.1 Computational ethods for the project related to guanine-lysine cross link

Explicit solvent, full atom molecular dynamics simulations were performed by using Amber12 software package[4] to explore the conformational landscape of KKK interacting with the a) trioligonucleotide TGT and b) the DNA duplex sequence. The system are build using both tleap and Nucleic acid builder (NAB) package available within Ambertools[4]. Standard Amber force field was applied: ff14SB[5] for KKK and parmbsc1[6] for TGT and 15bp oligonucleotide. For a meaningful description of the system, both macromolecules are explicitly solvated using TIP3P water in a truncated octahedron box with 12 Å buffer. 25 K+ ions were added into KKK-15bp systems, while one chorine Cl^- ion was added into KKK-TGT system to ensure neutrality of the solvation box and obtain a realistic salt concentration. Minimization is performed on those systems including 5000 steps of steepest decent and 5000 steps of conjugate gradient. Then, the temperature was increase from 0 to 300 K in a 30 ps thermalization run, followed by a 1 ns equilibration performed in NTP conditions. During the rest of the simulation, the temperature was kept constant at 300K using the Langevin thermostat with a collision frequency γln equal to $1ps^{-1}$. Particle Mesh Ewald method was used to treat long range interaction by employing a cut off of 9 Å. For KKK-TGT system, four independent trajectories of 500ns were run (thus 2 μs in total): trajectories 1 and 2 was run using a time step of 2fs, where as trajectories 3 and 4 was run using a time step of 4fs thanks to Hydrogen Mass Repartitioning (HMR)[1]. Whereas for KKK-15bp, four independent trajectories were run for 200 or 500ns (see table 7.2 in section 7.3.2, thus 1.4 μs in total): trajectories 1 and 3 was run using a time step of 2fs, whereas trajectories 2 and 4 was run using a time step of 4fs. Cpptraj module was used to perform cluster analysis. It was also used to calculate the

free binding energy based on Molecular Mechanics Generalized Born Surface Area post-processing (MM-GBSA)[9] (same protocol re-adapt from our previous work[10]).

7.2.2 Computational methods for the project related to the repair rates of CPDs

To model the interaction with the repair machinery, we considered the complex crystallized by Scrima et al.[11] (PDB code 4a09). The crystal structure consists of the DDB1-DDB2 complex bound to a 15-bp oligonucleotide containing a T<>T lesion (see Figure 7.1-a). In what follows, we focused on the interaction between DDB2 and DNA, while the DDB1 moiety was removed. This choice is justified by the low resolution for the DDB1 unit[11], due do its greater flexibility, and by the fact that it is not directly involved in DNA recognition and binding[12]. In addition to the T<>T CPD, we also mutated the DNA lesion to include C<>T, T<>C, and C<>C. In the case of isolated DNA and for the sake of simplicity and uniformity, we chose to use the same DNA sequence of the crystal structure, inserting the different CPD lesions (T<>T, C<>T, T<>C, and C<>C) at the central position (see Figure 7.1-b). The sequences were solvated in a TIP3P[7] water box. Potassium (K+) cations were then added to ensure electroneutrality of the simulation box.

Following the same computational protocol described above, the protein/nucleic acid complexes were solvated in a cubic box of water, to which 24 K+ ions were added to ensure electrical neutrality. The protonation states of the DDB2 enzyme were assigned using the Propka program[13]. Standard nucleic acids and amino-acids were modeled using the parm99 force field including the bsc1 correction to the nucleic acids potential[6], while water molecules were treated with the TIP3P potential energy function[7]. The force-field parameters for each CPD have been optimized following the usual Amber antechamber procedure. The atomic point charges were obtained by fitting the quantum-chemical restricted electrostatic potential (RESP)[14]. To that end, calculations at the HF level, using the 6- 31G* basis set, were performed following the RESP protocol. All MD simulations were conducted using the NAMD 2.13 code,[15] using the following protocol: 10,000 steps

of energy minimization, including 5,000 steps of steepest descent and 5,000 steps of conjugate-gradient steps were first performed. Next, the temperature was increased from 0 to 300K in a 30 ps thermalization run, using a Langevin thermostat. The computational assays were then equilibrated during 9 ns in the isobaric-isothermal ensemble (300 K, 1 atm), followed by 200 ns of production run. Particle Mesh Ewald (PME) conditions with a cut off of 9.0 Å were used consistently. The Shake-Rattle-Settle algorithms were employed to constrain bonds containing hydrogens to their equilibrium length. A time step of 2 fs was used to integrate the Newton equations of motion. The DNA global deformation and behavior were analyzed using the Curves+ code[16] to post-process the MD trajectories.

The free-energy profiles along the pseudo-dihedral angle (φe) defining the extrusion of the CPD from the DNA helix[17] were obtained using the combination of the extended adaptive biasing force (eABF) and metadynamics algorithms, coined meta-eABF.[18] The potential of mean force (PMF) calculations were performed scanning the region of the pseudo dihedral between 0 to 140 degrees in a single window. The PMF was calculated for the complex between DDB2 and the four CPD, as well as for the isolated oligonucleotides. Convergence of the PMF was achieved after 100 ns.

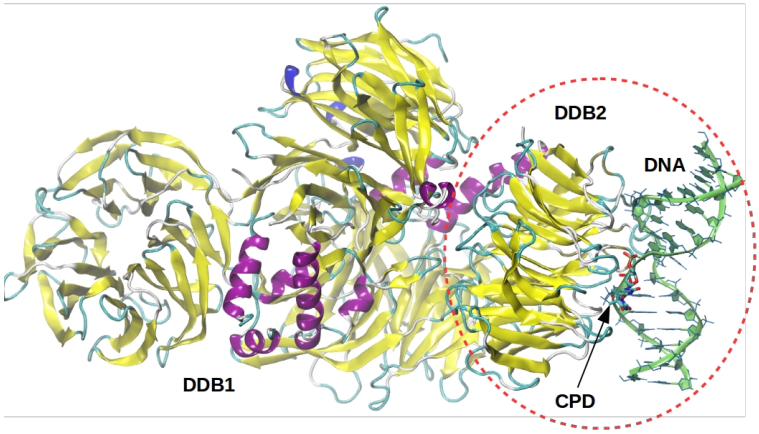

a)

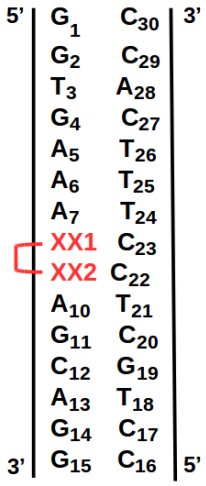

b)

Figure 7.1. *a) Crystal structure of DDB1-DDB2 protein bound to a CPD (T<>T) containing duplex, PDB: 4A09[11]. We only simulated the DNA recognition subunits (DDB2) evidenced with red dashed lines b) DNA sequence containing the CPD lesion (marked as XX).*

7.3 The Association and Chemical Bond Formation Mechanisms of Guanine-Lysine Cross-linking

In the following, the structures and interactions of the trilysine peptide KKK with a TGT trinucleotide and with the TGT-embedded 15-bp oligonucleotide will be presented in section 7.3.1 and 7.3.2, respectively, whereas the mechanistic pathway of deprotonation of the guanine radical cation leading to the formation of nitrogen reactive species is presented in section 7.3.3.

7.3.1 Association Modes between KKK and TGT

First, we investigate the supramolecular association between the tris-lysine peptide KKK (charged +3) and the doubly negatively-charged TGT trinucleotide. This KKK:TGT system has been chosen for performing experiments by one of us[19], with the underlying hypothesis that the structure of this adduct will correspond to the association of the two phosphate groups with the terminal Nε of lysine K1 and K3 (as schematized in Figure 2.3 in Chapter 2). The central side chain of K2 will then remain free to interact closely with the central guanine of the trinucleotide. This working hypothesis was tested along four independent, unbiased molecular dynamics simulations spanning 500 ns each.

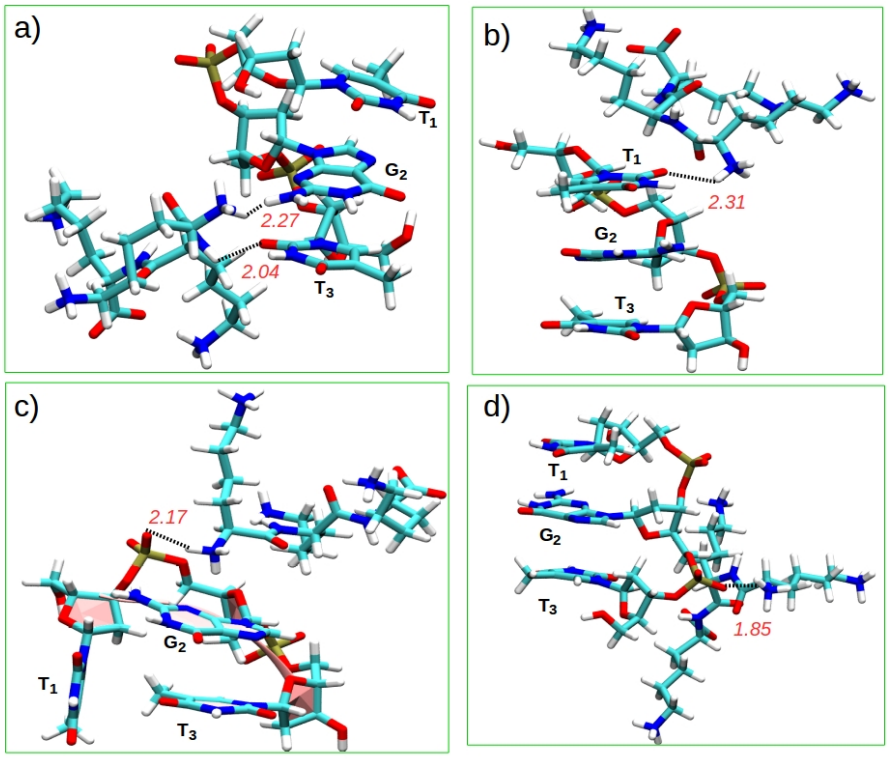

Figure 7.2. *Representative structures for the {KKK:TGT} complex of the four trajectories, obtained as the most prevalent along four 500ns molecular dynamics trajectory after cluster analysis.*

Our simulations reveal a much more dynamical and complex behaviour underlying the coexistence of competitive association patterns. Hence, one can surmise a rather complex and rough free energy landscape with the coexistence of a number of local minima separated by easily accessible barriers, and as a consequence an extended sampling reaching the microsecond scale was performed. Four dominant structures can be identified based on cluster analysis of the four independent trajectories and are represented in Figure 7.2, the percentage of prevalence are given in Table 7.1. Prevalences range between 61% and 69%, denoting a rather complex structural evolution and the co-existence of other structures. To gain insights into the strength of the binding

between KKK and TGT, we estimate binding free energies ΔG with the MMGBSA procedure[9], obtaining the values reported in Table 7.1. They range between -5.5 and -12.2 kcal.mol^{-1} also suggesting the competitive population of different conformations. Importantly, all the structures exhibiting a closer distance between the positively-charged amino groups and the phosphates are found to interact more strongly. However, purely electrostatic interactions are not the only factors regulating the KKK-TGT association. For instance, the ketonic oxygens of thymines T1 or T3 can develop hydrogen bonds with lysines side chain. It is interesting to note that the TGT oligonucleotide can adopt a conformation where T1 lies perpendicularly to T3 (T-shaped orientation shown in Figure 7.2 c) hence a situation in which the stacking of two aromatic nucleobases has been broken, whereas in absence of KKK and in the same conditions of simulations, the isolated TGT system remains in a stacked conformation (see Figure 7.3). The T-shape orientation in Figure 7.1-c is stabilized by a CH···π interactions and a short electrostatic hydrogen bond between the oxygen atom of the phosphate G2 and the amino hydrogen of 3'-end T3 (2.17 Å).

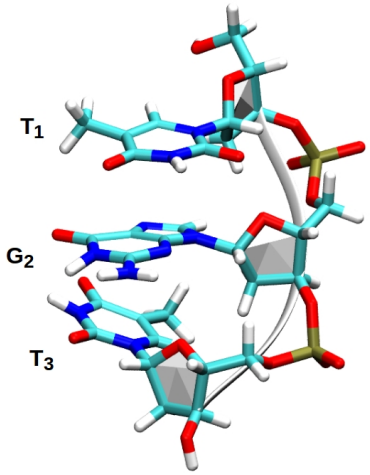

Figure 7.3. *Representative structure of isolated TGT trinucleotide after 200ns of simulation.*

System	Simulation time (prevalence)	$\Delta G^{binding}$ (kcal. mol^{-1})	Occurence of distances d(G/C8…K2/NZ) below 6 Å
Trajectory 1	500ns (65%)	-6.4±5.9	1.2%
Trajectory 2	500ns (65%)	-5.5±3.7	2.4%
Trajectory 3	500ns (69%)	-12.2 ±4.9	4.1%
Trajectory 4	500ns (61%)	-9.8±7.4	1.1%

Table 7.1. *Percentage of prevalence along the simulation time, binding free energy* $\Delta G^{binding}$ *(kcal. Mol*$^{-1}$*) and the occurrence of distance d(G/C8…K2/NZ) below 6 Å.*

Interestingly enough, the interaction of TGT with KKK and its three ammonium side chains, does not always rigidify the oligonucleotide by promoting two ammonium-phosphate interactions, as it was thought experimentally (see Figure 2.3 in Chapter 2). Indeed this case scenario is found only for one of the representative structure extracted from our MD simulation.

The formation of the guanine-lysine cross-link, whose existence was probed experimentally, implies a spatial proximity between the C8 carbon atom of the central guanine G2 and the terminal nitrogen of the central lysine K2. However, along our dynamics, the interatomic distance (G/C8···K2/NZ) rarely reaches values below 6 Å (see Table 7.1, last column). Interestingly, the most stable structure according the MM-GBSA analysis and corresponding to the T-shaped arrangement (Figure 7.2-c) features a higher proximity (4% of structures with an approaching distance below 6 Å). This indicates that the formation of a guanine-lysine cross-link, in addition to the electronic energy barrier could also imply an additional free energy penalty necessary to adopt a pre-arranged conformation more prone to react. However, the KKK:TGT complex is very flexible and

most probably this additional barrier should not exceed very few kcal.mol^{-1}, as also highlighted by the structurally rich landscape explored by the KKK:TGT complex.

7.3.2 Assembly between KKK and an Oligonucleotide

Molecular dynamics were performed using the same computational protocol as in the former case, to investigate the association of KKK to a guanine-rich 15-bp oligonucleotide, hence considering a case in which the oligonucleotides adopt a B-helix conformation in which some moieties such as the ketonic groups of thymines are less accessible to bind with external agents. This situation was sampled with four independent unbiased trajectories spanning a total time of 1.4 μs. The initial configuration is shown in Figure 7.4 where KKK was place near the center of the 15-bp oligonucleotide. After simulations, the four representative structures extracted after cluster analysis one per trajectory, are shown in Figure 7.5.

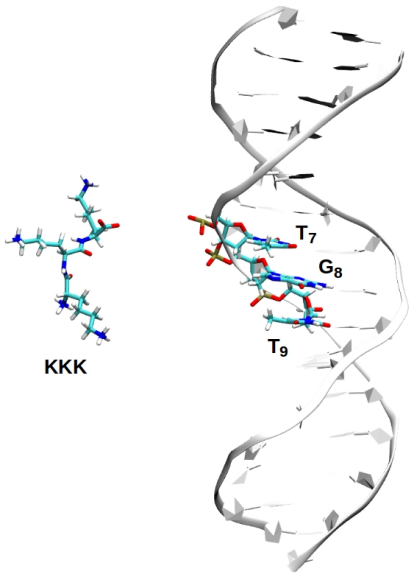

Figure 7.4. *Initial configuration of the 15bp oligonucleotide with the KKK peptide placed near the center of the duplex.*

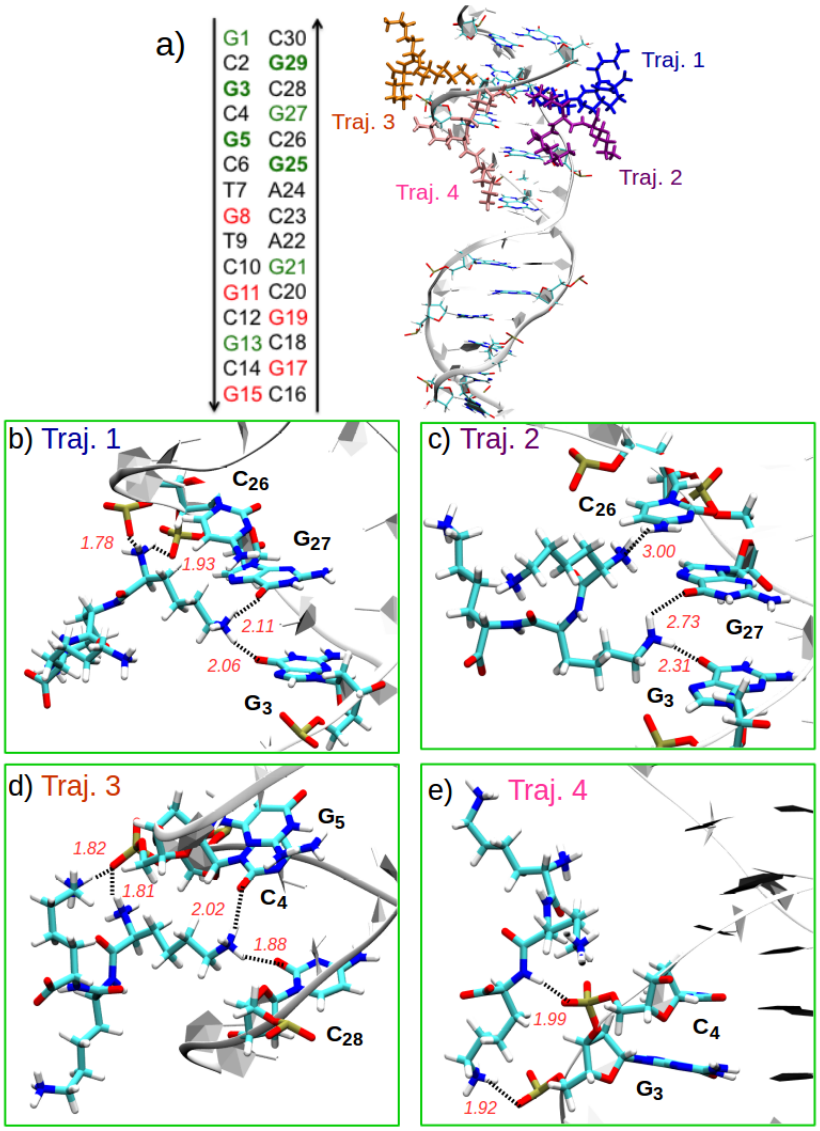

Figure 7.5. *a) Superimposed representation of KKK interacting with the 15-bp oligonucleotide for the four trajectories (color code below). The guanines in red display a low presence of lysines at 6 Å (<2%), whereas guanines in green present a proximity higher than 5% (higher than 10% for boldfaced guanines) b-e) (Zoom) Cartoon representations of four representative structures obtained upon molecular dynamics ranging between 200 and 500 ns (see Table 1) for KKK interacting with a 15-bp oligonucleotide.*

In agreement with the scenario evidenced for the trinucleotide, KKK presents several stable interaction modes with the double-stranded oligonucleotide, as expected from purely electrostatic considerations. The side chain of lysine is flexible enough to develop interactions with several moieties: first and foremost the phosphate groups, but also the ketonic oxygens of cytosine and guanine. We recently reported the same behaviour and non-covalent interaction patterns for other ubiquitous polyamines[10], such as putrescine, spermine and spermidine.

Over the 13 guanines, affinity towards KKK differs significantly, as can be seen from the representation given in Figure 7.5. Almost no interaction is found with the central guanines G8 and G11 (in red), even though KKK has been placed nearby the center of the duplex in the beginning of all the simulations (see Figure 7.4). Other guanines G15, G17 and G19 are cold spot for interaction with KKK. On the contrary, the 5'-end block of six guanines from G1 to G29 presents the highest affinity. Indeed we found along our four simulations that the -NH_3+ terminus of lysines K1, K2 and K3 lies in proximity of only three guanines per strand, namely the guanines G25, G3, G5, G25 and G27 by order of affinity, based on the distance criterion defined previously (also see Table 7.2). Furthermore, the estimated binding free energies, reported in Table 7.2, obtained for the representative structures reported in Figure 7.5 are coherent with the ones of the smaller trinucleotide even if the interaction tends to be more stable. The binding free energy can also be compared with the one estimated for the three biogenic polyamines for a very similar 16-bp DNA sequence with the same computational protocol.[10] Even with a total charge of +2, that happens to be equal to the charge of putrescine but lower than the charges of spermidine and of spermine, KKK develops a stronger interaction with the 15-bp sequence.

On the other hand no clear preference for either the major or minor groove can be clearly pointed out, as can be seen from Figure 7.5. Globally, it is apparent that when interacting with double stranded DNA, KKK still span a relative complex conformational space,

however the structural variability is significantly decreased, and more importantly precise binding site, or more properly guanine hot-spots my be underlined. This preference suggests that cytosines adjacent to guanines favour the binding of the polyamines: a close inspection of the representative structures in Figure 7.5 indeed reveals interactions between the –NH3+ moiety of KKK and the C=O and -NH2 exocyclic groups of cytosine. On the contrary, thymines possess a methyl group that cannot interact through hydrogen bonds with the terminal lysine's charged primary ammonium. Obviously the generality and universality of this sequence effect should to be confirmed for different sequences and with a sufficient sampling.

System	Simulation time (prevalence)	$\Delta G^{binding}$ (kcal. mol^{-1})	Occurence of distances d(G/C8…K2/NZ) below 6 Å
KKK@15-bp			
Trajectory 1	200 ns (98%)	-9.1±5.4	1% G27 Major Groove
Trajectory 2	500 ns (98%)	-13.1±6.7	Major Groove
Trajectory 3	200 ns (92%)	-18.6±7.3	1.2 % G5 Minor groove
Trajectory 4	500 ns (99%)	-14.9±10.1	0.6 % G3 DNA backbone
Polyamines@16-bp[10]			
Putrescine	150 ns (75%)	-7.1±3.7	Major groove
Spermidine	150 ns (92%)	-11.1±6.4	Minor groove
Spermine	150 ns (92%)	-13.5±6.4	DNA backbone

Table 7.2. *Percentage of prevalence along the simulation time, binding free energy $\Delta G^{binding}$ (kcal. mol^{-1}) and the occurrence of distance d(G/C8…K2/NZ) below 6 Å for KKK-15bp system. The same information for polyamines@16-bp system was taken from our previous work*[10].

Furthermore, one should also take into account the different flexibility evidenced by different DNA double-helix sequences that may strongly influence the interaction with KKK and overcome the electrostatic effects evidenced here. We also note that the most stable structure obtained with 500ns of sampling and which is also associated to the highest binding energy (-18.6±7.3 kcal.mol^{-1}) features two ammonium···phosphate salt bridges (Figure 7.5-c).

7.3.3. Reactive Nitrogen Species Production from Guanine Repair by Primary Amines

As it was shown by the classical MD trajectories, the interaction between the DNA and the positively-charged polyamines leads to stable adducts and appears as preferential, on the other hand the deprotonation of the guanine radical at physiological pH is supposed to be favourable and fast. Hence the question arises on the specific chemical mechanisms leading to the formation of guanine-amine cross-links. Even if a full description of the entire mechanism would be out of the scope of the present contribution we focus here on the possibility of the production of reactive species arising from the protonated primary amine (Scheme 7.1). We considered here the possible repair of the G• moiety by hydrogen transfer from the protonated amine group, that will in turn lead to a RNS that could induce the cross-over. This has been done studying by means of static QM and *ab initio* molecular dynamics (AIMD) methodologies a minimal systems composed of G• and the smallest primary amine, i.e. $CH_3NH_3^+$.

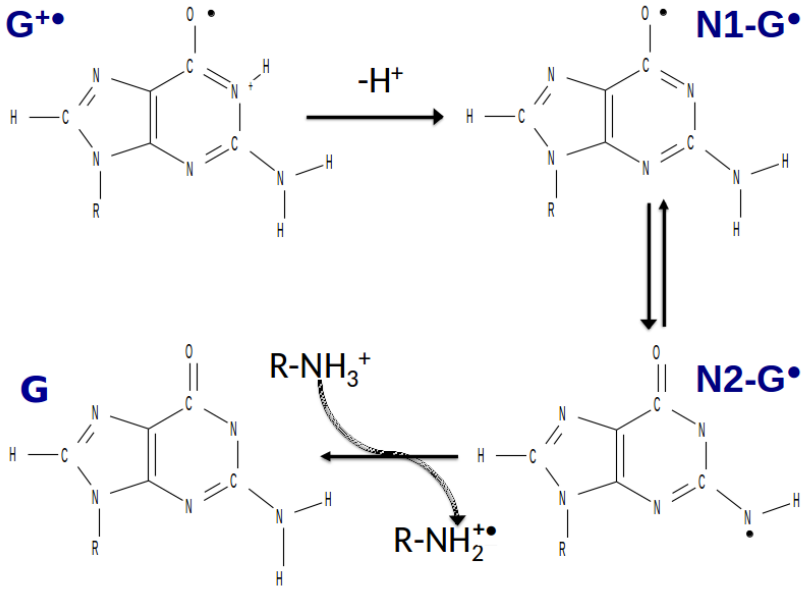

Scheme 7.1. *Reaction mechanisms leading to the deprotonation of the guanine radical cation, the equilibrium between the N1 and N2 form and the subsequent repair from a primary amine, resulting in the production of a reactive nitrogen radical cation.*

Upon deprotonation G• develops an equilibrium between the N1 and the N2 deprotonated forms, hence both possibilities. The repair involving hydrogen transfer to the N1 G• position, while it cannot be entirely ruled out, seems less probable since the reaction is found to be exergonic, as estimated via the rigid rotor approximation. Indeed, at equilibrium geometry the situation in which the radical is centered on guanine has a free energy of about 3.6 kcal.mol^{-1} lower than the CH3NH2$^{+\bullet}$ arrangement. Correspondingly AIMD trajectories starting from the reactants or products get trapped in local minima and show that both arrangements are stable enough to give rise to persistent aggregates.

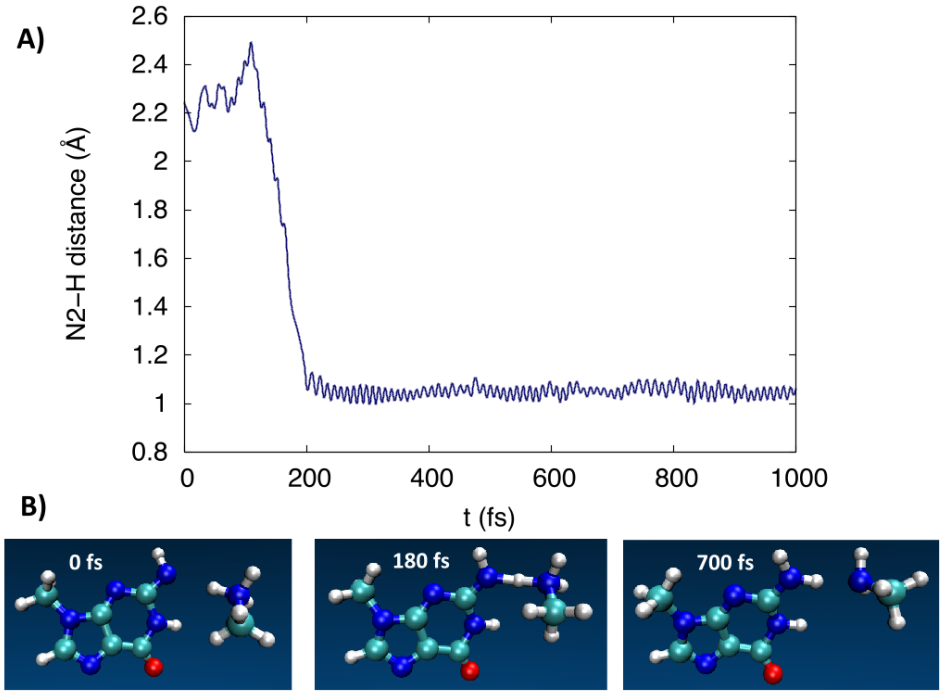

Figure 7.6. *A) Time evolution of the distance between the guanine N2 position and the transferable H during the AIMD trajectory. B) Representative snapshots extracted at the reactants (0 fs), transition state (180 fs) and products (700 fs) region.*

The situation is however, completely different when considering the N2 deprotonated G• isomer. In this case the spontaneous hydrogen transfer from the ammonium -NH3+ group leading to the repair of the guanine lesion is observed. This in turns produces a nitrogen centered radical that can be considered as a RNS and hence potentially leading to the attack at the C8 position. Interestingly enough, the hydrogen transfer is extremely fast and happens in the sub-ps scale, this point out to the fact that the former reaction is basically barrierless. This situation can be appreciated from the results presented in Figure 7.6 where we report the time-evolution of the distance between the G• N2 position

and the transferable H. After a first equilibration step in which the distance is coherent with the one of non covalently-interacting systems (about 2.5 Å) one observes a sharp decrease at around 200 fs followed by the stabilization at about 1.0 Å, and the establishment of the typical N-H vibration pattern indicative of the formation of a new chemical bond. As expected, the same picture is confirmed by the analysis of the localization of the unpaired electron that is localized on the guanine moiety at the beginning of the dynamic and on the amine nitrogen atom after the hydrogen transfer (Figure 7.7). Notably, those results have also been confirmed repeating the AIMD from different initial conditions leading to the same global picture.

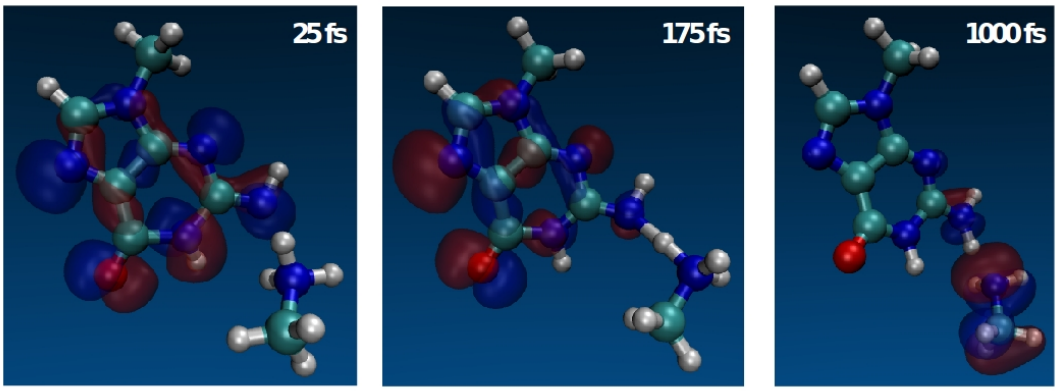

Figure 7.7. *Evolution of the spin density during the AIMD showing the transfer to the unpaired electron from the guanine to the primary amine molecules upon the hydrogen transfer.*

7.4 Repair Rates of Different CPD Sequences and Their Recognition by Repair Enzymes

In the following, I will first present the results of MD simulations and free energy calculations for isolated CPD-containing (T<>T, C<>T, T<>C, or C<>C)

oligonucleotides, following by the investigation of the same DNA sequence in the presence of DDB2 repair enzyme.

7.4.1 Isolated CPD-containing Oligonucleotides

In a first step we investigate the structural distortion of damaged oligonucleotides, featuring T<>T, C<>T, T<>C, or C<>C defects. All the simulations show a global common pattern pointing towards a structural stability and a similar behavior of the damaged strands. In particular, no significant difference either in the structure or in the dynamics of the four damaged- DNA, also compared to undamaged B-DNA[20], was evidenced. In Table 7.3, the DNA bending associated to each CPD lesion is reported, as this descriptor can capture global structural distortion[16]. All the strands experience a relatively moderate average bending, consistent with previous experimental[21] and theoretical works[22,23] and in line with the values measured for undamaged oligonucleotides of the same length. Furthermore, as far as this parameter is concerned the differences between the four lesions do not appear statistically significant and the CPD-containing strands globally behave as the undamaged DNA. The same conclusions can be drawn regarding the analysis of the extrusion angle (φe) of the four CPD lesions (see Figure 7.8 for the definition of reaction coordinate), reported in Table 7.3. Neither significant extrahelical character, nor spontaneous extrusion is observed despite the quite large values of the standard deviations; even though and not surprisingly, in the CPD lesions (φe) spans wider intervals compared to the undamaged oligonucleotide. Free energy profile is also calculated along the flipping reaction coordinate illustated in Figure 7.8 for the damaged-oligonucleotides, the results are presented in Figure 7.9. Indeed, while the minimum energy is previewed for angles centered in between 15 and 20°, the free-energy penalty for spanning the 0-140° region does not exceed 3 kcal/mol. Hence, the analysis of the structure and dynamics of the damaged DNA strands alone does not allow to rationalize the marked differences in the experimental repair rates.

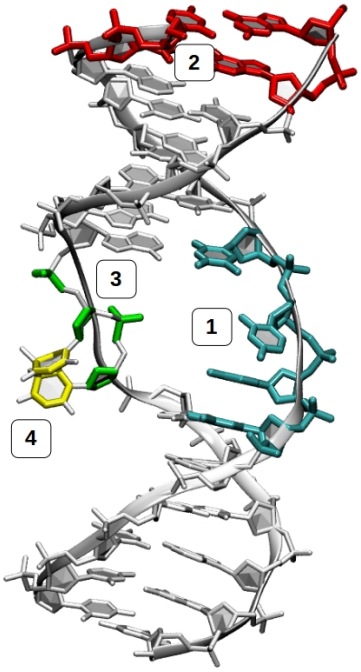

Figure 7.8 *Definition of dihedral angle taken from Zacharias et al.*[17] *in order to describe extrusion of CPD. The dihedral angle is formed by center of mass of four group of atoms: four residues situated opposite of CPD dimers (group 1 in cyan), four nucleotide situated at the end-of oligonucleotide (group 2 in red), backbone heavy atoms of CPD (group 3 in green), and heavy atoms of thymine base of CPD (group 4 in yellow).*

	Bending (in °)	φ_e (in °)
T<>T	27.5 ±16	16.6 ±25
T<>C	44.2 ± 13	23.9 ±16
C<>T	33.6 ±16	22.7 ±23
C<>C	31.6 ±15	10.0 ±22
Undamaged Strand	18.3 ± 9	21.0 ± 4

Table 7.3. *Bending and extrusion angles for isolated DNA. Values are averaged over the MD trajectory with standard deviations, extrusion is reported in correspondence to the CPD. See Figure 7.8 for the description of the extrusion angle.*

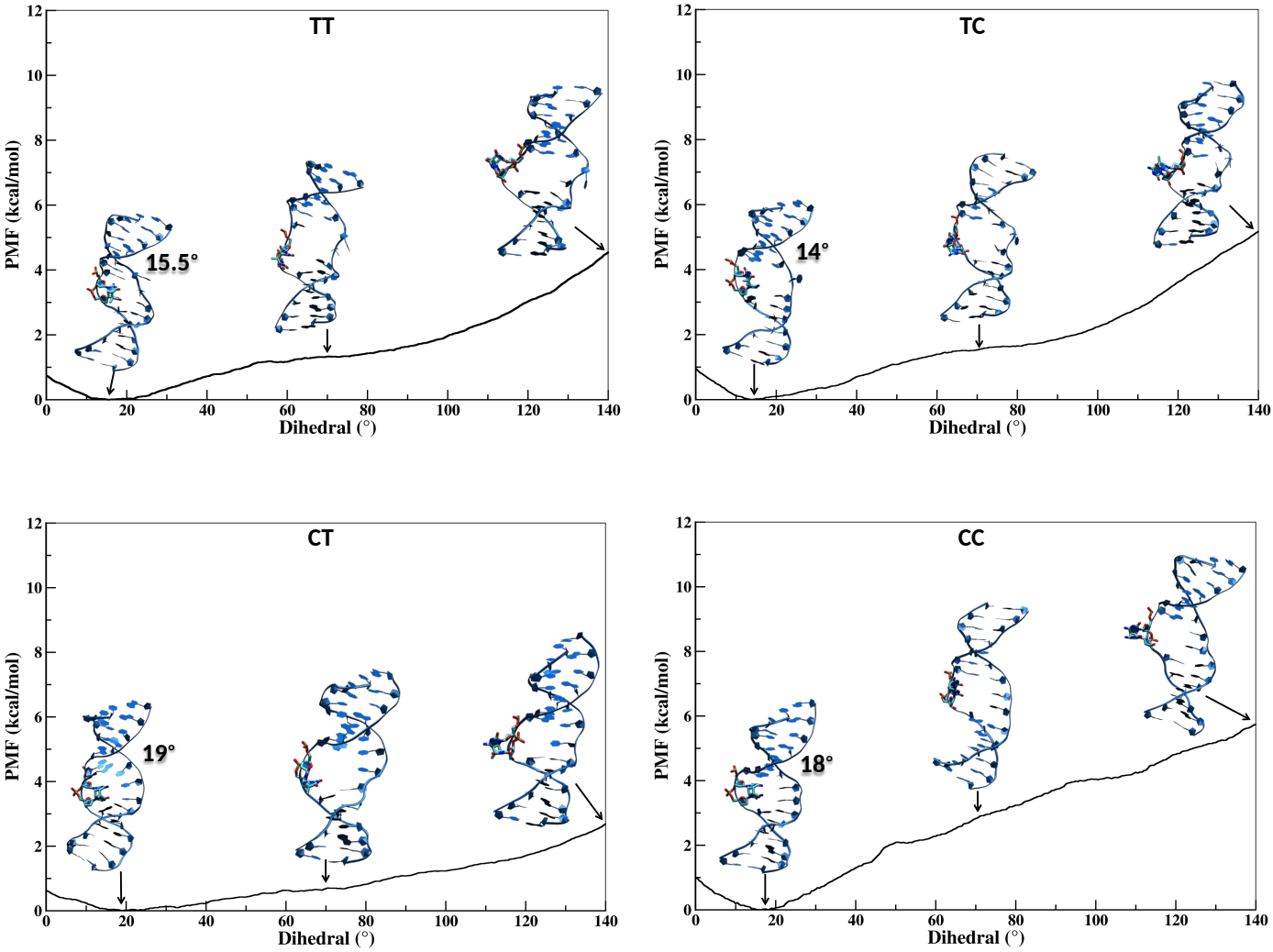

Figure 7.9. *PMF giving the free energy profiles along the pseudo dihedral describing the extrusion of the CPD lesion in the case of T<>T, T<>C, C<>T, and C<>C, respectively in free DNA. Representative snapshots at significant value of pseudo dihedral are shown for each with the value of the dihedral yielding the minimum value of the free energy.*

7.4.2 Interaction of CPD-containing Oligonucleotides with DDB2

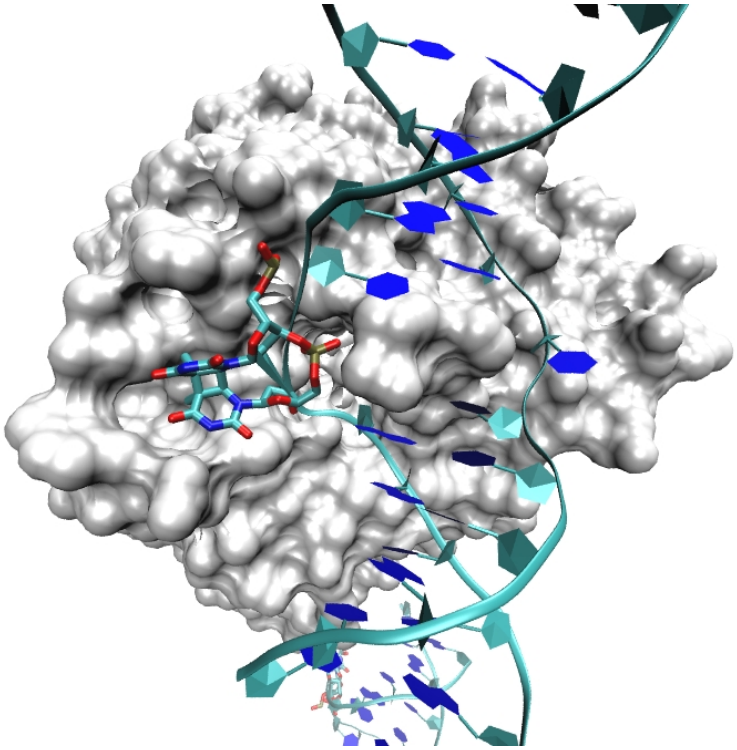

Figure 7.10. *Zoom of the contact region between DDB2 and T<>T as obtained from the crystal structure PDB: 4A09*[11]*. Protein is represented in surface while DNA in ribbon representation. The CPD lesion is evidenced in licorice mode.*

The next step we investigate the interaction of oligonucleotides featuring T<>T, C<>T, T<>C, or C<>C with the DDB2 enzyme. According to the DDB2/DNA crystal structure[11] as depicted in Figure 7.10, the DNA backbone is firmly anchored to DDB2 through the interactions with positively charged amino acids. The CPD lesion is flipped outside the helical structure and is accommodated in a globally hydrophobic pocket. The void in the DNA double helix is compensated by the insertion of a triad of amino acids (Phenylalanine F371, Glutamate Q372, Histidine H373). This interaction pattern, and in particular the CPD extrusions, is also accompanied by an important deformation of the DNA strand and by the formation of a bulge in its structure, allowing its recognition and

hence triggering the NER repair process. The results of the calculation of the free-energy profile along the flipping reaction coordinate (φe) however complement this picture.

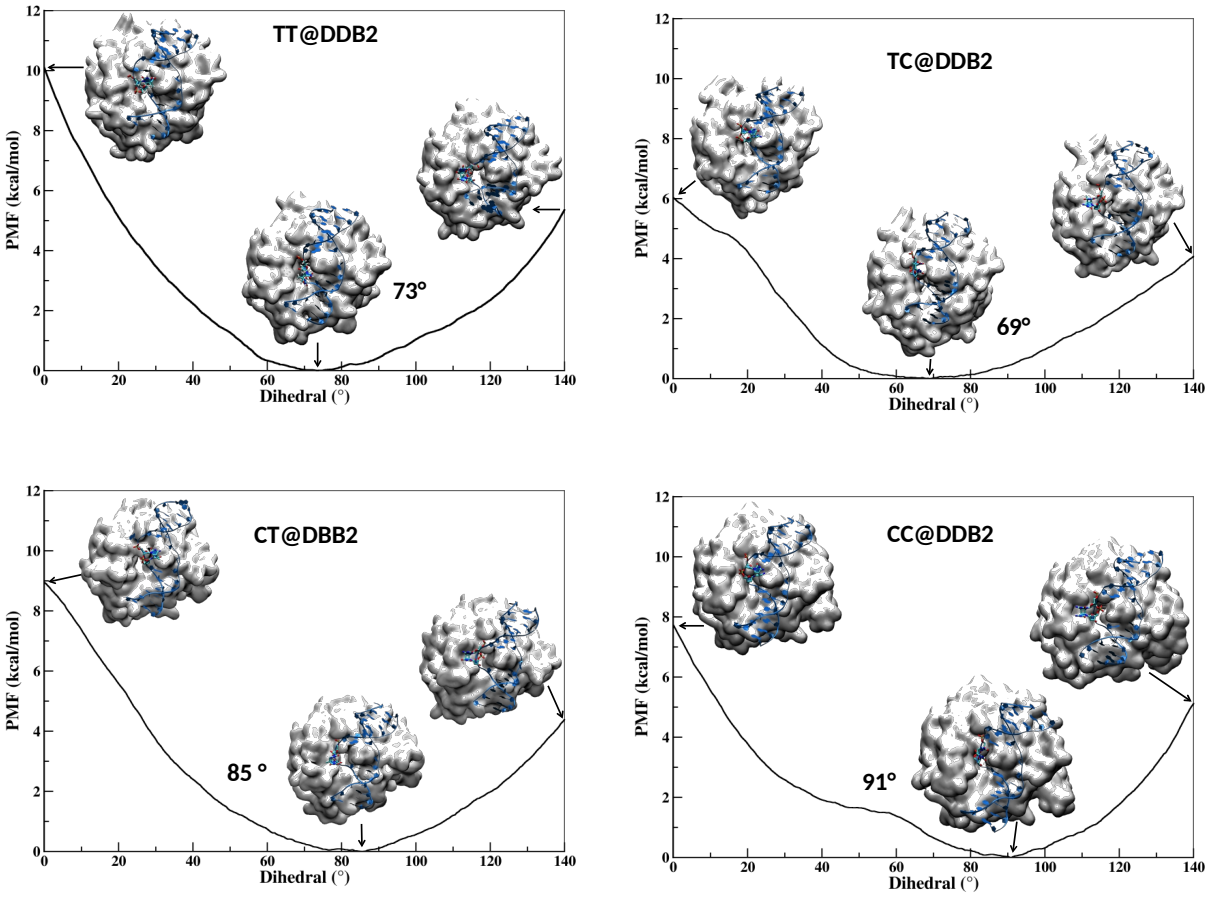

Figure 7.11. *PMF giving the free energy profiles along the pseudo dihedral φ_e describing the extrusion of the CPD lesion in the case of T<>T, T<>C, C<>T, and C<>C, respectively bound to the DDB2 protein. Representative snapshots at significant value of φ_e are shown for each of the complexes together with the value of the dihedral yielding the minimum value of the free energy.*

In Figure 7.11, the four different CPD give similar free energy profile along the φe coordinate leading to the extrusion of the lesion. Interestingly enough for the four considered cases the free energy profile can be represented by a quasi harmonic function of the pseudo dihedral variation. The free energy spanned during the extrusion process are also quite similar among the different CPDs and are of the order of 10 kcal/mol, which represent a considerable increase compared to the values observed for the isolated nucleic acids. Also a considerable shift of the equilibrium position of φe for the DDB2-bound as compared to the solvated DNA structures can be highlighted with the protein definitively stabilizing the extruded position of the lesion. However, subtle but significant, differences can be observed for the strand bearing a thymine or a cytosine in 5' position. Indeed 5'-C oligomers, i.e. C<>T and C<>C, show minimum free energy for larger values of φe at around 90°, while in the case of T<>T and T<>C the minimum in the free energy profile is observed at around 65°-70°. Hence, we shown that the presence of a cytosine at the 5' end of the lesion induces a more extruded configuration, in consistent to the one observed in the crystal structure of the DNA/DDB2 complex.

In order to rationalize the results of the PMF, and in particular the role played by the 5'-C, a analysis of the non-covalent interactions taking place between the protein and the CPD defect in the binding pocket is performed. In Figure 7.12, one can recognize a pattern of favorable interactions that can lock the CPD lesion, and whose strength can vary considerably depending on the 5'-residue. Specifically, the arginine R214 is involved in the stabilization of the DNA/protein interactions. In particular, one can notice that the interaction with the arginine's extremity may be favored by the presence of an exocyclic amino group $-NH_2$ on the 5'-cytosine that results in a more favorable interaction than the one with the methyl group of Thymine. In Figure 7.12 we report the correlation between the extrusion angle φe and the distance between the NH2 group of R214 and the DNA base counterpart. φe at 20°, i.e. at the free DNA equilibrium R214 is quite distant from the nucleobase and both T<>T and C<>T lesions behave similarly.

However, when the CPD is extruded significant differences between the two lesions are evidenced, and in particular C<>T shows the population of shorter distances than T<>T, indicating stronger and more stabilizing interactions. Moreover, the spread of the distances for T<>T is more important than for C<>T with in addition the former also presenting a double branched profile. All those factors once more correlate well with the observed repair rate.

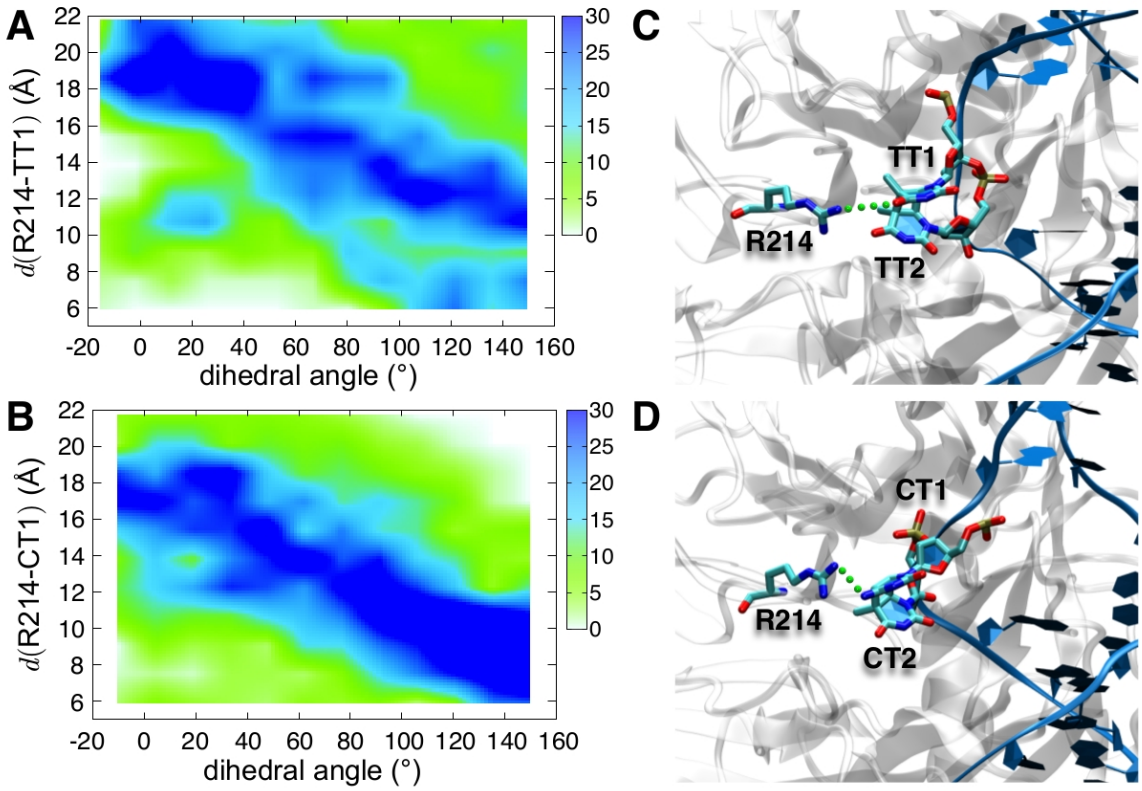

Figure 7.12. *Correlation between the dihedral angle defining the CPD extrusion and the distance between the guanidium group of the R214 residue and the 5' CPD nucleobase for T<>T (A) and C<>T (B). The specific atoms between which the distance has been calculated are specified in the C and D panel for T<>T and C<>T, respectively.*

7.5 Conclusion

In this chapter, we have examined the formation, damage recognition and/or repair of two types of DNA lesions by mean of theoretical modeling, mostly based on classical molecular dynamics with insights from implicit or explicit free energy calculations. In the first project, the binding of KKK towards a trioligonucleotide TGT and towards a 15-bp double-stranded DNA sequence has been fully investigated owing to molecular dynamics simulations. Our study reveals a more complex interaction pattern than for relative small amines. Indeed, and unlike aromatic drugs and photosensitizers, the conformational landscape of aliphatic or peptidic amines interacting with DNA is more delicate to capture, and leads to the coexistence of different structures and competitive binding modes that could be show significant binding free energies and may be separated by barriers of different magnitudes. In any case, and coherently with the results obtained for natural occurring polyamines, it appears that the binding driving force is mostly due to electrostatic interactions, and hence the positive protonated ammonium form, that is also the most abundant one at physiological pH conditions, is required to induce a strong binding. Furthermore, even if no clear preference is observed for minor or major groove binding, our results indicate that the KKK polypeptide is not exploring the DNA space uniformly. Instead it clearly shows a preference for some hot spots suggesting non trivial sequence effects guiding the association and thus the overall reactivity. Globally our results, while confirming the possible interactions also stress out the structural differences between KKK interacting with TGT or with a B-DNA oligomer. Even though the polyamines tails are flexible enough to induce specific interactions with the self-organized helical DNA including ketonic oxygen of cytosine and guanine.

The results of the classical MD, unequivocally point out that charged primary amine leads to favourable interactions with both model oligonucleotides and B-DNA sequences. Hence, this consideration raises the question of the reactivity leading to the formation of cross-links upon guanine oxidation. While the fast deprotonation of the guanine radical

cation is nowadays unambiguous, the outcome of the deprotonated radical is still a matter of more debate. In this study we clearly show that the guanine radical, especially for the N2 deprotonated isomer, can be readily repaired by hydrogen transfer from a primary ammonium group through a favourable and intrinsically barrierless reaction. This occurrence will however lead to the production of a reactive radical cation centered on the primary amine that will then be able to react to the G8 position of the nucleobase and determine the cross-link.

Our results also allow to clarify the experimental preference for the reaction with nitrogen derivatives, leading to cross-link, compared to the reaction with water, leading to the formation of 8-oxoG. Indeed, and despite the obvious predominance of water compared to amines, not only we have shown that the latter form rather protective arrangements leading to a possible water exclusion, but also that the cross-link reactivity is favoured by the preliminary repair of oxidized guanine that is indeed not possible for water.

In the second project, we have performed MD simulations combined with meta-eABF free energy calculations to rationalize the difference in the repair rates of the four CPDs (T<>T, C<>T, T<>C, or C<>C) evidenced experimentally in different cell types. The impact of the CPD lesions on the intrinsic structural behavior of the isolated DNA strands does not provide any rationale for a differential repair rate. Indeed, all the considered strands containing CPDs exhibit a similar dynamical behavior. On the contrary their interactions with the DDB2 enzyme responsible for triggering the repair processes show marked differences, as evidenced by the different free energy profiles. Indeed, for lesions containing a T in 5’ position the extrusion of the CPD is smaller than for the strand presenting 5’ C. This behavior, for the 5’-end thymine containing strands can be rationalized in terms of weaker non-covalent interactions with the amino-acids in the recognition pocket due to the lack of amino groups, and the presence of the electron richer methyl groups. As a consequence, the global structure of the DNA strand is less

affected, and in particular present a less prominent kink and bulge that are considered as checkpoints for the NER machinery to trigger the subsequent repair.

Note that the difference in the structure observed for the T<>T complex between the crystal structure and the MD may also be due to the close crystal packing that will hamper the CPD from repositioning. This situation is indeed reversed in the case of C<>C and especially C<>T containing strands. In this case the interactions in the pocket become much stronger and the CPD is stabilized in the extruded position, as evidenced by the larger value of φe providing the minimum in the free energy profile.

Our results, thanks to the combination of high-level simulation techniques and enhanced sampling protocols, provide new information on the molecular factors guiding the repair efficiency against DNA photolesions. Indeed, we show that the interaction of C<>T and C<>C strands with the DDB2 enzyme leads to much better recognized clusters, hence correlating with the observation that in skin, as well as in fibroblasts and keratinocytes the fastest removed CPD lesions are the ones presenting a cytosine at the 5’-end.

References

1. Bai, J., Zhang, Y., Xi, Z., Greenberg, M. M., and Zhou, C. Oxidation of 8-Oxo-7,8- dihydro-2-deoxyguanosine Leads to Substantial DNA-Histone Cross-Links within Nucle- osome Core Particles. *Chemical Research in Toxicology,* **2018**, 31, 1364–1372.

2. Kabir, A., & Kumar, G. S. Binding of the biogenic polyamines to deoxyribonucleic acids of varying base composition: base specificity and the associated energetics of the interaction. *PLoS One*, **2013**, *8*(7), e70510.

3. Mouret,S., Charveron,M., Favier,A., Cadet,J. and Douki,T. Differential repair of UVB-induced cyclobutane pyrimidine dimers in cultured human skin cells and whole human skin. *DNA Repair (Amst).*, **2008**, 7, 704–712.

4. D. Case, AMBER 12, University of California, San Francisco **2012**.

5. Maier, J. A., Martinez, C., Kasavajhala, K., Wickstrom, L., Hauser, K. E., & Simmerling, C. ff14SB: improving the accuracy of protein side chain and backbone parameters from ff99SB. *Journal of chemical theory and computation*, **2015**, 11(8), 3696-3713.

6. Ivani, I., Dans, P. D., Noy, A., Pérez, A., Faustino, I., Hospital, A., ... & Portella, G. Parmbsc1: a refined force field for DNA simulations. *Nature methods*, **2016**, *13*(1), 55.

7. Jorgensen, W. L., Chandrasekhar, J., Madura, J. D., Impey, R. W., & Klein, M. L. Comparison of simple potential functions for simulating liquid water. *The Journal of chemical physics*, **1983**, 79(2), 926-935.

8. Hopkins, C. W., Le Grand, S., Walker, R. C., & Roitberg, A. E. Long-time-step molecular dynamics through hydrogen mass repartitioning. *Journal of chemical theory and computation*, **2015**, *11*(4), 1864-1874.

9. Genheden, S., & Ryde, U. The MM/PBSA and MM/GBSA methods to estimate ligand-binding affinities. *Expert opinion on drug discovery*, **2015**, 10(5), 449-461.

10. Bignon, E., Chan, C. H., Morell, C., Monari, A., Ravanat, J. L., Dumont, E. Molecular Dynamics Insights into Polyamine–DNA Binding Modes: Implications for Cross-Link Selectivity. *Chemistry–A European Journal*, **2017**, *23*(52), 12845-12852.

11. Scrima,A., Fischer,E.S., Iwai,S., Gut,H. and Thoma,N.H. The Molecular Basis of Crl4(Ddb2/Csa) Ubiquitin Ligase Architecture, Targeting, and Activation. *Cell*, **2011**, 147, 1024.

12. Stoyanova,T., Roy,N., Kopanja,D., Raychaudhuri,P. and Bagchi,S. DDB2 (damaged-DNA binding protein 22) in nucleotide excision repair and DNA damage response. *Cell* Cycle, **2009**, 8, 4067–71.

13. Bas,D.C., Rogers,D.M. and Jensen,J.H. Very fast prediction and rationalization of pKa values for protein-ligand complexes. *Proteins Struct. Funct. Genet*., **2008**, 73, 765–783.

14. Wang,J., Cieplak,P. and Kollman,P.A. How well does a restrained electrostatic potential (RESP) model perform in calculating conformational energies of organic and biological molecules? *J. Comput. Chem.*, **2002**, 21, 1049–1074.

15. Phillips, J.C., Braun,R., Wang,W., Gumbart,J., Tajkhorshid,E., Villa,E., Chipot,C., Skeel,R.D., Kalé,L. and Schulten,K. Scalable molecular dynamics with NAMD. *J. Comput. Chem.*, **2005**, 26, 1781–1802.

16. Lavery,R., Moakher,M., Maddocks,J.H., Petkeviciute,D. and Zakrzewska,K. Conformational analysis of nucleic acids revisited: Curves+. *Nucleic Acids Res.*, **2009**, 37, 5917–5929.

17. Knips,A. and Zacharias,M. Both DNA global deformation and repair enzyme contacts mediate flipping of thymine dimer damage. *Sci. Rep.*, **2017**, 7, 41324.

18. Fu,H., Zhang,H., Chen,H., Shao,X., Chipot,C. and Cai,W. Zooming across the Free-Energy Landscape: Shaving Barriers, and Flooding Valleys. *J. Phys. Chem. Lett.*, **2018**, 9, 4738–4745.

19. Perrier, S., Hau, J., Gasparutto, D., Cadet, J., Favier, A., and Ravanat, J.-L. Characterization of Lysine-Guanine Cross-Links upon One-Electron Oxidation of a Guanine-Containing Oligonucleotide in the Presence of a Trilysine Peptide. *Journal of the American Chemical Society,* **2006**, 128, 5703–5710.

20. Gattuso,H., Assfeld,X. and Monari,A. Modeling DNA electronic circular dichroism by QM/MM methods and Frenkel Hamiltonian. *Theor. Chem. Acc.*, **2015**, 134.

21. Wang,C.I. and Taylor,J.S. Site-specific effect of thymine dimer formation on dAn.dTn tract bending and its biological implications. *Proc. Natl. Acad. Sci.*, **1991**, 88, 9072–9076.

22. Dehez, F., Gattuso, H., Bignon, E., Morell, C., Dumont, E. and Monari, A. Conformational polymorphism or structural invariance in DNA photoinduced lesions: implications for repair rates. *Nucleic Acids Res.*, **2017**, 45, 3654–3662.

23. Cooney,M.G. and Miller,J.H. Calculated distortions of duplex DNA by a cis, syn cyclobutane thymine dimer are unaffected by a 3’ TpA step. *Nucleic Acids Res.*, **1997**, 25, 1432–1436.

24. Lo,H.L., Nakajima,S., Ma,L., Walter,B., Yasui,A., Ethell,D. and Owen,L.B. Differential biologic effects of CPD and 6-4PP UV-induced DNA damage on the induction of apoptosis and cell-cycle arrest. *BMC Cancer*, **2005**, 5, 135.

25. Hu,J., Adebali,O., Adar,S. and Sancar,A. Dynamic maps of UV damage formation and repair for the human genome. *Proc. Natl. Acad. Sci.*, **2007**, 10.1073/pnas.1706522114.

26. Gattuso,H., Durand,E., Bignon,E., Morell,C., Georgakilas,A.G., Dumont,E., Chipot,C., Dehez,F. and Monari,A. Repair Rate of Clustered Abasic DNA Lesions by Human Endonuclease: Molecular Bases of Sequence Specificity. *J. Phys. Chem. Lett.*, **2016**, 7.

Conclusions and Perspectives

This thesis is devoted to theoretical modeling of the electronic properties of AuNPs (in a biological and chemical model environment as well as in vacuum) which are promising radiosensitizers intended to be used for enhancing radiotherapy performance in the near future for cancer treatment. In this experimental context, ionizing radiation mainly induces water radiolysis and produces reactive oxygen species (ROS), DNA damage and cell apoptosis. An amplification of ROS yield can be achieved in the presence of high-Z AuNPs. In our theoretical approach we have first considered the effect of water solvation on the relative stability of AuNPs, as a first model of the natural biological environment, in order to provide a better insight of water/AuNP interface for water radiolysis. The role of synthesis PEG ligands in the context of water radiolysis and the internalization of PEGylated AuNPs have been investigated in this thesis. Various size and morphology of AuNPs are considered at the density functional theory (DFT) level. Furthermore, the formation and repair of DNA lesions are also investigated by molecular dynamics (MD) simulations to rationalize experimental data and to improve our understanding concerning their importance related to cancer.

In Chapter 4, we have modeled six morphologies of AuNPs in vacuum with the size ranging from 0.9 to 3.4 nm. DFT calculations have been performed to investigate the relative stability of those optimized polyhedras by evaluating two descriptors available in the theoretical community: normalized cohesion energy and excess energy. By using the first descriptor, we have compared the stability of AuNPs by ordering the slopes and the offsets of the linear laws capturing the stability against $N^{-1/3}$ (N being the number of Au atoms). Truncated octahedra (to) have the most stable offset based on normalized cohesion energy, followed by icosahedra (ico) and Marks-decahedra (marks). The trend coming from the cohesion energy is, however, different from the one resulting from the calculation of excess energy. This latter showed that the AuNPs are competitive

energetically in the size range of 1-2 nm, above 2 nm, the stability follows the order: to > marks> ico. Apart from these discrepancies, both normalized cohesion energy and excess energy are not observable, therefore their predictive power with respect to the experiments is questionable. In the end of Chapter 4, we have proposed a new descriptor, nanoparticle surface energy, which is observable and has been measured, with a model to determine nanoparticle surface area at DFT level. The corresponding results have shown that the NP surface energy do not vary much when the size increases, in qualitative and quantitative agreement with recent measurements. Our analysis of AuNPs stability has thus reopened the discussion about the relevance of theoretical descriptors and their validation with respect to experiments.

In Chapter 5, in order to provide a first model describing the influence of the natural biological environment, we have explored the adsorption behavior of water on different size and shape of AuNPs with a static approach. The adsorption of isolated water molecule is first investigated, then the AuNPs are saturated on their surface by a complete and explicit water solvation shell. The most stable adsorption of one water molecule on various morphologies of AuNPs (0.9-1.8 nm) indicates that in general, corner is the preferential adsorption site and the strength of water binding is rather moderate and varies with the nanoparticle size and shape. Similar conclusions can be drawn for the adsorption of truncated octahedra AuNPs of larger size (0.9-3.6 nm). Regarding now the effect of the solvation shell surrounding AuNPs in the range 0.9-1.8 nm, the average adsorption energy per water molecule is quite constant regardless of size and shape of AuNPs, and is approximately twice stronger than the isolated adsorption, due to the formation of stabilizing hydrogen bonds (2 in average) between water molecules. Our static approach is also able to capture the transformation of metastable nanoclusters in vacuum: ino-decahedral NP (Au_{55} and Au_{147}) into corresponding icosahedra which are more stable through the interaction with water shells. At the end of this chapter, we have proposed electrostatic potential calculated at the DFT level for these solvated AuNPs model, in order to improve future parametrization of Monte Carlo Simulations developed

by our colleagues IPNL (Pr Michël Beuve and Floriane Poignant). The main results of Chapter 4 and 5 were published in the *Journal of Physical Chemisty Letters (*DOI*: 10.1021/acs.jpclett.8b03822).*

A more complex model and a more realistic chemical environment surrounding AuNPs have been further considered in Chapter 6, that is to say the simultaneous explicit hydration and PEGylation on AuNPs at the atomic level around 1 nm. At this NP size, in the case of the Au_{54} (deca), the PEG coating can deform significantly the NP geometry and extracts the corner atoms from their epitaxial position, leading to the formation of a stellated nanocluster. The stellation is possible due to the intermolecular stabilizing interactions of hydrogen bonds between PEG ligands or between PEG and water. The average interaction energy of PEG ligands with this stellated Au_{54} is relatively larger than the one obtained for more spherical shape of AuNPs (Au_{55} (ico) and Au_{79} (ito)). In agreement with experimental trends of cellular uptake of nanoparticle, a larger energy cost is thus needed in the case of Au_{54} (deca) to desorb PEG ligands and exchanging them with cell membrane, which is an important process responsible for the internalization of AuNPs. Finally, the PEGylation promotes the confinement of a few water molecules, at the proximity of the nanocluster, inside the organic layer. Such confinement occurs via stronger hydrogen bonds with thiol or ethylene glycol groups than those occurring outside the coating on the carboxylic moieties. To conclude, for radiotherapy applications, the PEG coating protects the metallic nanoparticles and makes them biocompatible and stable but also promotes the confinement of water molecules near the NP, which is desirable for photoexcitation and radiolysis to generate free radicals.

Finally in the last chapter of results, two projects are performed by using MD simulations in order to gain structural information of DNA lesions and their repair, two properties very difficult to characterize experimentally. In the first project, we have investigated the interaction mode of trilysine peptide with guanine-rich oligonucleotide, in which the binding affinity could provide insight in the initiation of lysine-guanine cross-links, if the

guanine of DNA is oxidized into radical cation. Our simulations with a sufficient long sampling have shown that several association modes are possible, with most of the binding driving force being the electrostatic interactions. The presence of neighboring cytosines has been identified as a factor favoring KKK binding with DNA. In the second project, MD simulations and free energy calculations are performed to interpret the experimental repair rate measurements of four CPD photo-lesions: T<>T, T<>C, C<>T, and C<>C. Their interaction with a recognition enzyme is examined at the atomic level. We have shown that T<>T and T<>C are displaced from the recognition binding pocket, hence hampering optimal repair, in contrast to C<>C and C<>T which experience excellent interaction with the repair protein interface. The free-energy calculations of CPD extrusion also correlate well with the experimental repair rate. Both projects were performed in collaboration with our coworkers from University of Nancy.

On the basis of the theoretical results obtained in this thesis, several perspectives can be considered to further investigate AuNPs models especially for providing a deeper understanding at the atomic level of the contribution of AuNPs to radiosensitizing effects, and of their catalytic role on water radiolysis before the diffusion of ROS into the cell and DNA lesions. The size range of AuNPs accessible by our DFT calculations is limited to 4 nm. The relative stability of AuNPs at larger size could be further evaluated by using Monte Carlo simulations, with a refinement of the parametrization of semi-empirical potentials based on our DFT calculations including dispersion. The interaction of AuNPs with the cell membrane as a function of their size and morphology could also be investigated by using coarse-grained molecular dynamics, not only to better understand the process of ligand exchange and endocytosis, but also to validate our static DFT model. In addition there is a gap between our solvated and PEGylated AuNPs models with the mesoscale Monte Carlo simulations developed by our colleagues at IPNL, in order to provide an accurate description of the photo-excitation of water molecules leading to the production of free-radicals. The use of our DFT based electrostatic potential could improve our understanding at this level. The study of water radiolysis at

TD-DFT level could also be a future challenge and follow-up project. Unfortunately performing TD-DFT calculations based on our AuNPs models would be computationally too expensive. A new collaboration has to be set with experts of TD-DFT calculations using powerful computational resources, in order to study the homolytic dissociation of water molecule in the presence of AuNPs embedded in a realistic biological and chemical environment. Finally, the structural of dynamical properties of DNA lesions such as protein-guanine cross-links and CPD in the nucleosome can be further investigated by our MD simulations, since few experimentally crystallized structures of such systems containing the lesion are already available in the literature and provide good starting structures for our calculations.

Chen-Hui CHAN's CV

Publications

1) Bignon, E., Chan, C. H., Morell, C., Monari, A., Ravanat, J. L., Dumont, E. Molecular Dynamics Insights into Polyamine–DNA Binding Modes: Implications for Cross-Link Selectivity. *Chemistry–A European Journal*, **2017**, 23 (52), 12845-12852.

2) Chan, C. H., Poignant, F., Beuve, M., Dumont, E., Loffreda, D. A Water Solvation Shell can Transform Gold Metastable Nanoparticles in the Fluxional Regime. *J. Phys. Chem. Lett.*, **2019**, 10 (5), 1092-1098.

3) Chan, C. H., Poignant, F., Beuve, M., Dumont, E., Loffreda, D. The PEGylation of Hydrated Gold Nanoparticles Promotes Stellated Clusters and Water Confinement inside the Organic Coating, 2019, to be submitted.

4) Hognon, C., Chan, C. H., Chipot, C., Douki, T., , Dehez, F., Ravanat, J.L., Dumont, E., Monari, A. Elucidating the different repair rates of cyclobutane pyrimidine dimers in DNA oligomers and their recognition by repair enzymes, 2019, to be submitted.

5) Chan, C. H., Monari, A., Ravanat, J.L., Dumont, E. Guanine-lysine cross-linking: characterizing the association and chemical bond formation mechanisms from molecular dynamics, 2019, to be submitted.

6) Iachella, M., de Morais, R.F., Chan, C. H, Loffreda, D. Introducing Composition-Stability Relations for Ordered Nanoalloys by Means of Surface Energy, 2019, to be submitted.

7) Poignant, F., Charfi, H., Chan, C. H, Dumont E., Loffreda, D., Testa E., Gervais B., Beuve M. Monte Carlo study of the free radical production under keV photon irradiation in the presence of gold nanoparticles. PartI: macroscopic scale. 2019, to be submitted.

Oral communications:

1) DocScilor (15/6/2017, Nancy, France)

2) PhD day (8/6/2018, Laboratoire de Chimie, ENS de Lyon)

3) GdR NanOperando (28/11- 30/11/2018, Lyon, France)

4) GdR SolvATE (4/2- 5/2/2019, Lyon, France)

Posters:

1) Forum CLARA (4/4/2017, Lyon, France)

2) Or-Nano (12/6-14/6 2017, Nancy, France)

3) WATOC (27/8 – 1/9/2017, Munich, Allemagne)

4) DNA Damage and Repair: Computations Meet Experiments (30/10- 3/11/2017, Leyde, les Pays-Bas)

5) International Workshop on Radiation Damage to DNA (27/5 – 1/6/2018, Aussois, France)

6) Gold 2018 (15/7-18/7Juillet 2018, Paris, France)

Formation and experience :

1) Winter School: Tutorials in Theoretical Chemistry (23/1- 2/2/2017, Luchon-Superbagnières, France)

2) Séjour dans le laboratoire SRSMC (5/3 -31/3/2018, Nancy, France) : 4 semaines

3) Writing scientific articles more clearly in English : 6h

4) Recherche et industrie : les enjeux de la Propriété Intellectuelle: 12h

5) Initiation à la production de documents sous LaTeX: 3h

Appendix A : Optimized Structures of Isolated Water Adsorption on AuNPs

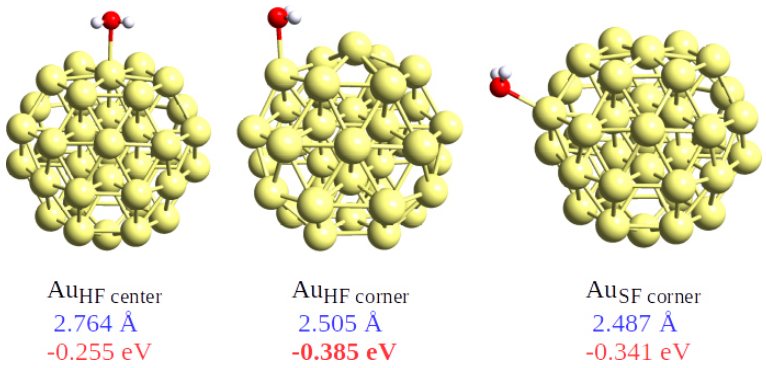

Figure A.1. *Optimized adsorption structures of water monomers on different top adsorption sites for Au_{38} (rto). The Au-O bond distances are reported in blue characters (Å), whereas the adsorption energies in red characters (eV) (the most stable structure with bold characters).*

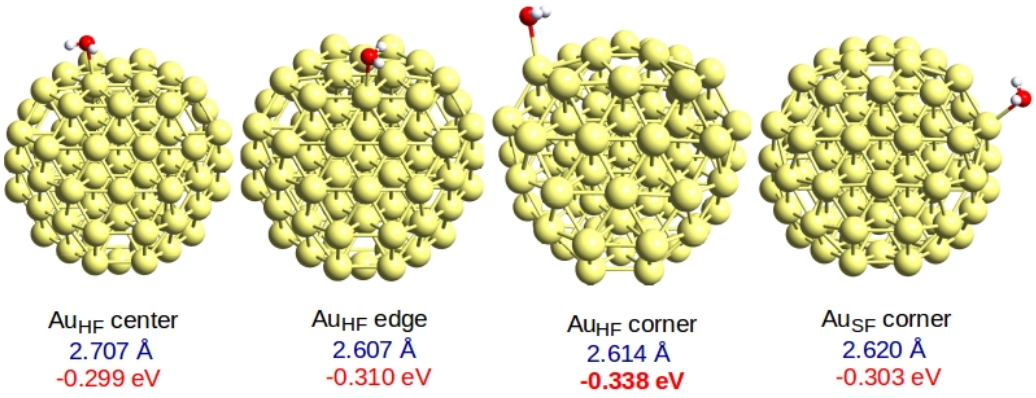

Figure A.2. *Optimized adsorption structures of water monomers on different top adsorption sites for Au_{79} (ito). The Au-O bond distances are reported in blue characters*

(Å), whereas the adsorption energies in red characters (eV) (the most stable structure with bold characters).

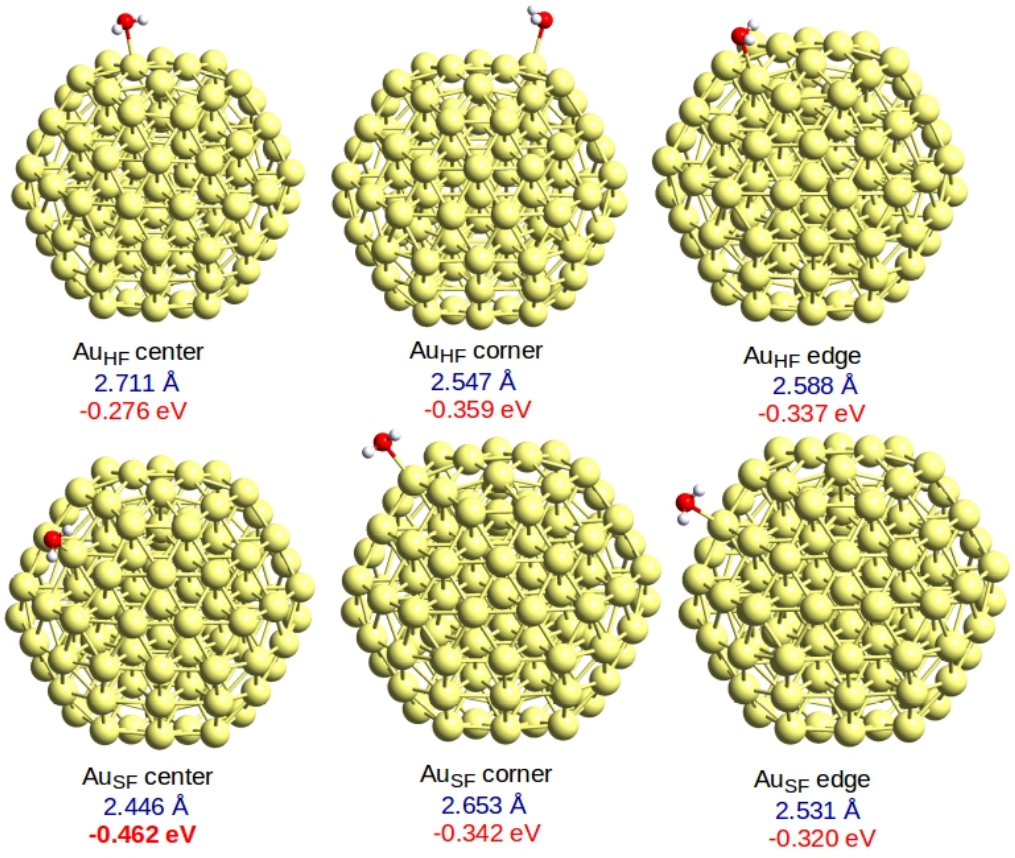

Figure A.3. *Optimized adsorption structures of water monomers on different top adsorption sites for Au_{116} (ito). The Au-O bond distances are reported in blue characters (Å), whereas the adsorption energies in red characters (eV) (the most stable structure with bold characters).*

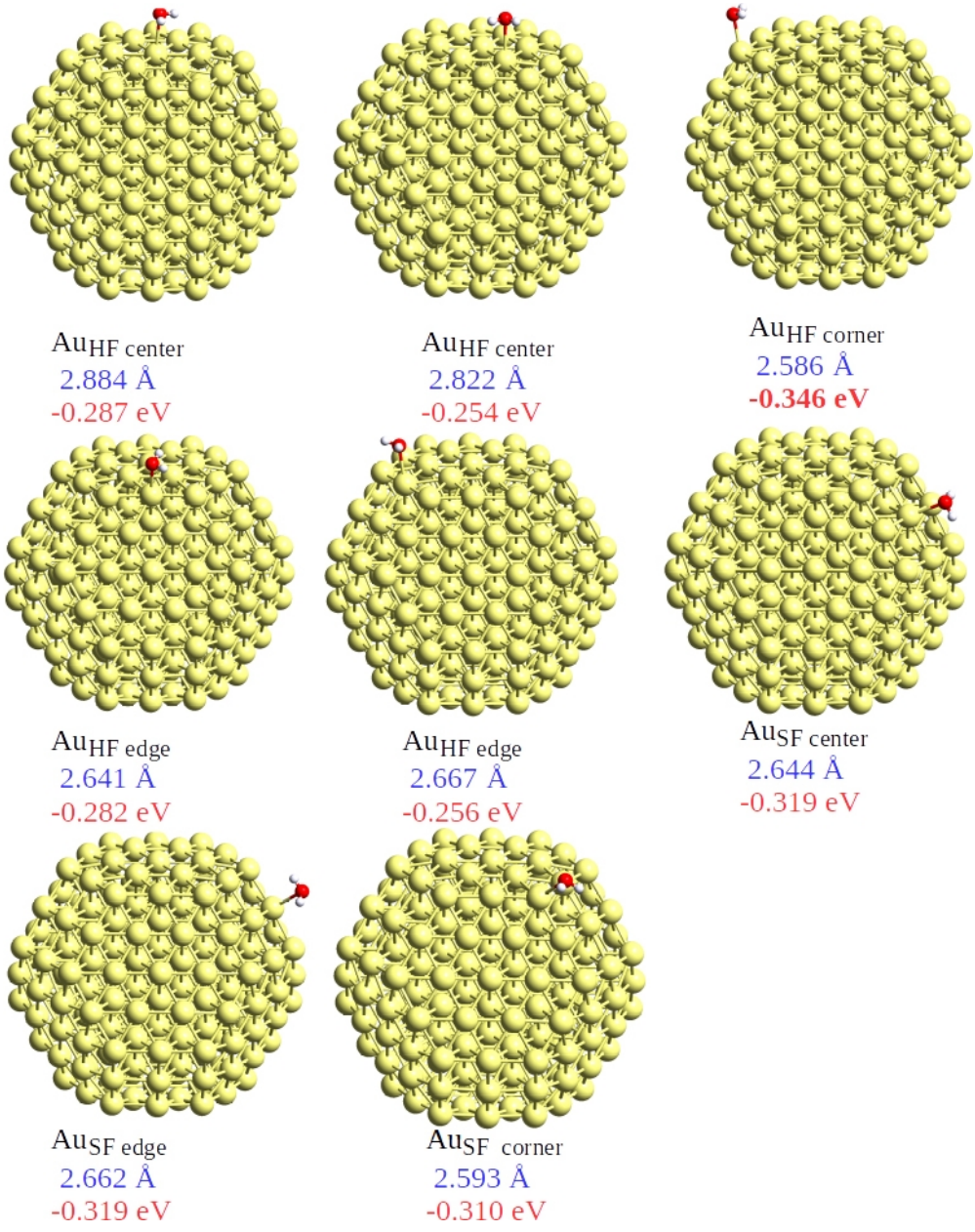

Figure A.4. *Optimized adsorption structures of water monomers on different top adsorption sites for Au_{201} (rto). The Au-O bond distances are reported in blue characters (Å), whereas the adsorption energies in red characters (eV) (the most stable structure with bold characters).*

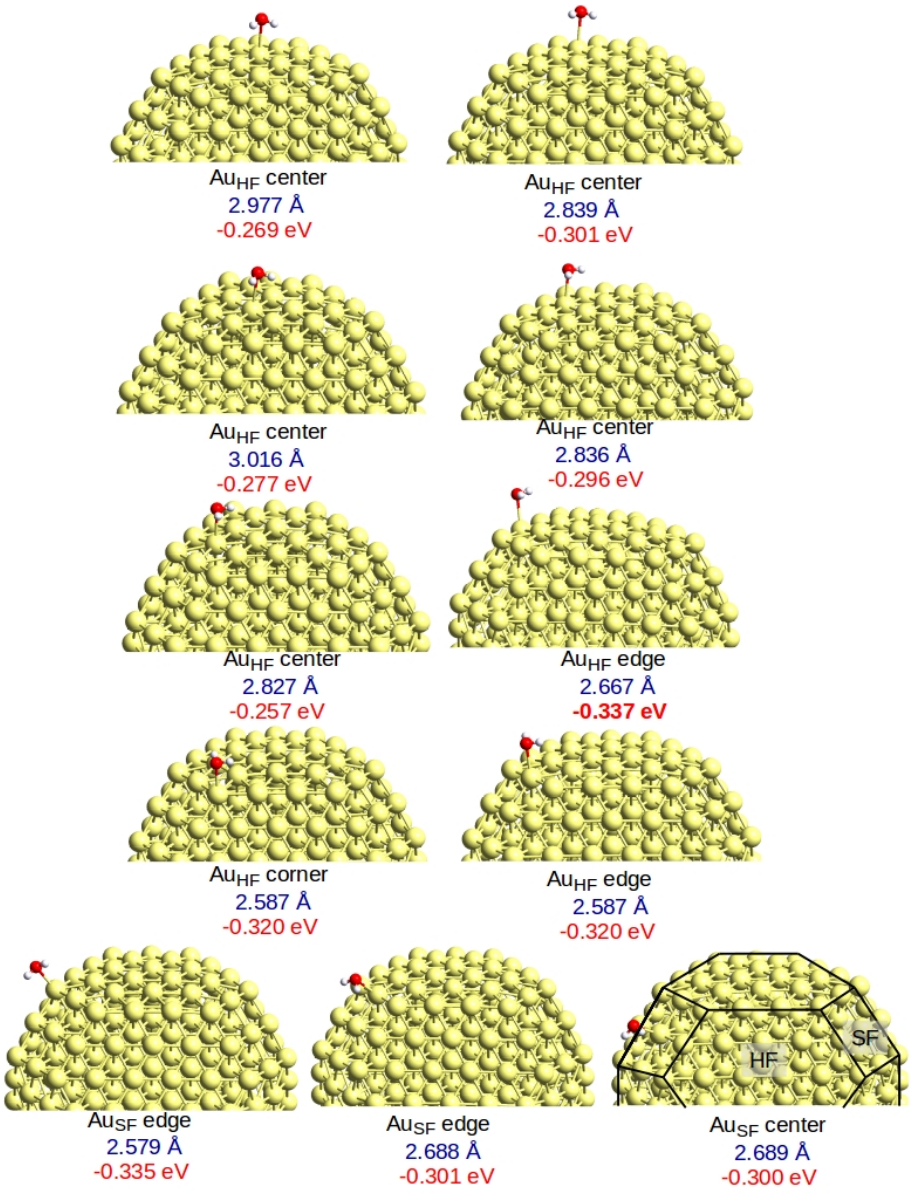

Figure A.5. *Optimized adsorption structures of water monomers on different top adsorption sites for Au_{314} (ito). HF and SF correspond to hexagonal and square facet, respectively. The Au-O bond distances are reported in blue characters (Å), whereas the adsorption energies in red characters (eV) (the most stable structure with bold characters).*

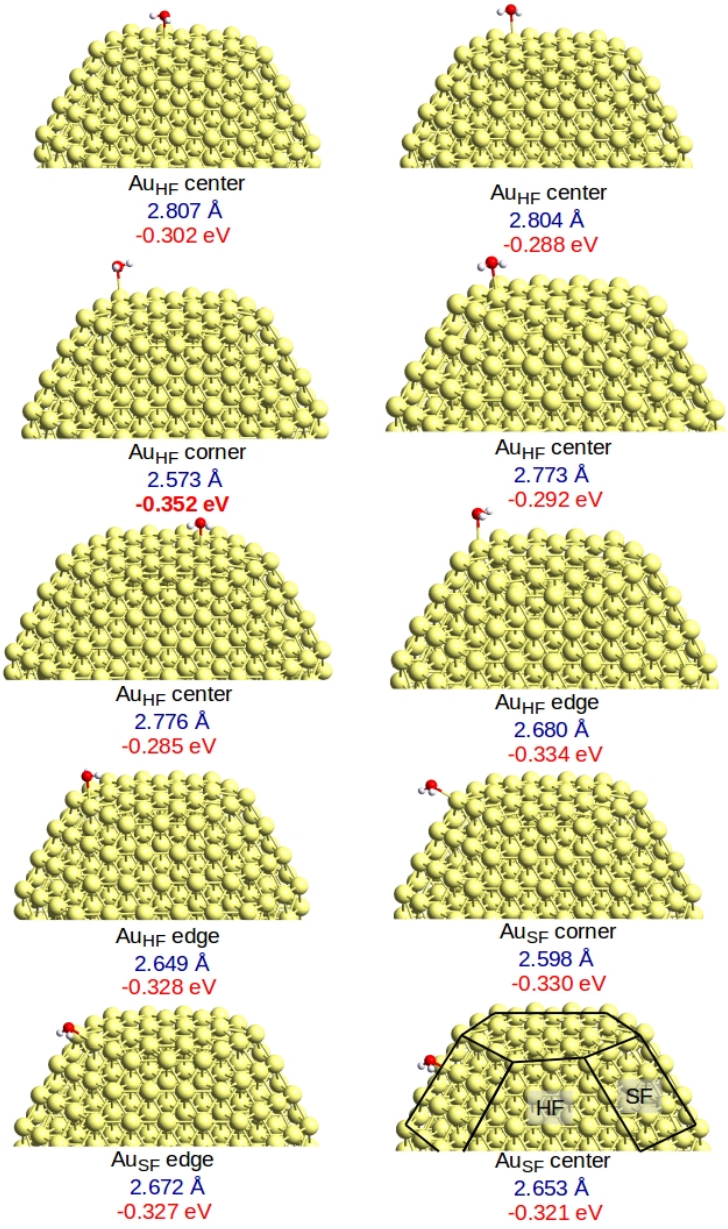

Figure A.6. *Optimized adsorption structures of water monomers on different top adsorption sites for Au_{405} (ito). HF and SF correspond to hexagonal and square facet, respectively. The Au-O bond distances are reported in blue characters (Å), whereas the adsorption energies in red characters (eV) (the most stable structure with bold characters).*

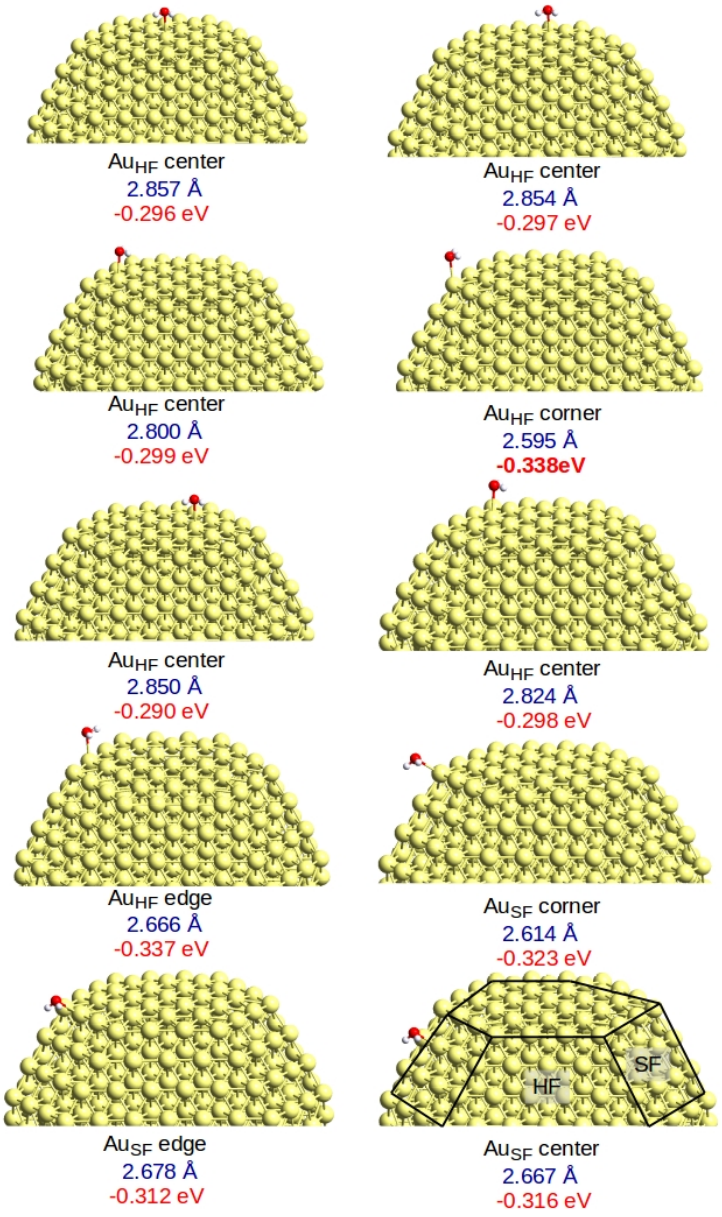

Figure A.7. *Optimized adsorption structures of water monomers on different top adsorption sites for* Au_{586} *(rto). HF and SF correspond to hexagonal and square facet, respectively. The Au-O bond distances are reported in blue characters (Å), whereas the adsorption energies in red characters (eV) (the most stable structure with bold characters).*

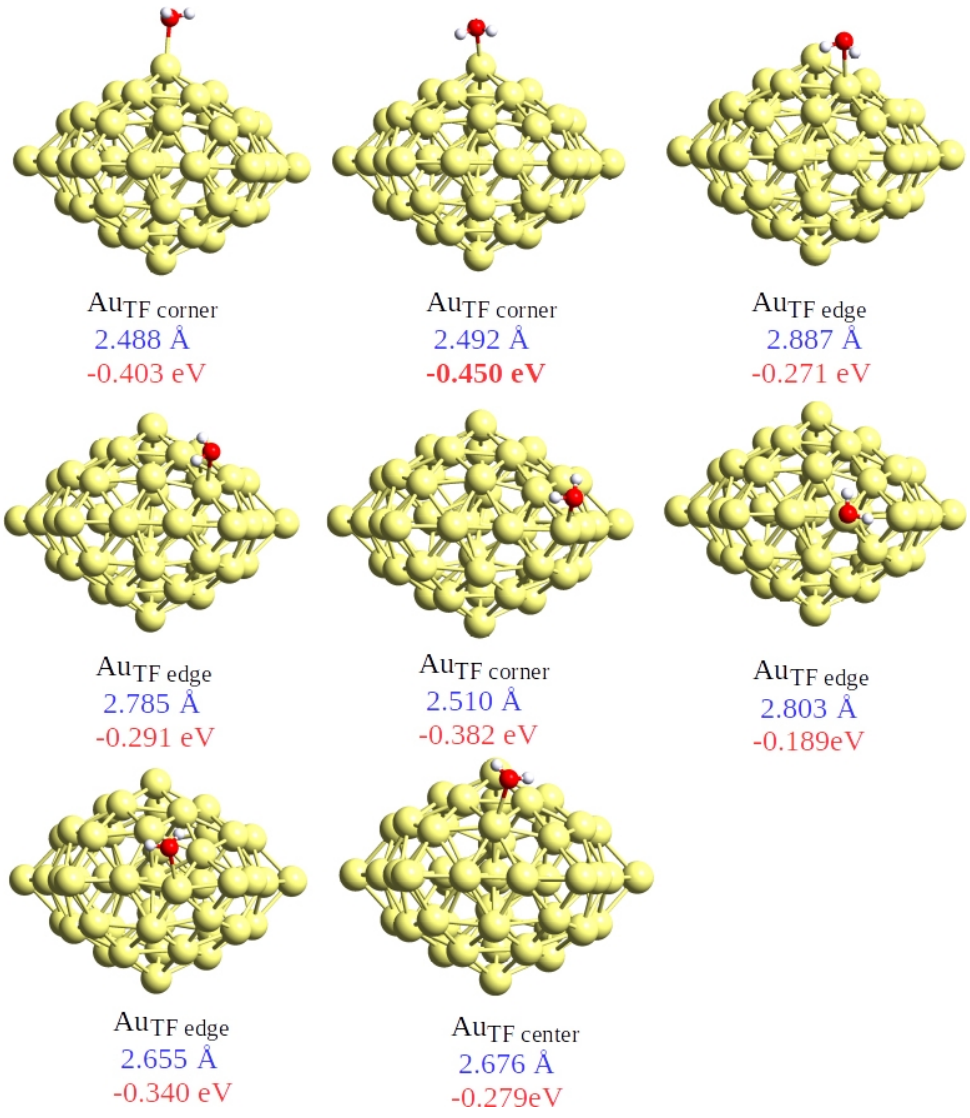

Figure A.8. *Optimized adsorption structures of water monomers on different top adsorption sites for Au_{54} (deca). The Au-O bond distances are reported in blue characters (Å), whereas the adsorption energies in red characters (eV) (the most stable structure with bold characters).*

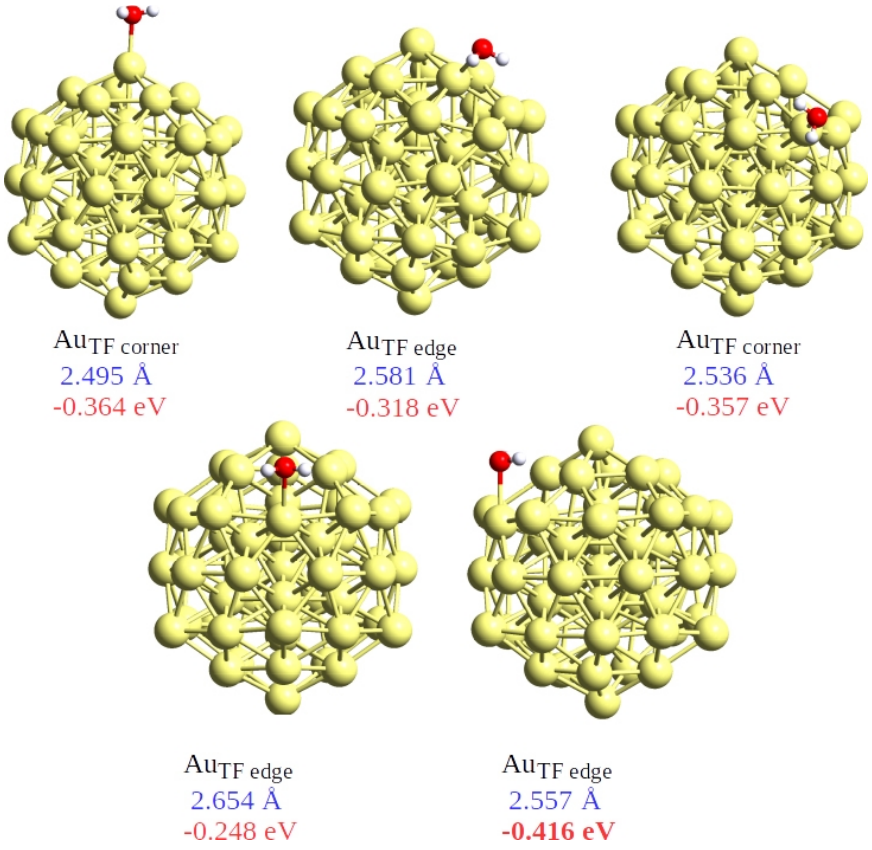

Figure A.9. *Optimized adsorption structures of water monomers on different top adsorption sites for Au_{55} (ico). The Au-O bond distances are reported in blue characters (Å), whereas the adsorption energies in red characters (eV) (the most stable structure with bold characters).*

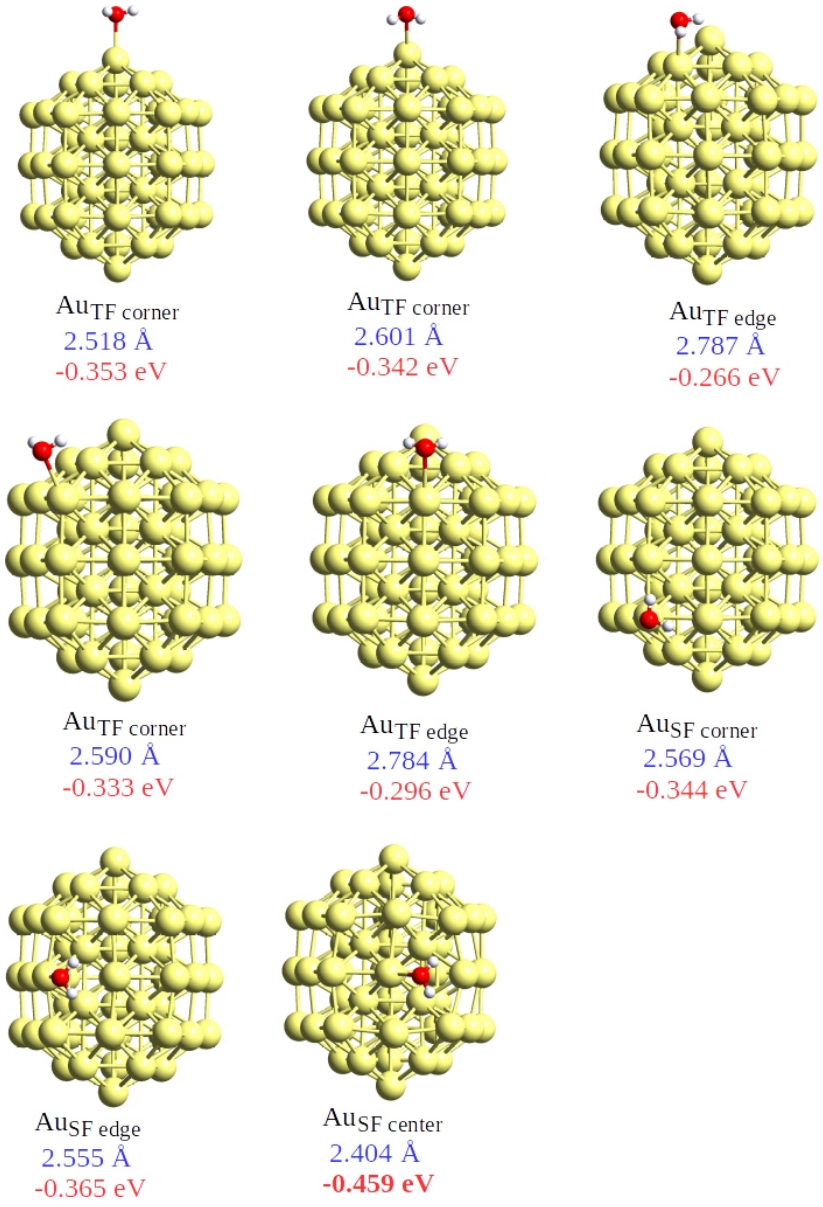

Figure A.10. *Optimized adsorption structures of water monomers on different top adsorption sites for Au_{55} (ino). The Au-O bond distances are reported in blue characters (Å), whereas the adsorption energies in red characters (eV) (the most stable structure with bold characters).*

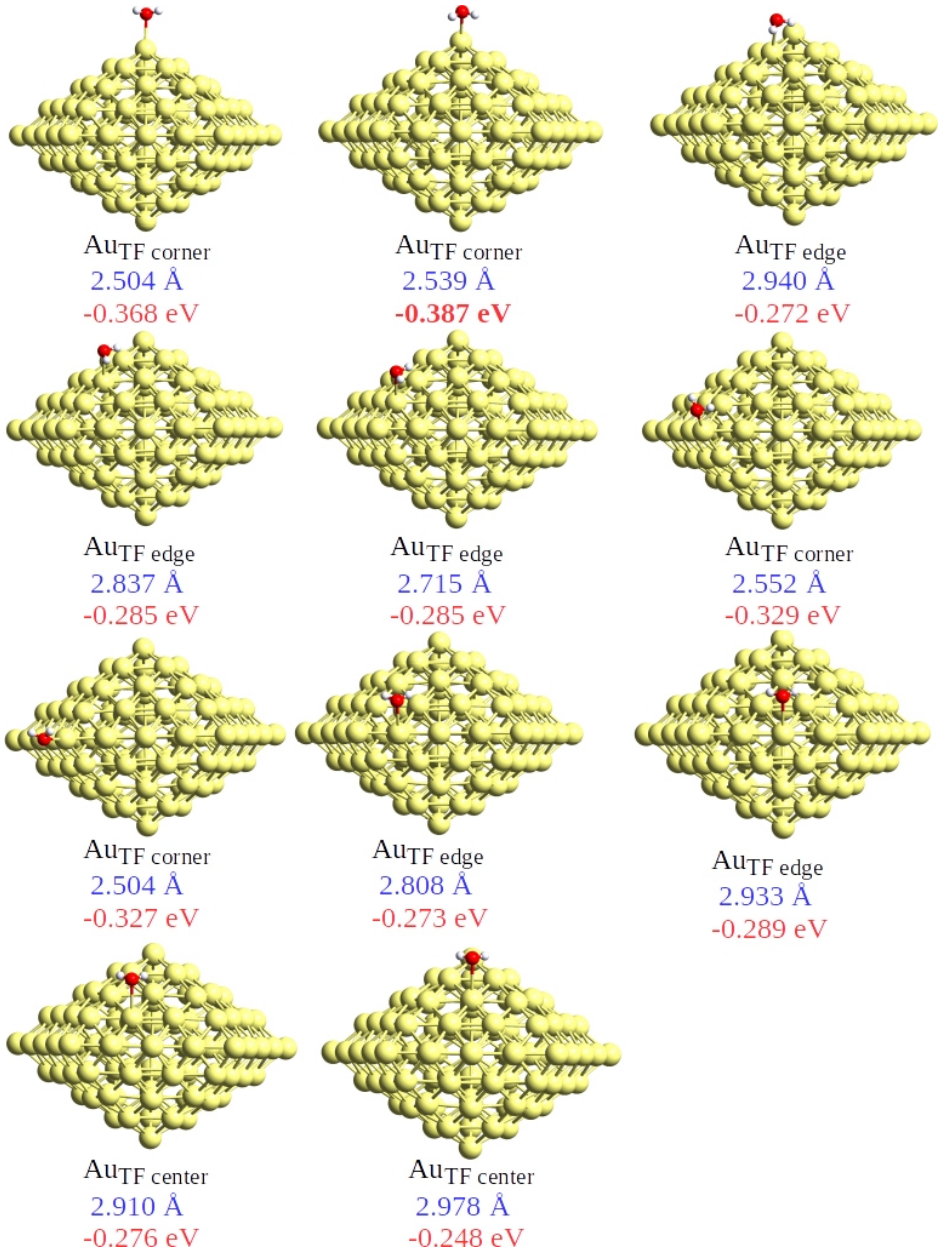

Figure A.11. *Optimized adsorption structures of water monomers on different top adsorption sites for Au_{105} (deca). The Au-O bond distances are reported in blue characters (Å), whereas the adsorption energies in red characters (eV) (the most stable structure with bold characters).*

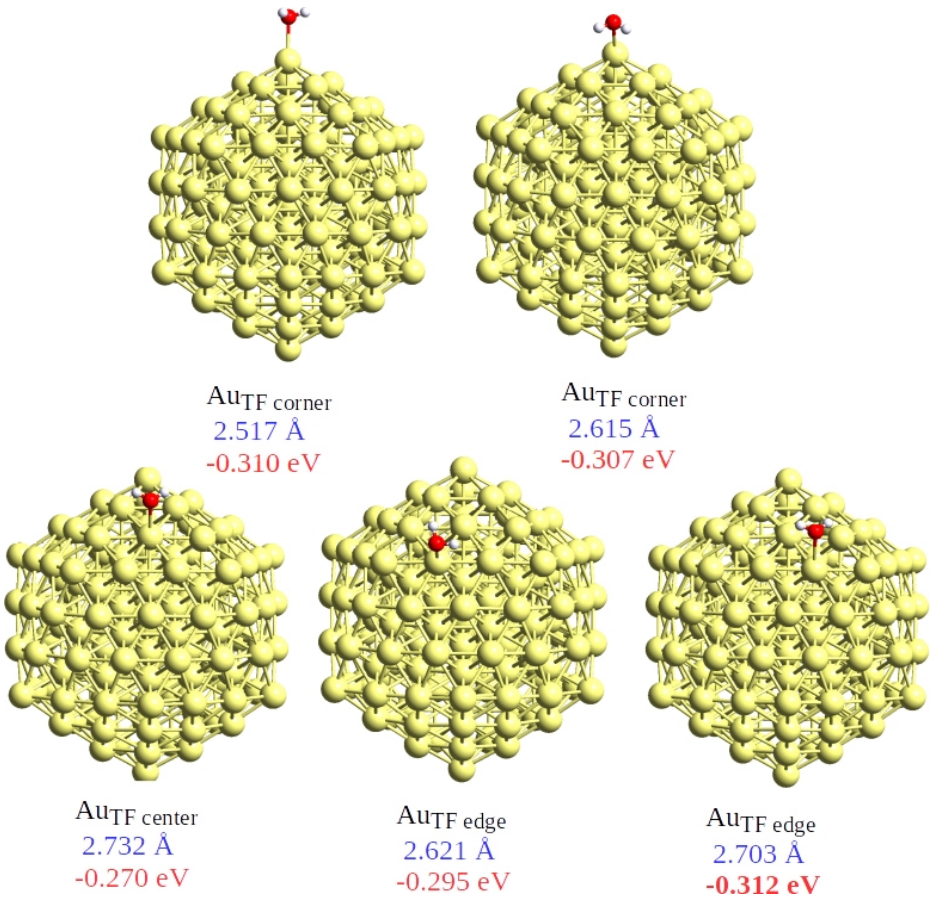

Figure A.12. *Optimized adsorption structures of water monomers on different top adsorption sites for Au_{147} (ico). The Au-O bond distances are reported in blue characters (Å), whereas the adsorption energies in red characters (eV) (the most stable structure with bold characters).*

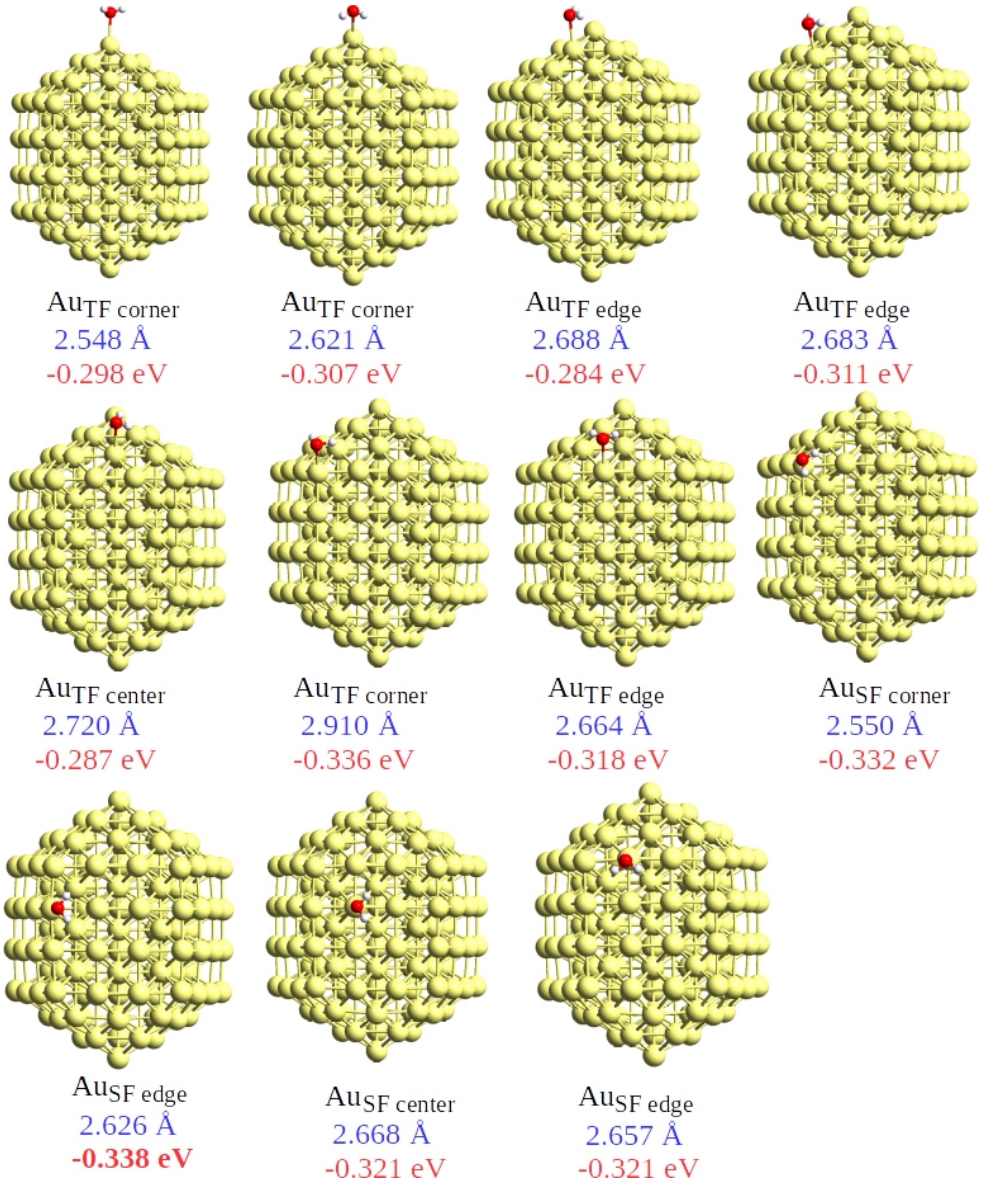

Figure A.13. *Optimized adsorption structures of water monomers on different top adsorption sites for* Au_{147} *(ino). The Au-O bond distances are reported in blue characters (Å), whereas the adsorption energies in red characters (eV) (the most stable structure with bold characters).*

Appendix B: DFT Electrostatic Potentials of Hydrated AuNPs

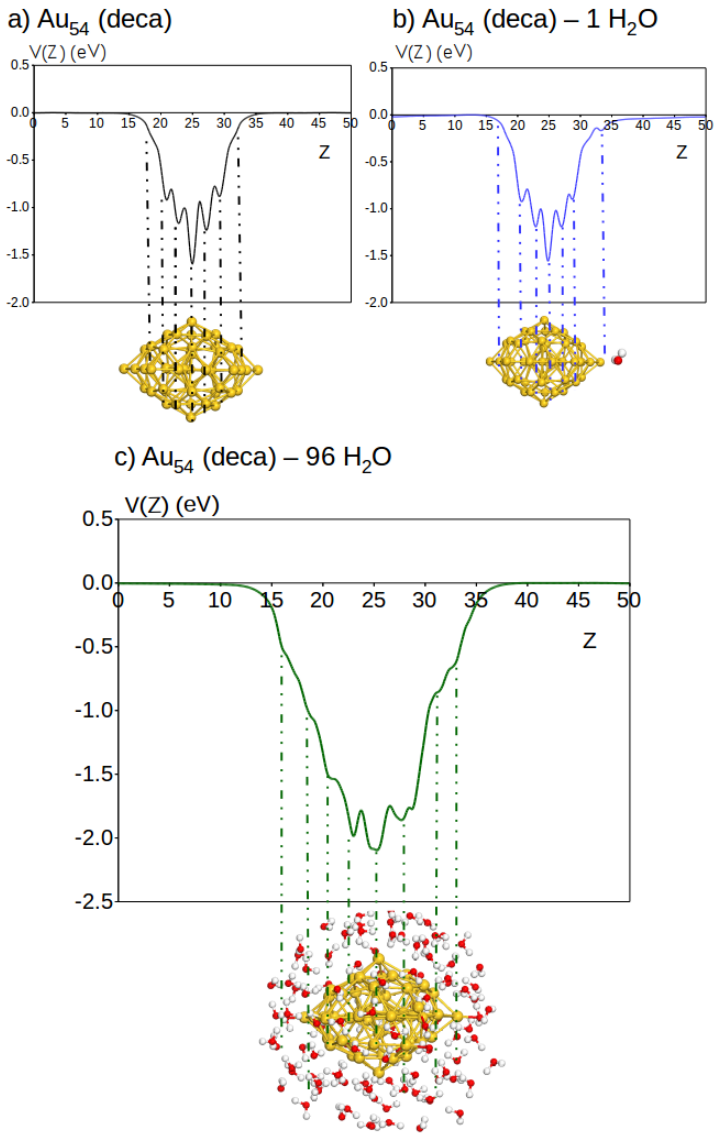

Figure B.1. *Average electrostatic potential [V(Z)] in eV along the direction of Z axis and its corresponding with the atomic plane of for the case of* Au_{54} *(deca) is plotted for the a) naked NP , b) NP with isolated water adsorption and c) NP with adsorption of one shell of water molecules.*

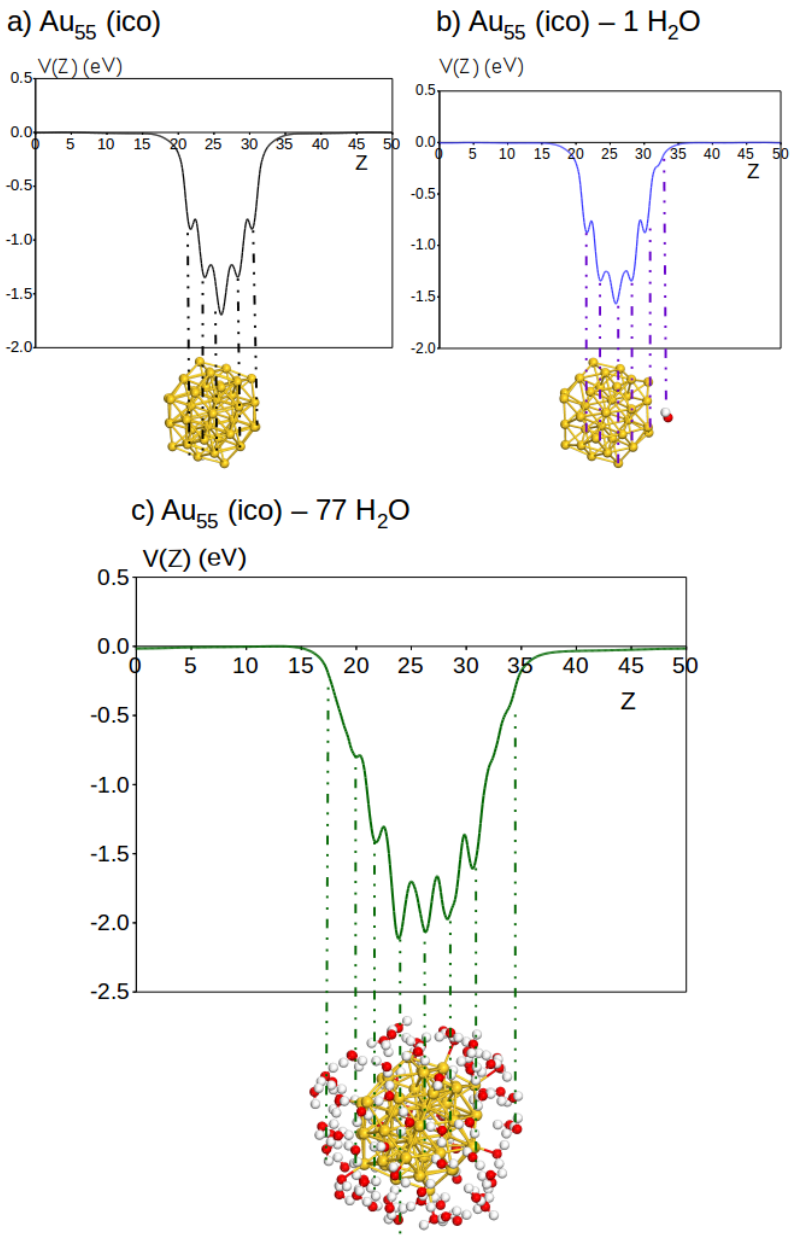

Figure B.2. *Average electrostatic potential [V(Z)] in eV along the direction of Z axis and its corresponding with the atomic plane of for the case of Au_{55} (ico) is plotted for the a) naked NP , b) NP with isolated water adsorption and c) NP with adsorption of one shell of water molecules.*

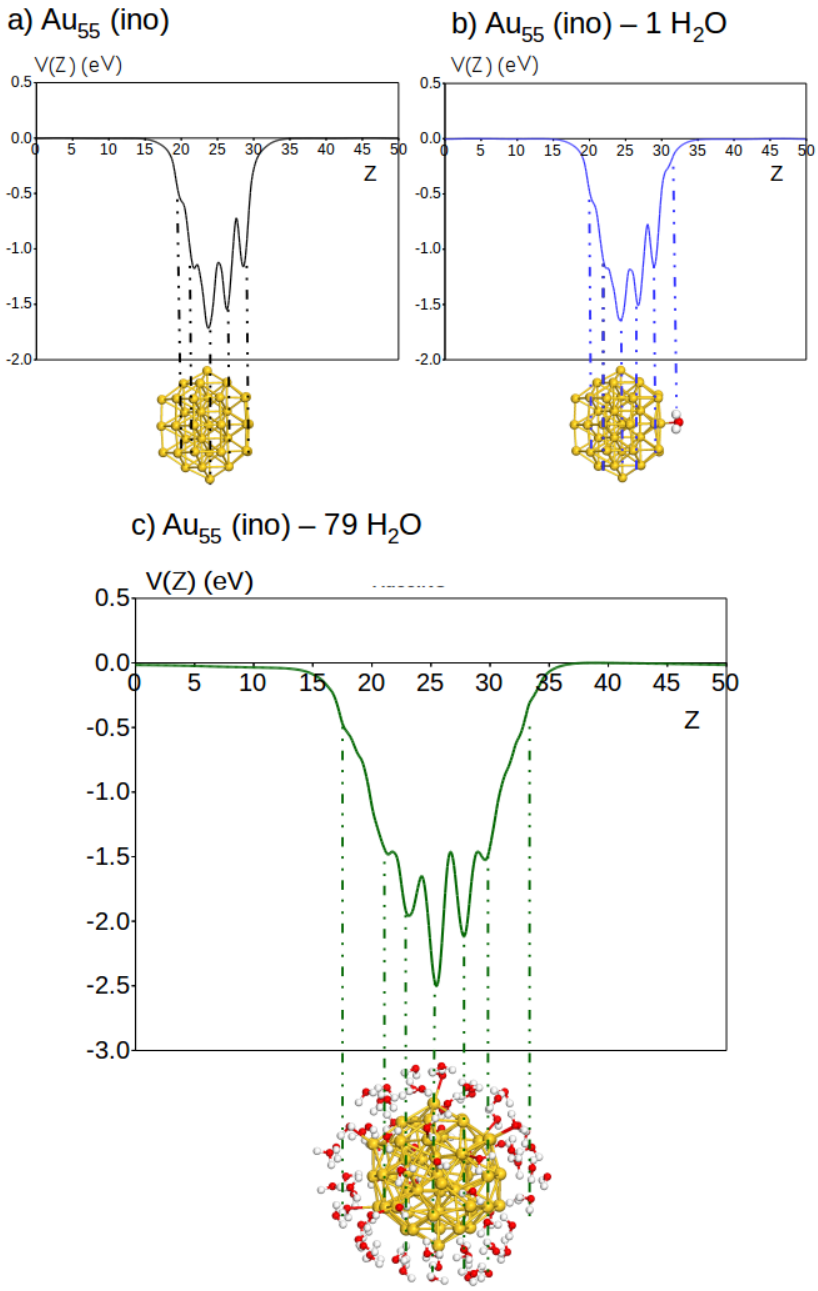

Figure B.3. *Average electrostatic potential [V(Z)] in eV along the direction of Z axis and its corresponding with the atomic plane of for the case of Au_{55} (ino) is plotted for the a) naked NP , b) NP with isolated water adsorption and c) NP with adsorption of one shell of water molecules.*

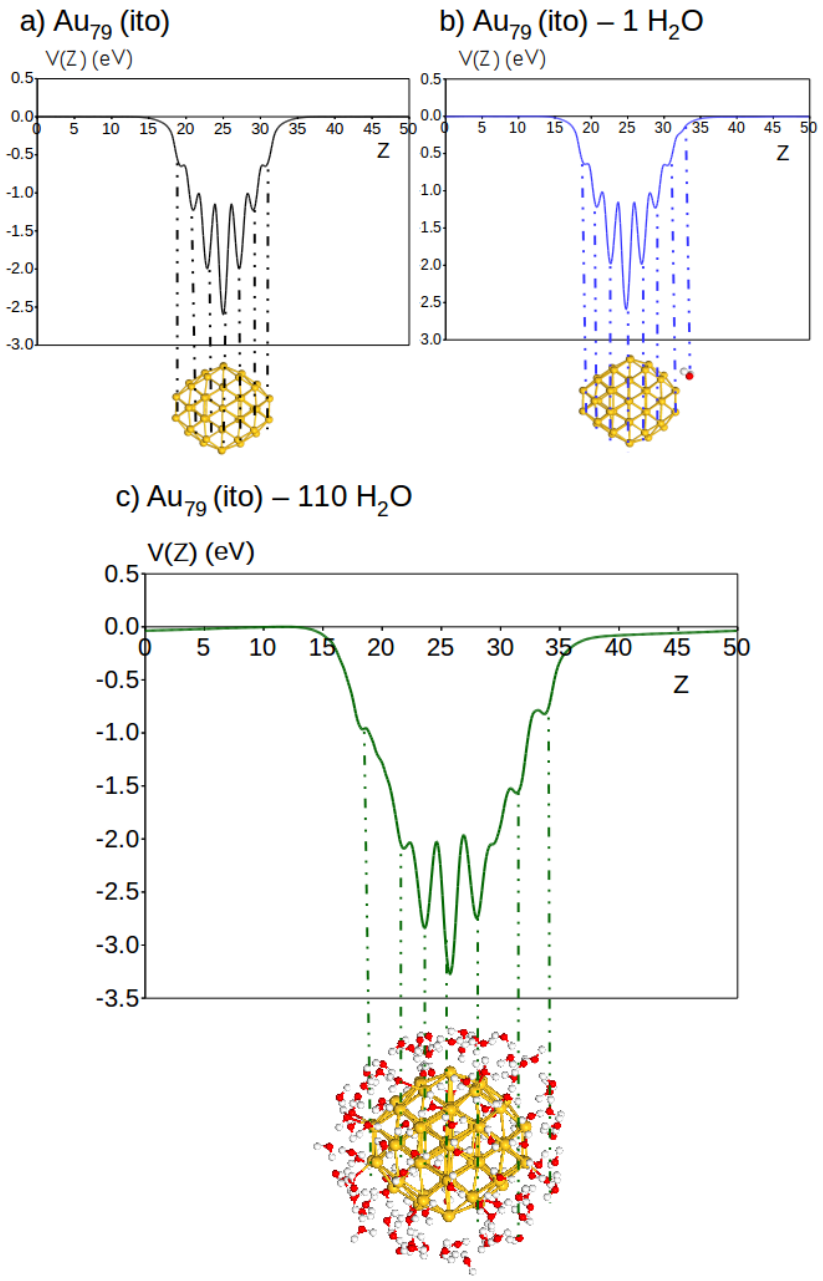

Figure B.4. *Average electrostatic potential [V(Z)] in eV along the direction of Z axis and its corresponding with the atomic plane of for the case of* Au_{79} *(ito) is plotted for the a) naked NP , b) NP with isolated water adsorption and c) NP with adsorption of one shell of water molecules.*

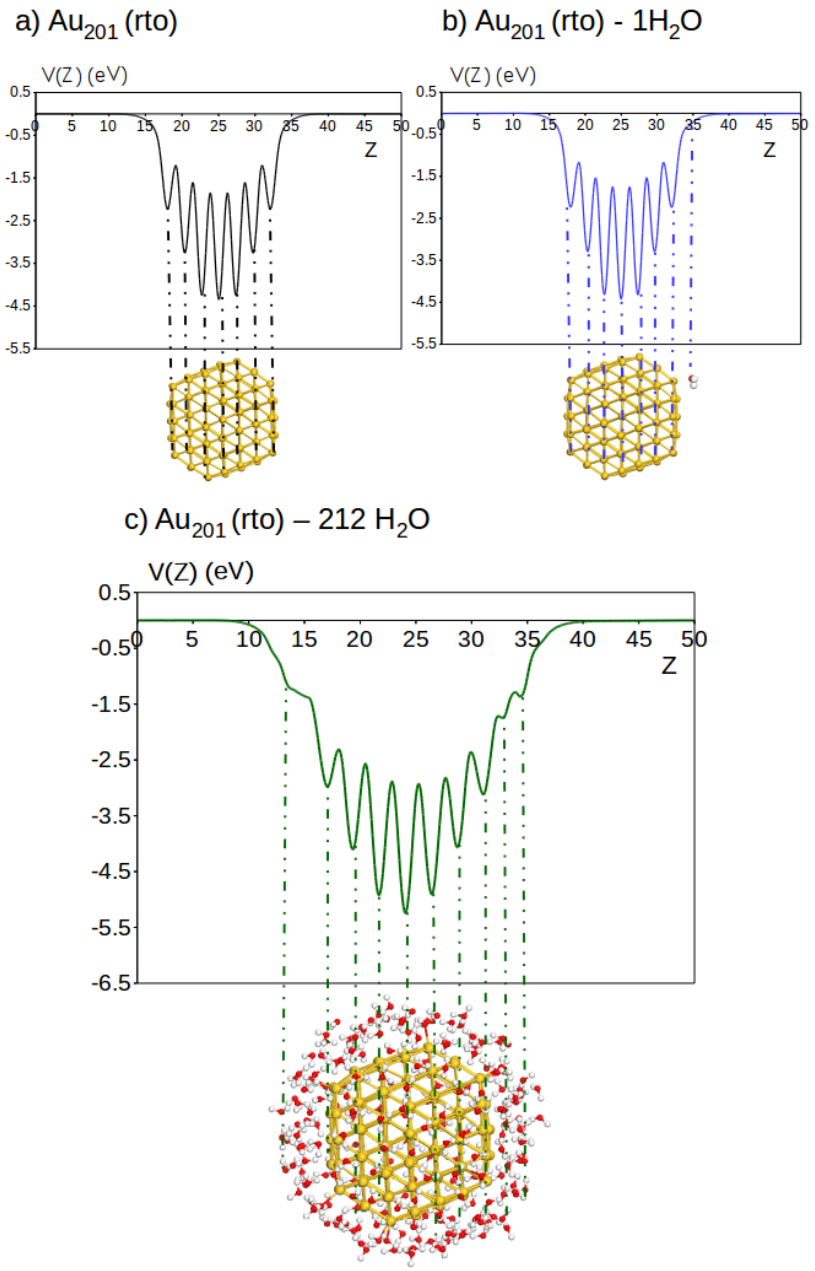

Figure B.5. *Average electrostatic potential [V(Z)] in eV along the direction of Z axis and its corresponding with the atomic plane of for the case of* Au_{201} *(rto) is plotted for the a) naked NP , b) NP with isolated water adsorption and c) NP with adsorption of one shell of water molecules.*